UNIVERSIDADE DE SÃO PAULO
INSTITUTO DE GEOCIÊNCIAS

Carbon and sulfur biogeochemical cycles in the Brazilian Ediacaran record

SERGIO CAETANO FILHO

Tese apresentada ao Programa de Pós-Graduação em Geociências - Geoquímica e Geotectônica para obtenção do título de Doutor em Ciências.

Área de concentração: Geotectônica

Orientadora: Prof[a]. Dr[a]. Marly Babinski

Coorientador: Prof. Dr. Ricardo I. F. Trindade

SÃO PAULO
2020

Serviço de Biblioteca e Documentação do IGc/USP
Ficha catalográfica gerada automaticamente com dados fornecidos pelo(a) autor(a)
via programa desenvolvido pela Seção Técnica de Informática do ICMC/USP

Bibliotecários responsáveis pela estrutura de catalogação da publicação:
Sonia Regina Yole Guerra - CRB-8/4208 | Anderson de Santana - CRB-8/6658

Caetano Filho, Sergio
Carbon and sulfur biogeochemical cycles in the Brazilian Ediacaran record / Sergio Caetano Filho; orientadora Marly Babinski; coorientador Ricardo Ivan Ferreira da Trindade. -- São Paulo, 2020.
282 p.

Tese (Doutorado - Programa de Pós-Graduação em Geoquímica e Geotectônica) -- Instituto de Geociências, Universidade de São Paulo, 2020.

1. Ediacarano. 2. Quimioestratigrafia. 3. Geoquímica isotópica. 4. Carbono. 5. Enxofre. I. Babinski, Marly, orient. II. Ivan Ferreira da Trindade, Ricardo, coorient. III. Título.

UNIVERSIDADE DE SÃO PAULO
INSTITUTO DE GEOCIÊNCIAS

Carbon and sulfur biogeochemical cycles in the Brazilian Ediacaran record

SERGIO CAETANO FILHO

Orientadora: Profa. Dra. Marly Babinski

Tese de Doutorado

Nº 629

COMISSÃO JULGADORA

Dra. Marly Babinski

Dr. Fabrício de Andrade Caxito

Dr. Huan Cui

Dra. Linda Christine Kah

Dra. Milene Freitas Figueiredo

Dra. Rosalie Tostevin

SÃO PAULO

2020

À minha família

Agradecimentos

Gostaria de enfatizar que o desenvolvimento técnico-científico desta tese foi possível graças ao apoio de muitos. Sendo assim, os meus agradecimentos são direcionados a dezenas de pessoas, em especial:

À minha orientadora, Prof[a]. Marly Babinski, que entre as minhas idas e vindas, há 11 anos exerce de forma impecável seu papel de orientadora e mestra. Obrigado pela confiança e pelas oportunidades a mim oferecidas.

Ao Dr. Gustavo Paula-Santos, quem também posso considerar meu orientador e mentor, pela iniciação nessa área, pelos ensinamentos e conselhos, e inúmeras conversas geológicas que sempre rendem boas ideias. Espero que ainda tenhamos uma longa parceria.

Ao grupo de quimioestratigrafia do IGc-USP, em especial, Cristian, Carolina, Juan e Paula, pelo trabalho em equipe exemplar e diversas discussões e integrações de dados.

Ao meu coorientador Prof. Ricardo Trindade, por importantes inserções e conselhos dados ao longo do projeto. Também agradeço a confiança e a oportunidade que me foi dada.

A toda equipe do Projeto Temático FAPESP "O Sistema Terra e a evolução da vida durante o Neoproterozoico", pelo suporte e discussões frutíferas acerca dos temas que nos une. Em especial aos professores Matheus Kuchenbecker, Humberto Reis e Juliana Leme, bem como aos sedimentólogos que tanto me ensinaram, Jhon Afonso e Prof[a]. Kamilla Amorim.

A todos os profissionais do Instituto de Geociências da Universidade de São Paulo, do CPGeo, em especial Alyne e Vasco.

A todos do Grupo de *Géochimie des Isotopes Stables* do Institut de Physique du Globe de Paris, em especial, a Dra. Magali Ader, Dr. Pierre Sansjofre, Dr. Pierre Cartigny, Dr. Nelly Assayag, Dr. Virgínia Rojas. Pelos parceiros de laboratório de enxofre Bryan, Amaury, Isabelle, Laetitia e Adeline.

Ao corpo técnico do *Laboratoire de Géociences Océan* da Universidade de Brest.

À Fundação de Amparo à Pesquisa do Estado de São Paulo (FAPESP) pelo financiamento desta pesquisa, via bolsas de estudos no país e no exterior (#2016/11496-5 e #2018/19302-0) e via Projeto Temático (#2016/06114-6).

Ao Conselho Nacional de Desenvolvimento Científico e Tecnológico (CNPq) pelo financiamento de parte desta pesquisa dentro do projeto #400764/2016-4.

Tão importante quanto, estão aqueles que sempre me apoiaram e se fizeram presentes de alguma forma durante esses últimos quatro anos:

À minha companheira e melhor amiga, Flávia. Pelo companheirismo, compreensão, paciência, suporte, amor e carinho. Obrigado por estar sempre ao meu lado e suportar todos os desafios dessa fase.

À minha família, meus pais, Sergio e Alaide, minha irmã Aline, meu cunhado Diogo e meu sobrinho e afilhado Joaquim que me trouxe muita alegria nesses últimos 3 anos. Obrigado pela união e suporte de sempre. Aqui se encerra um ciclo iniciado há 30 anos no qual vocês são grandes responsáveis e incentivadores.

Ao meus amigos de Turma 51 e graduação, que insistem em se manter por perto: Renato C., Bárbara, Renato M., Guilherme G., Guilherme N., Marcelo, Dailson, Paulo, Caio, Caramello.

Aos amigos da Maison du Brésil, que me acolheram e fizeram o ano longe de casa passar mais rápido, a base de muitos pães, queijos e vinhos.

Ao meu amigo Eric Siciliano, pela parceria firmada em terras francesas, IPAs, crepes e vinhos... e muitas discussões sobre a vida.

Ao meu amigo Raphael Pietzsch, pelos encontros no Velho Continente e por muitas conversas inspiradoras sobre ciência, vida, passado, futuro...

À minha amiga Alessandra Faresin, mesmo distante, sempre preocupada e presente.

Por fim, a todos aqueles que de alguma forma participaram desta etapa.

“In science every answer creates *many* more questions”

Edward O. Wilson

Resumo

Grandes inovações evolutivas estão associadas a significativas anomalias geoquímicas ao longo do registro sedimentar do Ediacarano, no final do Neoproterozoico, as quais por sua vez são atribuídas à oxigenação final da superfície terrestre, conhecido como Evento de Oxigenação do Neoproterozoico. Estudos envolvendo isótopos de carbono e enxofre são fundamentais para o estabelecimento de maiores eventos de oxidação, associados no tempo a aparições de assembleias de metazoários. Apesar da existência de intervalos pontuais no Ediacarano apresentando excursões acopladas de carbono e enxofre em diversas seções pelo globo, um número crescente de estudos aponta para modelos geoquímicos complexos que variam entre as bacias, de acordo com controles locais paleoambientais/paleoceanográficos. Tais observações justificam a execução de estudos isotópicos integrados a modelos sedimentológicos/estratigráficos apropriados, buscando a reconstrução da dinâmica da geoquímica marinha atuante durante a evolução dos primeiros animais. Neste sentido, a presente tese investiga duas unidades ediacaranas do Brasil localizadas em diferentes contextos geotectônicos, buscando a comparação entre a evolução isotópica de carbono pareado (carbonato e carbono orgânico) e múltiplos isótopos de enxofre para distinção de processos locais em relação àqueles de maior escala. Na região centro-leste brasileira, o Grupo Bambuí, Bacia do São Francisco, corresponde à uma bacia epicontinental ediacarana-cambriana com conteúdo fóssil bastante limitado e grandes anomalias isotópicas de carbono provavelmente associadas à restrição da bacia. Por outro lado, a Formação Tamengo, Grupo Corumbá, Faixa Paraguai Sul (centro-oeste brasileiro), apresenta um rico registro paleontológico de uma plataforma carbonática ediacarana localizada na margem do Gondwana Ocidental. O estudo de carbono pareado realizado nessas unidades possibilitou reconstruções distintas para ciclos de carbono em cada contexto, no qual a bacia epicontinental Bambuí atravessou grandes perturbações resultando em desacoplamento entre os ciclos de carbono bacinal e global, enquanto a rampa carbonática Tamengo apresentou pequenas anomalias aparentemente relacionadas à maior oxigenação em ambientes habitados pelos primeiros metazoários biomineralizantes. O registro isotópico de enxofre apresentou algumas similaridades entre as unidades, sugerindo uma forçante maior agindo sobre o sistema de enxofre das duas bacias. Entretanto, controles locais associados aos contextos geotectônicos específicos no Gondwana Ocidental resultaram em diferentes produtos. Um evento dramático de exaustão de sulfato no mar epicontinental Bambuí pode ter levado ao aumento de euxinia e, consequentemente, ambientes bastante tóxicos para colonização animal

dentro do continente. Tal evento pode ter resultado em concentrações baixas e limitadas de sulfato que pode também ter ocasionado uma mudança biogeoquímica na bacia, com predominância de metanogênese microbial como importante metabolismo. Esse processo no interior dos continentes pode ter sido responsável pela geração de grandes fluxos de metano para atmosfera com potencial impacto sobre o clima global na transição Ediacarano-Cambriano, possivelmente levando a Terra a deixar a era das grandes glaciações neoproterozoicas para um clima mais ameno e favorável ao pleno desenvolvimento da vida no Cambriano.

Abstract

Biological innovations associated with geochemical disturbances characterize the Ediacaran geological record, at the end of Neoproterozoic Era, which are attributed to the oxygenation of Earth's surface environments – the so-called Neoproterozoic Oxygenation Event. Carbon and sulfur stable isotopes studies are key tools to examine major oxidation events in the marine environment. Despite the existence of Ediacaran intervals that record coupled carbon and sulfur isotope anomalies worldwide, an increasing number of studies suggest that variation may also reflect local paleoenvironmental/ paleogeographic controls that differ basin to basin. These results justify detailed isotope geochemistry studies integrated through a proper sedimentological/stratigraphic assessment to decipher marine geochemistry dynamics acting when first animals were evolving. For this purpose, this thesis investigated two different Ediacaran settings from Brazil, aiming to compare the carbon and multiple sulfur isotope evolution and distinguish local and global processes. In the central-east Brazil, the Bambuí Group, São Francisco Basin, corresponds to an Ediacaran-Cambrian epicontinental basin with a very poor fossil record and well-known major carbon isotope disturbances probably associated with basin restriction. On the other hand, the Tamengo Formation, Corumbá Group, South Paraguay Belt (central-west Brazil), rocords a rich paleontological record within an Ediacaran carbonate platform located at the continental margin. Paired carbon isotopes for these two units allow reconstructions of carbon cycling within paleogeographic context, in which the epicontinental Bambuí sea experienced a greater degree of variability resulting from decoupling of basinal and global carbon cycles, whereas the Tamengo ramp records isotope signals apparently linked to enhanced oxygenation in environments inhabited by early biomineralizing metazoans. The sulfur isotope record in these basins points to a major forcing presiding over the sulfur system in both basins. However, local controls that depend on the tectonic context of these basins seem to have resulted in different responses. A dramatic event of sulfate exhaustion in the epicontinental Bambuí sea could have resulted in enhanced euxinia and toxic environments, challenging the colonization of the continental interior by early metazoans. On the other hand, sulfate depletion under sulfate-limited conditions may have favored a biogeochemical turnover in the basin for a methanogenic dominated environment, which could represent large methane fluxes to the atmosphere with potential impacts over global climate. Methanogenic basins in the continent interior might have contributed to drive Earth out from Neoproterozoic worldwide glaciations to a more warm planet, favorable to the full diversification of life in the Cambrian.

SUMMARY

1. INTRODUCTION

1.1. Motivation

The Ediacaran Period is an interval of extreme changes in the climatological and biological systems. It began with a recover from the global-scale Marinoan glaciation, followed by the appearance of several of biological innovations. Remarkable changes in the evolutionary history of the Earth are represented by the appearance of soft-bodied macroscopic metazoans assemblages in the middle Ediacaran, followed by the first biomineralizing organisms and development of complex ecological interactions in the late Ediacaran, preceding the Cambrian explosion (e.g. Knoll et al., 2006; Narbonne et al., 2012). Such climatological and biological changes are accompanied by geochemical disturbances in the carbon and sulfur isotope record. Taken together, they are consequently associated each other in a cause-and-effect relationship, often assigned to the final oxygenation of the Earth's surface (the Neoproterozoic Oxygenation Event – NOE; Och and Shields-Zhou, 2012).

A combination of both anoxic bottom conditions, varying from ferruginous to euxinic (e.g. Hurtgen et al., 2006; Canfield et al., 2008; Tostevin et al., 2016), and oxygenated bottom conditions (e.g. Canfield et al., 2007; McFadden et al., 2008; Sahoo et al., 2012; 2016; Ader et al., 2014; Wood et al., 2015) point to a complex redox distribution among marine environments, which makes it difficult to propose a single environmental scenario for the Ediacaran. Evidences for a late Neoproterozoic oxygenation event, especially through the Ediacaran, rely mainly in the carbon and sulfur isotope record presenting larger variations compared to the other periods of the geological record and interpreted as major redox disturbances in the Earth's surface (e.g. Kah et al., 2004; Fike et al., 2006; Halverson and Hurtgen, 2007). Elevated $\delta^{13}C_{carb}$ values are usually interpreted as enhanced organic matter burial resulting in an increase of the oxidizing power of the oceanic-atmospheric systems (Och and Shields-Zhou, 2012). Punctuated negative $\delta^{13}C_{carb}$ excursions also occur in the post-glacial Marinoan deposits, in the early Ediacaran, and in the middle Ediacaran (e.g. Fike et al., 2006; Halverson and Shields-Zhou, 2011). On the other hand, large variations in sulfur isotope compositions recorded both in sulfate and sulfide are believed to represent a small marine sulfate reservoir, which may have increased through the Ediacaran. Greater sulfur isotope fractionation between sulfate and sulfide are also interpreted as reflecting on increase in marine sulfate concentrations resulting from enhanced oxidative continental weathering, which would have boosted microbial sulfate reduction and might represent the onset of an

effective re-oxidative sulfur cycle in the marine environment (e.g. Canfield and Teske, 1996; Kah et al., 2004; Hurtgen et al., 2005; Fike et al., 2006; Halverson and Hurtgen, 2007).

Although carbon and sulfur isotope compositions seem to present coupled trends through the major events in the early and middle Ediacaran (e.g. Halverson and Hurtgen, 2007; Cui et al., 2015; Osburn et al., 2015), some studies have shown a more complex behavior for the carbon and sulfur isotope evolution between different basins, or even through a shallow to deep basin transect (Hurtgen et al., 2006; Loyd et al., 2012; 2013; Tostevin et al., 2017). Besides uncertainties related to temporal correlations and the lack of complete stratigraphic sections, local controls resulting from different paleogeographic/ paleoenvironmental conditions could produce different isotope signatures, making the reconstruction of a global marine scenario based on few sections difficult. Therefore, the understanding of the Ediacaran marine geochemistry and its relationship with biota distribution will be advanced through geochemical investigations accompanied by detailed assessment of paleogeography and paleoenvironment and which focus on the dynamics of biogeochemical processes rather than attempts to propose global conditions from single sections within specific basins.

For this purpose, the present study provides and compares the carbon and sulfur isotope evolution in two different settings both representing the Brazilian Ediacaran record in the context of the West Gondwana. In central-east Brazil, the São Francisco Basin encompasses Ediacaran to Cambrian deposits of the Bambuí Group, and records an epicontinental sea developed in response to late Neoproterozoic Brasiliano-Panafrican orogenies surrounding São Francisco Craton (e.g. Reis et al., 2016). The sedimentary record is characterized by a basal post-glacial cap carbonate succession followed by an interval with rare occurrences of *Cloudina* sp. and *Corumbella werneri*, late Ediacaran index fossils (Warren et al., 2014). The basal Bambuí Group records major disturbances in the carbon and strontium isotope record, attributable to its restricted basin character. Anomalous high $\delta^{13}C_{carb}$ values on the top of the basal late Ediacaran sequence, as well as $^{87}Sr/^{86}Sr$ ratios distinct from late Ediacaran values, suggest paleoenvironmental change reflecting progressive restriction to the open marine system (Paula-Santos et al., 2015; 2017). In this scenario, unusual high $\delta^{13}C_{carb}$ values could result from enhanced organic matter burial or the increase of methanogenesis influence during the progressive sulfate exhaustion (Santos et al., 2004; Martins and Lemos, 2007; Paula-Santos et al., 2017). Although such conditions might have limited the colonization by the early metazoans, the major forcing mechanisms remain uncertain. On the other hand, the Tamengo Formation within the Southern Paraguay Belt, as a

late Neoproterozoic fold and thrust belt domain in the central-west Brazil, represents mixed carbonate-siliciclastic deposition along a paleocontinental margin during late Ediacaran (e.g. Boggiani et al., 2010; Amorim et al., 2020). A rich fossil record is present in the Tamengo Formation, represented by abundant occurrences of *Cloudina lucianoi* and *Corumbella werneri* fossils, in a dynamic sedimentological environment (Gaucher et al., 2003; Babcock et al., 2005; Boggiani et al., 2010; Pacheco et al., 2015; Amorim et al., 2020). Such abundant biotic content, together with relatively short $\delta^{13}C_{carb}$ excursions and homogeneous $^{87}Sr/^{86}Sr$ ratios (~0.7085) indicate a stable marine setting connected to other late Ediacaran seas. Thus, results presented in this dissertation allow comparison between these very distinct settings, in which similarities and differences are discussed in terms of biogeochemical conditions operating when early metazoans were starting to inhabit marine benthic environments.

1.2. Objectives

Based on the proposed scenario, the main objectives of this study were:

(i) To provide the paired $\delta^{13}C$ (carbonate-organic carbon) and $\delta^{34}S$ (sulfate-sulfide) evolution for the Ediacaran record of carbonate rocks from the Tamengo Formation and basal Bambuí Group, accompanied by a paleoenvironmental model, to establish the biogeochemical dynamics for these different Ediacaran marine settings and its relationship to biota distribution. Multiple sulfur isotope constraints provide inferences about isotope effects acting during biogeochemical processes in these different basins;

(ii) For the São Francisco Basin, the aim was to explore the main mechanisms behind the major $\delta^{13}C$ positive excursion in the basal Bambuí Group, that has been linked to paleonvironmental change associated with the final Gondwana assembly. Scenarios previously envisaged for this anomaly might have represented barriers for the animal colonization in the late Ediacaran-early Cambrian, considering the scarce metazoan fossil record of this unit;

(iii) For the Corumbá Group, Southern Paraguay Belt, the investigation of carbon and sulfur isotope dynamics throughout the carbonate ramp would help to improve the understanding of conditions favorable to metazoan colonization of benthic environments.

The expected achievements will contribute for the understanding of Ediacaran marine biogeochemistry dynamics though different paleogeographic/paleoceanographic settings, and

may provide further insights concerning the disputed relationship between marine redox conditions and biological response.

1.3. Dissertation Outline

Results obtained during this research are presented in four manuscripts (Chapters 3 to 6), two of which are published, and the other two are being prepared for submission in peer-reviewed scientific journals. Before presenting these chapters, fundamentals are presented in Chapter 2, providing base for carbon and sulfur isotope investigations in the Ediacaran record as well as regarding the application of multiple sulfur isotope compositions in sedimentary rocks and paleoenvironmental studies. Discussions were divided to assess ideas provided by each group of data in order to gradually construct the main scenario proposed in the last manuscript (Chapter 6), culminating with the full integration of the data.

Chapter 3 presents the manuscript entitled "Sequence stratigraphy and chemostratigraphy of an Ediacaran-Cambrian foreland-related carbonate ramp (Bambuí Group, Brazil)" published in *Precambrian Research*. This chapter provides the stratigraphic framework for the basal Bambuí Group in different regions of the basin. This chapter provides the framework for further chemostratigraphic discussions by constraining spatio-temporal evolution of geochemical proxies within the basin. Furthermore, this study also identified a new basin-wide geochemical feature, that appears to also occur in other late Ediacaran basins worldwide.

Chapter 4 explores the extreme positive $\delta^{13}C$ excursions recorded in the middle Bambuí Group. The manuscript entitled "A large epeiric methanogenic Bambuí sea in the core of Gondwana Supercontinent?" was published in *Geoscience Frontiers*. This chapter proposes that anomalous ^{13}C-enrichment recorded in both carbonate and organic carbon from the Bambuí Group does not fit conventional models usually applied to positive excursions of marine carbon. Instead, recorded values are similar to modern methanogenic environments, and may be consisted with interpretations of basin restriction during West Gondwana assembly, and have implications for both animal colonization and global climate.

Chapter 5 presents paired $\delta^{13}C$ data for the Tamengo Formation, through stratigraphic sections that represent both inner to outer domains of the carbonate ramp (following a model from Amorim et al., 2020). The manuscript entitled "Paired carbon isotope and early diagenetic signatures suggest complex oxygenation in late Ediacaran benthic marine environments" is in preparation for submission. It focuses on occurrences of high variability

in $\delta^{13}C$ recorded in carbonate and organic carbon associated with lower-rank stratigraphic cycles bearing abundant occurrences of *Cloudina* bioaccumulations. These isotope disturbances are discussed in terms of enhanced organic carbon remineralization possibly associated with benthic oxic environments inhabited by these metazoans.

Chapter 6 encompasses multiple sulfur isotope data from the two studied units, focusing on the occurrence of the so-called superheavy pyrite. The manuscript entitled "Multiple sulfur isotope constraints in marginal and epicontinental marine settings through late Ediacaran-Cambrian: Superheavy $\Delta^{34}S$ pyrite trends, sulfate-distillation cycles and implications for early animal colonization" is being prepared for submission. This manuscript proposes a mechanism to explain the genesis of anomalous superheavy pyrite in the late Ediacaran-Cambrian record. In this chapter, similarities and differences between sulfur and carbon cycling in continental margin and epicontinental seas, represented by Tamengo Formation and Bambuí Group, respectively, are discussed, with implications for animal colonization through late Ediacaran-early Cambrian marine habitats. The multiple sulfur isotope data also supports the scenario of methanogenic basin proposed in the Chapter 4 for the middle Bambuí Group.

Finally, Chapter 7 summarizes results and discussions developed through chapters 3 to 6 in a brief integrative conclusion of the dissertation. Remaining questions and recommendations are proposed for future studies in these units and/or focused on the same theme.

2. FUNDAMENTALS

2.1. The Neoproterozoic Oxygenation Event and the Ediacaran Carbon and Sulfur Isotope Record

The oxygenation of the Earth's surface is believed to shows two primary thresholds, encompassing around two billion years since the first widespread oxygenation event in the Archean-Paleoproterozoic transition until reaching atmospheric oxygen levels close to the modern values during the late Neoproterozoic (Canfield, 2005; Holland, 2006; Shields-Zhou and Och, 2011; Och and Shields-Zhou, 2012). The interval between these major events would have been marked by stable low-oxygen conditions, characterized by low geochemical variability and lack of biological innovations (Holland, 2006; Anbar and Knoll, 2002).

After the first step in the Earth's surface oxygenation, referred to as the Great Oxygenation (or Oxidation) Event (GOE ~2.4 to 2.0 Ga; e.g. Canfield, 2005; Holland, 2006), a second threshold in atmospheric oxygen levels is associated with the interval between 0.85 to 0.54 Ga, the so-called Neoproterozoic Oxygenation Event (NOE; Shields-Zhou and Och, 2011; Och and Shields-Zhou, 2012). Evidence supporting this event includes disturbances on the carbon and sulfur cycles (e.g. Hurtgen et al., 2005; Fike et al., 2006; Fike and Grotzinger, 2008), and variation observed in other redox-sensitive geochemical proxies (e.g. trace metals, Fe speciation; Canfield et al., 2007; 2008; Sahoo et al., 2016). Most important, this event is accompanied by the first appearance of complex metazoans assemblages in the Ediacaran (Narbonne, 2005), which lead to the cause-and-effect discussion between NOE and complex life evolution.

The Ediacaran C and S isotope record presents extreme variations linked to major changes in the redox state of the oceans (Fig. 2.1). The $\delta^{13}C$ value is a parameter susceptible to spatial variation in the modern ocean (Kroopnick, 1985), and also with potential decoupling with global carbon cycle within shallow platforms (Swart, 2008; Geyman and Maloof, 2019). Lateral variability identified in some Ediacaran carbonate platforms (e.g. Ader et al., 2009; Wang et al., 2016), for instance, have been assinged to different geochemical conditions and local signals (oxygenated, sulfate-reducing, and methanogenic zones). Sulfur isotope compositions from both marine sulfate and pyrite are also very heterogeneous throughout Edicaran deposits, including high lateral variability within basin transects (e.g. Hurtgen et al., 2006; Loyd et al., 2012; 2013). Sulfur isotope heterogeneity can be assigned to a generally smaller Neoproterozoic sulfate reservoir compared with the modern ocean, which

is reflected in large isotope fluctuations compared with Phanerozoic record (e.g. Kah et al., 2004; Fig. 2.1). Still, major $\delta^{13}C$ and $\delta^{34}S$ trends are identified in the Ediacaran record on a global scale, probably reflecting global changes in the ocean-climate system, such as the post-glacial Marinoan cap carbonates in the early Ediacaran and the Shuram-Wonoka anomaly in the middle Ediacaran (e.g. Hurtgen et al., 2006; Halverson and Hurtgen, 2007; Halverson and Shields-Zhou, 2011; Cui et al., 2015).

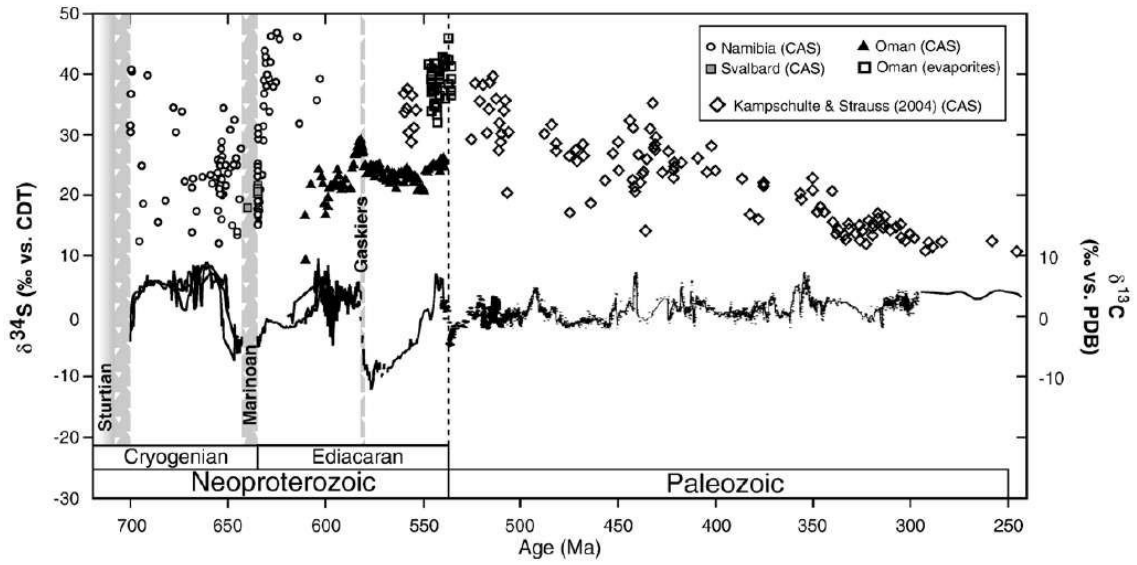

Figure 2.1: $\delta^{34}S_{sulfate}$ and $\delta^{13}C_{carb}$ evolution for the Neoproterozoic and Paleozoic era (extracted from Halverson and Hurtgen, 2007).

In the early Ediacaran, cap carbonate deposition in the aftermath of the Marinoan glaciation (Knoll et al., 2006) is recorded worldwide and is characterized by negative $\delta^{13}C_{carb}$ values (~ −6‰) followed by a recovery to values around zero (the Maieberg Anomaly; Halverson and Shields-Zhou, 2011). Several hypotheses have been proposed for this carbon isotope signature, such as: (i) upwelling of ^{12}C-enriched bottom waters due to biological pump and ocean stratification during glacial periods (Grotzinger and Knoll, 1995; Knoll et al., 1996); (ii) atmospheric CO_2 distillation reflecting enhanced post-glacial continental weathering under extreme high pCO_2 (300 to 400 times higher than the present atmospheric values) leading to lower carbon isotope compositions in DIC (Hoffman et al., 1998); (iii) destabilization of methane hydrates and methane oxidation (e.g. Kennedy et al., 2008; 2011; Wang et al., 2008); or (iv) oxidation of a large DOC reservoir (e.g. Lang et al., 2016). These events are still disputed, with each one presenting some inconsistencies (e.g. Hoffman and Schrag, 2002). Sulfur isotope compositions of marine sulfate in the early Ediacaran seem to

present an increase in $\delta^{34}S$ values in the aftermath of Marinoan glaciation, as reported for deposits from Namibia (Maieberg Formation; Hurtgen et al., 2002; 2006), China (Doushantuo Formation; Goldberg et al., 2005), Oman (Fike et al., 2006), and Brazil (Araras Group; Sansjofre et al., 2016). However, lateral variation has been detected through a platform to basin transect for some cases (e.g. Hurtgen et al., 2006). These results pointed to caution to global correlations based on $\delta^{34}S_{sulfate}$ and to non-steady state conditions following Marinoan glaciation. Some authors interpreted the increase in $\delta^{34}S_{sulfate}$ and $\Delta^{34}S$ throughout the early Ediacaran as an increase in marine sulfate reservoir and in the isotope fractionation during microbial sulfate reduction, possibly in response to increasing atmospheric O_2 (Fike et al., 2006; Halverson and Hurtgen, 2007). On the other hand, multiple sulfur isotope data from sulfates of Brazilian early Ediacaran deposits (Araras Group) suggested a drastic decrease in marine sulfate due to enhanced pyrite burial under non-steady state conditions, which in turn may have led to increases in atmospheric pO_2 (Sansjofre et al., 2016). Crockford et al. (2016) also presented multiple sulfur isotope data for barite in post-Marinoan sucessions, modeling a low sulfate reservoir (~0.1 to 10% of modern values), with low influence of sulfur re-oxidative cycling.

The Shuram-Wonoka $\delta^{13}C_{carb}$ anomaly is the most striking chemostratigraphic feature in the middle Ediacaran (~580 Ma), which is found in several Ediacaran deposits throughout the globe. The nature of this great negative $\delta^{13}C_{carb}$ excursion is still disputed, mainly regarded as oxidation of a huge DOC reservoir (e.g. Fike et al., 2006) or the release and oxidation of methane derived from hydrates (Bjerrum and Canfield, 2011; Macdonald et al., 2013; Cui et al., 2017). The $\delta^{34}S_{sulfate}$ and $\delta^{34}S_{pyrite}$ record seem to accompany the negative $\delta^{13}C_{carb}$ excursion through Shuram-Wonoka event, with a decrease of ~20 and 10‰ for $\delta^{34}S_{pyrite}$ and $\delta^{34}S_{sulfate}$, respectively (Cui et al., 2015). The overall interpretation is an increase in the surface oxidative weathering, pyrite oxidation and organic matter (Cui et al., 2015; Osburn et al., 2015), marked by increases in CAS concentration in some sections, suggesting increases in the marine sulfate levels (Loyd et al., 2013; Cui et al., 2015; Osburn et al., 2015). This is also interpreted as an increase in atmospheric pO_2, leading to high sulfate concentrations, considering that such great oxidation event, represented by the Shuram-Wonoka anomaly, would require huge amounts of oxidants (Halverson and Hurtgen, 2007).

Towards the Precambrian-Cambrian boundary, the late Ediacaran record presents some similarities in the $\delta^{34}S$ evolution between different basins. $\delta^{34}S_{sulfate}$ values increase in some sections, reaching unusual high values (> 35‰; Tostevin et al., 2017). In Oman, positive $\delta^{34}S$ excursions in both sulfate and sulfide from the Ara Group (the Ara Anomaly,

Fike and Grotzinger, 2008) are interpreted as an increase in the pyrite burial due to enhanced bioproductivity and organic matter burial. Tostevin et al. (2017) presented increases in $\delta^{34}S$ values from 30 to 38‰ between 550 and 547 Ma, and also ascribed to an increase in pyrite burial. Cui et al. (2016) registered increases in $\delta^{34}S_{pyrite}$ in late Ediacaran deposits from Namibia (548 to 541 Ma), accompanied by increases in $\delta^{13}C_{carb}$. These authors interpreted this positive $\delta^{34}S_{pyrite}$ excursion as a transition from bacterial sulfur disproproportionation environment to sulfate-rich conditions, enhanced bacterial sulfate-reduction (decrease in $\Delta^{34}S$) and pyrite formation, favoring fossil preservation through pyritization. Nevertheless, the most striking feature of late Ediacaran sulfur record is the occurrence of unusually ^{34}S-enriched pyrites (up to +80‰), which may be heavier than the coexisting sulfate, the so-called superheavy pyrites (Ries et al., 2009). Among hypothesis proposed for a primary origin of these anomalous signatures, most of them rely in scenarios of microbial sulfate reduction under low and limited sulfate reservoir, amplifying distillation effects and ^{34}S-enrichment, but with major mechanism behind these conditions still uncovered (Canfield, 2004; Shen et al., 2008; Ries et al., 2009).

In the early Cambrian, coupled behavior of $\delta^{13}C_{carb\text{-}org}$ became a typical feature throughout Phanerozoic carbon isotope evolution and may be linked to ecological innovations (Ishikawa et al., 2013; Shields-Zhou and Zhu, 2013). The dominant decoupled behavior before the early Cambrian would result from high bioproductivity and carbon remineralization, reflecting in relatively low rates of organic carbon burial and higher Dissolved Organic Carbon reservoir (DOC), which is inconsistent with a previous major oxidation event in terminal Neoproterozoic. In turn, a coupled behavior would reflect enhanced carbon burial, decreasing the size of DOC, which may be related to planktic metazoan evolution and fecal pellets deposition, strenghting the biological pump (Ishikawa et al., 2013). However, both euxinic and ferruginous conditions are also reported in Cambrian deposits (Goldberg et al., 2007, Feng et al., 2014), implying that the classical Neoproterozoic geochemical conditions persisted through Ediacaran-Cambrian transitions in some basins.

As can be noted, the attempt to find a common carbon and sulfur behavior through the global Ediacaran record has been a difficult task. Sulfur isotope compositions from both sulfate and sulfide are particularly heterogeneous among different Ediacaran basins. Although it is likely that the high amplitude of the sulfur isotope variation results from a much smaller marine sulfate reservoir compared to the modern one, this scenario would also favor a control by local processes linked to specific geological settings, varying from basin to basin (e.g. Hurtgen et al., 2002; 2006; Loyd et al., 2012; 2013; Tostevin et al., 2017). It is therefore

important to provide the coupled carbon and sulfur evolution for a given Ediacaran succession, accompanied by a careful consideration of the paleogeographic and paleoenvironmental context. This approach will allow identifying biogeochemical interactions acting, discriminating local from global signals, and making inferences about the regional paleoenvironmental/paleoceanographic conditions, helping to improve the understanding of the carbon and sulfur dynamics in the marine Ediacaran world.

2.2. Multiple Sulfur Isotopes Constraints on the Sulfur Cycle

Intense development of a multiple sulfur isotope approach to the sulfur cycle, by measurements ofthe three sulfur isotope compositions ($^{33}S/^{32}S$, $^{34}S/^{32}S$, and $^{36}S/^{32}S$) has permitted better constraint of sulfur fractionation processes and their significance on the geological record (e.g. Farquhar et al., 2000; Farquhar et al. 2003; Farquhar and Wing, 2003; Johnston et al., 2005a,b; Ono et al., 2006; Ono, 2008; Johnston et al., 2008a,b; Johnston, 2011). Early investigations on sulfur isotope fractionations showed an overall linear relationship between $\delta^{34}S$, $\delta^{33}S$, and $\delta^{36}S$ values for the most part of fractionation processes ($\delta^{33}S \sim 0.5 \times \delta^{34}S$ and $\delta^{36}S \sim 2.0 \times \delta^{34}S$; e.g. Hulston and Thode, 1965). For this reason, the majority of the sulfur isotope investigations through the past century did not focus on the minor isotope compositions ($^{33}S/^{32}S$ and$^{36}S/^{32}S$), which were not believed to provide additional information beyond conventional $\delta^{34}S$ analysis. This relationship derives from differences in mass (i.e. vibrational energy during isotope substitution; e.g. Urey, 1947) during the isotope fractionation processes (equilibrium thermodynamic, kinetic, and biological), the so-called mass-dependent array (Fig.2.2; Equation 1):

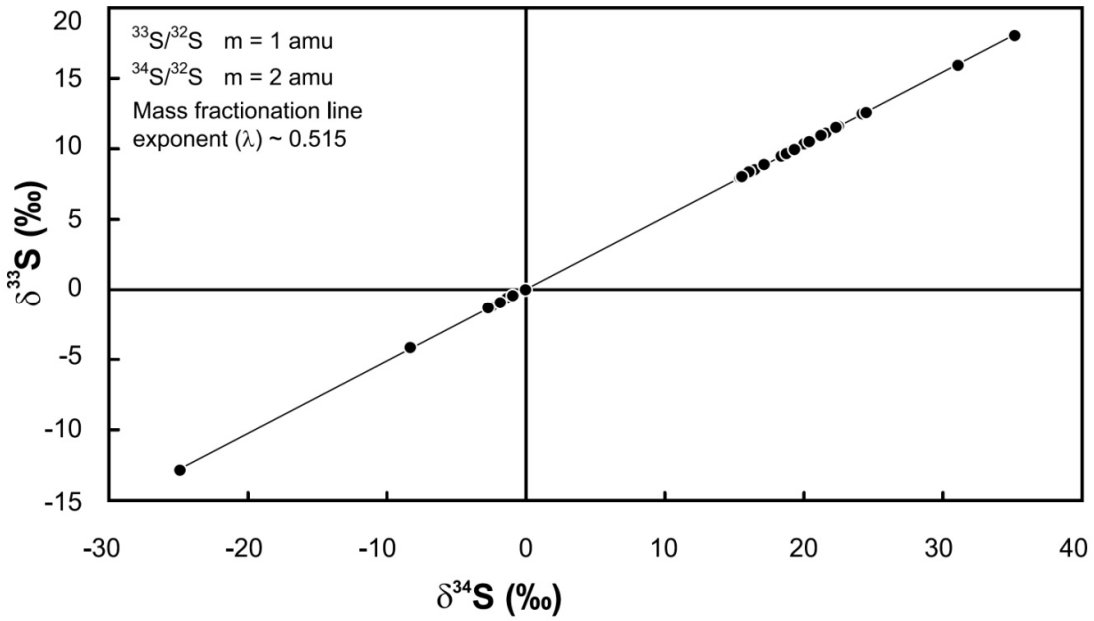

Figure 2.2: Diagram $\delta^{34}S$ *vs* $\delta^{33}S$ for sulfides and sulfates younger than 2.0 Ga (extracted from Farquhar and Wing, 2003 and references therein). The mass-dependent array is defined by a $^{33}\lambda$ coefficient of ~0.515 and represents average effects of a variety of mass-dependent processes, rather than a specific process. For the relationship between ^{32}S, ^{33}S and ^{34}S, the mass-dependent effect drives $\delta^{33}S$ variations in the half of magnitude of $\delta^{34}S$ variations.

$$\delta^{3x}S = {}^{3x}\lambda \times \delta^{34}S \qquad \text{(Eq. 1)}$$

where $\delta^{3x}S$ represents the minor isotope composition of interest and λ is the isotope substitution coefficient, more precisely set as 0.515 for $\delta^{33}S$ and 1.89 for $\delta^{36}S$ (Ono et al., 2006; Johnston et al., 2007).

An essential parameter to the multiple sulfur isotope investigations is the capital delta notation (Equation 2), which quantifies the deviation of the $\delta^{3x}S$ values from the mass-dependent array. Note that the $\Delta^{33}S$ and $\Delta^{36}S$ are different from the capital notation for $\Delta^{34}S$, which is the difference between $\delta^{34}S$ of sulfide and sulfate.

$$\Delta^{3x}S = \delta^{3x}S - 1000 \times [(1 + \delta^{34}S/1000)^{3x}\lambda - 1] \qquad \text{(Eq. 2)}$$

Therefore, a $\Delta^{3x}S \sim 0$‰ is expected for processes holding mass-dependent relationship. However, some processes do not obey mass-dependent laws and produce anomalous $\Delta^{3x}S$ values, significantly different from zero, associated with mass-independent fractionations. Previously, absolute thresholds (e.g. $\Delta^{33}S$ and $\Delta^{36}S \pm 0.20$‰; Farquhar et al., 2000) were used to distinguish significant non-zero values and, consequently, mass-independent signatures.

Later, considering the identification of anomalous $\Delta^{33}S$ and $\Delta^{36}S$ values produced by different mass-dependent fractionation processes, more recent studies have applied the relationship between $\delta^{34}S$, $\Delta^{33}S$ and $\Delta^{33}S$ to improve the distinction between mass-independent and mass-dependent effects (Ono et al., 2006; Farquhar et al., 2007; Johnston et al., 2007). The $\Delta^{36}S/\Delta^{33}S$ ratios of mass-independent effects range between –1 to –2‰ (Farquhar et al., 2007; Johnston, 2011), whereas mass-dependent fractionations present ratios of ~ –7 and –9‰, considering theorical equilibrium and dissimilatory sulfate reduction experiments (Ono et al., 2006; Farquhar et al., 2007; Johnston, 2011). Another useful parameter to distinghish mass-independent *vs* mass-dependent fractionations is the $^{33}\lambda$. Mass-dependent fractionations produce lower $^{33}\lambda$ deviations from ~0.515, whereas mass-independent fractionations can produce larger variations of $^{33}\lambda$ (from ~ 0.4 to 0.7; Johnston, 2011).

For rocks older than 2.45 Ga, $\Delta^{33}S$ varies across a range of values (> 1‰), followed by a transitional interval between 2.45 and 2.09 Ga of moderate but significant non-zero $\Delta^{33}S$, from −0.1 to +0.2‰, and finally homogeneous $\Delta^{33}S$ ~ 0‰ after 2.09 Ga. These multiple sulfur isotope signatures support the interpretation of a very distinct sulfur cycle in the Archean-Paleoproterozoic compared to the modern sulfur cycle, established after ~ 2.0 Ga, controlled by the primitive oxygen-depleted Earth's atmospheric composition and consequent photochemical reactions with mass-independent fractionation effects (Farquhar and Wing, 2003). After 2.0 Ga, homogeneous $\Delta^{33}S$ signatures around zero point to mass-dependent fractionation processes controlling the isotope sulfur record, marking the onset of oxidative weathering of continents and consequent enhanced sulfate supply to the oceans resulting from an increase in oxygen levels (> 10^{-2} PAL; Farquhar and Wing, 2003). From this point lies a different approach for the multiple sulfur isotope studies, related to the identification of main biological processes involved in the ancient sulfur cycle and to isotope effects during sulfur isotope fractionation. High precision analytical techniques have provided measurements of slight variations in the multiple sulfur isotope compositions of mass-dependent fractionation processes, as systematic small deviations of $\Delta^{33}S$ and $\Delta^{36}S$, and consequently, specific values of $^{33}\lambda$ and $^{36}\lambda$ attributed to different metabolisms (e.g. Farquhar et al., 2003; Johnston et al., 2005a; 2007; 2008a; Ono, 2008).

Among mass-dependent fractionation processes, both equilibrium thermodynamic and biological processes can produce a wide range of $\delta^{34}S$ values, but only biological processes produce significant non-zero $\Delta^{33}S$ and $\Delta^{36}S$, and $^{33}\lambda$ and $^{36}\lambda$ deviating from 0.515 and 1.90 values, respectively (Farquhar et al., 2003; Ono et al., 2006; Johnston et al., 2007; 2008a).

This demonstrates the usefulness of multiple sulfur isotopes to distinguish biotic *vs* abiotic signatures (Johnston et al., 2008a). Considering biological fractionation processes, experimental studies with sulfate-reducing and sulfur disproportionation organisms have shown that $\delta^{34}S$ is not an efficient proxy to distinguish these metabolisms (e.g. Farquhar et al., 2003; Johnston et al., 2005a,b; 2008a,b). On the other hand, systematic differences in triple isotope compositions ($^{33}S/^{32}S$, $^{34}S/^{32}S$, and $^{36}S/^{32}S$) show potential in identifying influence of sulfate-reduction and/or sulfur disproportionation (Johnston et al., 2007; 2008a). Thus, models based on multiple sulfur isotope distributions have been developed to track different metabolisms on the Proterozoic sulfur isotope record (Johnston et al., 2005b; 2008b).

Another application of the multiple sulfur isotope analyses, and most important for the present project, is to explore isotope effects such as the Rayleigh distillation predictions to potentially identify events of marine sulfate drawdown through pyrite burial (e.g. Canfield, 2001; Sansjofre et al., 2016). Rayleigh equations can predict the evolution of isotope compositions ($R = {}^{3x}S/^{32}S$) for residual sulfate ($^{3x}R_{res} = {}^{3x}R_{initial} \times F^{(\alpha-1)}$); instantaneous product ($^{3x}R_{ip} = {}^{3x}\alpha \times {}^{3x}Rinitial \times F^{(\alpha-1)}$) and pooled product ($^{3x}R_{pp} = [{}^{3x}Rinitial \times (1-F^{\alpha})] / (1 - F)$) in a closed system for sulfate distilation, in which the product is represented by pyrite analyzed, F is the fraction of residual sulfate, and α is the isotope fractionation between sulfate and sulfide ($^{3x}\alpha = {}^{34}\alpha^{3x\lambda}$). Thus, specific trends can be defined by measuring two isotope compositions involved in the same fractionation process.

3. SEQUENCE STRATIGRAPHY AND CHEMOSTRATIGRAPHY OF AN EDIACARAN-CAMBRIAN FORELAND-RELATED CARBONATE RAMP (BAMBUÍ GROUP, BRAZIL)

Sergio Caetano-Filho, Gustavo M. Paula-Santos, Cristian Guacaneme, Marly Babinski, Carolina Bedoya-Rueda, Marília Peloso, Kamilla Amorim, Jhon Afonso, Matheus Kuchenbecker, Humberto L.S. Reis, and Ricardo I.F. Trindade

3.1. Abstract

In the terminal Neoproterozoic, drastic climate changes associated with biological innovations are coupled to isotope and elemental geochemical anomalies. However, lateral variability and local depositional controls may affect global geochemical signals, which can only be tracked through a proper stratigraphic/paleogeographic assessment. Here, we investigate the sequence stratigraphy and chemostratigraphy of the basal units of the Bambuí Group, central-east Brazil. This stratigraphic unit records a foreland basin system developed during the Ediacaran-Cambrian West Gondwana assembly and represents a 1st-order sequence, in which the two lowermost 2nd-order sequences record major geochemical disturbances. The first 2nd-order sequence started with deposition of a transgresive systems tract, possibly in a post-glacial scenario, which accompanies a negative-to-positive $\delta^{13}C_{carb}$ excursion. The early highstand stage represents the establishment of a marine carbonate ramp throughout the basin. In terms of chemostratigraphy, it corresponds to a $\delta^{13}C_{carb}$ plateau close to 0‰ and Sr/Ca ratios around 0.001. The late highstand stage coincides with a remarkable increase in Sr content and Sr/Ca ratios at basinal scale. Occurrences of the *Cloudina* sp. late Ediacaran index fossil were reported in this stage. An erosive unconformity associated to a dolomitic interval, locally including subaerial exposure features, mark the top of the first 2nd-order sequence. This sequence boundary heralds an abrupt increase in $\delta^{13}C_{carb}$ values, up to +14‰. These extremely high $\delta^{13}C_{carb}$ values and high Sr/Ca ratios persist throughout the overlying sequence, as a result of the progressive and enhanced restriction of the foreland basin. Basin restriction at this stage has implications for the paleontological and chemostratigraphic record of epicontinental basins of the West Gondwana in the terminal Ediacaran. Late Ediacaran Sr-rich intervals in these basins show unusually non-radiogenic $^{87}Sr/^{86}Sr$ ratios, which may represent local depositional controls and deviations from the

modern oceanographic models. Physiographic barriers and stressful conditions in these conditions likely represented extreme environments for metazoan colonization.

3.2. Introduction

The Ediacaran is known as a period of drastic climate change and biological innovations, marked by rapid transitions from icehouse to greenhouse conditions and the appearance of complex metazoan assemblages (e.g. Knoll et al., 2006; Narbonne et al., 2012). Together with important plate tectonic reorganizations, all these events have been depicted in complex cause-and-effect relationships (e.g. Canfield et al., 2007; Campbell and Squire, 2010; Och and Shields-Zhou, 2012). Remarkable isotope and elemental geochemical anomalies recorded in marine sedimentary rocks are among the main supporting evidence to reconstruct these paleoenvironmental and paleoceanographic conditions. In the last decades a large number of isotopic and geochemical studies in the Neoproterozoic were reported, mainly concerning carbon, strontium and sulfur isotopes, as well as elemental data (e.g. iron speciation and rare earth elements distributions; for a review, see Och and Shields-Zhou, 2012). The reproducibility of major geochemical disturbances worldwide has been explained by some authors by the occurrence of at least two events of oxidation of global significance for the Ediacaran: one in the aftermath of the Marinoan glaciation and the other in the middle to late Ediacaran Shuram-Wonoka anomaly (e.g. Hurtgen et al., 2006; Halverson and Hurtgen, 2007; Kaufman et al., 2007; Halverson and Shields-Zhou, 2011; Cui et al., 2015).

In spite of the increasing number of studies on the geochemistry and C-O-Sr isotopes in the Neoproterozoic, just a few of them are accompanied by paleoenvironmental assessments supported on sedimentological and stratigraphic analyses. The available cases have shown a significant spatial variability for some geochemical trends depending on changes in sedimentary conditions, suggesting important local controls on the rock chemistry (e.g. Hurtgen et al., 2006; Ader et al., 2009). This suggests that caution must be taken when interpreting chemostratigraphic data from a single section in terms of global correlations. When it comes to epicontinental basins, like those of the Ediacaran-Cambrian West Gondwana, integrating stratigraphic and isotope geochemistry becomes even more important in order to understand the marine geochemical dynamics, its stratigraphic significance, chronostratigraphic relationships and to distinguish local/regional from global controls.

Here we investigate the carbonate-dominated strata of the Sete Lagoas Formation (Bambuí Group), preserved in the southern and central-eastern São Francisco Basin, central-

east Brazil. According to the most recent tectono-stratigraphic reconstructions, the Bambuí Group records an Ediacaran-Cambrian foreland basin cycle developed during the Brasiliano/PanAfrican West Gondwana assembly (e.g. Alkmim and Martins-Neto, 2012; Reis and Suss, 2016; Reis et al., 2016; 2017; Fig. 3.1 and 3.2). At the basal Sete Lagoas Formation, there is a carbonate succession directly overlying diamictite deposits, which display a negative $\delta^{13}C_{carb}$ excursion with values close to −3‰ decreasing to −5‰, followed by a gradual increase to values close to 0‰. This basal carbonate succession have been interpreted as a cap carbonate interval in the context of the Neoproterozoic snowball events (e.g. Hoffman et al., 1998; Hoffman and Schrag, 2002), with a depositional age still disputed (Sturtian – Babinski et al., 2007; Vieira et al., 2007a; Marinoan – Caxito et al., 2012; 2018; Uhlein et al., 2016; mid- to late Ediacaran – Kuchenbecker et al., 2016a; Paula-Santos and Babinski, 2018). Topward the unit, an extreme $\delta^{13}C_{carb}$ positive excursion to values as high as +16‰ occurs and have been considered a regional chemostratigraphic marker in the basin (Iyer et al., 1995; Santos et al., 2004; Vieira et al., 2007a; Martins and Lemos, 2007; Paula-Santos et al., 2015; 2017). Such extreme positive $\delta^{13}C_{carb}$ values are rare in the sedimentary record (e.g. Cui et al., 2018) and may be related to a restricted environment driven by the West Gondwana assembly (Paula-Santos et al., 2015; 2017).

Despite the abundance of $\delta^{13}C_{carb}$ data for the Sete Lagoas Formation, basinwide chemostratigraphic studies coupled to stratigraphic analyses are relatively scarce. Recent advances in the tectonostratigraphic framework, based on seismic, drill core and outcrop data (Reis et al., 2016; Reis and Suss, 2016; Reis et al., 2017; Perrella Jr. et al., 2017), allow better understanding of the Bambuí $\delta^{13}C_{carb}$ evolution, as well as other geochemical proxies. For this purpose, we present an integrated stratigraphic-chemostratigraphic analysis from the basal Bambuí Sequence, by correlating the southern and northern forebulge domains of the basin (Sete Lagoas and Januária basement highs, respectively; Fig. 3.1A). The identification of two main $\delta^{13}C_{carb}$ excursions and a new strontium-rich carbonate interval provides further details on the tectonosedimentary evolution of the basin. Major paleoenvironmental changes driven by tectonic basin restriction have implications on the Ediacaran-Cambrian metazoan colonization and on the use of chemostratigraphy as a global correlation tool in these cases.

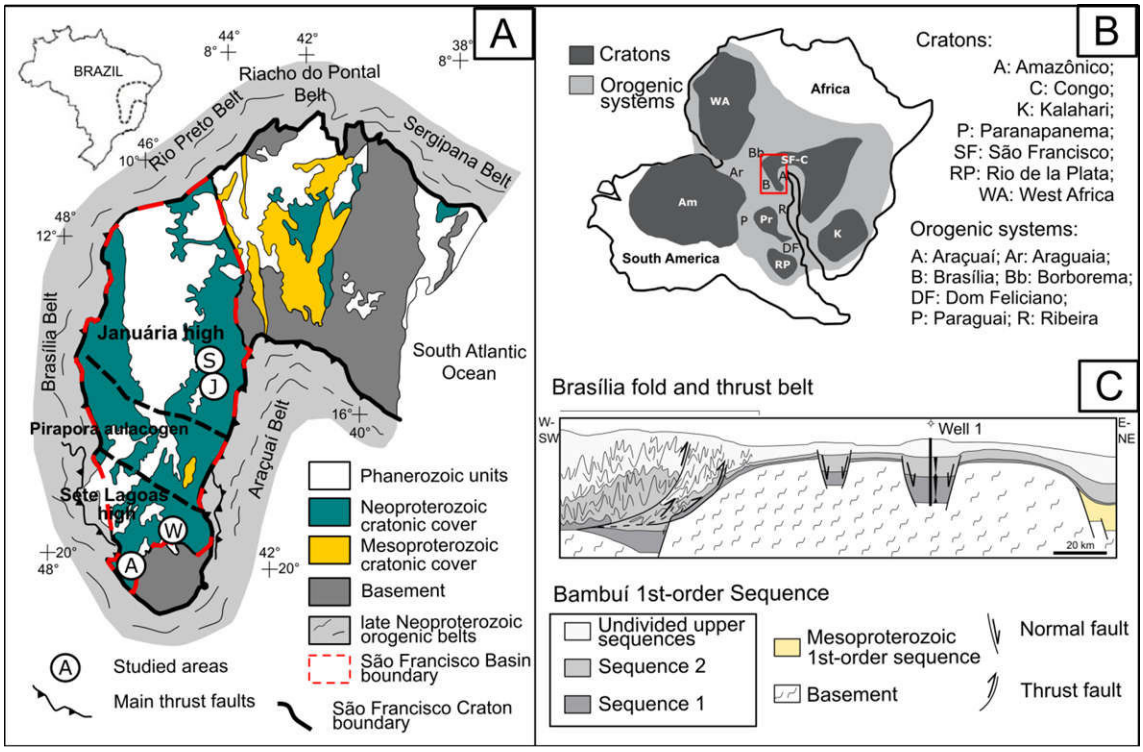

Figure 3.1: A) Geological map of the São Francisco Basin, central east Brazil (J = Januária section; S = Santa Maria da Vitória section; A = Arcos section; W = Well 1 section; Modified from Alkmim et al., 2006 and Reis and Suss, 2016). B) Paleogeographic reconstruction of the late Neoproterozoic West Gondwana (modified from Alkmim et al., 2006). C) Schematic seismic profile and location of the Well 1 section studied in the Sete Lagoas basement high, southern São Francisco Basin (Modified from Reis and Suss, 2016).

3.3. Geological Setting

3.3.1. The São Francisco Basin and the Bambuí Sequence

The São Francisco Basin is a polycyclic intracratonic basin, which records a tectonosedimentary evolution from the Paleoproterozoic to the Mesozoic (Alkmim e Martins-Neto, 2012; Reis et al. 2016). The basin covers an area of ~350,000 km² in the central-east Brazil, within the homonymous craton (Fig. 3.1A). It is surrounded by late Neoproterozoic fold-and-thrust belts at the east, west, and north, and its southern limit is marked by an erosional unconformity between Proterozoic basin-fill units and Archean-Paleoproterozoic basement assemblages. To the northeast, the basin is bounded by the Neoproterozoic Paramirim deformation corridor.

Two major large-scale tectonic elements may be recognized in the São Francisco Basin (e.g., Reis et al., 2016): i) Proterozoic rifts and ii) Ediacaran foreland fold-thrust belts. The buried and NW-trending Pirapora Aulacogen is the most striking rift structure preserved.

Hosting the thickest Proterozoic strata so far documented in the cratonic domain, it is bounded by two basement highs: i) the Sete Lagoas high, to the south, and ii) the Januária high, to the north (Fig. 3.1A; Reis et al., 2016). This geotectonic display was apparently formed during the Paleoproterozoic and was active through the entire Proterozoic evolution of the basin (Reis and Suss, 2016; Reis et al. 2016; 2017). The overburden imposed in the margins of the São Francisco paleoplate by multiple and diachronic Ediacaran mountain belts resulted in the development of a foreland basin system, represented by deposits of the Bambuí Group, as a 1st-order sequence (e.g., Martins-Neto, 2009; Alkmim and Martins-Neto, 2012). The continentward advance of these marginal orogens subsequently culminated with the development of two foreland fold-thrust belts of opposite vergence (Fig. 3.1A). These belts affect both the syn-orogenic and the older Proterozoic strata at the western and eastern borders of the São Francisco Basin (Reis et al., 2016).

The Bambuí Group lithostratigraphy (Fig. 3.2; Costa and Branco, 1961; Dardenne, 1978) encompasses a basal diamictite and the overlying mixed carbonate-siliciclastic deposits of the Sete Lagoas, Serra de Santa Helena, Lagoa do Jacaré, Serra da Saudade, and Três Marias formations. We consider the Carrancas Formation as the basal diamictite unit of the Bambuí Group, rather than the Jequitaí Formation (following Vieira et al., 2007b; Kuchenbecker et al., 2011; 2016a; Reis and Suss, 2016; Reis et al., 2016). The Jequitaí Formation is an older diamictite unit, chronologically related to the Macaúbas Group (e.g. Uhlein, 2007), in the Araçuaí orogen. Even so, the position and significance of these diamictitic units at the base of the Bambuí Group has been still matter of debate (e.g. Uhlein et al., 2017). These units are distributed in four 2nd-order sequences and apparently evolved under unusual tectonic conditions, in a basinal setting almost completely surrounded by orogenic fronts and under a strong influence of preexisting tectonic features (for a detailed review, see Reis et al., 2016; 2017; Fig. 3.1 and 3.2). Most of its regional stratigraphic architecture, however, is associated with the Brasília Orogen that bounds the São Francisco basin to the west and controlled the sedimentary dispersal of the Bambuí units during late Neoproterozoic (Martins-Neto, 2009; Alkmim and Martins-Neto, 2012; Reis et al., 2017).

The basal 2nd-order sequence comprises the Carrancas Formation and the overlying Sete Lagoas Formation, as an initial transgression over the craton (e.g. Vieira et al., 2007a,b; Caxito et al., 2012; Paula-Santos et al., 2015; 2017; Kuchenbecker et al., 2016a; Reis and Suss, 2016; Perrella Jr. et al., 2017). The Carrancas Formation encompasses oligomictic to polymictic diamictites, rhythmites, and local occurrences of sandstones, black shales and dolomites, in a fine-upward stacking pattern (e.g. Uhlein et al., 2012). The nature of this unit

remains uncertain, regarding its glacial origin (Romano, 2007; Vieira et al., 2007b; Rocha-Campos et al., 2011; Tuller et al., 2008; 2010; Uhlein et al., 2012; Kuchenbecker et al., 2016a; Reis and Suss, 2016). A glacial event in the basal Bambuí Group is inferred by the relationship between these diamictite deposits and the overlying cap carbonate interval from the Sete Lagoas Formation, which displays aragonite pseudomorphs and a negative $\delta^{13}C_{carb}$ excursion extending to −5‰ (Fig. 3.2). The overlying carbonate succession presents a shallowing-upward pattern, which encompasses argillaceous to pure limestones and subordinated black shales (e.g. Vieira et al., 2007a,b; Kuchenbecker et al., 2016a; Reis and Suss, 2016; Perrella Jr. et al., 2017; Paula-Santos et al., 2017).

The overlying 2nd-order sequences are represented by the upper Sete Lagoas, Serra de Santa Helena, Lagoa do Jacaré, and Serra da Saudade formations (Reis et al., 2016; Fig. 3.2). The upper Sete Lagoas Formation is composed of dark-colored limestones, marlstones, and stromatolites, restricted to the eastern border of the basin (Santos et al., 2004; Vieira et al., 2007a,b; Paula-Santos et al., 2015; 2017). The fine-grained siliciclastic sediments of Serra de Santa Helena and Serra da Saudade formations thicken westwards, conformably overlying the lower Sete Lagoas Formation (Martins and Lemos, 2007). The Lagoa do Jacaré Formation encompasses dark-colored clastic limestones, frequent occurrences of oolitic calcarenites, as carbonate banks and lenses interbedded in the fine-grained siliciclastics (Dardenne, 1978).The Bambuí Sequence ends with the deposition of the final 2nd-order sequence corresponding to coastal to continental deposits of the Três Marias and Gorutuba formations (Chiavegatto, 1992; Castro and Dardenne, 2000; Uhlein, 2014; Kuchenbecker et al., 2016b; Reis et al., 2016; Fig. 3.2).

These 2nd-order sequences have lateral equivalents of delta and submarine fan deposits exposed in the western border of the basin and are represented by the Samburá and Lagoa Formosa formations (Castro e Dardenne, 2000; Dardenne et al., 2003; Uhlein et al., 2011; 2017; Fig. 3.2).

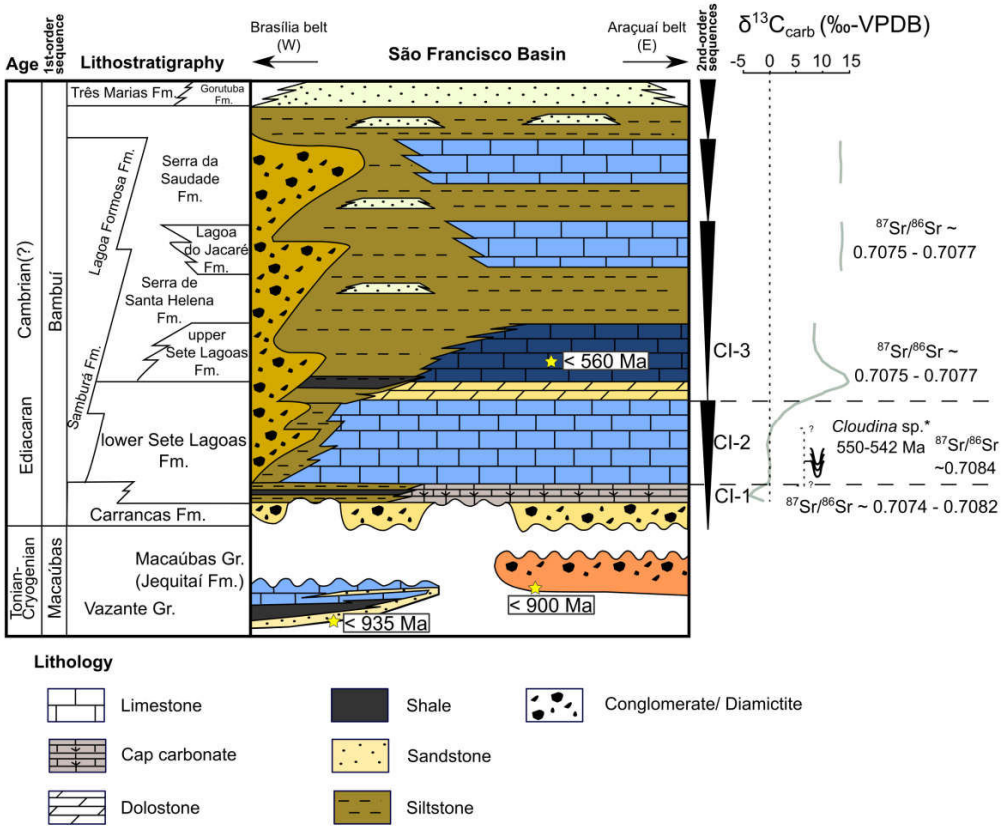

Figure 3.2: Lithostratigraphy of the 1st-order Bambuí Sequence, São Francisco Basin, and chemostratigraphy evolution (thicknesses not to scale, after Reis et al., 2016; Paula-Santos et al., 2017). Maximum depositional ages obtained by U-Pb geochronology in detrital zircon grains are represented by the yellow stars (Vazante Group – Rodrigues et al., 2012; Macaúbas Group – Babinski et al., 2012; upper Sete Lagoas Formation – Paula-Santos et al., 2015). Chemostratigraphic Intervals (CI) from Paula-Santos et al. (2017) are shown. *Cloudina* sp. occurrences from Warren et al. (2014) and Perrella Jr. et al. (2017).

3.3.2. Chemostratigraphyof the basal Bambuí Group

Considering the abundant $\delta^{13}C_{carb}$ database for the basal Bambuí Group and new $^{87}Sr/^{86}Sr$ ratios for its basal units, Paula-Santos et al. (2017) proposed its subdivision into three Chemostratigraphic Intervals (CI), which would represent major paleoenvironmental changes in the basin (Fig. 3.2). The CI-1 corresponds to the Sete Lagoas cap carbonates with negative $\delta^{13}C_{carb}$ from −3 to −5‰ followed by a recover to values around 0‰. This $\delta^{13}C_{carb}$ evolution is accompanied by an increase in $^{87}Sr/^{86}Sr$ ratios from 0.7074 to 0.7082, during the transgression over the craton (Babinski et al., 2007; Vieira et al., 2007a,b; Caxito et al., 2012; Kuchenbecker et al, 2016a). In the middle Sete Lagoas Formation, the CI-2 corresponds to the

interval of $\delta^{13}C_{carb}$ around 0‰ and $^{87}Sr/^{86}Sr$ ratios of ~0.7084. Occurrences of *Cloudina* sp. (Warren et al., 2014), a late Ediacaran index fossil (Grotzinger et al., 2000) are reported for this interval. The CI-3 comprises the upper Sete Lagoas, Serra de Santa Helena, and Lagoa do Jacaré formations, with very high $\delta^{13}C_{carb}$ values reported from +8 to +16‰ (Fig. 3.2). The $^{87}Sr/^{86}Sr$ ratios in CI-3 drop to ~0.7075 and are lower than the usual values for the late Ediacaran-early Cambrian (≥0.7080; Halverson et al., 2007). This stage would record a restricted setting in terms of surface connection with other epicontinental seas and the open ocean, preventing isotope homogenization. The highly ^{13}C-enriched carbonate values have been proposed to result from enhanced organic carbon burial and/or from methanogenesis within an anoxic basin (Iyer et al., 1995; Paula-Santos et al., 2017).

3.3.3. Age constraints on the basal Bambuí Group

The age of the Bambuí Group is still disputed (Babinski et al., 2007; Rodrigues, 2008; Pimentel et al., 2011; Caxito et al., 2012; 2018; Warren et al., 2014; Paula-Santos et al., 2015). Babinski et al. (2007) presented a Pb-Pb isochron age of 740 ± 22 Ma for the Sete Lagoas cap carbonate (basal 2nd-order sequence, lower Sete Lagoas Formation; Fig. 3.2) and correlated this unit to the Sturtian glacial event. Pimentel et al. (2011), after Rodrigues (2008), presented a maximum depositional age of ~610 Ma for the upper Sete Lagoas Formation (U-Pb dating of detrital zircon grains from the second 2nd-order sequence; Fig. 3.2). Caxito et al. (2012) claimed an early Ediacaran age (~635 Ma) for the basal Sete Lagoas Formation, based on $^{87}Sr/^{86}Sr$ ratios of ~0.7075 throughout the unit, the negative to positive $\delta^{13}C_{carb}$ excursion and sedimentological features of the Sete Lagoas cap carbonate, representing the post-Marinoan glaciation signal. Later, Caxito et al. (2018) provided a Pb-Pb isochron age of 608 ± 19 Ma for the same cap carbonate interval, which corroborates the early Ediacaran age. However, Warren et al. (2014) reported occurrences of late Ediacaran index fossils *Cloudina* sp. and *Corumbella werneri* (550-543 Ma; Grotzinger et al., 2000), within the lower to middle Sete Lagoas Formation (CI-2; Fig. 3.2). In addition, Paula-Santos et al. (2015) provided U-Pb ages from detrital zircon grains retrieved from the upper Sete Lagoas Formation, setting a maximum depositional age of 560 Ma, which are in accordance with the basal fossil occurrences (Fig. 3.2). Given this up-to-date geochronological setting, either Sturtian (~720 Ma) or Marinoan (~635 Ma) ages proposed for the basal cap carbonate interval would require an 85-170 m.yr.-long hiatus within the basal 2nd-order sequence, which is hard to reconcile with the sedimentary record of the basin. In the absence of such long hiatus, the glaciation

could be even younger (Kuchenbecker et al., 2016a; Paula-Santos and Babinski, 2018). Nevertheless, the tectonosedimentary evolution presented herein is independent of absolute ages for the Bambuí Sequence and was conceived to incorporate further age constraints, as long as they are accompanied by a proper stratigraphic control.

3.4. Materials and Methods

3.4.1. Studied sections

Two composite sections were sampled in the Januária Basement High (Januária and Santa Maria da Vitória sections, Fig. 3.1A), whereas two drill cores were sampled in the Sete Lagoas Basement High (Arcos and Well 1 sections; Fig. 3.1A).

In the Januária High, the Januária and Santa Maria da Vitória sections (Fig. 3.3 and 3.4, respectively) are composed of three continuous sections (Fig. 3.1). The composite sections were constructed and analysed based on sequence stratigraphy, $\delta^{13}C$ profiles, and available geological maps (Martinez, 2007; Conceição Filho and Miranda, 2003). Overall, in these areas the basal Bambuí Sequence directly overlies the crystalline basement, with rare occurrences of the Carrancas diamictite. They include the sedimentary strata of the lower Sete Lagoas, Serra de Santa Helena and Lagoa do Jacaré formations (Caxito et al., 2012; 2018; Perrela Jr., 2017; Okubo et al., 2018; Fig. 3.2, 3.3 and 3.4), which are unconformably overlain by the Mesozoic Urucuia Group (Sgarbi et al., 2001). Local occurrences of *Cloudina* sp., a late Ediacaran index fossil, were reported in this area (Warren et al., 2014; Perrela Jr. et al., 2017), although we did not identify any specimen in the studied sections.

In the Sete Lagoas High, Arcos and Well 1 sections correspond to two drill cores previously studied by Kuchenbecker et al. (2016a) and Reis and Suss (2016), respectively. They record thick successions of the basal Bambuí Group, represented by Carrancas and Sete Lagoas formations (Fig. 3.5 and 3.6). The Well 1 section encompasses the thickest succession of the basal Bambuí Sequence analysed in this study (~430 m; Fig. 3.6). This succession fills NE-trending forebulge grabens, formed during the flexural uplift and migration of the Sete lagoas Basement High under strong influence of pre-existing basement structures (Reis and Suss, 2016; Reis et al., 2017).

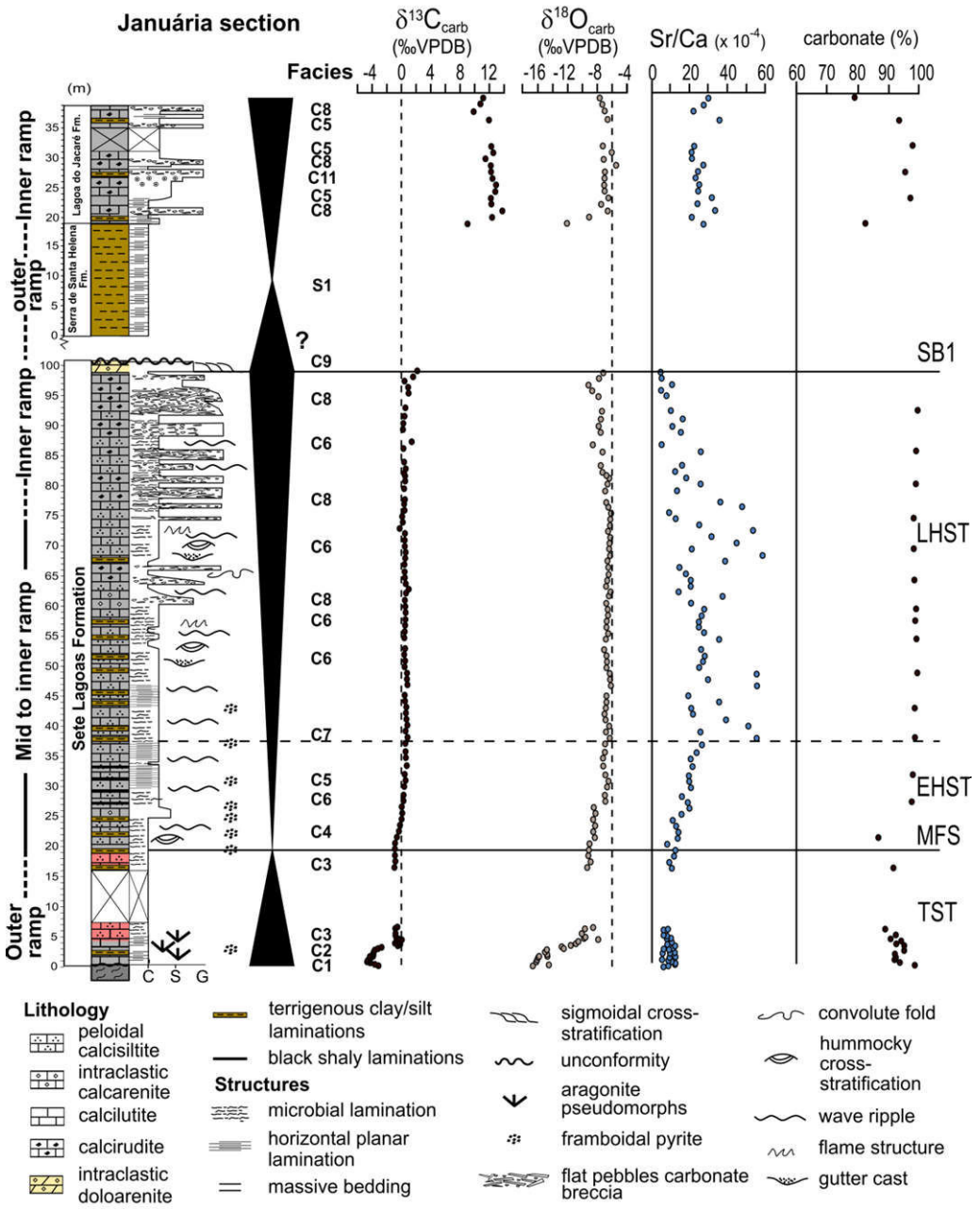

Figure 3.3: The Januária section – sequence stratigraphy, facies associations and chemostratigraphy. Limestones are distinguished by two colors – reddish and grey. System tracts: TST – Transgressive System Tract; MFS – Maximum Flooding Surface; EHST – Early Highstand System Tract; LHST – Late Highstand System Tract; SB1 – Sequence Boundary. Granulometry scale: C – clay; S –sand; G – gravel.

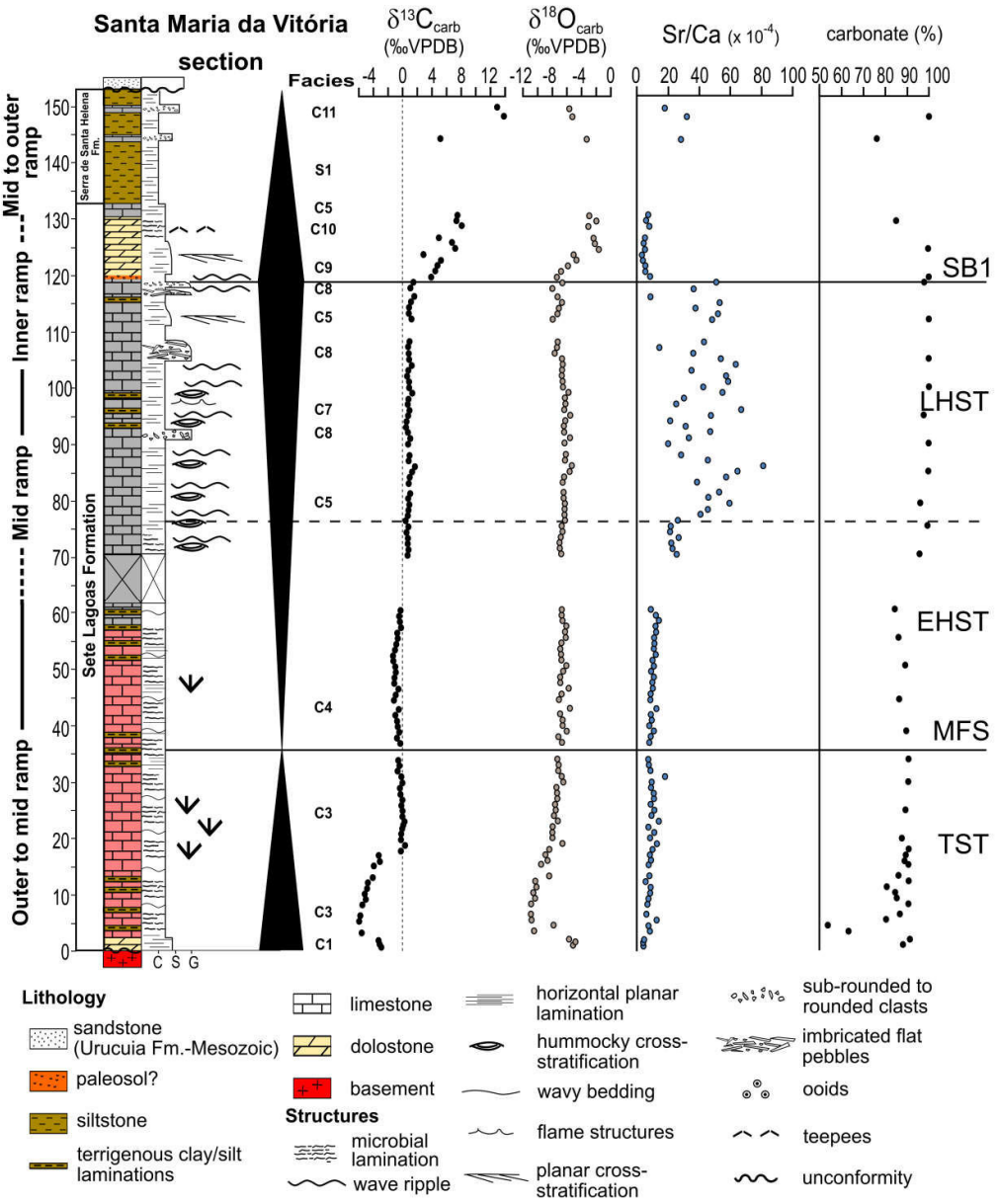

Figure 3.4: The Santa Maria da Vitória section – sequence stratigraphy, facies associations and chemostratigraphy. Limestones are distinguished by two colors – reddish and grey. System tracts: TST – Transgressive System Tract; MFS – Maximum Flooding Surface; EHST – Early Highstand System Tract; LHST – Late Highstand System Tract; SB1 – Sequence Boundary. Granulometry scale: C – clay; S –sand; G – gravel.

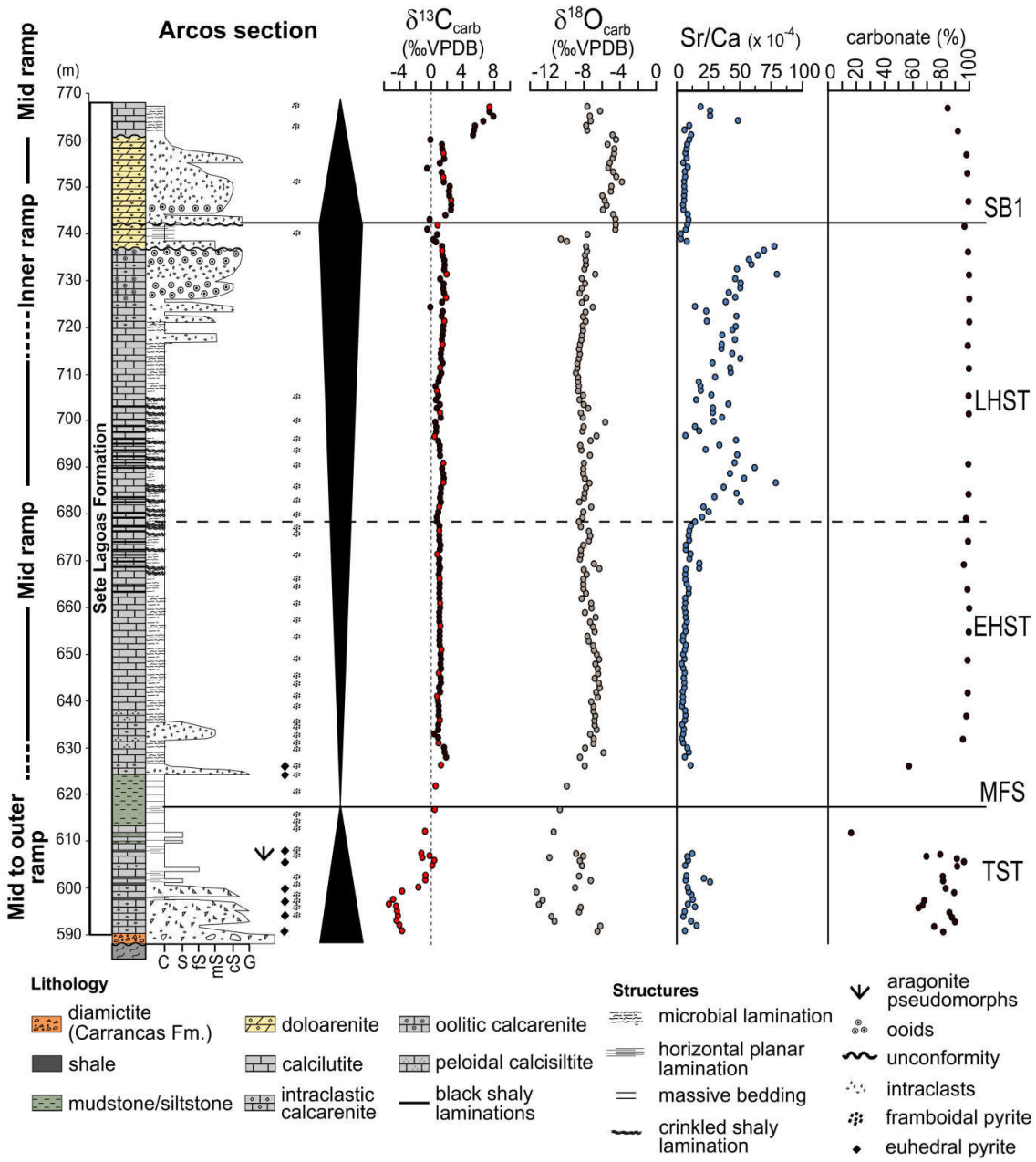

Figure 3.5: The Arcos section – sequence stratigraphy, facies associations and chemostratigraphy. System tracts: TST – Transgressive System Tract; MFS – Maximum Flooding Surface; EHST – Early Highstand System Tract; LHST – Late Highstand System Tract; SB1 – Sequence Boundary. Granulometry scale: C – clay; S – silt; fS – fine sand; mS – medium sand; cS – coarse sand; G – gravel. Red dots in the $\delta^{13}C_{carb}$ profile represent analyses presented previously by Kuchenbecker et al.(2016a).

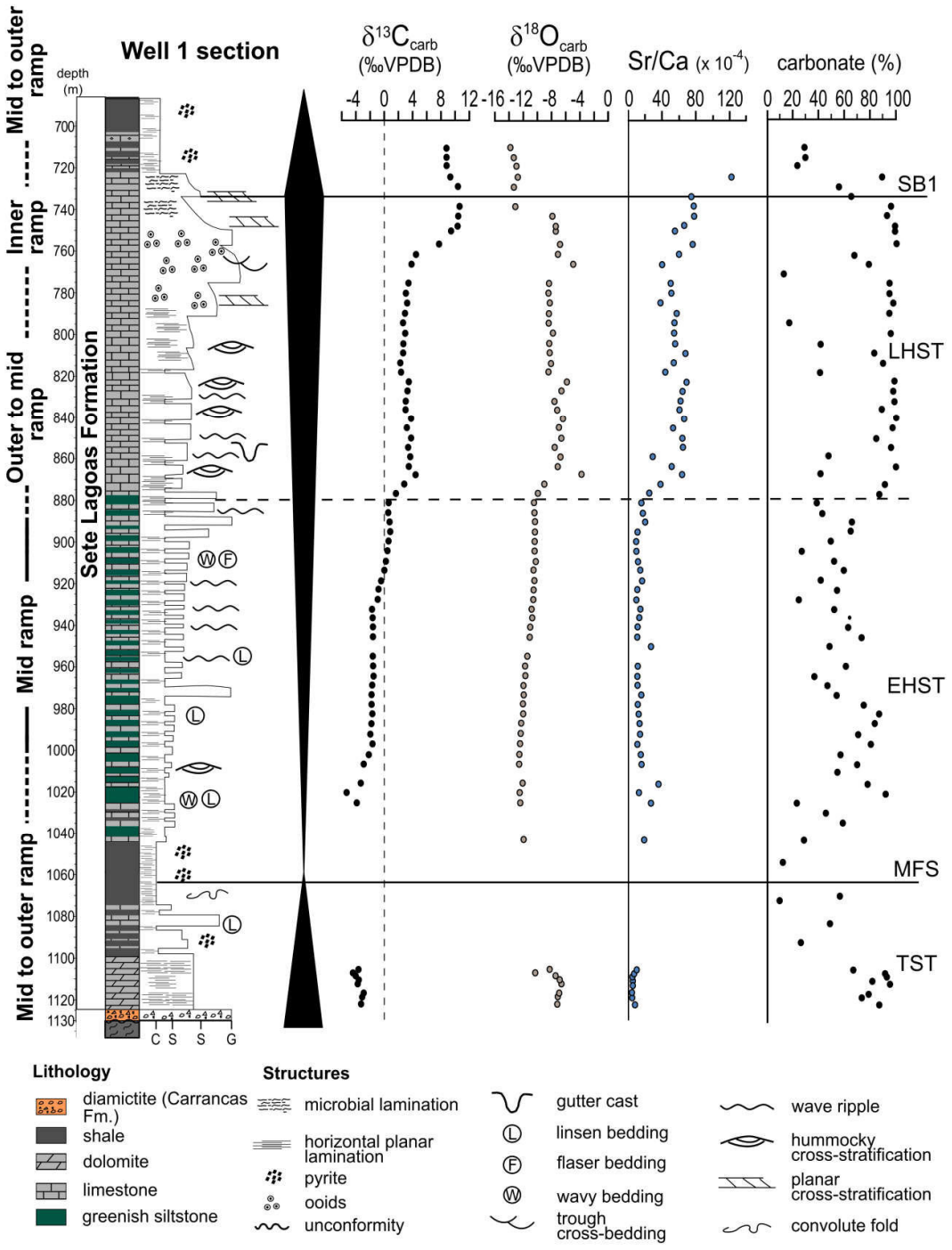

Figure 3.6: The Well 1 section – sequence stratigraphy, facies associations and chemostratigraphy. System tracts: TST – Transgressive System Tract; MFS – Maximum Flooding Surface; EHST – Early Highstand System Tract; LHST – Late Highstand System Tract; SB1 – Sequence Boundary. Granulometry scale: C – clay; S – silt; fS – fine sand; mS – medium sand; cS – coarse sand; G – gravel.

3.4.2. Carbonate facies and sequence stratigraphy

Carbonate facies were defined based on the classification of Dunham (1962), expanded by Embry and Klovan (1971) and Wright (1992)(Table S1 – Appendix A). The term 'rudstone' was used for clast-supported carbonate rocks with grains coarser than 2 mm and sparry matrix, whereas 'bindstone' was used for *in situ* benthic microbial limestones with peloidal matrix supporting rock framework. From Wright's (1992) classification, the term calcimudstone was adopted for mud-dominated rocks composed of more than 90% of lime mud. Carbonate ramp classification follows concepts of Tucker and Wright (1990).

Sequence stratigraphy nomenclature follows review studies from Catuneanu et al. (2009; 2011). The concept of the Bambuí 1st-order sequence follows stratigraphic framework from several previous studies in the basin (e.g. Martins-Neto and Alkmim, 2001; Martins-Neto et al., 2001; Martins-Neto, 2009; Reis et al., 2016). The 2nd-order sequences record different stages of subsidence, related to foreland regime of the Bambuí Sequence (e.g. Martins-Neto, 2009; Reis and Alkmim et al., 2015; Reis et al., 2016).

3.4.3. Carbon and oxygen stable isotope analysis

For carbon and oxygen stable isotope analysis, about 10 mg of carbonate powder was obtained by microdrilling carbonate matrix in areas devoid of fractures, terrigenous components or any late diagenetic carbonate features. The carbonate powders were reacted with orthophosphoric acid at 72 ºC and the released CO_2 was extracted through a continuous flow in a Thermo Finnigan GasBench II. C and O isotope compositions were determined in a Delta V Advantage IRMS at the Stable Isotope Laboratory of the Center for Geochronological Research, University of São Paulo (CPGeo/USP). The isotope compositions are reported in the delta notation relative to the Vienna Pee-Dee Belemnite (V-PDB – ‰). The analytical precision was less than ±0.07‰ for $\delta^{18}O$ and ±0.05‰ for $\delta^{13}C$.

3.4.4. Elemental geochemical analysis and carbonate content

Calcium and strontium content for 507 samples of carbonate rocks were obtained through X-ray fluorescence, using a portable XRF device Thermo Scientific Niton XL3t, gently provided by the Geological Survey of Brazil (CPRM). Polished slabs were prepared and carbonate-rich layers of each sample were selected for elemental analysis, avoiding terrigenous laminations. A blank (pure SiO_2) and the reference material QC 180-673

(Thermo, Germany) were run each 30 analysis. All Sr content measurements for the blank were below the limit of detection of the equipment, whereas the average standard error for Sr measurements in the reference material was ± 1 ppm. For Ca measurements, the blank presented values below 0.1% and the average standard error for the reference material was ± 0.1%. A correlation coefficient of +0.93 between Sr content and Sr/Ca ratios attests the efficiency of the portable XRF device in Sr measurements (Table S2 – Appendix A). The application of this technique allowed analysis of all collected samples, and thus a high resolution of the Sr content along the sections.

Carbonate contents were obtained through decarbonatation of 3–5 g of carbonate rock powders with 25 mL of HCl 5 M. The tubes containing samples and acid solution were heated at 80 ºC for 2 h for a complete dissolution of dolomite. Reaction continued overnight at room temperature. Insoluble residues were rinsed, dried, weighted and the carbonate fraction leachated was calculated.

3.5. Results

3.5.1. Geochemistry

In the 140 m-thick Januária section (Fig. 3.3), a total of 121 samples were collected in a stratigraphic resolution of 0.2 m for the cap carbonate interval and 1 m for the rest of the section. Santa Maria da Vitória section (Fig. 3.4) is 155 m-thick and 115 samples were collected with a stratigraphic resolution of ~1 m. For Arcos section (Fig. 3.5), a total of 113 new $\delta^{13}C_{carb}$ and $\delta^{18}O_{carb}$ data were acquired in addition to the previous data presented by Kuchenbecker et al. (2016a), resulting in a new stratigraphic resolution of 1 m. In the Well 1 section (Fig. 3.6), a total of 75 carbonate rocks were analyzed for carbon and oxygen isotope compositions, in a resolution of 3 m for the cap dolostone interval and 5 m for the rest of the section.

$\delta^{13}C_{carb}$ values vary in a wide rage, from −7.78 to +13.92‰, as expected for the basal Bambuí Group, which encompasses a cap carbonate interval (negative values) and a extreme positive $\delta^{13}C_{carb}$ excursion, at the base and top of Sete Lagoas Formation, respectively. $\delta^{18}O_{carb}$ values range from −16.70 to −1.66‰, with the heavier isotope compositions associated with dolomitic intervals at the top of Sete Lagoas Formation (Fig. 3.4 and 3.5). Sr contents vary from 34 to 3353 ppm, with increasing values topwards the sections. Sr/Ca ratios show similar behaviour, varying from 0.0003 to 0.0121 (Fig. 3.3–3.6). Carbonate contents

vary from 10 to 99%, with average of 90%. All the results are presented in Table S2 of the Supplementary Material (Appendix A).

Regarding a post-depositional alteration assessment for the $\delta^{13}C_{carb}$ and $\delta^{18}O_{carb}$ values, only Santa Maria da Vitória section exhibited a strong positive correlation for $\delta^{18}O_{carb}$ *vs* $\delta^{13}C_{carb}$ ($r = 0.73$, $p(\alpha) < 0.01$; Fig. 3.7), which would suggest diagenesis imprint over isotope compositions (e.g. Hudson, 1977; Veizer et al., 1999). However, the variations of $\delta^{13}C_{carb}$ profile in the Santa Maria da Vitória section are stratigraphically correlated with other studied sections, which yielded moderately to weak $\delta^{18}O_{carb}$ *vs* $\delta^{13}C_{carb}$ correlation (Fig. 3.7). The lack of a positive correlation between $\delta^{18}O_{carb}$ and $\delta^{13}C_{carb}$ for most part of the data makes a meteoric diagenesis overprint unlikely (e.g. Hudson, 1977). The wide lateral continuity of major $\delta^{13}C_{carb}$ trends through the basin hinders a burial diagenesis effect over these carbonate rocks. Fluids involved in burial diagenesis are far depleted in carbon compared to the carbonate units, with the related processes occurring at low fluid/rock ratios due to increase of physical and chemical compaction. Furthermore, the carbon isotope system shows a very weak thermodynamic dependency, with negligible thermal isotope effects during burial (Renard, 1986). Thus, late diagenesis seems to be incapable to promote the carbon isotope re-equilibrium during the neomorphism in carbonate units (e.g. Hudson, 1977). Finally, considering early marine diagenesis, the carbon isotope compositions of the neoformed carbonates may reflect pore water that may be in equilibrium with the marine bottom waters, or to some extent, influenced by early diagenetic metabolisms (i.e. aerobic to anaerobic metabolisms related to organic matter degradation). The later processes can also be interpreted as primary signals if we consider that they may provide important information about bottom redox conditions, and so, the paleoenvironmental evolution. Therefore, the long-term $\delta^{13}C_{carb}$variation (second-order scale) tracked in basinal-scale (hundreds to thousands of kilometers in area) for the Bambuí Group, coupled to the lack of $\delta^{18}O_{carb}$ *vs* $\delta^{13}C_{carb}$ correlation for most of sections, support the carbon isotope evolution as a reliable proxy to constraint paleoenvironmental changes through the Bambuí Sequence.

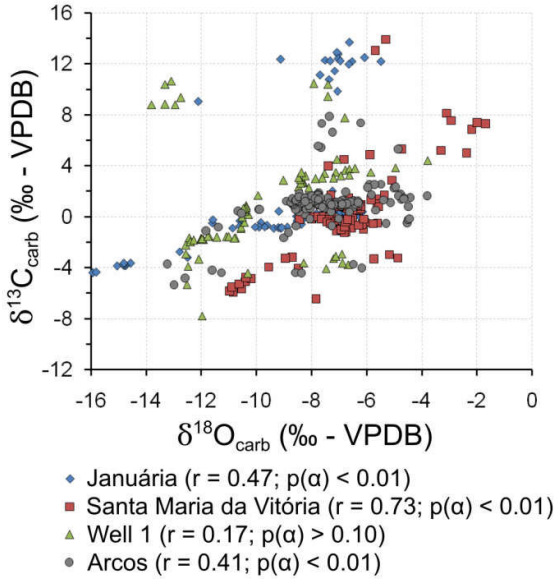

Figure 3.7: $\delta^{18}O_{carb}$ *vs* $\delta^{13}C_{carb}$ cross plots for the studied sections in the basal Bambuí Group.

3.5.2. Sedimentary facies and facies associations of the basal Bambuí Group

Twelve sedimentary facies were identified in the northern Januária High (Table S1, Appendix A; Fig. 3.8). Comprising mixed carbonate-siliciclastic successions, these facies record dominantly subaqueous sedimentary processes operating within a carbonate platform. In the basal 2nd-order sequence (i.e., Carrancas and Sete Lagoas formations), these successions represent outer to inner carbonate ramp associations (Tucker and Wright, 1990; Flugel, 2004). A similar ramp geometry has been identified in previous studies through seismic data and the overall facies characteristics (e.g. Martins and Lemos, 2007; Zalán and Romeiro-Silva, 2007; Vieira et al., 2007b; Reis and Suss, 2016; Perrella Jr. et al., 2017). This succession grades upward into the siliciclastic-dominated and carbonate-dominated settings of the Serra de Santa Helena and Lagoa do Jacaré formations, respectively, in the overlying 2nd-order sequence from the Bambuí Sequence (Fig. 3.3 and 3.4).

Facies associations from the Januária High are described below. The detailed sedimentary-stratigraphic evolution of the Arcos and Well 1 sections of the southern Sete Lagoas High (Fig. 3.5, 3.6, and 3.9) were provided by Kuchenbecker et al. (2016a) and Reis and Suss (2016), respectively, and will be discussed with the new geochemical data for correlation purposes in section3.6.1.

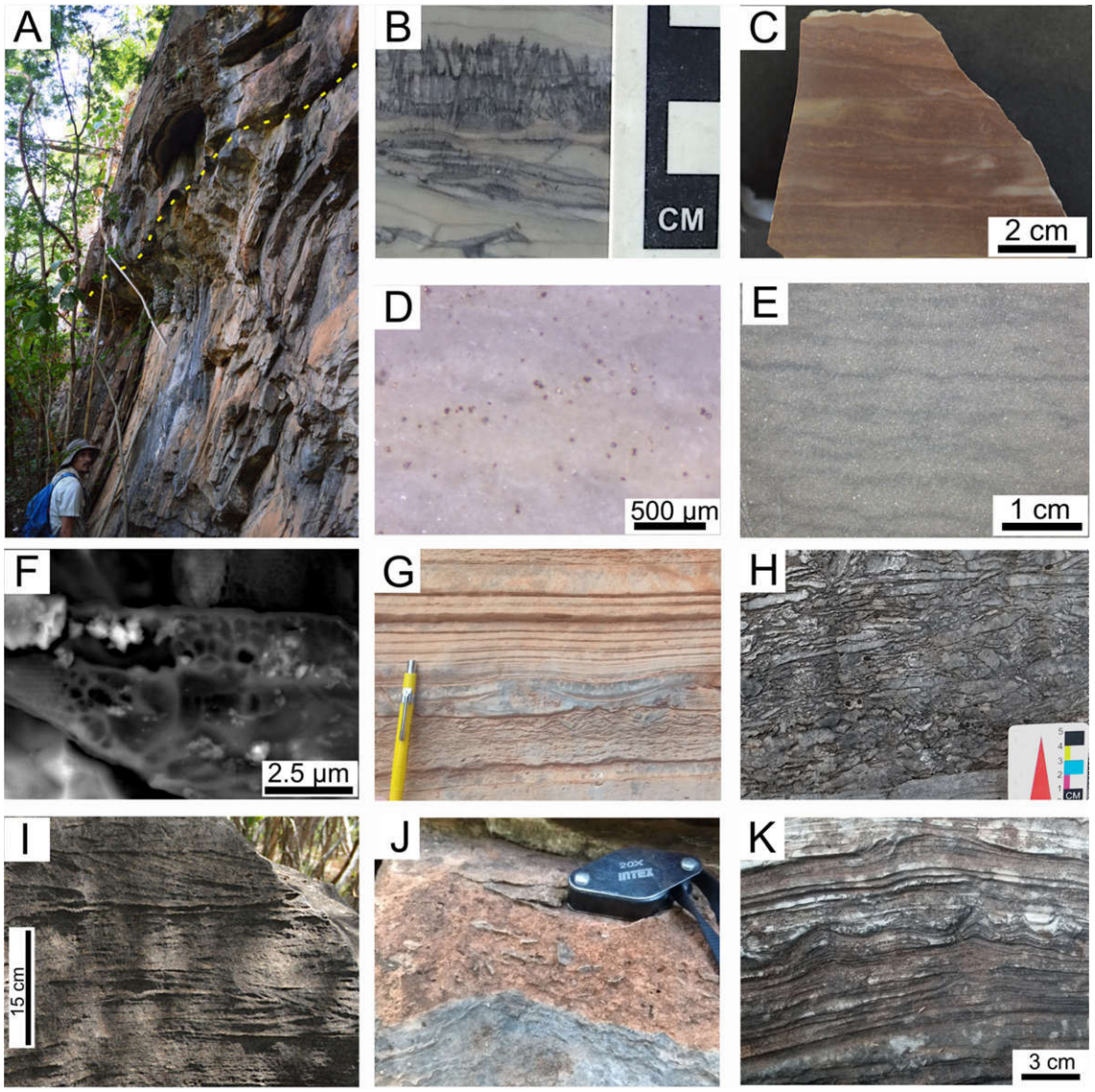

Figure 3.8: Carbonate facies from the Januária High domain, northern São Francisco Basin. A) Basal contact (yellow line) between Sete Lagoas Formation cap carbonate and gneiss from the basement. B) Detail of aragonite pseudomorphs crystal fans from facies C2. C) Reddish peloidal bindstone from facies C3. D) Facies C4, detail for the abundance in framboidal pyrite within the matrix. E) Dark grey peloidal bindstone from facies C6, detail for the irregular microbial lamination, as arborescent structures. F) SEM imagem from organic films within facies C6, presenting honeycomb-like structures associated with EPS. G) Tempestite cycle deposit – basal intraclastic layers followed by hummocky cross-stratification and planar-parallel lamination in mid ramp deposits. H) Flat-pebbled carbonate breccia from facies C8. I) Sets with tangencial cross-stratification in intertidal dolomites (facies C9). J) Possible paleosol layer in the Santa Maria da Vitória section. This level is associated with a $\delta^{13}C$ discontinuity (Fig. 4). K) Stromatolitic dolostones from facies C10.

3.5.2.1. Outer to Mid Ramp Facies Association

Mid to outer ramp facies associations from the Januária High domain encompass facies C1, C2, C3, and S1 (Fig. 3.3 and 3.4; Table S1 – Appendix A). Facies C1, C2, and C3 correspond to the base of the lower Sete Lagoas Formation and the initial transgression over the forebulge domain. Siltstones and mudstones from facies S1 are fine-grained terrigenous siliciclastic sedimentation associated with the Serra de Santa Helena Formation, marking the drowning of the carbonate ramp (Fig. 3.3 and 3.4).

At the basal contact with the basement (Fig. 3.8A), the Sete Lagoas Formation is intensively recrystallized, as a thin (< 1m) massive white crystalline limestone layer in the Januária section and a 3 m-thick dolomitic limestone layer in the base of Santa Maria da Vitória section (facies C1; Table S1 – Appendix A). Light grey calcimudstones from facies C2 are composed of micritic matrix and frequent seafloor cements of aragonite pseudomorphs crystal fans (up to 1 cm; Fig. 3.8B). Reddish laminated bindstones (facies C3; Fig. 3.8C) also present aragonite pseudomorphs, as smaller crystals disposed in irregular crusts (< 0.5 cm). Horizontal planar-parallel lamination from facies C2 and S1 points to suspension/particle settling, whereas irregular and discontinuous lamination from facies C3 suggests a microbial-related precipitation. The lack of oscillatory-related sedimentary structures and the presence of well-preserved seafloor cement in facies C2 and C3 suggest deposition below the storm wave base level (e.g. Vieira et al., 2015; Okubo et al., 2018). Occasional occurrences of wave rippled cross bedding in facies C3 (Fig. 3.4) suggest a rebound of the wave base level to the mid ramp domain, between the storm and fair-weather wave base levels.

3.5.2.2. Mid to Inner Ramp Facies Association

This facies association comprises C4, C5, C6, and C7 facies (Table S1 – Appendix A). Pinkish to light grey bindstones from facies C4 occur at the base to the middle portion of the Sete Lagoas Formation (Fig. 3.3 and 3.4). This facies presents peloidal matrix (20 to 30 μm) and frequent terrigenous mud laminae. Framboidal pyrite is abundant and suggests anoxic sulfidic early diagenesis environment (e.g. Wilkin and Barnes, 1997; Fig. 3.8D). Local occurrences of thin layers (1-2 cm) of intraclastic packstones within facies C4 mark changes in the base level in the inner ramp domain. The microbial lamination of facies C4 is marked by sets of wave rippled cross bedding and hummocky cross-stratification, suggesting deposition between storm wave and fair weather wave base levels.

Topwards, the mid ramp domain is dominated by dark grey bindstones (C6), and associated dark gray calcimudstones (C5) with variable amount of terrigenous mud laminae (C7; Fig. 3.3 and 3.4). Bindstones from the facies C6 exhibit peloidal matrix and irregular lamination, resembling crusts (Fig. 3.8E) with abundant organic films. These organic features display honeycomb-like structures and can be associated with microbial extracellular polymeric substances (EPS; e.g. Schaudinn et al., 2007; Fig. 3.8F). All these facies display sets of wavy bedding and hummocky cross-stratification, including tempestite cycles (Fig 3.8G), representing the mid ramp domain between the storm wave and fair weather wave base levels. Local occurrences of wave ripples mark a transition to the inner ramp domain, above the fair-weather wave base (e.g. Tucker and Wright, 1990).

3.5.2.3. Inner Ramp Facies Association

Inner ramp environments comprise high-energy shallow water carbonate facies (C8, C9, C10, and C11; Table S1 – Appendix A) at the top of the basal Sete Lagoas Formation and the overlying Serra de Santa Helena and Lagoa do Jacaré formations.

Intraclastic rudstones occur as carbonate breccias of facies C8 and are remarkable stratigraphic levels defining sequence boundaries at Januária High domain (e.g. Martínez, 2007; Perrella Jr. et al., 2017), occurring in both sections (Fig. 3.3 and 3.4). These breccias are composed of intraformational limestones fragments, as flat pebbles to cobbles (2 to 10 cm) and subrounded pebbles (0.5 to 2 cm). The clasts are poorly-sorted and support the fabrics, with a close packing (Fig. 3.8H). They occur as massive layers from 0.5 to 2 m, which thicken upward in the basal sequence (Fig. 3.3). Occasionally fining-upward pattern and frequent imbricated flat pebbles occur at the base of the layers. Some levels also resemble reworked teepee structures. Due to high compaction, contacts between carbonate breccia layers and underlying facies are sharp planar surfaces, often associated with stilolytes. The layers are continuous in a kilometer scale, and can be tracked through the top of the hills in the area of Januária city. Considering the abundance of flat pebbles, the oligomictic (intraclastic) character and the association with wave ripple facies below and above (Fig. 3.3), these carbonate breccias were attributed to the inner ramp domain, in a shallow marine environment, probably related to variations in the base level and consequent exposure, locally re-worked by tidal currents and storm-driven events (Flugel, 2004; Perrella Jr. et al., 2017).

Dolomitization is observed at the top of Sete Lagoas Formation in the area (Fig. 3.3 and 3.4). In Januária section, intraclastic dolograinstones (facies C9; Table S1 – Appendix A)

occur at the top of section and are composed of subangular intraclasts, with dissolution features, as vugular to moldic porosity. They also display sets of planar to trough cross-stratification associated with intertidal environment (Fig. 3.8I). In the Santa Maria da Vitória section, a thicker dolomite interval (~10 m-thick) was described, with a variety of shallow water facies, including subaerial exposure features in a supratidal domain (Fig. 3.4). A possible paleosol layer was described at the base of this interval (Fig. 3.8J) and marks a sharp discontinuity in the $\delta^{13}C_{carb}$ profile (Fig. 3.4). The overlying dolomitic interval starts with deposition of intertidal dolomites with sets of planar cross-stratification (facies C9), followed by laminated to domical dolomitic stromatolites from facies C10 (Fig. 3.8K). This dolomitization is interpreted in terms of a lowstand condition related to the sequence boundary. We suggest a dolomitization model of a meteoric-marine mixing zone (e.g. Badiozamani, 1973; Flugel, 2004), considering the dolomitization of intertidal facies during early diagenesis in the shallower areas of the carbonate ramp, which is not restricted to supratidal facies and is associated with dissolution features. Nevertheless, despite the absence of evaporitic minerals, usual high $\delta^{18}O$ values in this dolomite interval (Fig. 3.4 and 3.5) suggest more evaporitic conditions in these shallow environments.

Finally, oolitic to intraclastic grainstones represent the inner ramp domain and correspond to grainstones shoals associated with Lagoa do Jacaré Formation (facies C11) interbedded within pelites from Serra de Santa Helena Formation (Table S1 – Appendix A). In Januária section, this facies composes a 17 m-thick interval associated with calcimudstones and collapse breccias, in shallow water domain (Fig. 3.3). In Santa Maria da Vitória section, this facies occurs as oolitic grainstone lenses within pelites from the Serra de Santa Helena Formation (Fig. 3.4).

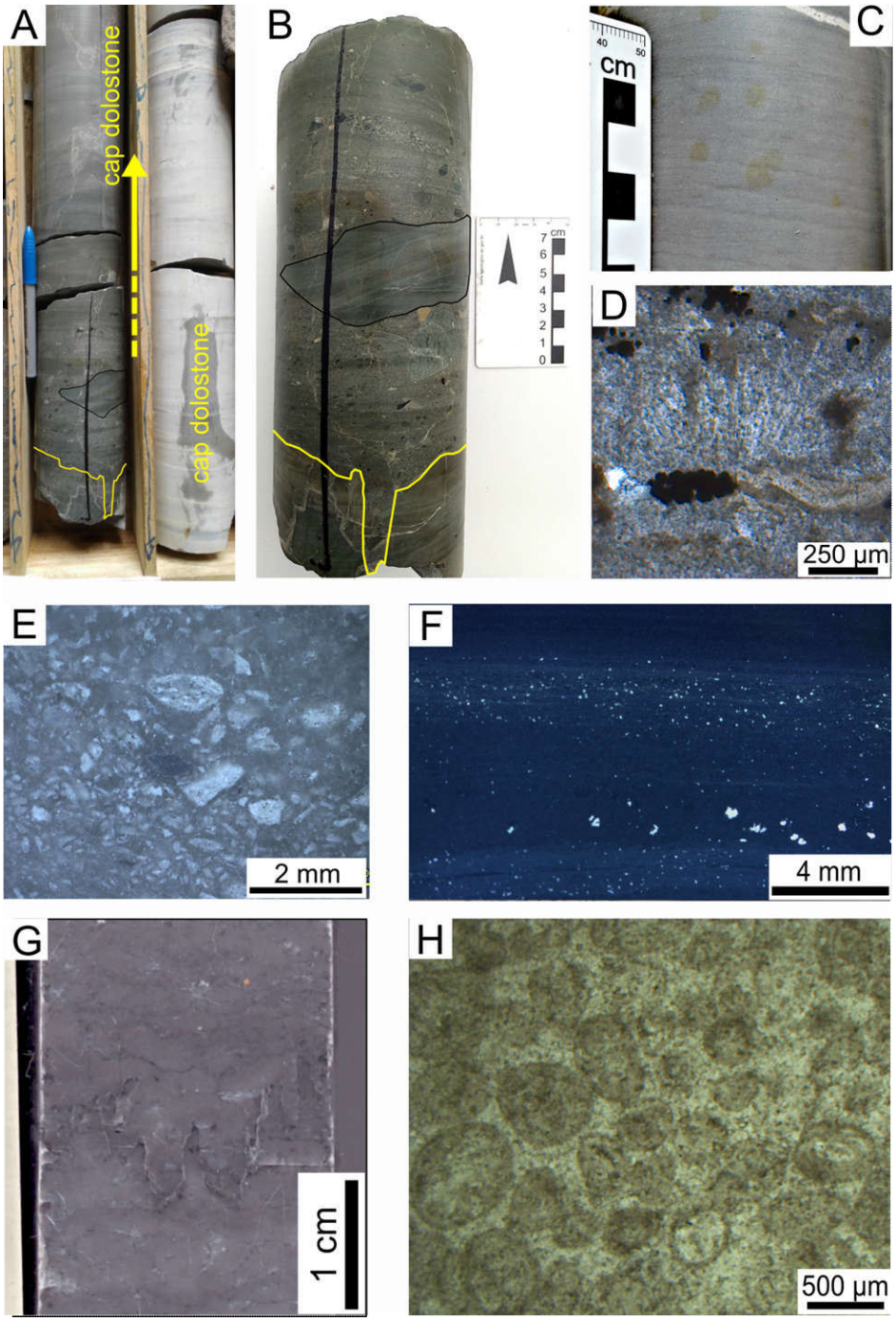

Figure 3.9: Carbonate facies from the Sete Lagoas High domain, southern São Francisco Basin. A) Basal contact between diamictites and the basement (yellow line). The diamictite turns into the cap dolostones. B) Detail of the polymictic diamictite layer. C) Dolomudstones with microbial lamination. D) Aragonite psudomorphs in thin section from the cap carbonate interval of Arcos section. E) Intraclastic grainstone from the Arcos section. F) Polished slab of a black shale sample from the Well 1 section. Pyrites are the brighter grains within the matrix. G) Grey bindstones from the Arcos section, detail for the shrub-like structures in the microbial lamination. H) Thin section of a oolitic grainstone from the Arcos section.

3.6. Discussion

3.6.1. Sequence stratigraphy and chemostratigraphy of the basal Bambuí Group

In order to correlate the basal Bambuí Group between the Januária and Sete Lagoas highs, we first access the stratigraphic evolution between these distinct forebulge domains in a second-order scale, based on recognition of system tracts and stratigraphic surfaces of basin-scale correlation. The Bambuí Group in Januária High domain display similar transgressive-regressive stratigraphic pattern identified in Sete Lagoas High by previous studies (Vieira et al., 2007a,b; Kuchenbecker et al., 2016a; Reis and Suss, 2016). A high-resolution analysis of the forebulge dynamics of this basal 2nd-order sequence in a basinal scale was possible, through correlation of two notable stratigraphic surfaces (the maximum flooding surface – MFS – and the first sequence boundary – SB1; Fig. 3.10 and 3.11). The chemostratigraphic evolution of $\delta^{13}C$ values and Sr/Ca ratios was assessed in the identified system tracts, exploring similarities and differences between the different domains. The major $\delta^{13}C_{carb}$ trends show a reliable use for intrabasinal regional correlations in 2nd-order sequence stratigraphy scale, and alongside Sr/Ca ratios, provide insights concerning major paleoenvironmental changes through the basal Bambuí Sequence (Fig. 3.11).

3.6.1.1. Transgressive Systems Tract

The transgressive system tract represents the initial transgression over the forebulge domain on the Bambuí basin cycle, with a retrogradational pattern of mixed siliciclastic-carbonate facies until the maximum flooding surface, which is the turning point to a regressive succession and progradational stacking pattern (e.g. Catuneanu et al., 2011; Fig.3.10 and 11). Such initial transgression resulted in sedimentary deposits of Carrancas and Sete Lagoas formations, directly overlying the basement (Fig. 3.9A and 3.8A, respectively). The nature of the basal diamictites remains uncertain. Some authors have suggested glacial influence over the deposition of Carrancas Formation (Romano and Knauer, 2003; Romano, 2007; Kuchenbecker et al., 2011; 2016a; Rocha-Campos et al., 2011), whereas others assumed that no glacial features were observed, interpreting it as gravity flows associated with basement highs and graben-filling deposits (Uhlein et al., 2012; Tuller et al., 2010), or even as fluvial deposits in incised basement valleys (Vieira et al., 2007b). Kuchenbecker et al. (2013) interpreted the diamictite layer from Arcos section as a lodgement tillite, based on its relation to irregularities in the basement and also on deformation pattern of the clasts, whereas

Reis and Suss (2016) also described a syn-sedimentary deformation which was associated with a post-glacial event in the diamictite layer of the Well 1 section.

The basal diamictites gradually grade into carbonate rocks from the basal Sete Lagoas Formation (Fig. 3.9A, 3.9B, and 3.9C), marked by a fining-upward pattern and more carbonatic matrix topwards (Reis and Suss, 2016). Aragonite pseudomorphs occur only in a single level at Arcos section (Fig. 3.5 and 3.9D), whereas Well 1 section lacks such a classical cap carbonate sedimentary feature. Nevertheless, well-developed aragonite pseudomorph crystals were described in the basal sequence in Sete Lagoas High (Babinski et al., 2007; Vieira et al., 2007a; 2015; Paula-Santos et al., 2017). On the other hand, sections from Januária High display several levels of aragonite pseudomorph crystal fans (Fig. 3.3, 3.4 and 3.8B) in the transgressive succession deposited directly over the basement, mostly associated with pinkish to reddish limestones. We attribute the low expression of aragonite pseudomorphs in the southern sections to: (i) higher energy character of the early transgressive deposits in these sections, with intraclastic grainstones and rudstones in Arcos section (Fig. 3.5 and 3.9E) and dolomudstones with hummocky cross-stratification in Well 1 section (Fig. 3.6; Reis and Suss, 2016); and (ii) abundance of terrigenous fine-grained siliciclastics in deeper facies (Fig. 3.5 and3.6), probably due to closer proximity of these sections to the basin edge. Therefore, our sections located at Januária High seem to represent a more alkaline and low-energy deeper environments (Fig. 3.10), free from significant terrigenous input and in more favorable conditions to develop aragonite fans seafloor cements (e.g. Okubo et al., 2018).

In Sete Lagoas High, the maximum flooding surface was set in the middle of a mudstone/shale succession, as the deeper facies of Arcos and Well 1 section at the outer ramp domain (Fig. 3.5, 3.6, and 3.9F; Kuchenbecker et al., 2011; 2016a; Reis and Suss, 2016). In Januária High, an interval of reddish to light gray peloidal bindstones with more frequent pelitic laminations and lacking sedimentary structures related to oscillatory or unidirectional flows (facies C3 and C4; Fig. 3.3, 3.4, and 3.10) was chosen as the deeper environments of the outer ramp domain, and so as the maximum flooding surface (Fig. 3.3 and 3.4).

Regarding the carbon isotope evolution, the transgressive system tract is marked by a negative to positive $\delta^{13}C_{carb}$ excursion (Fig. 3.11). In Januária High, the $\delta^{13}C_{carb}$ curve starts with values close to −3‰ in a negative excursion to values around −6.5‰, followed by an inflection to a positive excursion up to values around 0‰ (Fig. 3.3 and 3.4). Topwards until the maximum flooding surface (Fig. 3.11), the $\delta^{13}C_{carb}$ curve presents a slight decrease to

values around −1‰. In Sete Lagoas High, Arcos section display the same $\delta^{13}C_{carb}$ trend for the initial transgression as Januária High, starting with values close to −4‰ in a negative excursion to−5.5‰, with a recover to 0‰ followed by a slight decrease to −1‰ until the maximum flooding surface (Fig. 3.6 and 3.11). Well 1 section yielded a very similar negative excursion at the basal dolostone interval, but unfortunately, no carbonate facies were available for isotope analysis for the rest of the transgressive system tract (Fig. 3.6 and 3.11), which is dominated by black shales of deeper settings in the forebulge graben (Fig. 3.10). From Arcos, Januária, and Santa Maria da Vitória sections, the maximum flooding surface matches a $\delta^{13}C_{carb}$ trend, as an inflection to a slight positive excursion at the base of the overlying early highstand system tract (Fig. 3.11).

Sr contents for this initial transgressive system tract are low, varying from 34 to 463 ppm, with an average and median of 217 and 223 ppm, respectively (n = 110). This is reflected in low average Sr/Ca ratio of 0.001. The exception is a sample with aragonite pseudomorph crystal fans, which has concentration higher than 3000 ppm (sample 17-CM-03f; Table S2 – Appendix A). As expected by mineralogy effect related to crystal structure (e.g. Holland et al., 1963; 1964; Banner, 1995), these aragonite values are not considered as representing the general paleoenvironmental condition. The low Sr content of these carbonate rocks may be due to high terrigenous content at this stage and/or to neomorphism, highlighted by recrystallized limestones and some occurrences of dolomitization.

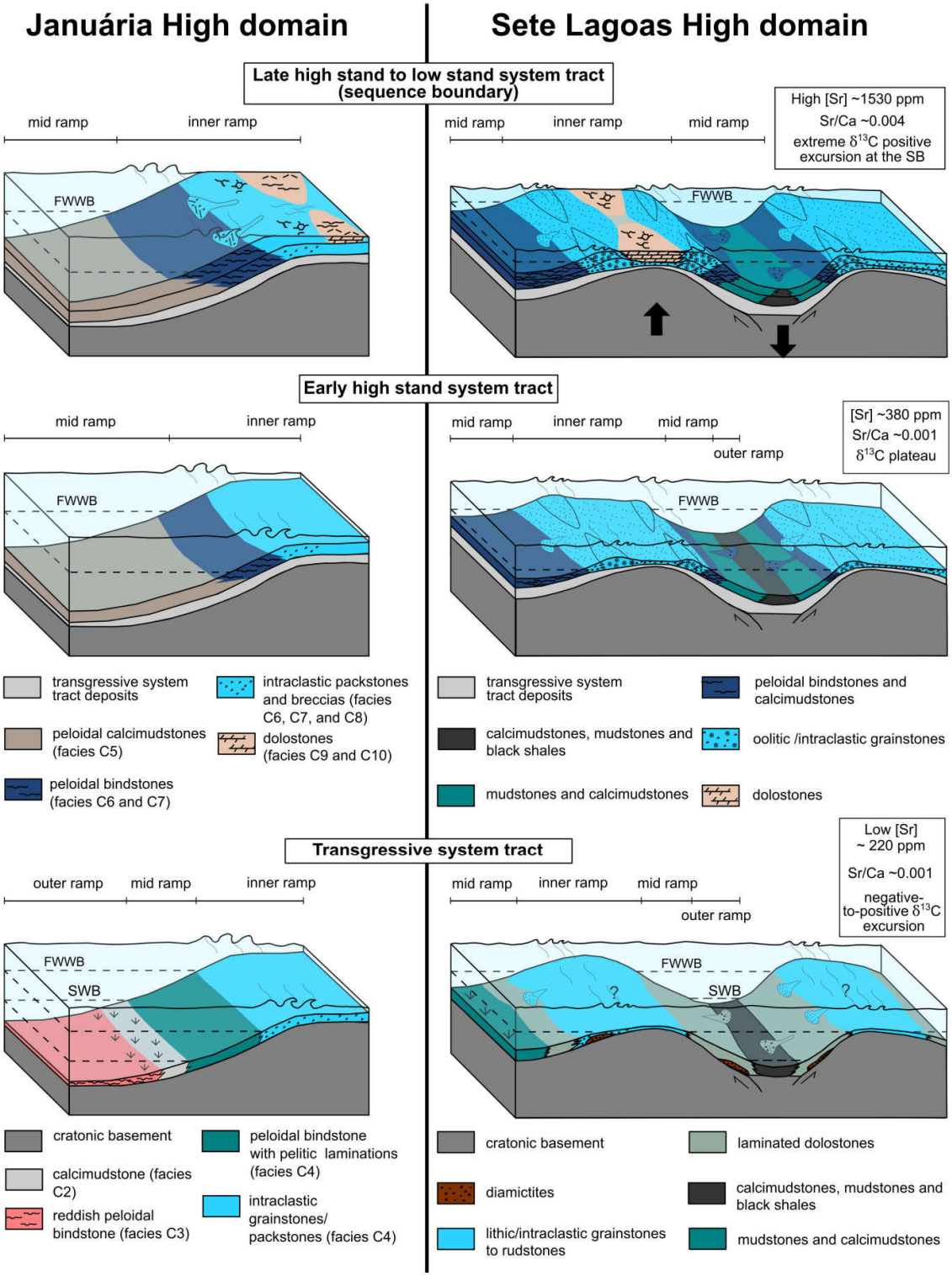

Figure 3.10: Tectonosedimentary evolution of the basal Bambuí Sequence for the two domains studied in the São Francisco Basin. The main geochemical features for each stage in a basinal scale are given in the boxes on the right. FWWB – Fair Weather Wave Base level; SWB – Storm Wave Base level.

3.6.1.2. Early Highstand Systems Tract

The early highstand system tract initiates after the maximum flooding surface (Fig. 3.11), marking a change in the stacking pattern from a retrogradational to a progradational setting within the middle part of Sete Lagoas Formation (Fig. 3.10 and 3.11; e.g. Catuneanu et al., 2009; 2011). In Januária, Santa Maria da Vitória, and Arcos sections (Fig. 3.3, 3.4 and 3.5), this stage is marked by dark-gray calcimudstones to bindstones (facies C5 and C6; Fig. 3.8E, 3.8F, and 3.9G), with very low terrigenous contents. In the forebulge graben domain, a limestone-mudstone rhythmite interval with hummocky cross-stratification, wave ripples and heterolithic bedding marks this stage (Fig. 3.6 and 3.11).

The $\delta^{13}C_{carb}$ evolution is very similar between Januária, Santa Maria da Vitória, and Arcos sections (Fig. 3.3, 3.4, and 3.5), with a slight positive excursion right after the maximum flooding surface (Fig. 3.11), reaching a plateau of values between 0 and +1‰. Well 1 section shows a distinctive $\delta^{13}C_{carb}$ pattern, with a more expressive positive excursion after the maximum flooding surface, from −7‰ to a plateau around −1.5‰, followed by a new positive excursion to values around 0‰ at the top of the early highstand stage (Fig. 3.6 and 3.11). These lower $\delta^{13}C_{carb}$ values probably derive from a higher dissolved organic carbon pool in the deep waters of the forebulge graben sub-basin (i.e. thick transgressive black shales deposits; Fig. 3.6 and 3.9F), which could have been oxidized during the early regression, releasing light carbon into solution. Strontium contents for this stage increase in average to 381 ppm, with a median of 316 ppm (n = 138), however, with average Sr/Ca ratio of 0.001, similar to the initial transgressive system tract. Thus, the $\delta^{13}C_{carb}$ and Sr contents from the early highstand stage represent the stabilization of the marine carbonate ramp in the sequence, with predominance of carbonate rocks after the initial mixed carbonate-siliciclastic interval of the transgressive stage.

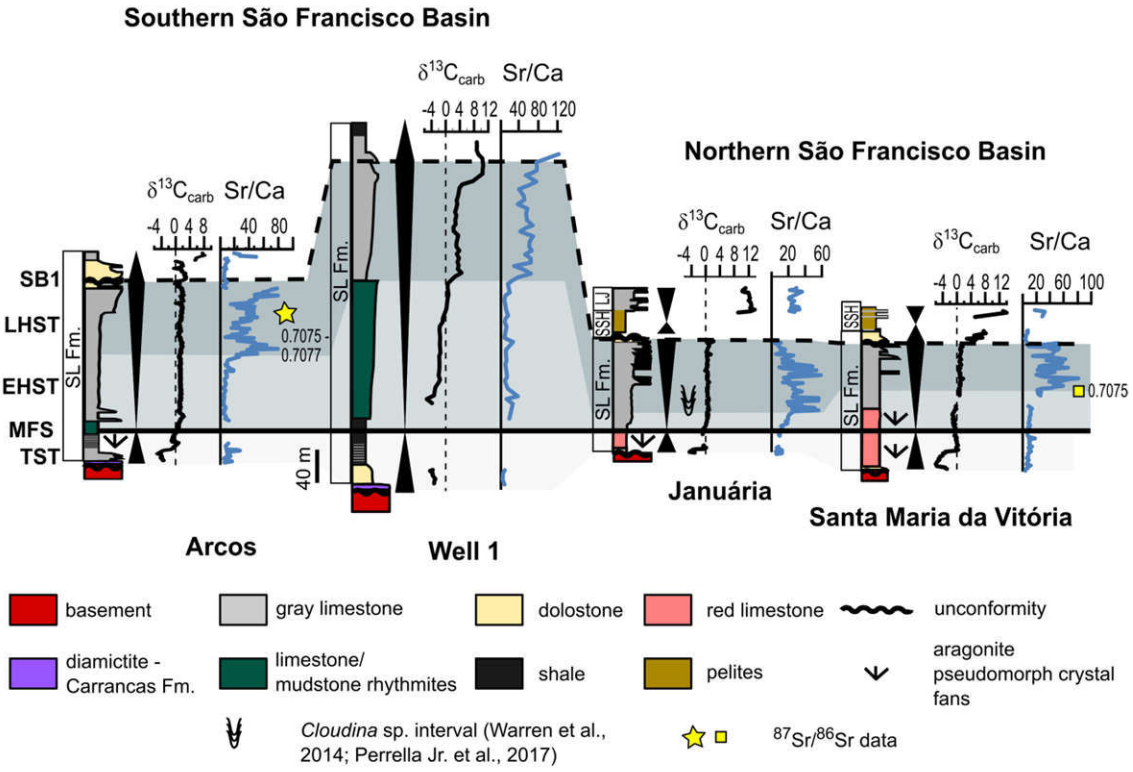

Figure 3.11: Stratigraphic-chemostratigraphic correlations for the basal Bambuí Sequence between the southern and northern domains of the São Francisco Basin (Sete Lagoas and Januária highs, respectively). $\delta^{13}C_{carb}$ data are in ‰ V-PDB and Sr/Ca multiplied by 10^4. $^{87}Sr/^{86}Sr$ data from Kuchenbecker et al. (2016a) for the Arcos section (star), and from Caxito et al. (2018) for the Santa Maria da Vitória area (square). TST: Transgressive System Tract; MFS: Maximum Flooding Surface; EHST: Early Highstand System Tract; LHST: Late Highstand System Tract; SB1: Sequence Boundary. Lithostratigraphic units: SL – Sete Lagoas Formation; SSH – Serra de Santa Helena Formation; LJ – Lagoa do Jacaré Formation. Stratigraphic sections are in the same vertical scale.

3.6.1.3. Late Highstand Systems Tract

The late highstand system tract is considered as the final stage of progradational stacking pattern, representing the carbonate ramp climax throughout the basin, and display chemostratigraphic features related to major paleoenvironmental changes in the basal Bambuí Sequence (Fig. 3.10 and 3.11). A regional increase in the Sr content and Sr/Ca ratios of carbonates was first time detected in basinal scale, and recognized as a chemostratigraphic marker between the early and late highstand system tracts. It is characterized by very pure carbonate rocks in both domains studied and marks the climax of carbonate factory in the basal sequence throughout the forebulge domain. This stage is dominated by dark-grey bindstones and peloidal calcimudstones with hummocky cross-stratification to wave ripples of

mid to inner ramp domain in the upper part of Sete Lagoas Formation in the studied areas (Fig. 3.3, 3.4, 3.5, and 3.6). On the top, coarse-grained limestones mark the most proximal deposits at the end of regressive cycle (Fig. 3.11). Carbonate breccias layers (facies C8, Table S1 – Appendix A) becomes thicker and frequent towards the top of this interval in Januária High (Fig. 3.3, 3.4, and 3.8H), whereas intraclastic to oolitic grainstones end the sequence at Sete Lagoas High (Fig. 3.5, 3.6, and 3.9H).

With exception of Well 1 section located in a forebulge graben, the sequence boundary that ends the late highstand system tract is marked by an erosive unconformity within the top of Sete Lagoas Formation, associated with a dolomitic interval and subaerial exposure features (Fig. 3.10 and 3.11). In Sete Lagoas High domain, the sequence boundary was positioned at a collapse breccias layer within the dolomitic interval (Fig. 3.5; Kuchenbecker et al., 2011). In Januária High domain, a possible paleosol thin layer (Fig. 3.4 and 3.8J) was chosen as the sequence boundary in Santa Maria da Vitória section, and matches an abrupt break in the $\delta^{13}C_{carb}$ profile (Fig. 3.4 and 3.11), whereas in Januária section, the sequence boundary was placed in the contact between carbonate breccias and intertidal dolomites with planar to trough cross-stratification (Fig. 3.3 and 3.8I). In Well 1 section, it was set in a layer of microbial limestones with possible salt pseudomorphs, interpreted as shallower facies of the basal sequence (for the detailed stratigraphic analysis, see Reis and Suss, 2016). At the top, a gradual transition from dark-grey calcimudstones-black shale rhythmites to a thick black shale interval (Fig. 3.6) sets a new transgression in the following 2nd-order sequence. This sequence boundary is considered as a correlative conformity related to erosional unconformity observed in other sections. The singular behavior of the $\delta^{13}C_{carb}$ profile in Well 1 section illustrates this character, without any major break (Fig. 3.6 and 3.11).

From the early highstand to the late highstand stage, the $\delta^{13}C_{carb}$ profile remains a plateau between 0 and +1‰ in Januária, Santa Maria da Vitória, and Arcos sections (Fig. 3.3, 3.4, 3.5, and 3.11). Again, the exception is Well 1 section that displays a positive $\delta^{13}C_{carb}$ excursion at the beggining of this stage, reaching a plateau around +3 to +4‰ (Fig. 3.6). This particular $\delta^{13}C_{carb}$ evolution is interpreted as local controls over the forebulge graben, such as stratified water column. The higher carbonate carbon isotope fractionation reflects deeper environments, in which increased organic carbon preservation and burial might have driven lateral variations of $\delta^{13}C_{carb}$ values. Well 1 section also shows that the remarkable $\delta^{13}C_{carb}$ positive excursion initiates at the end of the late highstand stage, closely related to the sequence boundary. In other sections, it is not possible to point where the positive excursion

started, due to unconformities associated with dolomitization in the overlying 2nd-order sequence (Fig. 3.11).

Remarkable increases in Sr content and Sr/Ca ratios characterize the late highstand system tract in all studied sections and are the main chemostratigraphic features of this stage (Fig. 3.11; Table S2 – Appendix A). The average Sr content for this stage is 1529 ppm, with a median of 1554 ppm and a maximum value of 3353 ppm, considerably higher than the average for ancient limestones (~500 ppm; Morse and Mackenzie, 1990; Reimann and Caritat, 1998). Such increase in Sr content of carbonate rocks is not followed by a change in the carbonate facies through highstand stages (Fig. 3.3, 3.4, and 3.5), neither by any major increase in carbonate content (Fig. 3.12A). A systematic increase in Sr/Ca ratios is observed in all studied sections, with average of 0.004 (Fig. 3.11), and also is not followed by an increase in carbonate content (Fig. 3.12B). The lack of correlation between [Sr] and Sr/Ca ratios with carbonate content, and predominance of pure carbonate rocks within the late highstand stage (carbonate content > 95%; Fig 3.12; Table S2 – Appendix A) suggest that the Sr-enrichment is related to a higher incorporation of this element in carbonate minerals and may represent a significant paleoenvironmental change in the basin.

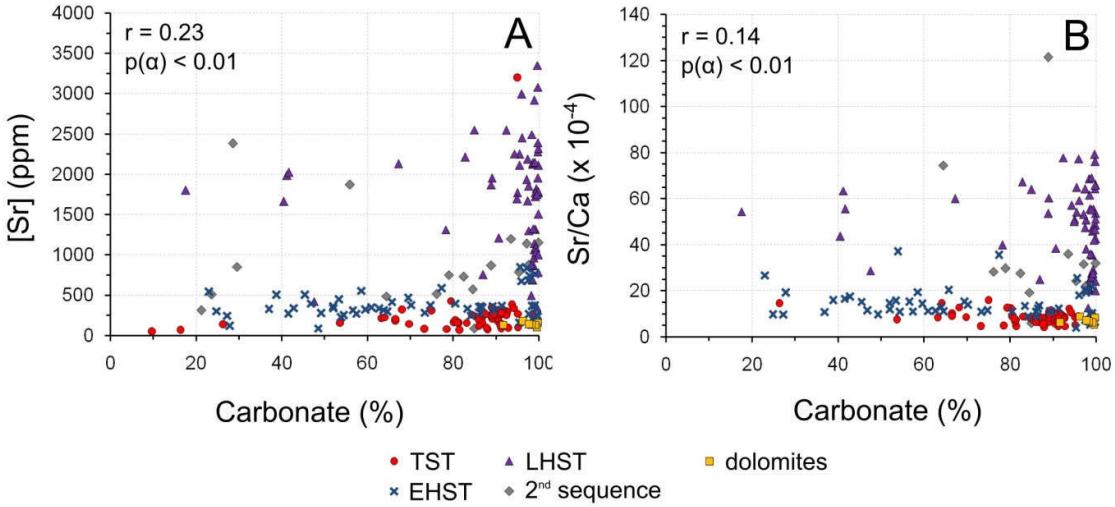

Figure 3.12: Cross plots of carbonate content *vs* [Sr] (A) and carbonate content *vs* Sr/Ca (B) for each system tract. TST: Transgressive System Tract; EHST: Early Highstand System Tract; LHST: Late Highstand System Tract. Increases in [Sr] and Sr/Ca are associated with the late highstand system tract and overlying 2nd sequence, with no correlation with carbonate contents.

Several parameters control Sr incorporation in carbonate minerals, such as primary mineralogy, temperature, salinity, vital effect, and Sr/Ca ratios of the coeval aqueous system (Morse and Mackenzie, 1990; Flügel, 2004). Despite the challenge in testing an aragonite precursor due to the very low preservation of this metastable mineral (Tucker and Wright, 1990), the association of high Sr/Ca ratios with aragonitic conditions is frequent in literature (e.g. Veizer and Demovic, 1974; Sandberg, 1983; Morse and Mackenzie, 1990; Flügel, 2004). Due to crystalline structural controls of aragonite lattice, Sr^{2+} is more easily incorporated in this carbonate mineral compared to low Mg calcite (Holland et al., 1963; 1964). This results in great Sr enrichments in modern biogenic and abiogenic aragonite components (corals, algae, aragonite muds and ooids; [Sr] > 7000 ppm; Kinsman, 1969; Morse and Mackenzie, 1990). On the other hand, other processes can account for increased incorporation of Sr in calcite, without requiring an aragonite precursor. Rapid precipitation rates of calcite (Morse and Bender, 1989 and references therein) and hypersaline and restricted environments (e.g. Veizer and Demovic, 1974; Pietzsch et al., 2018) can also result in high Sr calcite.

As noted by Cui et al. (2016), high Sr concentrations seem to be a common feature in late Ediacaran deposits, especially in *Cloudina*-bearing intervals in South China (Sawaki et al., 2010; Cui et al., 2016) and Namibia (Ries et al., 2009). Wood et al. (2018) provided detailed microfaciological study in *Cloudina* deposits from the Nama Group, with early diagenetic acicular pseudomorphed aragonite cements with high Sr contents (~1900 ppm), as well as Sr-rich *Cloudina* skeletons (up to 1600 ppm). In Brazilian late Ediacaran record, the *Cloudina*-bearing Tamengo Formation, in the Southern Paraguay Belt, also exhibit very high Sr contents (~ 2800 ppm), reaching maximum values of 10289 ppm for oolitic grainstones (Boggiani et al., 2010). The *Cloudina*-bearing Polanco Formation, Rio de la Plata Craton, also displays high Sr contents (> 2000 ppm; Gaucher et al., 2009). In this study, although we did not describe any occurrence of *Cloudina* sp. in our samples, the late highstand stage of the Januária section (Fig. 3.3 and 3.11) is the interval in which *Cloudina* sp. is reported (Warren et al., 2014; Perrella Jr. et al., 2017). *Cloudina* sp. occurrences were described in the middle Sete Lagoas Formation, basal Bambuí Group, in the same area of our Januária composite section (Fig. 3.3), associated with microbial limestones (i.e. facies C6) with $\delta^{13}C_{carb}$ values ~0‰ (Warren et al., 2014; Perrella Jr. et al., 2017), preceding carbonate breccias interval (i.e. facies C8) at the top of sequence (Fig. 3.3 and 3.11; Perrella Jr. et al., 2017). Therefore, the association between *Cloudina* sp. occurrences and the late highstand stage at the basal sequence is supported by $\delta^{13}C_{carb}$ correlations and sequence stratigraphy evolution for the Januária city area (Perrella Jr. et al., 2017).

Whether aragonitic conditions (Cui et al., 2016; Wood et al., 2008), high alkalinity and high carbonate precipitation rates (Cui et al., 2016), or hypersalinity and environmental restriction caused the increasing Sr content, a clear relationship between these enrichments and the regressive trend is observed in the basal Bambuí Group. The aragonitic conditions in the late highstand stage would be compatible with the shallower facies reported within this interval, considering aragonite as the main carbonate mineral in shallow marine carbonate environments (e.g. Morse and Mackenzie, 1990). High Sr influx, high alkalinity, and consequently high rates of carbonate precipitation (e.g. Cui et al., 2016) are also possible scenarios for the basal Bambuí Group, as proposed by previous studies in the basin (Paula-Santos et al., 2015; 2017; 2018). Paula-Santos et al. (2015; 2017) proposed high Sr influx due to chemical weathering of ancient carbonates from the surrounding orogenic belts to explain the low $^{87}Sr/^{86}Sr$ ratios in Sr-rich carbonates from the upper Sete Lagoas and Lagoa do Jacaré formations. This interval corresponds to the overlying second sequence, with $^{87}Sr/^{86}Sr$ ratios mismatching the expected ones for late Ediacaran-Cambrian. It would represent a more restricted stage of the basin disconnected from the coeval seas (CI-3; Paula-Santos et al., 2017; Fig. 3.2). Paula-Santos et al. (2018) also inferred a high alkalinity for this paleoenvironment, based on shale-normalized REE patterns. Extremely heavy carbon isotope compositions, high Sr contents and Sr/Ca ratios persist through the overlying sequence (with the exception of dolomite intervals; Fig. 3.3, 3.4, 3.5, and 3.6). These observations suggest that the paleoenvironmental change at the late highstand of the basal sequence was long-lived, probably related to the progressive basin restriction driven by the advances of orogenic fronts (Paula-Santos et al., 2017; Uhlein et al., 2019).

3.6.2. Tectonosedimentary evolution of the Bambuí Sequence

The integrated stratigraphic-chemostratigraphic approach on the basal 2nd-order sequence of the Bambuí Sequence sustains and gives more details on the foreland-related tectonic dynamics for accommodation space generation in the basin, in which tectonic pulses likely control the onset of transgressive-regressive sequences (e.g. Martins-Neto, 2009; Alkmim and Martins-Neto, 2012; Reis and Alkmim, 2015; Reis and Suss, 2016; Reis et al., 2017). Two of the studied sections correspond to drill cores at the basal 2nd-order sequence (Carrancas and lower Sete Lagoas formations; Fig. 3.5 and 3.6) and do not show any major unconformity. Therefore, we discard a 85 m.yr hiatus within the basal Bambuí 2nd-order sequence, as hypothesized by previous studies to fit late Ediacaran ages for the middle part of

the Sete Lagoas Formation (*Cloudina* sp. interval, Fig. 3.11) with the early Ediacaran age proposed for the basal Sete Lagoas cap carbonates (e.g. Uhlein et al., 2016; 2017; 2019; Caxito et al., 2012; 2018). An unconformity of such magnitude would have resulted in a notable stratigraphic surface, which was not observed so far, even considering drill core and seismic data (e.g. Kuchenbecker et al., 2016a; Reis and Suss, 2016; Reis et al., 2017).

Considering recent reports for *Cloudina* sp. late Ediacaran index fossil (549 – 542 Ma; Grotzinger et al., 2000) at the basal sequence and detrital zircon grain populations younger than 560 Ma for the overlying sequence (Paula-Santos et al., 2015; Fig. 3.2), it is more reasonable to position the basal Bambuí Group in the middle to late Ediacaran (Kuchenbecker et al., 2016a; Paula-Santos and Babinski, 2018). As discussed by Reis et al. (2017), the apparent inconsistency between the depositional age of the foreland Bambuí Sequence and the main collisional phase of the Brasília fold-and-thrust belt at east (~630 Ma; Valeriano et al., 2004; Pimentel et al., 2011) may be explained by loss of sedimentary record consumed by the orogenic front (Kuchenbecker, 2014) and/or due to unusual foreland setting, completely surrounded by diachronous orogenic belts.

As proposed by Reis and Suss (2016), a regional flexure promoted reactivation of previous structures of the craton, generating the forebulge grabens (Well 1 section; Fig. 3.1C and 6). An eustatic sea level rise resulted in accommodation and start of deposition of the Bambuí Sequence. A thicker transgressive succession is recorded within the forebulge graben (Well 1 section, Fig. 3.10 and 3.11), due to local accommodation controls in the forebulge graben domain compared to paleohighs (Reis and Suss, 2016). A relatively tectonic quiescence marks the regressive phases (early and late highstand system tracts; Fig. 3.10 and 11), represented by the establishment of carbonate ramp and carbonate factory climax in the middle to the upper part of Sete Lagoas Formation. A coeval regional increase of Sr content and Sr/Ca ratios in the late highstand system tract is observed, a possible result of a maximum alkalinity and/or aragonitic stage on the top of the basal 2nd-order sequence. A new foreland-related tectonic pulse would have promoted graben subsidence reactivation and uplift of the forebulge paleohighs (Fig. 3.10). This sequence boundary dynamics is represented by the correlative conformity in the graben, as a gradual drowning, whereas the other sections present unconformity surfaces related to a forced regression, marked by subaerial exposure features and dolomitization of intertidal facies (Fig. 3.10 and 3.11). $\delta^{13}C_{carb}$ profiles reflect this spatial dynamics as continuous positive excursion in the graben and isotope discontinuities associated with the sequence boundary in other sections (Fig. 3.11). Furthermore, the tectonic control over the 2nd-order sequences is supported by drastic change

in provenance between the two basal sequences at the southern Sete Lagoas High (Paula-Santos et al., 2015), from Mesoproterozoic to Tonian sources for the basal sequence ($\delta^{13}C_{carb}$ ~ 0‰) to predominantly Ediacaran sources in the overlying sequence ($\delta^{13}C_{carb}$> +10‰).

The overlying second sequence is siliciclastic-dominated, as shown by fine-grained terrigenous sediments from Serra de Santa Helena Formation (Fig. 3.3, 3.4, 3.6 and 3.11). This is a sedimentary filling pattern of the Bambuí basin cycle, with increasing siliciclastic contents towards the top, probably in response to orogenic fronts advance, from both sides (e.g. Reis et al., 2016; Fig. 3.1A and 3.2). The extreme positive $\delta^{13}C_{carb}$ values reached at the sequence boundary between the first and second sequences remain anomalous high for carbonate rocks through the second sequence (Fig. 3.11). It may record a long-lived restriction driven by Gondwana assembly, promoting an isolation of the marine reservoir from other seas (Paula-Santos et al., 2017). $\delta^{13}C$ values only return to normal marine values at the top of the Bambuí Sequence, as low as +1‰ in the Jaíba Member carbonates (Uhlein et al., 2019).

Regarding the use of the $\delta^{13}C_{carb}$ as a correlation tool, our stratigraphic correlations demonstrate that, at least in the 2nd-order scale, the carbon isotope evolution shows trends trackable in basinal scale, over hundreds to thousands of kilometers. However, we suggest caution in using absolute $\delta^{13}C_{carb}$ values instead of $\delta^{13}C_{carb}$ trends to correlated isolated sections. Well 1 section shows that local depositional controls may result either in decrease or increase in $\delta^{13}C_{carb}$ compared to lateral equivalent sections. Furthermore, the Bambuí Group displays several pieces of evidence of geochemical disturbances due to restriction in an epicontinental setting that may hamper global correlations.

3.6.3. The West Gondwana assembly and basin restriction: implications for the paleontological and chemostratigraphic record

The basin restriction tracked by the stratigraphic-chemostratigraphic evolution of the Bambuí Sequence may provide some insights on fossil distribution and marine geochemical dynamics through terminal Neoproterozoic West Gondwana assembly. The high [Sr] and Sr/Ca interval identified in the late Ediacaran Bambuí Group and elsewhere was interpreted by Cui et al. (2016) as a period of high alkalinity and favorable conditions to the calcareous biomineralization. Indeed, this seems to be a geochemical feature of several *Cloudina-bearing* deposits worldwide (Dengying Formation, South China; Sawaki et al., 2010; Cui et al., 2016; Nama Group, Namíbia; Ries et al., 2009; Wood et al., 2018; Tamengo Formation, central-

west Brazil; Boggiani et al., 2010; Arroyo del Soldado Group; Uruguay; Gaucher et al., 2009) and also matches the stage from which rare *Cloudina* occurrences were reported within the Bambuí Group (Fig. 3.11). However, considering the poor paleontological record of the Ediacaran-Cambrian São Francisco Basin, some particularities of the Bambuí Sequence might represent stressing conditions for metazoan colonization.

The Sr-enriched interval precedes the extreme positive $\delta^{13}C_{carb}$ excursion in the basal Bambuí Sequence and persists topwards. Some studies reported the association between shallow hypersaline and/or restricted carbonate environments and high Sr content (e.g. Veizer and Demovic, 1974; Pietzsch et al., 2018). Hypersalinity conditions are difficult to interpret in the absence of evaporite minerals, although some indications of salt pseudomorphs were reported for Well 1 section (Reis and Suss, 2016). Relatively heavy oxygen isotope compositions observed in dolomites at the top of the basal sequence (Fig. 3.4 and 3.5) could also be indicative of more evaporitic conditions. On the other hand, basin restriction is a solid interpretation for the Bambuí basin cycle, based on the extreme $\delta^{13}C_{carb}$ positive excursion at the sequence boundary between the basal and overlying 2nd-order sequences (Fig. 3.11), as well as on seismic (Reis et al., 2016) and provenance data (Paula-Santos et al., 2015) which demonstrates a foreland setting.

The anomalously high $\delta^{13}C_{carb}$ values in the Bambuí Group are related to enhanced restriction of the basin (Iyer et al., 1995; Santos et al., 2004; Martins and Lemos, 2007; Vieira et al., 2007a; Paula-Santos et al., 2017; Uhlein et al., 2019), which could result from a complex interplay of increased rates of organic carbon burial and influence of microbial methanogenesis in shallow environments (for detailed discussion, see Paula-Santos et al., 2017). The classical organic carbon burial hypothesis finds support in black shales and dark-colored carbonates associated with the positive excursion, in a scenario of restricted circulation pattern and enhanced anoxia (e.g. Iyer et al., 1995; Vieira et al., 2007a; Paula-Santos et al., 2017). On the other hand, if organic carbon burial played the main role on the extreme $\delta^{13}C_{carb}$ values, it would require an increase in the fraction of organic carbon buried up to 65%, which is not a reliable value under steady-state assumptions (Iyer et al., 1995; Paula-Santos et al., 2017). Therefore, it is likely that other processes such as methanogenesis also acted in the basin, influencing carbonate precipitation with extreme isotopically heavy carbon compositions (e.g. Birgel et al., 2016). Other scenarios equally related to a restricted basin, as increases in $\delta^{13}C_{input}$ due to carbonate weathering in the surrounding orogens and higher contribution of authigenic carbonate precipitation, were proposed for the ^{13}C-enriched

carbonates from the Bambuí Group (Uhlein et al., 2019), but still lack more robust data to test.

Despite that the methanogenic hypothesis is difficult to test, the scenario of disconnection with marginal seas and basin isolation in the very core of Gondwana supercontinent (Fig. 3.1B) could have resulted in sulfate distillation due to sulfide precipitation through microbial sulfate reduction. This plausible sulfate exhaustion would favor methanogenic metabolisms, which can influence the dissolved inorganic carbon pool with very $^{13}CO_2$-enriched isotope compositions (e.g. Whithicar et al., 1986; Meister et al., 2011; Birgel et al., 2015). Apart the physiographic barriers to fossil migration, the paleogeographic isolation and related methanogenesis scenario could have resulted in very stressful conditions to benthic colonization (e.g. hypersalinity, high alkalinity, anoxia). Nevertheless, we stress that further paleontological investigations must be carried in different areas of the basin, aiming to understand taphonomical and paleoenvironmetal controls over fossil distribution, which is very poor-constrained so far. Our sequence stratigraphy-chemostratigraphic approach provides basis for further investigations on lateral distribution of late Ediacaran fossils *Cloudina* sp. and *Corumbella werneri* in the basin (Warren et al., 2014; Perrella Jr. et al., 207).

Finally, the identification of the Sr-rich interval in the regressive phase of the basal sequence may have some implications for the Sr isotope stratigraphy. Paula-Santos et al. (2017) demonstrated how the representative $^{87}Sr/^{86}Sr$ ratios have been biased by previous studies in the basin, due to the presence of this Sr-rich carbonates in the Bambuí Group. In most of the cases, the less radiogenic $^{87}Sr/^{86}Sr$ ratios of ~0.7075 to 0.7077 in the Sr-rich carbonates were chosen as representative for the entire carbonate succession (e.g. Babinski et al., 2007; Caxito et al., 2012; 2018; Paula-Santos et al., 2015; Kuchenbecker et al., 2016a). These non-radiogenic ratios were mostly associated with the carbonate rocks of the upper Sete Lagoas and Lagoa do Jacaré formations, in the second sequence of the Bambuí Group ($\delta^{13}C_{carb}$> +8‰; CI-3 from Paula-Santos et al., 2017). For the basal sequence, focused by this study, $^{87}Sr/^{86}Sr$ ratios of 0.7080-0.7083 were observed, which would be in accordance with the late Ediacaran fossil *Cloudina* sp. reported within this sequence (CI-2 from Paula-Santos et al., 2017). Such drop in $^{87}Sr/^{86}Sr$ ratios would be coupled to the $\delta^{13}C_{carb}$ positive excursion (Fig. 3.11). However, considering our stratigraphic-chemostratigraphic regional correlation, $^{87}Sr/^{86}Sr$ ratios of 0.7075-0.7077 presented by Kuchenbecker et al. (2016a) for the Arcos section are positioned in the Sr-rich interval on the top of the basal sequence, preceding the $\delta^{13}C_{carb}$ positive excursion (Fig. 3.11). This interval is correlated to the *Cloudina*-interval in

the Januária section (Fig. 3.11), mismatching the proposed $^{87}Sr/^{86}Sr$ ratios for the late Ediacaran-early Cambrian (> 0.7080; Halverson et al., 2007). The same is valid for the $^{87}Sr/^{86}Sr$ ratiosof 0.7075 reported by Caxito et al. (2012; 2018) in the area of Santa Maria da Vitória section. Despite the authors considered this ratio to attest an early Ediacaran age for the underlying cap carbonate interval, the $\delta^{13}C_{carb}$ evolution and Sr contents presented by them correspond to our Sr-enriched late highstand stage, and consequently, to the late Ediacaran *Cloudina* interval (Fig. 3.11).

As noted by Paula-Santos et al. (2017), unradiogenic$^{87}Sr/^{86}Sr$ ratios are not unusual features in late Ediacaran carbonates from the West Gondwana. $^{87}Sr/^{86}Sr$ ratios as low as 0.7073 are reported for Polanco Formation, Arroyo del Soldado Group, Rio de la Plata Craton (Gaucher et al., 2005, 2009), and even lower, from 0.7069 to 0.7075, for the Sierras Bayas Group, Argentina (Kawashita, 1996), all bearing *Cloudina* fossils. Future Sr isotope studies should consider possible disturbances in the Sr budget at this context, evidenced by regional increase in Sr contents. The assumptions based on the modern global oceanographic Sr system may not be hold in restricted basins inside large continental areas (e.g. residence times). This could have led to great lateral and stratigraphic Sr isotope variability due to local paleohydrologic controls (e.g. Doebert et al., 2014; Pietzsch et al., 2018) on epicontinental seas, which can compromise the application of $^{87}Sr/^{86}Sr$ ratios as a global correlation tool in these cases.

3.7. Conclusions

Integrated stratigraphic-chemostratigraphic analysis of the basal Bambuí Sequence allowed investigation of $\delta^{13}C_{carb}$ and Sr/Ca evolution in the light of system tracts that compose the basal 2nd-order sequences. The results revealed solid trends of reliable use of such proxies to regional correlation, as well as particular features related to different domains of the basin (Januária *vs* Sete Lagoas basement highs). This approach provided improvements in paleoenvironmental evolution understanding, which is based on the stratigraphic evolution and independent of an absolute age. Furthermore, our approach provides basis for further paleontological investigations in the basin, especially to understand the spatial controls over poorly-constrained late Ediacaran fossil distribution.

The initial transgression comprises basal diamictites from Carrancas Formation in a gradual transition to the cap carbonates from the basal Sete Lagoas Formation, in a possible post-glacial scenario. This initial transgressive system tract is marked by a $\delta^{13}C_{carb}$ negative-

to-positive excursion from values around −3‰ decreasing to −5‰, followed by a recover around 0‰. At the end of this stage, the maximum flooding surface is associated to a slight $\delta^{13}C_{carb}$ negative excursion to values around−1‰. Sr contents and Sr/Ca ratios are low for this stage, around 230 ppm and 0.001, respectively, due to intense neomorphism processes and high terrigenous contents. Highly pure calcimudstones and bindstones dominate the early highstand system tract and set the establishment of a mature carbonate ramp throughout the basin. The $\delta^{13}C_{carb}$ profile exhibits a plateau between 0 and +1‰, with average Sr content around 400 ppm and Sr/Ca ratios still close to 0.001.

The late highstand system tract corresponds to the middle to upper Sete Lagoas Formation and is characterized by a [Sr]-enriched interval of basinal scale, first time reported here, with [Sr] and Sr/Ca averages of ~1500 ppm and 0.004, respectively. This interval matches the *Cloudina* sp. occurrences in the basin and seems to be a common geochemical feature in late Ediacaran *Cloudina*-bearing deposits worldwide. High alkalinity and possibly an aragonitic stage, driven by progressive basin restriction, may explain the increased incorporation of Sr in carbonate minerals. $\delta^{13}C_{carb}$ values remain in a plateau around 0 and +1‰ during this stage. The sequence boundary between the basal and overlying 2^{nd}-order sequences is associated with the well-known extreme $\delta^{13}C_{carb}$ positive excursion, reaching up to +14‰ in the Bambuí Group. It is represented by an erosive unconformity to correlative conformity surface (in the forebulge grabens), with associated shallow water dolomitization and subaerial exposure. This is a result of forebulge dynamics controlling the 2^{nd}-order sequences, in which a tectonic pulse causes the graben subsidence reactivation and forced regression at paleohighs. The persistent high $\delta^{13}C_{carb}$ values and Sr/Ca ratios towards the overlying sequence suggest that the paleoenvironmental changes resulted from a long-lived restriction, due to the advance of orogenic fronts.

The major paleoenvironmental changes tracked by chemostratigraphic evolution of the basal Bambuí Group, associated with very poor fossil content for this late Ediacaran-Cambrian(?) unit, have implications for metazoan colonization and chemostratigraphy in the context of West Gondwana assembly. Restricted conditions might have resulted in stressful conditions (e.g. hipersalinity, high alkalinity, anoxia, methanic conditions) for metazoan organisms, as well as a physiographic barrier to fossil migration. Nevertheless, we also stress the need of further paleontological investigations for a better understanding of fossil distribution in the Bambuí Group. Regarding the use of the chemostratigraphy as global correlation tool, low $^{87}Sr/^{86}Sr$ ratios associated with [Sr]-rich intervals seem to be a common

feature in late Ediacaran deposits from the West Gondwana, which may be related to local disturbances in the Sr budget. Therefore, the assumptions made for $^{87}Sr/^{86}Sr$ evolution based on the modern oceanographic system may not be hold in these epicontinental basins.

3.8. Acknowledgements

This study was funded by the São Paulo Research Foundation (FAPESP) thematic project grant #2016/06114-6. We would like to thank Lhoist and Petra Energia S.A., for providing drill core samples to our study; to Marcio Remédios, Mauricio Pavan Silva, and Francisco Ferreira de Campos, from the Geological Survey of Brazil (CPRM), for providing technical support with the portable XRF analysis; and to LIESP/CPGeo and LCT/USP staff, specially to Alyne Barros and Renato Contessotto, for the technical support in data acquisition. Sergio Caetano Filho holds a FAPESP scholarship grant #2016/11496-5. Gustavo Paula-Santos holds a FAPESP post-doc grant #2017/00399-1. Marly Babinski, Ricardo Trindade and Matheus Kuchenbecker are fellows of the Brazilian Research Council (#307563/2013-8, #206997/2014-0 and #309106/2017-6, respectively). Finally, we thank to Dr. Huan Cui and the anonymous reviewer for the constructive suggestions for this manuscript.

3.9. References

Ader, M., Macouin, M., Trindade, R.I.F., Hadrien, M.H., Yang, Z., Sun, Z., Besse, J., 2009. A multi layered water column in the Ediacaran Yangtze platform? Insights from carbonate and organic matter paired $\delta^{13}C$. Earth and Planetary Science Letters 288, 213–227.

Alkmim, F.F., Martins-Neto, M., 2012. Proterozoic first-order sedimentary sequences of the São Francisco craton, eastern Brazil. Marine and Petroleum Geology 33 (1), 127–139.

Alkmim, F.F., Marshak, S., Pedrosa-Soares, A.C., Peres, G.G., Cruz, S.C., Whittington, A., 2006. Kinematic evolution of the Araçuaí–West Congo orogen in Brazil and Africa: nutcracker tectonics during the Neoproterozoic assembly of Gondwana. Precambrian Research 149, 43–63.

Babinski, M., Pedrosa-Soares, A.C., Trindade, R.I.F., Martins, M., Noce, C.M., Liu, D., 2012. Neoproterozoic glacial deposits from the Araçuaí orogen, Brazil: Age, provenance and correlations with the São Francisco craton and West Congo belt. Gondwana Research 21, 451–465.

Babinski, M., Vieira, L.C., Trindade, R.I.F., 2007. Direct dating of the Sete Lagoas cap carbonate (Bambuí Group, Brazil) and implications for the Neoproterozoic glacial events. Terra Nova 19, 401–406.

Badiozamani, K., 1973. The Dorag dolomitization model – application to the middle Ordovician of Wisconsin. Journal of Sedimentary Petrology 43(4), 965−984.

Banner, J.L., 1995. Application of the isotope and trace element geochemistry of strontium to studies of diagenesis in carbonate systems. Sedimentology 42, 805−824.

Birgel, D., Meister, P., Lundberg, R., Horath, T.D., Bontognali, T.R.R., Bahniuk, A.M., Rezende, C.E., Vasconcelos, C., McKenzie, J.A., 2015. Methanogenesis produces strong ^{13}C enrichment in stromatolites of Lagoa Salgada, Brazil: a modern analogue for Paleo-/Neoproterozoic stromatolites? Geobiology 13, 245–266.

Boggiani, P.C., Gaucher, C., Sial, A.N., Babinski, M., Simon, C.M., Riccomini, C., Ferreira, V.P., Fairchild, T.R., 2010. Chemostratigraphy of the Tamengo Formation (Corumbá Group, Brazil): a contribution to the calibration of the Ediacaran carbon-isotope curve. Precambrian Research 182, 382–401.

Campbell, I.H., Squire, R.J., 2010. The mountains that triggered the Late Neoproterozoic increase in oxygen: the second great oxidation event. Geochimica et Cosmochimica Acta 74 (15), 4187–4206.

Canfield, D.E., Poulton, S.W., Narbonne, G.M., 2007. Late-Neoproterozoic deep-ocean oxygenation and the rise of animal life. Science 315, 92–94.

Castro, P.T.A., Dardenne, M.A., 2000. The sedimentology, stratigraphy and tectonic context of the São Francisco Supergroup at the southern boundary of the São Francisco craton, Brazil. Revista Brasileira de Geociências 30, 345–437.

Catuneanu, O., Abreu, V., Bhattacharya, J.P., Blum, M.D., Dalrymple, R.W., Eriksson, P.G., Fielding, C.R., Fisher, W.L., Galloway, W.E., Gibling, M.R., Giles, K.A., Holbrook, J.M., Jordan, R., Kendall, C.G.St.C., Macurda, B., Martinsen, O.J., Miall, A.D., Neal, J.E., Nummedal, D., Pomar, L., Posamentier, H.W., Pratt, B.R., Sarg, J.F., Shanley, K.W., Steel, R.J., Strasser, A., Tucker, M.E., Winker, C., 2009. Towards the standardization of sequence stratigraphy. Earth-Science Reviews 92, 1−33.

Catuneanu, O., Galloway, W.E., Kendall, C.G.St.C., Miall, A.D., Posamentier, H.W., Strasser, A., Tucker, M.E., 2011. Sequence stratigraphy: methodology and nomenclature. Newsletters on Stratigraphy 44 (3), 173–245.

Caxito, F.A., Frei, R., Uhlein, G.J., Dias, T.G., Árting, T.B., Uhlein, A, 2018. Multiproxy geochemical and isotope stratigraphy records of a Neoproterozoic Oxygenation Event in the Ediacaran Sete Lagoas cap carbonate, Bambuí Group, Brazil. Chemical Geology 481, 119–132.

Caxito, F.A., Halverson, G.P., Uhlein, A., Stevensson, R., Dias, T.G., Uhlein, G.J., 2012. Marinoan glaciation in east Central Brazil. Precambrian Research 200-203, 38–58.

Chiavegatto, J.R.S., 1992. Análise estratigráfica das sequências tempestíticas da Formação Três Marias (Proterozóico Superior), na porção meridional da Bacia do São Francisco (MSc Dissertation). Universidade Federal de Ouro Preto (UFOP), Brazil, 196 pp.

Conceição Filho, V.M., Miranda, L.L.F., 2003. Bacia do São Francisco entre Santa Maria da Vitória e Iuiú, Bahia: geologia e potencialidade econômica. Companhia Baiana de Pesquisa Mineral, Salvador. 76 p.

Costa, M.T., Branco, J.J.R., 1961. Roteiro para excursão Belo Horizonte-Brasília. Congresso Brasileiro de Geologia, 14, Belo Horizonte, Brazil, 15, 25 pp.

Cui, H., Kaufman, A.J., Peng, Y., Liu, X.M., Plummer, R.E., Lee, E.I., 2018. The Neoproterozoic Hüttenberg $\delta^{13}C$ anomaly: genesis and global implications. Precambrian Research 313, 242–262.

Cui, H., Kaufman, A.J., Xiao, S., Peek, S., Cao, H.,Min, X., Cai, Y., Siegel, Z., Liu, X.M., Peng, Y., Schiffbauer, J.D., Martin, A.J., 2016. Environmental context for the terminal Ediacaran biomineralization of animals. Geobiology 14, 344–363.

Cui, H., Kaufman, A.J., Xiao, S., Zhu, M., Zhou, C., Liu, X.M, 2015. Redox architecture of an Ediacaran ocean margin: integrated chemostratigraphic ($\delta^{13}C$– $\delta^{34}S$–$^{87}Sr/^{86}Sr$–Ce/Ce*) correlation of the Doushantuo Formation, South China. Chemical Geology 405, 48–62.

Dardenne, M.A., 1978. Síntese sobre a estratigrafia do Grupo Bambuí no Brasil Central. Congresso Brasileiro de Geologia, 30, Recife, Brazil, Proceedings 2, 507–610 pp.

Dardenne, M.A., Pimentel, M.M., Alvarenga, C.J.S., 2003. Provenance of conglomerates of the Bambuí, Jequitaí, Vazante and Ibiá groups: Implications for the evolution of The Brasília Belt. Simpósio Nacional de Estudos Tectônicos, 9, Armação de Búzios, Brazil, Abstracts, pp 47–49.

Doebbert, A.C., Johnson, C.M., Carroll, A.R., Beard, B.L., Pietras, J.T., Rhodes Carson, M., Norsted, B., Ashley Throckmorton, L., 2014. Controls on Sr isotopic evolution in lacustrine systems: Eocene Green River Formation, Wyoming. Chemical Geology 380, 172–189.

Dunham, R.J., 1962. Classification of carbonate rocks according to depositional texture. In: Ham, W.E. (Ed.), Classification of carbonate rocks. American Association of Petroleum Geologists Memoir, pp. 108–121.

Embry, A.F., Klovan, J.E., 1971. A late Devonian reef tract on northeastern Banks Island, N.W.T. Bulletin of Canadian Petroleum Geology 19, 730-781.

Flügel, E., 2004. Microfacies of Carbonate Rocks. Analysis, Interpretation and Application. Springer, Berlin, 2004. 976 p.

Gaucher, C., Poiré, D.G., Gómez-Peral, L., Chiglino, L., 2005. Litoestratigrafia, bioestratigrafia y correlaciones de las sucesiones sedimentarias Neoproterozoico–Cambrico del Craton del Rio de la Plata (Uruguay y Argentina). Latin American Journal of Sedimentology and Basin Analysis 12 (2), 145–160.

Gaucher, C., Sial, A.N., Poiré, D.G., Gómez-Peral, L., Ferreira, V.P., Pimentel, M.M., 2009. Chemostratigraphy, Neoproterozoic-Cambrian evolution of the Río de la Plata paleocontinent. In: Gaucher, C., Sial, A.N., Halverson, G.P., Frimmel, H.E. (Eds.), Neoproterozoic-Cambrian Tectonics, Global Change and Evolution: A Focus on Southwertern GondwanaDevelopments in Precambrian Geology. Elsevier, Amsterdam, pp. 115–122.

Grotzinger, J.P., Waters, W.A., Knoll, A.H., 2000. Calcified metazoans in thrombolite stromatolite reefs of the terminal Proterozoic Nama Group, Namibia. Paleobiology 26 (3), 334–359.

Halverson, G.P., Dudás, F.O., Maloof, A.C., Bowring, S.A., 2007. Evolution of the $^{87}Sr/^{86}Sr$ composition of Neoproterozoic seawater. Palaeogeography Palaeoclimatology Palaeoecology 256 (3–4), 103–129.

Halverson, G.P., Hurtgen, M.T., 2007. Ediacaran growth of the marine sulfate reservoir. Earth and Planetary Science Letters 263, 32–44.

Halverson, G.P., Shields-Zhou, G., 2011. Chemostratigraphy and the Neoproterozoic glaciations. In: Arnaud, E., Halverson, G.P., Shields-Zhou, G. (Eds.), The Geological Record of Neoproterozoic Glaciations. Geological Society, London, Geological Society Memoir 36, pp. 51–66.

Hoffman, P.F., Kaufman, A.J., Halverson, G.P., Schrag, D.P., 1998. A Neoproterozoic snowball Earth. Science 281, 1342–1346.

Hoffman, P.F., Schrag, D.P., 2002. The snowball Earth hypothesis: testing the limits of global change. Terra Nova 14, 129–155.

Holland, H.D., Borcsik, M., Munoz, J.L., Oxburgh, U.M., 1963. The coprecipitation of Sr^{2+} with aragonite and of Ca^{2+} with strontianite between 90 and 100ºC. Geochimica et Cosmochimica Acta 27, 957−977.

Holland, H.D., Holland, H.J., Munoz, J.L., 1964. The coprecipitation of cations with $CaCO_3$. II. The coprecipitation of Sr^{2+} with calcite between 90 and 100ºC. Geochimica et Cosmochimica Acta 28, 1287−1302.

Hudson, J.D., 1977. Stable isotopes and limestone lithification.Journal of Geological Society 133(6), 637−660.

Hurtgen, M.T., Halverson, G.P., Arthur, M.A., Hoffman, P.F., 2006. Sulfur cycling in the aftermath of a Neoproterozoic (Marinoan) snowball glaciation: Evidence for a syn-glacial sulfidic deep ocean. Earth and Planetary Science Letters 245, 551–570.

Iyer, S.S., Babinski, M., Krouse, H.L., Chemale, F., 1995. Highly ^{13}C enriched carbonate and organic matter in the Neoproterozoic sediments of the Bambuí Group, Brazil. Precambrian Research 73, 271–282.

Kaufman, A.J., Corsetti, F.A., Varni, M.A., 2007. The effect of rising atmospheric oxygen on carbon and sulfur isotope anomalies in the Neoproterozoic Johnnie Formation, Death Valley, USA. Chemical Geology 237 (1–2), 47–63.

Kawashita, K., 1996. Rochas carbonáticas neoproterozoicas da América do Sul: idades e inferências quimioestratigráficas. (Livre Docência Thesis). Universidade de São Paulo, Brazil. 126 p.

Kinsman, D.J.J., 1969. Interpretation of Sr^{2+} concentrations in carbonate minerals and rocks. Journal of Sedimentary Petrology 49,937−944.

Knoll, A.H., Walter, M.R., Narbonne, G.M., Christie-Blick, N., 2006. The Ediacaran Period: a new addition to the geologic time scale. Lethaia 39, 13–30.

Kuchenbecker, M. 2014. Relações entre coberturas do Cráton do São Francisco e bacias situadas em orógenos marginais: o registro de datações U-Pb de grãos detríticos de zircão e suas implicações geotectônicas. PhD dissertation, Universidade Federal de Minas Gerais, Belo Horizonte, Brazil, 175 p.

Kuchenbecker, M., Atman, D., Costa, R.D., Pedrosa-Soares, A.C., Babinski, M., 2016b. A Formação Gorutuba: sedimentação litorânea a continental na margem leste da Bacia Bambuí (MG). Geologia USP – Série Científica 16(2), 67–81.

Kuchenbecker, M., Babinski, M., Pedrosa-Soares, A.C., Costa, R.D., Lopes-Silva, L., Pimenta, F., 2013. Proveniência e análise sedimentar da porção basal do Grupo Bambuí em Arcos (MG). Geologia USP – Série Científica 13(4), 49–61.

Kuchenbecker, M., Babinski, M., Pedrosa-Soares, A.C., Lopes-Silva, L., Pimenta, F., 2016a. Chemostratigraphy of the lower Bambuí Group, southwestern São Francisco Craton, Brazil: insights on Gondwana paleoenvironments. Brazilian Journal of Geology 46(1), 145–162.

Kuchenbecker, M., Lopes-Silva, L.L., Pimenta, F., Pedrosa-Soares, A.C., Babinski, M., 2011. Estratigrafia da porção basal do Grupo Bambuí na região de Arcos (MG): uma contribuição com base em testemunhos de sondagem. Geologia USP – Série Científica 11(2),45–54.

Martínez, M.I., 2007. Estratigrafia e tectônica do Grupo Bambuí no norte do estado de Minas Gerais (MSc dissertation). Universidade Federal de Minas Gerais, Brazil, 147 pp.

Martins, M., Lemos, V.B., 2007. Análise estratigráfica das sequências neoproterozoicas da Bacia do São Francisco. Revista Brasileira de Geociências 37 (4), 156–167.

Martins-Neto, M., Alkmim, F.F., 2001. Estratigrafia e evolução tectônica das bacias neoproterozoicas do Paleocontinente São Francisco e suas margens: registro da quebra de Rodínia e colagem de Gondwana. In: Pinto, C.P., Martins-Neto, M.A. (Eds.), Bacia do São Francisco: Geologia e Recursos Naturais. Sociedade Brasileira de Geologia (SBG), Belo Horizonte, pp. 31–54.

Martins-Neto, M.A., 2009. Sequence stratigraphic framework of Proterozoic successions in eastern Brazil. Marine and Petroleum Geology 26, 163–176.

Martins-Neto, M.A., Pedrosa-Soares, A.C., Lima, S.A.A., 2001. Tectono-sedimentary evolution of sedimentar basins from late Paleoproterozoic to late Neoproterozoic in the São Francisco craton and Araçuaí fold belt, eastern Brazil. Sedimentary Geology 141–142, 343–370.

Meister, P., Gutjahr, M., Frank, M., Bernasconi, S.M., Vasconcelos, C., McKenzie, J.A., 2011. Dolomite formation within the methanogenic zone induced by tectonically driven fluids in the Peru accretionary prism. Geology 39, 563–566.

Morse, J.W., Bender, M.L., 1989. Partition coefficients in calcite: an examination of factors influencing the validity of experimental results and their application to natural systems. Chemical Geology 82, 265−277.

Morse, J.W., Mackenzie, F.T., 1990. Geochemistry of sedimentary carbonates. Developments in Sedimentology 48, Elsevier 708 p.

Narbonne, G.M., Xiao, S., Shields, G.H., Gehling, J.G., 2012. The Ediacaran Period. In: Gradstein, F.M., Ogg, J.G., Schmitz, M., Ogg, G., (Coordinators), The Geologic Time Scale 2012. Elsevier Publisher, Oxford, pp. 413–435.

Och, L.M., Shields-Zhou, G.A., 2012. The Neoproterozoic oxygenation event: environmental perturbations and biogeochemical cycling. Earth-Sciences Reviews 110, 26–57.

Okubo, J., Muscente, A.D., Luvizotto, G.L., Uhlein, G.J., Warren, L.V., 2018. Phosphogenesis, aragonite fan formation and seafloor environments following the Marinoan glaciation. Precambrian Research 311, 24–36.

Paula-Santos, G.M., Babinski, M. 2018. Sedimentary provenance in the southern sector of the São Francisco Basin, SE Brazil. Brazilian Journal of Geology 48(1), 51−74.

Paula-Santos, G.M., Babinski, M., Kuchenbecker, M., Caetano-Filho, S., Trindade, R.I.F., Pedrosa-Soares, A.C., 2015. New evidence of an Ediacaran age for the Bambuí Group in southern São Francisco craton (eastern Brazil) from zircon U-Pb data and isotope chemostratigraphy. Gondwana Research 28, 702–720.

Paula-Santos, G.M., Caetano-Filho, S., Babinski, B., Enzweiler, J., 2018. Rare earth elements of carbonate rocks from the Bambuí Group, southern São Francisco Basin, Brazil, and their significance as paleoenvironmental proxies. Precambrian Research 305, 327−340.

Paula-Santos, G.M., Caetano-Filho, S., Babinski, M., Trindade, R.I.F, Guacaneme, C., 2017. Tracking connection and restriction of West Gondwana São Francisco Basin through isotope chemostratigraphy. Gondwana Research 42, 280−305.

Perrella Jr., P., Uhlein, A., Uhlein, G.J., Sial, A.N., Pedrosa-Soares, A.C., Lima, O.N.B., 2017. Facies analysis, sequence stratigraphy and chemostratigraphy of the Sete Lagoas Formation (Bambuí Group), northern Minas Gerais State, Brazil: evidence of a cap carbonate deposited on the Januária basement high. Brazilian Journal of Geology 47, 59−77.

Pietzsch, R., Oliveira, D.M., Tedeschi, L.R., Queiroz Neto, J.V., Figueiredo, M., Vazquez, J.C., Souza, R.S., 2018. Palaeohydrology of the Lower Cretaceous pre-salt lacustrine system, from rift to post-rift phase, Santos Basin, Brazil. Palaeogeography, Palaeoclimatology, Palaeoecology 507, 60−80.

Pimentel, M.M., Rodrigues, J.B., DellaGiustina, M.E.S., Junges, S., Matteini, M., Armstrong, R., 2011. The tectonic evolution of the Neoproterozoic Brasília Belt, central Brazil, based on SHRIMP and LA-ICPMS U-Pb sedimentary provenance data: a review. Journal of South American Earth Sciences 31, 345–357.

Reimann, C.; Caritat, P., 1998. Chemical Elements in the Environment. Factsheets for the geochemist and environmental scientist. Springer, Berlin, 398 p.

Reis, H.L.S., Alkmim, F.F., 2015. Anatomy of a basin-controlled foreland fold-thrust belt curve: the Três Marias salient, São Francisco basin, Brazil. Marine Petroleum Geology 66(4), 711–731.

Reis, H.L.S., Alkmim, F.F., Fonseca, R.C.S., Nascimento, T.C., Suss, J.F., Prevatti, L.D., 2016. The São Francisco Basin. In: Heilbron, M., Cordani, U.G., Alkmim, F.F. (Eds.), São Francisco Craton, Eastern Brazil, Regional Geology Reviews. Springer, Switzerland, pp. 117–143.

Reis, H.L.S., Suss, J.F., 2016. Mixed carbonate-siliciclastic sedimentation in forebulge grabens: an example from the Ediacaran Bambuí Group, São Francisco Basin, Brazil. Sedimentary Geology 339, 83–103.

Reis, H.L.S., Suss, J.F., Fonseca, R.C.S., Alkmim, F.F., 2017. Ediacaran forebulge grabens of the southern São Francisco basin, SE Brazil: Craton interior dynamics during West Gondwana assembly. Precambrian Research 302, 150–170.

Ries, J.B., Fike, D.A., Pratt, L.M., Lyons, T.W., Grotzinger, J.P., 2009. Superheavy pyrite ($\delta^{34}S_{pyr}$> $\delta^{34}S_{CAS}$) in the terminal Proterozoic Nama Group, southern Namibia: a consequence of low seawater sulfate at the dawn of animal life. Geology 37, 743–746.

Renard, M., 1986. Pelagic carbonate chemostratigraphy (Sr, Mg, O-18, C-13). Marine Micropaleontology 10, 117−164.

Rocha-Campos, A.C., Brito-Neves, B.B., Babinski, M., Santos, P.R., Oliveira, S.M.B., Romano, A., 2011. Moema laminites: a newly recognized Neoproterozoic (?) glaciogenic unit, São Francisco Basin, Brazil. In: Arnaud, E., Halverson, G.P., Shields-Zhou, G. (eds), The Geological Record of Neoproterozoic Glaciations. Geological Society, London, Memoirs, 36, 535–540.

Rodrigues, J.B., 2008. Proveniência dos sedimentos dos grupos Canastra, Ibiá, Vazante e Bambuí. Um estudo de zircões detríticos e idades modelo Sm-Nd (PhD dissertation). Universidade de Brasília, Brazil, 141 pp.

Rodrigues, J.B., Pimentel, M.M., Buhn, B., Matteini, M., Dardenne, M.A., Alvarenga, C.J.S., Armstrong, R.A., 2012. Provenance of the Vazante Group: New U-Pb, Sm-Nd, Lu-Hf isotopic data and implications for the tectonic evolution of the Neoproterozoic Brasília Belt. Gondwana Research 21, 439–450.

Romano, A.W., 2007. Geologia da Folha Pará de Minas (SE.23-Z-C-IV), escala 1:100.000: nota explicativa. UFMG/CPRM-Serviço Geológico do Brasil, Belo Horizonte, Brazil.

Romano, A.W., Knauer, L.G., 2003. Evidências da glaciação neoproterozoica na base do Grupo Bambuí - região de Onça do Pitangui - Minas Gerais. Simpósio de Gelogia de Minas Gerais, 12, Ouro Preto, Brazil, Proceedings 1, p. 27.

Sandberg, P.A., 1983. An oscillating trend in Phanerozoic non-skeletal carbonate mineralogy. Nature 305, 19−22.

Santos, R.V., Alvarenga, C.J.S., Babinski, M., Ramos, M.L.S., Cukrov, N., Fonseca, M.A., Sial, A.N., Dardenne, M.A., Noce, C.M., 2004. Carbon isotopes of Mesoproterozoic–Neoproterozoic

sequences from southern São Francisco craton and Araçuaí Belt, Brazil: Paleogeographic implications. Journal of South American Earth Sciences 18, 27–39.

Santos R.V., Alvarenga C.J.S., Dardenne M.A., Sial A.N., Ferreira V.P., 2000. Carbon and oxygen isotope profiles across Meso-Neoproterozoic limestones from central Brazil: Bambuí and Paranoá groups. Precambrian Research 104, 107–122.

Sawaki, Y., Ohno, T., Tahata, M., Komiya, T., Hirata, T., Maruyama, S., Windley, B.F., Han, .J, Shu, D., Li, Y., 2010. The Ediacaran radiogenic Sr isotope excursion in the Doushantuo Formation in the Three Gorges area, South China. Precambrian Research 176, 46–64.

Schaudinn, C., Stoodley, P., Kainovic, A., O'Keeffe, T., Costerton, B., Robinson, D., Baum, M., Ehrlich, G., Webster, P., 2007. Bacterial biofilms, other structures seen as mainstream concepts. Microbe 2(5), 231−237.

Sgarbi, G.N.C., Sgarbi, P.B.A., Campos, J.E.G., Dardenne, M.A., Penha, U.C., 2001. Bacia Sanfranciscana: O registro fanerozoico da Bacia do São Francisco. In: Pinto, C.P., Martins-Neto, M.A. (Eds.), Bacia do São Francisco: Geologia e Recursos Naturais. Sociedade Brasileira de Geologia, Belo Horizonte, pp. 93−138.

Shields-Zhou, G., Och, L., 2011. The case for a Neoproterozoic oxygenation event: geochemical evidence and biological consequences. GSA Today 21 (3), 4–11.

Tucker, M.E., Wright, V.P., 1990. Carbonate sedimentology. Blackwell, Oxford, 482 pp.

Tuller, M.P., Ribeiro, J.H., Signorelli, M., Feboli,W.L., Pinho, J.M.M., 2008. Proposta de uma nova seção-tipo da Formação Carrancas, Grupo Bambuí, na região de Inhaúma, Minas Gerais. In: Congresso Brasileiro de Geologia, 44, Belém, Brazil, Proceedings, pp. 929.

Tuller, M.P., Ribeiro, J.H., Signorelli, N., Féboli, W.L., Júlio Murilo Martino Pinho, J.M.M., 2010. Projeto Sete Lagoas –Abaeté, CPRM –Serviço Geológico do Brasil, Belo Horizonte, 160p., 2010

Uhlein, A., Baptista, M.C., Seer, H.J., Caxito, F.A., Uhlein, G.J., Dardenne, M.A., 2011. A Formação Lagoa Formosa, Grupo Bambuí (MG): Sistema deposicional de leque submarino em bacia de antepais. Geonomos 19(2), 163–172.

Uhlein, A., Trompette, R., Egydio-Silva, M., Vauchez, A. 2007. A glaciação Sturtiana (750 Ma), a estrutura do rifte Macaúbas-Santo Onofre e a estratigrafia do Grupo Macaúbas, Faixa Araçuaí. Geonomos 15, 45–60.

Uhlein, G.J., 2014. Proveniência sedimentar e estratigrafia das formações Carrancas e Lagoa Formosa e a evolução do Grupo Bambuí (635-570 Ma) em Minas Gerais (MSc thesis). Universidade Federal de Minas Gerais (UFMG), Brazil, 161 pp.

Uhlein, G.J., Carvalho, J.F.M.G., Uhlein, A., Caxito, F.A., Halverson, G.P., Sial, A.N., 2012. Estratigrafia e sedimentologia da Formação Carrancas, Grupo Bambuí, nas regiões de Belo Horizonte e Pitangui, MG. Geonomos 20(2), 79−97.

Uhlein, G.J., Uhlein, A., Halverson, G.P., Stevenson, R., Caxito, F.A., Cox, G.M., Carvalho, J.F.M.G., 2016. The Carrancas Formation, Bambuí Group: a record of pre-Marinoan sedimentation on the southern São Francisco craton, Brazil. Journal of South American Earth Sciences 71, 1–16.

Uhlein, G.J., Uhlein, A., Stevenson, R., Halverson, G.P., Caxito, F.A., Cox, G.M., 2017. Early to late Ediacaran conglomeratic wedges from a complete foreland basin cycle in the southwest São Francisco Craton, Bambuí Group, Brazil. Precambrian Research 299, 201−116.

Uhlein, G.J., Uhlein, A., Pereira, E., Caxito, F.A., Okubo, J., Warren, L.V., Sial, A.N., 2019. Ediacaran paleoenvironmental changes recorded in the mixed carbonate-siliciclastic Bambuí Basin, Brazil. Palaeogeography, Palaeoclimatology, Palaeoecology 517, 39–51.

Valeriano, C.M., Machado, N., Simonetti, A., Valadares, C.S., Seer, H.J., Simões, L.S.A., 2004. U-Pb geochronology of the southern Brasília belt (SE-Brazil): sedimentary provenance, Neoproterozoic orogeny and assembly of West Gondwana. Precambrian Research 130, 27–55.

Veizer, J., Ala, D., Azmy, K., Bruckschen, P., Buhl, D., Bruhn F., Carden, G.A.F., Diener, A., Ebneth, S., Godderis, Y., Jasper, T., Korte, C., Pawellek, F., Podlaha, O.G., Strauss, H., 1999. $^{87}Sr/^{86}Sr$, $\delta^{13}C$ and $\delta^{18}O$ evolution of Phanerozoic seawater. Chemical Geology 161, 59−88.

Veizer, J., Demovic, R., 1974. Strontium as a tool in facies analysis. Journal of Sedimentary Petrology 44(1), 93−115.

Vieira, L.C., Almeida, R.P., Trindade, R.I.F., Nogueira, A.C.R., Janikian, L., 2007b. A Formação Sete Lagoas em sua área tipo: Fácies, estratigrafia e sistemas deposicionais. Revista Brasileira de Geociências 37(4), 1–14.

Vieira, L.C., Nédélec, A., Fabre, S., Trindade, R.I.F., Almeida, R.P., 2015. Aragonite crystal fans in Neoproterozoic cap carbonates: a case study from Brazil and implications for the post–Snowball Earth coastal environment. Journal of Sedimentary Research 85, 285−300.

Vieira, L.C., Trindade, R.I.F, Nogueira, A.C.R., Ader, M. 2007a. Identification of a Sturtian cap carbonate in the Neoproterozoic Sete Lagoas carbonate plataform, Bambuí Group, Brazil. Comptes Rendus Geoscience 339, 240−258.

Warren, L.V., Quaglio, F., Riccomini, C., Simões, M.G., Poiré, D.G., Strikis, N.M., Anelli, L.E., Strikis, P.C., 2014. The puzzle assembled: Ediacaran guide fossil Cloudina reveals an old proto-Gondwana seaway. Geology 42(5), 391−394.

Whithicar, M.J., Faber, E., Schoell, M., 1986. Biogenic methane formation in marine and freshwater environments: CO_2 reduction versus acetate fermentation? Isotope evidence. Geochimica et Cosmochimica Acta 50, 693–709.

Wilkin, R.T., Barnes, H.L., 1997. Formation processes of framboidal pyrite. Geochimica et Cosmochimica Acta 61, 323−339.

Wood, R., Bowyer, F., Penny, A., Poulton, S.W., 2018. Did anoxia terminate Ediacaran benthic communities? Evidence from early diagenesis. Precambrian Research 313, 134−147.

Wright, V.P., 1992. A revised classification of limestones. Sedimentary Geology 76, 177−186.

Zalán, P.V., Romeiro-Silva, P.C., 2007. Bacia do São Francisco. Boletim de Geociências Petrobrás 15(2), 561–571.

4. A LARGE EPEIRIC METHANOGENIC BAMBUÍ SEA IN THE CORE OF GONDWANA SUPERCONTINENT?

Sergio Caetano-Filho, Pierre Sansjofre, Magali Ader, Gustavo M. Paula-Santos, Cristian Guacaneme, Marly Babinski, Carolina Bedoya-Rueda, Matheus Kuchenbecker, Humberto L.S. Reis, and Ricardo I.F. Trindade

4.1.Abstract

Carbon isotope compositions of both sedimentary carbonate and organic matter can be used as key proxies of the global carbon cycle and of its evolution through time, as long as they are acquired from waters where the dissolved inorganic carbon (DIC) is in isotope equilibrium with the atmospheric CO_2. However, in shallow water platforms and epeiric settings, the influence of local to regional parameters on carbon cycling may lead to DIC isotope variations unrelated to the global carbon cycle. This may be especially true for the terminal Neoproterozoic, when Gondwana assembly isolated waters masses from the global ocean, and extreme positive and negative carbon isotope excursions are recorded, potentially decoupled from global signals. To improve our understanding on the type of information recorded by these excursions, we investigate the paired $\delta^{13}C_{carb}$ and $\delta^{13}C_{org}$ evolution for an increasingly restricted late Ediacaran-Cambrian foreland system in the West Gondwana interior: the basal Bambuí Group. This succession represents a 1st-order sedimentary sequence and records two major $\delta^{13}C_{carb}$ excursions in its two lowermost lower-rank sequences. The basal cap carbonate interval at the base of the first sequence, deposited when the basin was connected to the ocean, hosts antithetical negative and positive excursions for $\delta^{13}C_{carb}$ and $\delta^{13}C_{org}$, respectively, resulting in $\Delta^{13}C$ values lower than 25‰. From the top of the basal sequence upwards, an extremely positive $\delta^{13}C_{carb}$ excursion is coupled to $\delta^{13}C_{org}$, reaching values of +14 and −14 ‰, respectively. This positive excursion represents a remarkable basin-wide carbon isotope feature of the Bambuí Group that occurs with only minor changes in $\Delta^{13}C$ values, suggesting change in the DIC isotope composition. We argue that this regional isotopic excursion is related to a disconnection between the intrabasinal and the global carbon cycles. This extreme carbon isotope excursion may have been a product of a disequilibria between the basin DIC and atmospheric CO_2 induced by an active methanogenesis, favored by the basin restriction. The drawdown of sulfate reservoir by microbial sulfate reduction in a poorly ventilated and dominantly anoxic basin would have triggered methanogenesis and

ultimately methane escape to the atmosphere, resulting in a ^{13}C-enriched DIC influenced by methanogenic CO_2. Isolated basins in the interior of the Gondwana supercontinent may have represented a significant source of methane inputs to the atmosphere, potentially affecting both the global carbon cycle and the climate.

4.2. Introduction

Major carbon isotope excursions during the Neoproterozoic Era have been interpreted in terms of global perturbation of carbon cycle (e.g. Halverson et al. 2005; Sansjofre et al. 2011), diagenetic overprint (Derry, 2010; Knauth and Kennedy, 2009), and regional perturbation of carbon cycle (e.g. Ader et a., 2009; Cui et al., 2018; Uhlein et al., 2019). Perturbations in the global carbon cycle were proposed to be driven by changes in organic matter burial rates (f_{org}), methane oxidation events, the proportion of authigenic carbonate precipitation, and oxidation of a large DOC reservoir (e.g. Rothman et al., 2003; Halverson et al., 2009; Schrag et al., 2013). During the Cryogenian and Ediacaran, the generally high $\delta^{13}C_{carb}$ values are most commonly interpreted as resulting from enhanced organic matter burial at the global scale leading to a second major oxygenation event in the Earth's history, the Neoproterozoic Oxygenation Event (Och and Shield Zhou, 2012). This large positive isotopic excursion over tens of millions of years is punctuated by rapid negative excursions associated with major glacial events (Halverson et al., 2009 and references therein).

Despite the rich carbon isotope record for Neoproterozoic basins worldwide, the identification of local to regional effects on the marine carbon cycle in these basins are rarely considered (e.g. Ader et al., 2009; Cui et al., 2018). Regional to local parameters may be particularly critical to DIC isotope composition from shallow platforms, epeiric seas and restricted basins, resulting in secular changes in carbon isotope compositions from carbonate sediments decoupled from the global carbon cycle (e.g. Fanton and Holmden, 2007; Swart, 2008; Geyman and Maloof, 2019). Such geotectonic scenarios were common during the assembly of the West Gondwana supercontinent at the Ediacaran-Cambrian transition, when large epicontinental marine basins were developed completely or partially isolated from the global ocean, such as those represented by Otavi and Bambuí groups, in São Francisco-Congo craton (e.g. Paula-Santos et al., 2017; Cui et al., 2018). In particular, the Ediacaran-Cambrian Bambuí Group, São Francisco Basin (central-east Brazil) represents a foreland system formed during Brasiliano/Pan-African orogenic cycle, in a geotectonic setting progressively surrounded by fold-thrust belts (Reis et al., 2016). This unit records an extreme positive

$\delta^{13}C_{carb}$ excursion across the basin, reaching up to +16‰ (e.g. Iyer et al., 1995; Fig. 4.1A), which is anomalously high with respect to the signal of other time-equivalent successions worldwide (e.g., Halverson et al., 2009). This excursion has been referred to as the Middle Bambuí Excursion (MIBE; Uhlein et al., 2019), and is associated with the sequence boundary between the two lowermost sequences from the Bambuí Group (Caetano-Filho et al., 2019).

Although several authors interpreted the MIBE as a result from the progressive restriction of the basin in the very core of Gondwana supercontinent (Iyer et al., 1995; Paula-Santos et al., 2017; Caetano-Filho et al., 2019; Uhlein et al., 2019), the mechanism behind these very high ^{13}C-enrichment remains poorly constrained. Here we present new organic carbon isotope data ($\delta^{13}C_{org}$) on three sections of the Bambuí Group from different sectors of the basin for which carbonate carbon isotope data ($\delta^{13}C_{carb}$) and a basin-wide sequence stratigraphy framework are already available (Reis and Suss, 2016; Caetano-Filho et al., 2019). We use the paired $\delta^{13}C_{org}$ and $\delta^{13}C_{carb}$ data to provide additional constraints on the mechanisms behind the ^{13}C-enrichments in these deposits and their implication for the local and global environmental conditions during the Ediacaran-Cambrian transition.

4.3. Geological Setting

In western South America, São Francisco craton represents one of the inner and stable part of one of the paleocontinents involved in the assembly of Gondwana, by the end of Neoproterozoic Era (e.g. Heilbron et al. 2017). During these diachronous collisional events, several orogenic belts evolved around the craton, giving rise to a complex foreland system in its interior, recorded in the rocks of the Bambuí Group (e.g. Reis et al. 2016).

The Bambuí Group encompasses the basal diamictite of the Carrancas Formation which is overlain by mixed carbonate-siliciclastic deposits from Sete Lagoas, Serra de Santa Helena, Lagoa do Jacaré, Serra da Saudade and Três Marias formations (Fig. 4.1B). These lithostratigraphic units correspond to the most expressive strata exposed in the southern São Francisco Craton (i.e., the intracratonic São Francisco basin) and record a 1st-order foreland basin cycle (Fig. 4.1A and B; for a detailed review see Reis et al., 2016). We focus here on the lower to middle sedimentary successions of the Bambuí Group. These successions comprise two basin-wide and transgressive-regressive 2nd-order sequences that record major changes in the carbon isotope record (e.g. Caetano-Filho et al., 2019; Uhlein et al., 2019).

The basal 2nd-order sequence unconformably overlies Archean/Paleoprtoerozoic basement assemblages and Paleoproterozoic to early Neoproterozoic sedimentary successions

of the São Francisco basin (Reis et al., 2016). Its basal portion marks a transgressive systems tract (TST), which is composed of coarse-grained siliciclastic deposits of the Carrancas Formation grading upward into cap carbonate rocks of the basal Sete Lagoas Formation (e.g. Kuchenbecker et al., 2016; Paula-Santos et al., 2015; 2017; Reis and Suss, 2016; Vieira et al., 2007). The basal cap carbonate displays a typical negative $\delta^{13}C_{carb}$ excursion extending to −5‰ that recovers upsection to values near 0‰. The cap carbonate interval encompasses dolostones and limestones with several layers of aragonite pseudomorphs and barite crystal fans (Babinski et al., 2007; Vieira et al., 2007; Kuchenbecker et al, 2016; Okubo et al., 2018; Crockford et al. 2019). The TST are overlain by mixed carbonate-siliciclastic deposits of the middle Sete Lagoas Formation. These successions define an overall shallowing upward pattern, marking a highstand systems tract (HST). An early highstand systems tract (EHST) is characterized by a thick mixed siliciclastic-carbonate facies deposited in the deeper carbonate ramp ramp, grading upward into shallower mid-ramp microbial limestones. The late highstand systems tract (LHST) is marked by dark-grey pure microbial limestones mostly marking mid ramp strata that pass upward into high-energy shallow water carbonate facies. The late HST carbonate successions are associated with a remarkable basin-scale increase in the Sr/Ca on the carbonate deposits probably driven by enhanced alkalinity and/or more aragonitc conditions (Caetano-Filho et al., 2019; Paula-Santos et al., 2020). The whole HST shows relatively stable $\delta^{13}C_{carb}$ values near 0‰ (e.g. Kuchenbecker et al., 2016; Paula-Santos et al., 2017; Reis and Suss, 2016; Vieira et al., 2007; Caetano-Filho et al., 2019).

A sequence boundary between the two 2nd-order sequences is marked by a major subaerial exposure recorded by supratidal carbonate deposits (Reis and Suss, 2016; Caetano-Filho et al., 2019). The overlying 2nd-order sequence begins with deposition of transgressive limestones of the upper Sete Lagoas Formation and deep water deposits from the Serra de Santa Helena Formation. These deposits grade upward into regressive deltaic-related and platformal siliciclastics of the middle to upper Serra de Santa Helena Formation and shallow marine carbonates of the Lagoa do Jacaré Formationa (Reis et al., 2016; Fig. 4.1B).

In this sequence stratigraphic framework, the MIBE corresponds to the large positive $\delta^{13}C_{carb}$ excursion starting in the end of the regressive stage of the basal sequence, with high values persisting through the overlying 2nd-order sequence (e.g. Santos et al., 2004; Paula-Santos et al., 2017; Uhlein et al., 2019). It is characterized by gradual positive excursion in the deeper domains of forebulge grabens and by a sharp discontinuity in paleohigh successions (Caetano-Filho et al., 2019). The MIBE is accompanied by low $^{87}Sr/^{86}Sr$ ratios (~0.7075-0.7077; Paula-Santos et al., 2017; Fig. 4.1), very unradiogenic compared with the expected

values for the late Ediacaran (>0.7080; e.g. Halverson et al., 2010). These isotope anomalies have been interpreted as the result of the progressive restriction of the Bambuí foreland system during the Brasiliano/Pan-African cycle at the end of Neoproterozoic Era (e.g. Paula-Santos et al., 2017). The foreland-related nature of the Bambuí Group and its progressive restriction through time are supported by paleogeographic reconstructions (e.g. Tohver et al., 2006), the tectono-sedimentary filling pattern of the basin as constrained by seismic and drill core data (Reis and Alkmim, 2015; Reis and Suss, 2016; Reis et al., 2017), and by a drastic change in detrital provenance at the transition between the two basal sequences. It is evidenced by U-Pb ages in detrital zircon grains, which change from Mesoproterozoic and Tonian in the basal sequence to exclusively Ediacaran in the overlying one, interpreted as resulting from a rapid source-rock exhumation within neighboring orogenic belts (Paula-Santos et al., 2015).

Late Ediacaran metazoan fossils *Cloudina* sp. and *Corumbella werneri* (549-541 Ma; Grotzinger et al., 2000; Amthor et al., 2003) were reported in the middle Sete Lagoas Formation (~40 to 50 m from the basement; Warren et al., 2014; Perrella Jr. et al., 2017), ascribed to the LHST of the basal sequence (Caetano-Filho et al., 2019). U-Pb ages for detrital zircon grains provide a maximum depositional age of 560 Ma for the overlying sequence, in the upper Sete Lagoas Formation (Paula-Santos et al., 2015) (Fig. 4.1B). The cap carbonate interval at the base of the unit presents contrasting Pb-Pb isochron ages for different areas of the basin (740 ± 22 Ma, Babinski et al., 2007; 608 ± 19 Ma, Caxito et al., 2018). Pb-Pb isochron ages for the cap carbonate interval would imply a time span of at least ~80 m.yr.-long between the cap carbonate and the LHSTof the basal 2nd-order sequence where *Cloudina* occurs. However, no stratigraphical evidence has been found so far to support the possible existence of condensation levels or hiatuses in the corresponding interval. Recent stratigraphic studies, based on detailed stratigraphic information from drill cores, indicate a continuous sedimentation in the basin throughout the basal sequences (Reis and Suss, 2016; Kuchenbecker et al., 2016; Caetano-Filho et al., 2019).

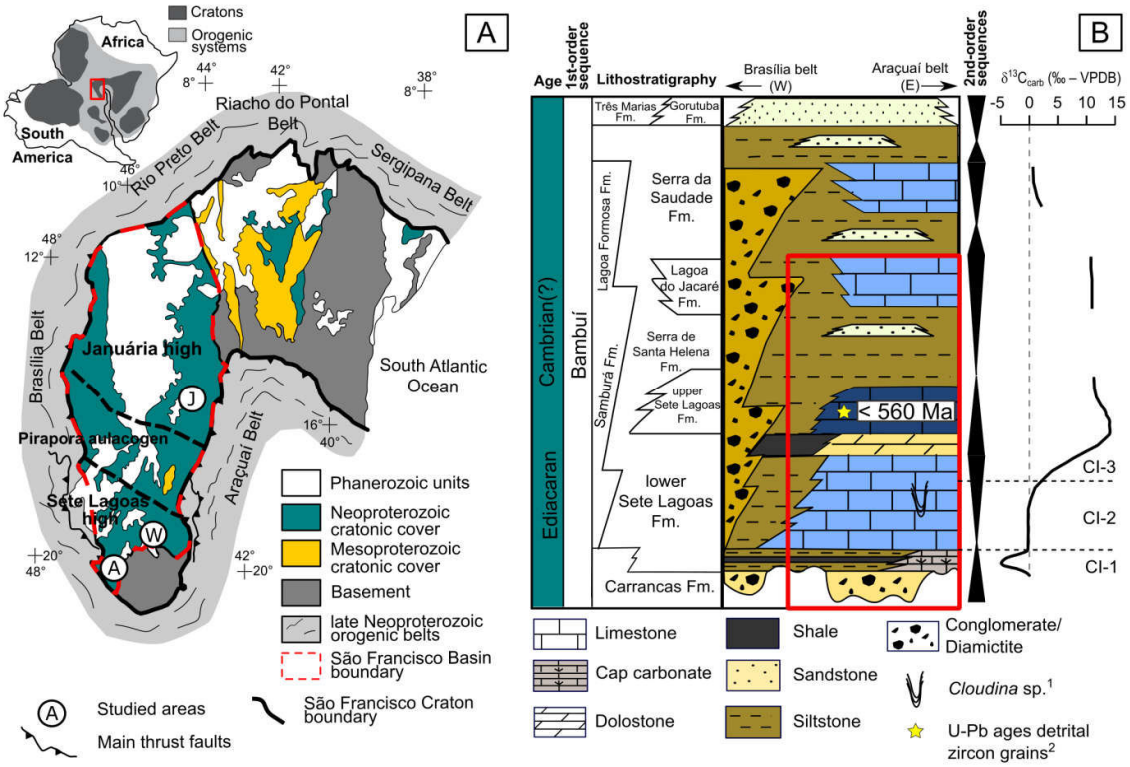

Figure 4.1: A) São Francisco Craton geological map (modified from Alkmim et al., 2006 and Reis et al., 2016). Studied sections: A – Arcos; W – Well 1; and J – Januária. B) Stratigraphic chart from the Bambuí Group (after Reis et al., 2016). [1]Fossil occurrence from Warren et al. (2014); [2]Age from Paula-Santos et al. (2015). Carbon isotope evolution based on Paula-Santos et al. (2017), Caetano-Filho et al. (2019) and Uhlein et al. (2019). The red rectangle marks the studied interval.

4.4. Materials and Methods

4.4.1. Studied sections and previous $\delta^{13}C_{carb}$ and $\delta^{18}O_{carb}$ data

Here we report carbon isotope compositions of organic carbon for three stratigraphic sections. Two of them were sampled from continuous drill core that encompass the two basal 2nd-order sequences at the southern portion of the basin, along the Sete Lagoas basement high (Arcos and Well 1 sections; Fig. 4.1A, 4.2 and 4.3). The third one is a composite outcrop section sampled in the northern area, nearby Januária city (north of Minas Gerais state). It encompasses the two basal sequences on the Januária basement high (Januária section; Fig. 4.1A and 4.4). Detailed sedimentological description, $\delta^{13}C_{carb}$ and $\delta^{18}O_{carb}$ data for these sections were previously provided by Kuchenbecker et al. (2016), Reis and Suss (2016) and Caetano-Filho et al. (2019), and are summarized below. Stratigraphic correlation between the

studied sections was carried with basis on the 2nd-order stacking patterns and bounding surfaces (e.g. Reis and Suss, 2016; Caetano-Filho et al., 2019 and references therein; Fig. 4.5). Two remarkable 2nd-order stratigraphic surfaces were identified: (i) the maximum flooding surface in the basal 2nd order sequence, and (ii) the sequence boundary between the two 2nd-order sequences, marked by unconformities and dolomitization processes that were described within basinal paleohighs (Arcos and Januaria sections). The HST was divided in early (EHST) and late (LHST) based on a basinal increase in Sr/Ca ratios. This increase is neither related to facies nor to carbonate content, and is recorded both in shallow- (Januária) and deep-water (Well 1) sections. It was interpreted as a significant paleoenvironmental change recorded throughout the basin, with possibly enhanced alkalinity, more aragonitic conditions and/or even hypersalinity, which persist to the overlying sequence (Figs. 4.2, 4.3, and 4.4; Table S1 – Supplementary Materials; Appendix B; Caetano-Filho et al., 2019; Paula-Santos et al., 2020).

4.4.1.1. Arcos Section

The Arcos section is a 180 m-thick predominantly carbonate succession (Fig. 4.2). Transgressive strata are represented by a thin layer of polymictic diamictite of the Carrancas Formation unconformably overlying the Archean basement and intraclastic and mixed siliciclastic-carbonate grainstones and packstones of the Sete Lagoas Formation (Fig. 4.6A). These successions grade upward into calcimudstones with aragonite pseudomorphs crystal fans (Fig. 4.6B), as typical features of cap carbonates. A massive layer of greenish siltstones sets the 2nd-order maximum flooding surface. The EHST stage encompasses pure microbial limestones (Fig. 4.6C), which persist through most part of the LHST. The upper part of LHST encompasses shallower facies represented by intraclastic to peloidal packstones/grainstones (Fig. 4.6D) and oolitic grainstones. Dolomitization processes affected these shallow water carbonate facies within the 2nd-order sequence boundary, which was set in a collapse breccia layer (Fig. 4.2; Kuchenbecker et al., 2016). This process was accompanied by dissolution, culminating with vugular and moldic porosity (Fig. 4.6E). In the overlying sequence, above the shallow water dolostone interval, dark-grey calcimudstones (Fig. 4.7A) and microbial limestones of the upper Sete Lagoas Formation mark a new transgressive systems tract (Fig. 4.2).

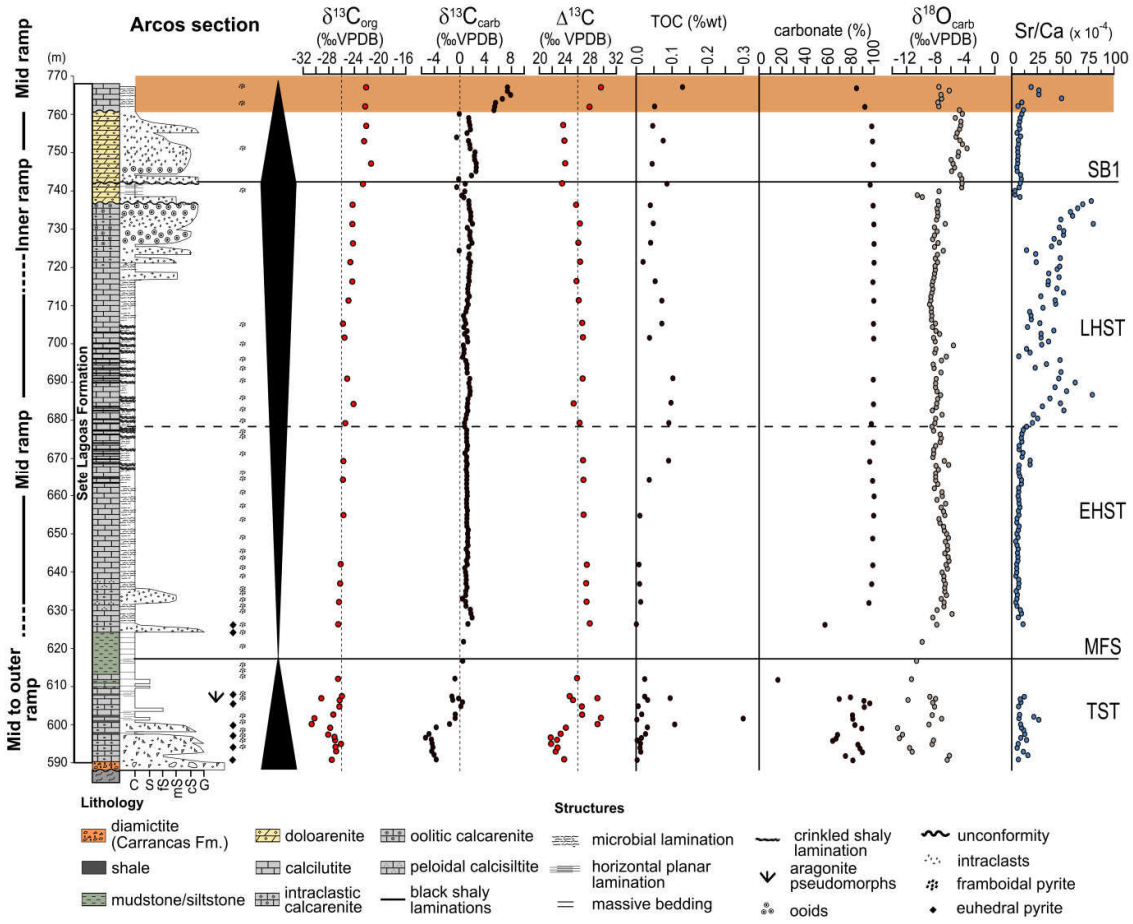

Figure 4.2: $\delta^{13}C_{org}$, $\delta^{13}C_{carb}$ and $\Delta^{13}C$ evolution of the Arcos section. $\delta^{13}C_{carb}$, $\delta^{18}O_{carb}$ and Sr/Ca ratios from Kuchenbecker et al. (2016) and Caetano-Filho et al. (2019). Orange rectangle marks the MIBE interval.

Regarding $\delta^{13}C_{carb}$ and $\delta^{18}O_{carb}$ data (Fig. 4.2; Table S1 – Appendix B; Kuchenbecker et al., 2016; Caetano-Filho et al., 2019), the TST encompasses a negative-to-positive excursions for both $\delta^{13}C_{carb}$ and $\delta^{18}O_{carb}$ profiles, typical of cap carbonate deposits. From the base of the section to the base of EHST, $\delta^{13}C_{carb}$ starts with values around −4‰ down to −5‰, followed by a positive excursion to 1‰, whereas $\delta^{18}O_{carb}$ initiates with values from −6 to −13‰, with a recover to values around –8‰ (Fig. 4.2). $\delta^{13}C_{carb}$ and $\delta^{18}O_{carb}$ profiles remain in a plateau through the whole HST, with values around 1‰ and −8‰, respectively. The dolostone interval presents $\delta^{13}C_{carb}$ values between 0 and 2‰, with some slightly negative spikes. $\delta^{18}O_{carb}$ values of dolostones are heavier compared with the rest of the section, reaching −4‰, which was interpreted as a possible influence of saline brines during early diagenetic dolomitization (Caetano-Filho et al., 2019). Above the dolostone interval,

dark grey limestones from the upper sequence presents abrupt isotope shifts, as a positive $\delta^{13}C_{carb}$ excursion from 5 to 8‰, and $\delta^{18}O_{carb}$ in a plateau around −8‰ (Fig. 4.2).

4.4.1.2. Well 1 Section

The Well 1 section is a 430 m-thick mixed siliciclastic-carbonate succession deposited in a forebulge graben domain, representing deeper environments and the thickest succession of the basal sequences of Bambuí Group (Fig. 4.3; Reis and Suss, 2016, Caetano-Filho et al., 2019). Within its basal transgressive systems tract, it contains a thin layer of polymictic diamictite of the Carrancas Formation, which grades upward into microbial dolostones (Fig. 4.6F) of the basal Sete Lagoas Formation (Fig. 4.3) and thick organic-rich black shales. These fine-grained siliciclastics define a 2nd-order maximum flooding surface (Fig. 4.3 and 4.6G). The early highstand systems tract (EHST) is marked by the overlying greenish siltstones interbedded with light gray limestones (Fig. 4.6H), which were deposited under the influence of storm waves and restricted subaqueous gravitational flows in outer to mid-carbonate ramp setting (Reis and Suss, 2016). These strata grade upward into mid- to inner-carbonate ramp successions composed of intraclastic grainstones to packstones, mudstones oolitic grainstones and microbial limestones (Fig. 4.7B). Fine to coarse-grained limestones comprise the late highstand systems tract (LHST), which is bounded in the top by a 2nd-order erosional surface recorded within supratidal carbonate deposits (Fig. 4.3; Reis and Suss, 2016). In the overlying 2nd-order sequence, dark gray microbial limestones of the upper Sete Lagoas Formation grade into fine-grained siliciclastics of the Serra de Santa Helena Formation, defining the new transgressive systems tract (Fig. 4.3 and 4.7C).

For the basal dolostone interval, the $\delta^{13}C_{carb}$ profile presents a slightly negative excursion from −3 to −4‰, coupled to a negative $\delta^{18}O_{carb}$ excursion from −7 to −10‰ (Fig. 4.3). Although these dolostones lack sedimentary features typical of cap carbonates, the gradual contact with the underlying diamictite from Carrancas Formation, the observed isotope excursions and available subsurface data allow correlate these successions with other cap carbonate successions in the basin (Fig. 4.5). Above the thick transgressive black shale interval, the $\delta^{13}C_{carb}$ profile increases progressively from −7 to 0‰ within the EHST deposits (Fig. 4.3), accompanied by a $\delta^{18}O_{carb}$ increase from −12 to −10‰. The transition between EHST and LHST is marked by an increase in $\delta^{13}C_{carb}$ values to a plateau around 3‰. LHST exhibits $\delta^{18}O_{carb}$ values ranging between −6 and −8‰. The MIBE is set in the end of LHST, as an extreme $\delta^{13}C_{carb}$ positive excursion from 4 to 11‰, followed by a slight decrease to

values near 9‰ in the overlying sequence (Fig. 4.3). The $\delta^{18}O_{carb}$ values drop to −13‰ during MIBE in Well 1 section.

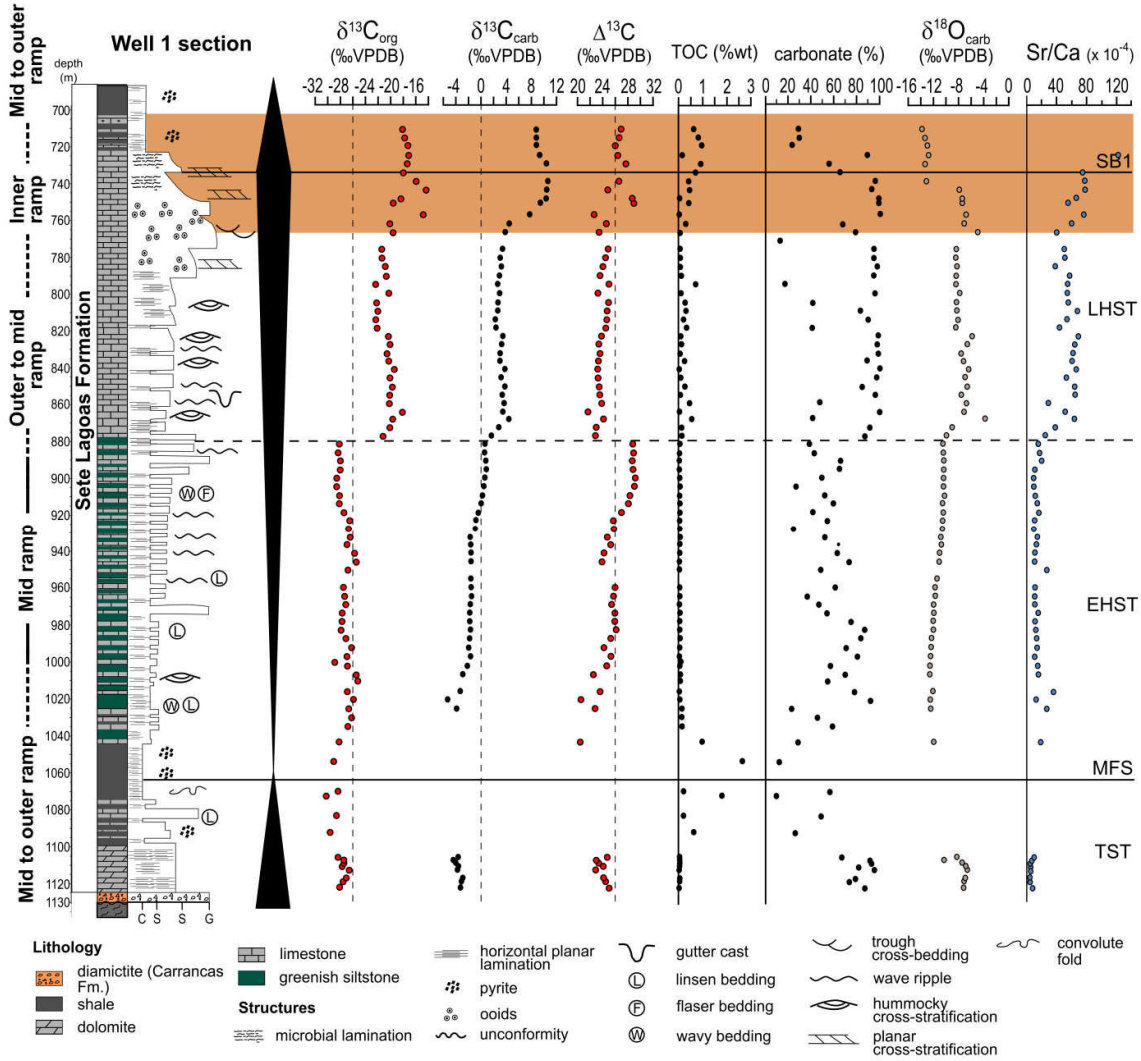

Figure 4.3: $\delta^{13}C_{org}$, $\delta^{13}C_{carb}$ and $\Delta^{13}C$ evolution of the Well 1 section. $\delta^{13}C_{carb}$, $\delta^{18}O_{carb}$ and Sr/Ca ratios from Caetano-Filho et al. (2019). Orange rectangle marks the MIBE interval.

4.4.1.3. Januária section

The Januária section is a ~140 m-thick carbonate-dominated succession that record some of the shallowest domains observed among the studied sections (Fig. 4.4). It contains within its basal portion transgressive cap carbonate succession of the lower Sete Lagoas Formation, which unconformably overlies Archean/ Paleoproterozoic basement assemblages. The cap carbonate is composed of massive layers of light gray calcimudstones and microbial

limestones with common occurrences of aragonite pseudomorph crystal fans (Fig. 4.6I) and grades upward into reddish to pinkish calcimudstones to microbial limestones (Fig. 4.6J). Bounded by 2nd-order maximum flooding surface, this transgressive systems tract is overlain by highstand pinkish to light gray calcimudstones with hummocky cross-stratifications and abundant terrigenous clay laminae (Fig. 4.4; Caetano-Filho et al., 2019). The EHST and the lower portion of the LHST in the Januária section are dominated by dark gray microbial limestones (Fig. 4.6K), commonly comprising meter-scale cycles with storm-bedded grading upward to rippled limestones. The upper LHST, on the other hand, is dominated by flat pebble intraclastic carbonate breccias, interpreted as proximal deposits from gravitational flows developed in response to exposure and reworking of inner ramp strata (Perrella Jr. et al., 2017; Caetano-Filho et al., 2019), and peritidal carbonate successions. Sequence boundary was set at the base of an overlying dolostone interval, represented by intertidal facies with sigmoidal cross-stratification (Fig. 4.6L), at the top of Sete Lagoas Formation. The transgressive systems tract of the overlying 2nd-order sequence is recorded mostly by siltstones from the Serra de Santa Helena Formation. These strata grade upward into regressive shallow water carbonate facies of the Lagoa do Jacaré Formation, which are made up by laminated calcimudstones (Fig. 4.7D), intraclastic grainstones (Fig. 4.7E) and subordinated layers of carbonate breccias.

The $\delta^{13}C_{carb}$ profile starts with typical negative-to-positive excursion associated with cap carbonate interval, from −3 to −5‰, followed by a recover to values between −1 and 0‰ (Fig. 4.4). $\delta^{18}O_{carb}$ covaries with $\delta^{13}C_{carb}$, in a negative excursion from −14 to −16‰, followed by a positive excursion to −9‰. After the maximum flooding surface, the $\delta^{13}C_{carb}$ profile presents a plateau of values between 0 and 1‰ for the whole HST stage. The $\delta^{18}O_{carb}$ profile also presents a plateau of values around −6‰, with a slight decrease to −9‰ at the end of LHST stage. In the overlying sequence, shallow water carbonate facies from the Lagoa do Jacaré Formation represents the MIBE in Januária section, with extreme $\delta^{13}C_{carb}$ values near 12‰, reaching up to 14‰. $\delta^{18}O_{carb}$ profile are relatively stable near −7‰ during this interval (Fig. 4.4).

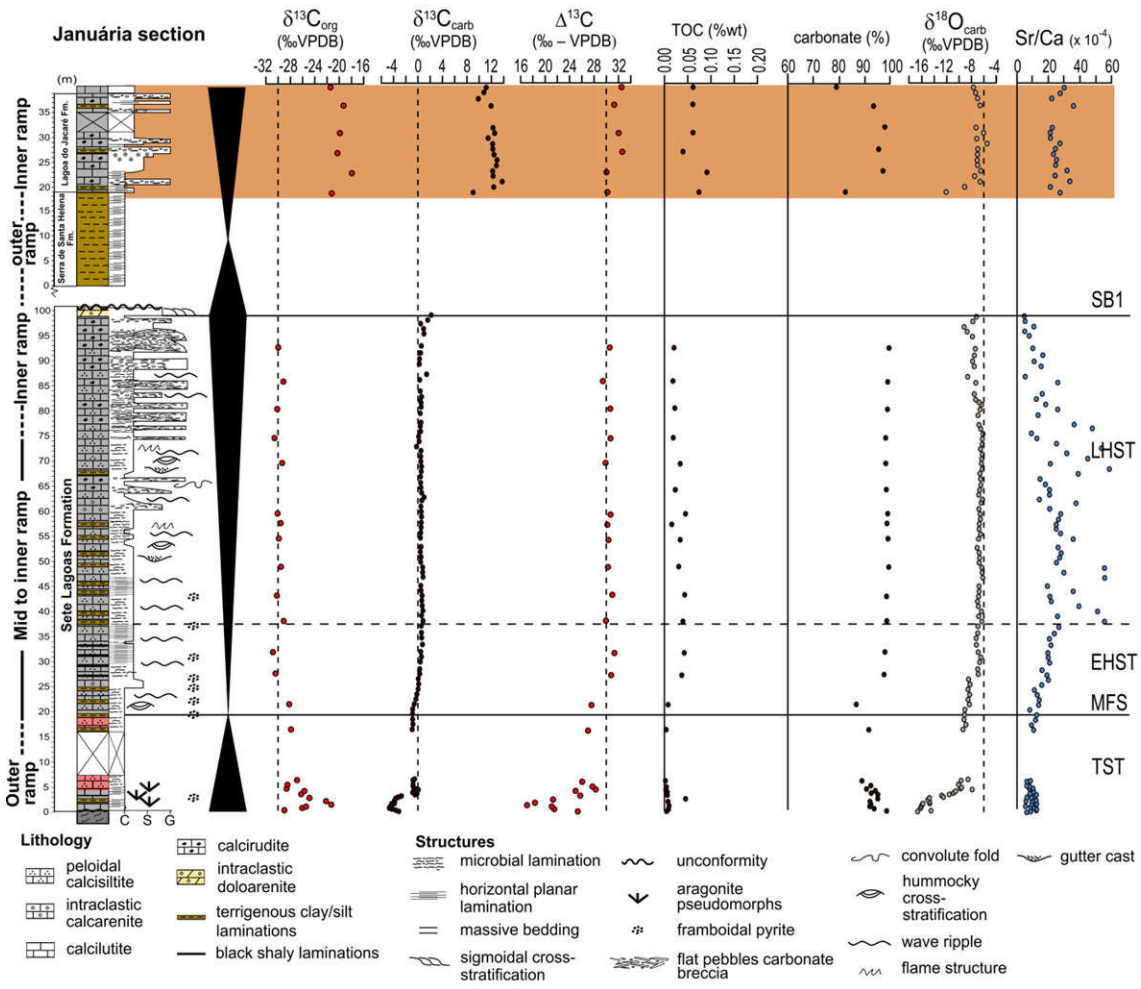

Figure 4.4: $\delta^{13}C_{org}$, $\delta^{13}C_{carb}$ and $\Delta^{13}C$ evolution of the Januária section. $\delta^{13}C_{carb}$, $\delta^{18}O_{carb}$ and Sr/Ca ratios from Caetano-Filho et al. (2019). Orange rectangle marks the MIBE interval.

4.4.2. Carbonate and TOC contents and $\delta^{13}C_{org}$ analyses

A subset of 158 samples previously analyzed for $\delta^{13}C_{carb}$ (Caetano-Filho et al., 2019) was selected for $\delta^{13}C_{org}$ analyses, in a stratigraphic resolution of 1 m for the cap carbonate interval (except Well 1 section, with 3 m resolution) and 5 m for the rest of section. Organic carbon was analyzed after a pre-acidification to remove the carbonate phases. About 3 to 5 g of carbonate rock powder were reacted with 25 mL of HCl 5N 12h at 25°C then heated at 80°C for 2h. Residues were rinsed three to four times in distilled water until reaching neutral pH then dried in an oven at 50-60 ºC. Insoluble residues were weighted allowing the carbonate contents to be calculated (Table S1 – Appendix B). About 5 to 10 mg of the decarbonated powder were weighted in tin capsules for measurements of TOC and $\delta^{13}C_{org}$ in

an elemental analyzer Thermo Scientific EA Flash 2000 coupled to a Thermo Scientific Delta V+ at the Pôle de Spectométrie Océan, University of Western Brittany, France. The detailed mass spectrometry methodology is described in Pasquier et al. (2018). A total of 158 organic carbon stable isotope compositions were measured. $\delta^{13}C_{org}$ average uncertainty calculated based on measurements of internal standard was lower than 0.2‰ (2σ).

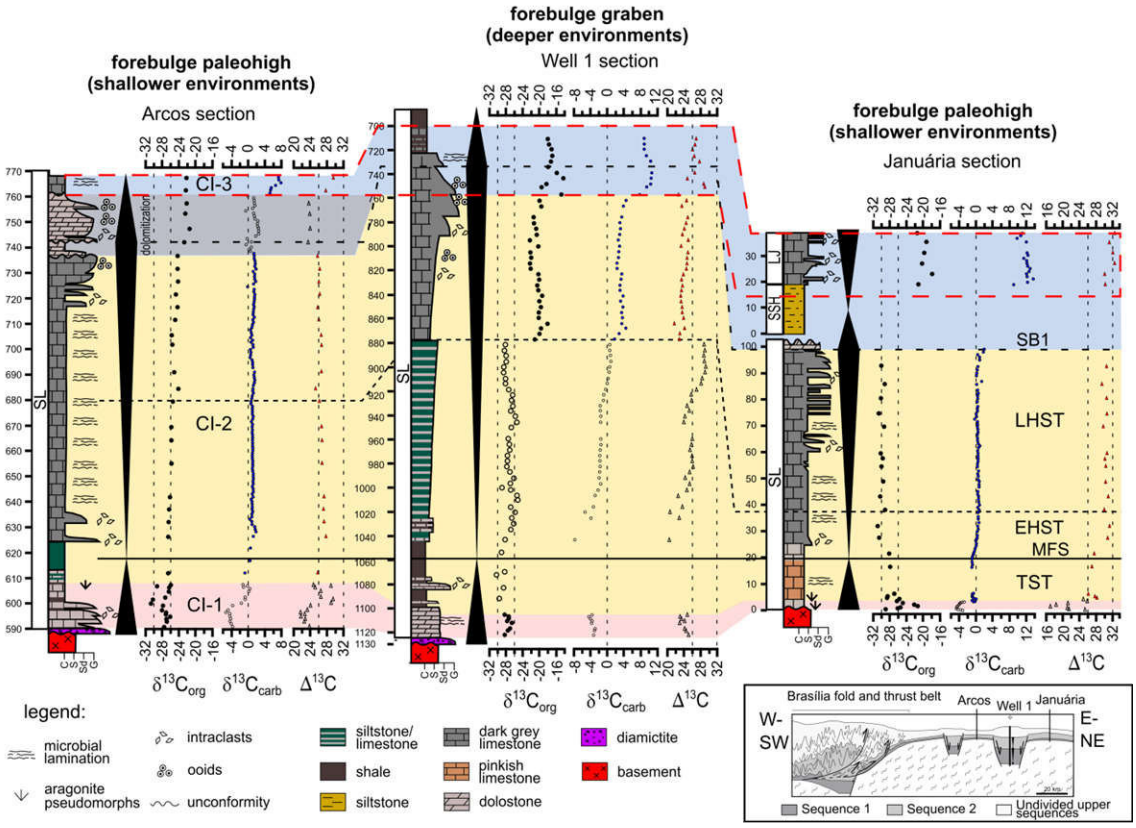

Figure 4.5: $\delta^{13}C_{org}$, $\delta^{13}C_{carb}$ and $\Delta^{13}C$ evolution for the three studied sections representing basal Bambuí Group. Correlation lines represent sequence stratigraphy division from Caetano-Filho et al. (2019): TST – Transgressive Systems tract; HST – Highstand Systems tract; MFS – Maximum Flooding Surface; SB1 – Sequence Boundary 1. Lithostratigraphy: SL – Sete Lagoas Formation; SSH – Serra de Santa Helena Formation; LJ – Lagoa do Jacaré Formation. Colored intervals represent Chemostratigraphic Intervals (CI) from Paula-Santos et al. (2017). Granulometry scale: C – clay; S – silt; Sd – sand; G – gravel. Open symbols mark samples that were interpreted as possible altered. The red dashed rectangle highlights the MIBE interval. In the bottom right corner, the schematic seismic profile for São Francisco basin with the position of sections in the forebulge domain (modified from Reis and Suss, 2016).

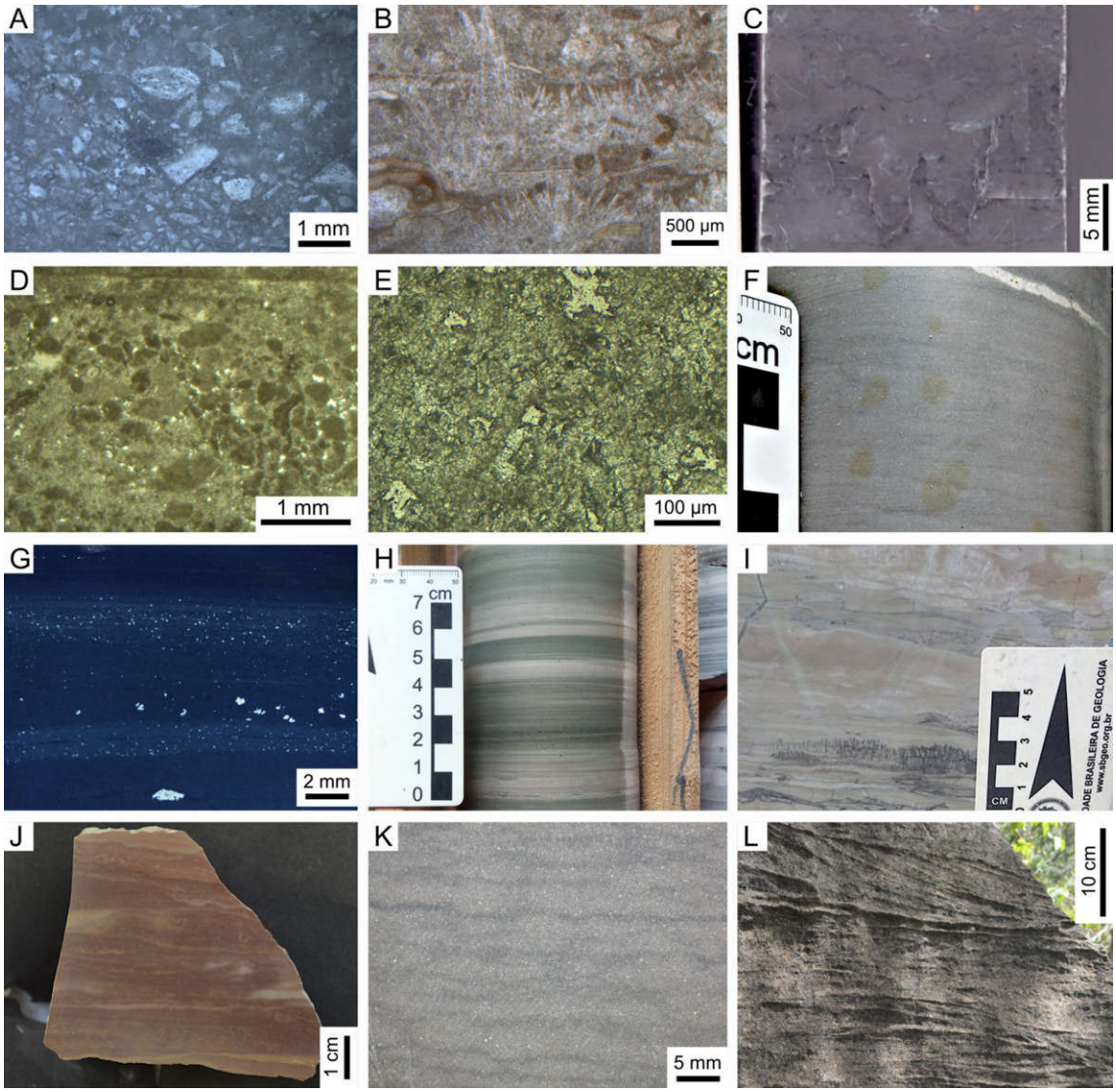

Figure 4.6: Sedimentary facies from the basal Sete Lagoas Formation, representing the basal sequence from the Bambuí Group. A) Intraclastic grainstone from cap carbonate interval of Arcos section. This basal interval presents frequent filled fractures and fluid percolation features. B) Plane polarized thin section image of calcimudstone from the cap carbonate interval of the Arcos section. Detail for aragonite pseudomorph crystal fans. C) Polished slab of a microbial limestone from the HST stage of the Arcos section. D) Plane polarized thin section image of peloidal packstone from the LHST stage of the Arcos section. E) Plane polarized thin section image from dolostone from the top of Arcos sections, showing intense dolomitization and vugular porosity. F) Microbial dolostone from cap carbonate interval of Well 1 section. G) Polished slab from a black shale sample from the base of Well 1 section. H) High frequency greenish siltstones and grey calcimudstones interbedding from the EHST stage of the Well 1 section. I) Calcimudstone with aragonite pseudomorph crystal fans from the cap carbonate interval from Januária section. J) Polished slab of a reddish calcimudstone from the TST stage of Januária section. K) Polished slab of a microbial limestone from the HST stage of the Januária section. L) Outcrop of the dolostone interval from the upper part of basal sequence in Januária section, with tangential cross-stratification.

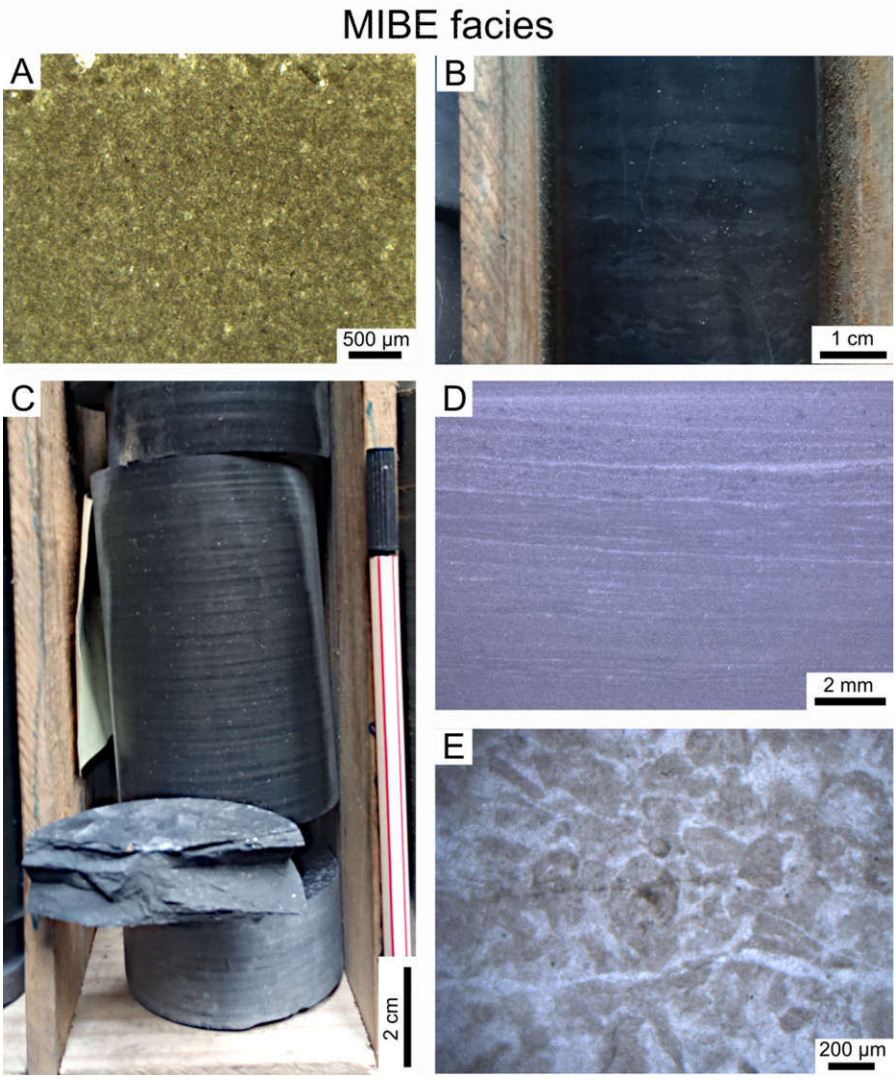

Figure 4.7: Sedimentary facies from the MIBE interval. A) Plane polarized thin section image of a calcimudstones from the Arcos section (Sete Lagoas Formation). B) Drill core interval of microbial limestones from the Well 1 section (Sete Lagoas Formation). C) High frequency interbedding of black shales and dark calcimudstones from the upper sequence of Well 1 section (Sete Lagoas Formation). D) Polished slab of a laminated calcimudstone from the upper sequence of Januária section (Lagoa do Jacaré Formation). E) Plane polarized thin section image of an intraclastic grainstone from the upper sequence of Januária section (Lagoa do Jacaré Formation).

4.5. Results

4.5.1. Carbonate and TOC content

Isotope data, TOC and carbonate content are given in Table S1 (Appendix B). Carbonate facies dominates the base of Bambuí Group, with limestone samples yielding average and median carbonate contents of 81 and 91%, respectively. Black shale intervals

from the Well 1 section (Fig. 4.3) present average and median carbonate contents of 31 and 28%, respectively. Overall, TOC values are low, varying from 0.00 to 2.64%. TOC values higher than 0.50% are only reported for black shale intervals in Well 1 section. The rest of the section exhibits an average TOC content of 0.12% (n = 76), with the EHST siliciclastic interval exhibiting the lowest values (Fig. 4.3). Januária and Arcos sections yield very low TOC contents, with an average value of 0.04% (n = 75; Fig. 4.2 and 4.4).

4.5.2. $\delta^{13}C_{org}$,$\delta^{13}C_{carb}$ and $\Delta^{13}C$ patterns

$\delta^{13}C_{org}$ data for the three studied sections is shown in figures 4.2, 4.3, 4.4 and 4.5 together with $\delta^{13}C_{carb}$ previously obtained for the limestone samples (Caetano-Filho et al., 2019) and the isotope difference between carbonate and organic matter ($\Delta^{13}C = \delta^{13}C_{carb} - \delta^{13}C_{org}$). Our data reveal that $\delta^{13}C_{org}$ and $\delta^{13}C_{carb}$ trends are independent of sedimentary facies, and record similar trends trackable at a basinal scale, from shallow to deep parts of the carbonate ramp, with exception of terrigenous-rich EHST interval from Well 1 section (Fig. 4.5). Three main isotope patterns are observed, which coincide with previously identified chemostratigraphic intervals (CI-1, CI-2 and CI-3) and sequence stratigraphic stages (Paula-Santos et al., 2017; Caetano-Filho et al., 2019):

(i) In the cap carbonate interval at the base of Sete Lagoas Formation, corresponding to part of the TST of the first sequence, $\delta^{13}C_{carb}$ starts at around −5‰ and increases upward to values of 0‰ (CI-1; Fig. 4.5). The $\delta^{13}C_{org}$ is decoupled from the $\delta^{13}C_{carb}$, with an antithetical behavior, starting with a $\delta^{13}C_{org}$ increase from about −29‰ to about −25‰, in Arcos and Well sections (Fig. 4.2 and 4.3, respectively), and to the highest value of ~ −21‰ in Januária section, followed by a decline to values of about −30‰ (Fig. 4.4). Consequently, the $\Delta^{13}C$ profile evolves dramatically, attaining values lower than 25‰ when $\delta^{13}C_{carb}$ values are negative.

(ii) At the middle of the Sete Lagoas Formation, at the end of the TST and throughout the HST, $\delta^{13}C_{carb}$ values form plateaus around 0‰, except for Well 1 section (CI-2; Fig. 4.5). $\delta^{13}C_{org}$ profiles also form plateaus at values around −30‰ in Januária and −25‰ in Arcos. Consequently, lateral variations are also observed in $\Delta^{13}C$ values, from +30‰ in Januária to +26‰ in Arcos. Well 1 section shows a distinct pattern for this interval. $\delta^{13}C_{carb}$ varies from around −2‰ in the EHST, to +4‰ in the LHST, while $\delta^{13}C_{org}$ increases from −27‰ to −21‰. There is a marked discontinuity for both $\delta^{13}C_{carb}$ (from 0 to +4‰) and $\delta^{13}C_{org}$ (from –28 to –20‰), clearly controlled by a lithological change from high-frequency interbedded

siltstones and limestones to very pure dark-colored limestone, which results in a sharp $\Delta^{13}C$ decrease from +29 to +24‰.

(iii) Right below the sequence boundary in Well 1 section or slightly above it in the two other sections, heavy isotope compositions are observed for both $\delta^{13}C_{carb}$ and $\delta^{13}C_{org}$ (CI-3; Fig. 4.2). $\delta^{13}C_{carb}$ values reach +14‰ (Januária section) whereas $\delta^{13}C_{org}$ values can reach –14‰ (Well 1 section). Minor differences in $\delta^{13}C_{carb}$ and $\delta^{13}C_{org}$ values between sections result in slight differences in $\Delta^{13}C$ values, which are around +31‰ in Januária section, +28‰ in Arcos section and +27‰ in Well 1 section. The transition between the chemostratigraphic intervals 2 and 3 (CI-2 to CI-3) is not recorded in Januária section, whereas in Arcos section it is represented by a dolomite interval.

4.6. Discussion

4.6.1. Assessing putative $\delta^{13}C_{carb}$ and $\delta^{13}C_{org}$ diagenetic overprints and the significance of $\Delta^{13}C$

$\Delta^{13}C$ values potentially record information on the type of photosynthesis (e.g. oxygenic *vs* anoxygenic photosynthesis) or on its conditions of operation (e.g. high *vs* low $[CO2]_{aq}$; Hayes et al., 1999). But before such values are interpreted in these terms it is essential to verify that organic matter and carbonates were formed from the same DIC pool. Specifically, this implies that organic and carbonate carbon isotope compositions have not been overprinted by post-depositional processes, and that neither carbonate nor organic matter are detrital, remobilized from another depositional environment or formed in separate zones of the water column presenting contrasted DIC isotope signatures.

Experimental studies and observations on modern environments show that post-depositional processes impacting the isotope values of the organic carbon fraction, such as early diagenetic microbial activity, thermal maturation, and metamorphism result in a maximum of about ±2‰ difference in the $\delta^{13}C_{org}$ (e.g. Galimov, 2004; Lehmann et al., 2002; Macko et al., 1994; McKirdy and Powell, 1974; Simoneit et al., 2004; Yamaguchi et al., 2010). In our samples, the limited influence of oxidative weathering of sedimentary organic matter is confirmed by the good agreement of $\delta^{13}C_{org}$ chemostratigraphic evolution between sections sampled from drill cores (Arcos and Well 1; Fig. 4.2, 4.3 and 4.5) and the section sampled from outcrops (Januária; Fig. 4.4 and 4.5), and with their respective stratigraphic evolution. Considering that drill core sampling from Arcos and Well 1 sections come from

different parts of the basin (forebulge paleohigh and forebulge graben) most likely representing distinct burial conditions, the coupled stratigraphic-chemostratigraphic trends also argue against the influence of oxidative weathering during the post-depositional evolution of the studied strata. In addition, the lack of correlation between TOC and $\delta^{13}C_{org}$ (Fig. 4.8 A-C) also supports the idea that early diagenetic alteration of organic matter does not seem to control, at least to the first order, the observed $\delta^{13}C_{org}$ variations in the studied sections. Regardless the thermal maturity of the studied samples (Reis and Suss, 2016), no metamorphic features have been observed suggesting a limited influence of thermal processes on their overall carbon isotopic content. Hence, the full range of $\delta^{13}C_{org}$ values (from −32 to −17‰) observed in the studied sections cannot be accounted for post-depositional processes, even if minor influences of the order of 2‰ are possible.

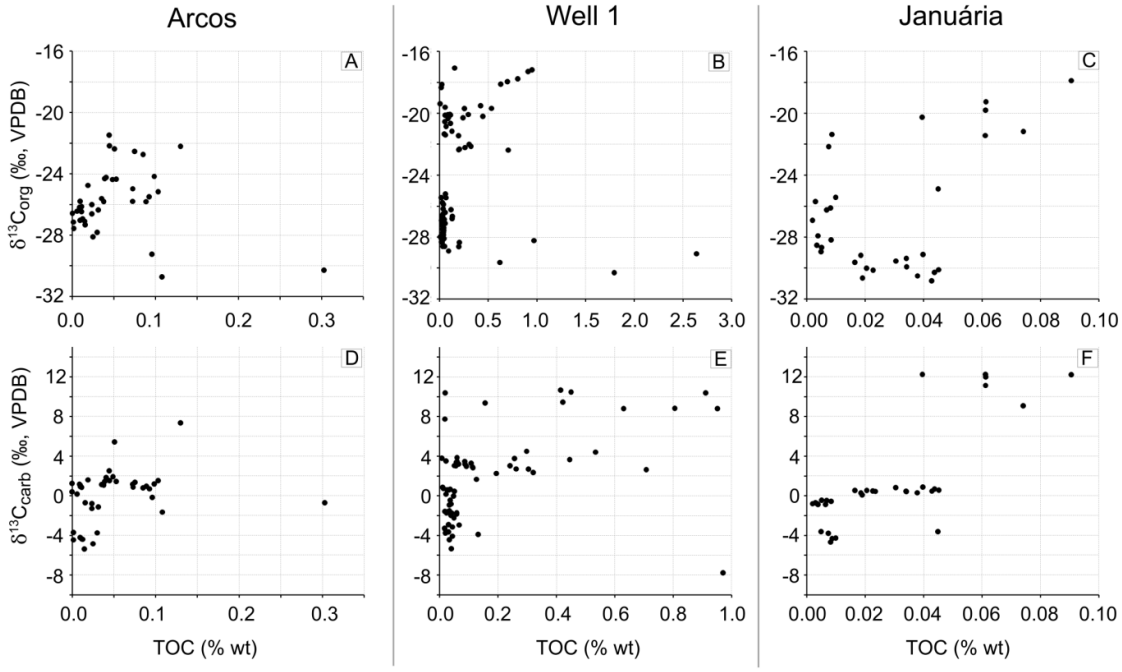

Figure 4.8: TOC *vs* $\delta^{13}C_{carb}$ and TOC *vs* $\delta^{13}C_{org}$ diagrams for the three studied sections.

In addition to the post-depositional alteration of the $\delta^{13}C_{org}$, another factor that can affect the $\Delta^{13}C$ is the presence of detrital organic matter. Here, the similarity of $\delta^{13}C_{org}$ trends at the basin scale argues against a detrital organic matter influence, considering that the sections are positioned hundreds of kilometers apart. It is unlikely that a detrital influence would dominate homogeneously the basinal $\delta^{13}C_{org}$ signal, specially resulting in uniformly high $\delta^{13}C_{org}$ values for the MIBE. Moreover, detrital lean limestones dominate the MIBE

intervals in the studied sections (Fig. 4.2, 4.3 and 4.4; Table S1 – Appendix B), supporting that a significant influence of detrital organic matter over the major isotope trends is unlikely. The EHST stage of Well 1 is an exception due to the dominance of siltstones and mudstones with very low TOC content (Fig. 4.3), and is the most susceptible interval for detrital organic contamination. The high amount of detrital material and low TOC content of this interval in Well 1 section (Fig. 4.3; Table S1 – Appendix B) may explain the facies-dependency behavior of $\delta^{13}C_{org}$ profile, which displays an abrupt increase at the transition with the overlying carbonate-dominated LHST interval.

In comparison, carbonate carbon isotope fractionation is more likely to be affected by post-depositional processes. As discussed in Caetano-Filho et al. (2019), the negative $\delta^{13}C_{carb}$ excursions recorded in the cap carbonates at the base of the studied sections and the positive $\delta^{13}C_{carb}$ excursion at the top (MIBE) are trackable at basinal scale and are not facies-dependent. This stratigraphic $\delta^{13}C_{carb}$ pattern was thus assumed to be primary at the 2nd-order. Here we can reevaluate this assumption using $\Delta^{13}C$ values, considering that $\Delta^{13}C$ values in the 26-32‰ range (Fig. 4.5) result from a typical photosynthesis isotope effect when CO_2 partial pressure is higher than 500 ppm, while lower value may potentially indicate altered $\delta^{13}C_{carb}$ values or distinct pools of DIC used for organic and carbonate reservoirs (e.g. Hayes et al., 1999). The majority of samples present $\Delta^{13}C$ values in the normal range, supporting the assumption that the isotope patterns are primary. Only a limited number of intervals present $\Delta^{13}C$ values lower than the 26-32‰ range, and require a reassessment of potential overprinting of $\delta^{13}C_{carb}$ values by diagenesis. These intervals are highlighted as empty symbols in figures 4.5 and 4.9 and correspond to: (i) the base of the cap carbonate interval in all sections; (ii) the major part of the early highstand stage at Well 1 section (from 1060 to 880 m depth); (iii) the major part of the late highstand stage at Well 1 section, and (iv) the dolostone interval in Arcos section.

Our analysis of the impact of diagenesis on $\delta^{13}C_{carb}$ will take in account petrological observations and covariation between $\delta^{18}O_{carb}$ and $\delta^{13}C_{carb}$. In addition, a negative trend in a TOC *vs* $\delta^{13}C_{carb}$ diagram (Fig. 4.8) can also be used to infer precipitation of early diagenetic carbonates, as a result of what is often called organic diagenesis, where microbial respiration of organic matter delivers ^{12}C-enriched carbon into the pore fluid (e.g. Ader and Javoy, 1998; Sansjofre et al., 2011). Such trends are more likely to be seen in shaly intervals, where the low permeability prevents pore waters from equilibrating with the overlying seawater and the organic substrate is usually high for microbial respiration. The same trend could also result

from organic carbon remineralization in late diagenesis processes, although it is less important due to low fluid/rock interactions in a highly compacted condition. In our samples, no correlation between TOC and $\delta^{13}C_{carb}$ (Fig. 4.8 D-F) can be seen for intervals with low $\Delta^{13}C$, even when shaly levels are present. Therefore, it is not possible to conclusively argue that $\delta^{13}C_{carb}$ were overprinted by organic diagenesis.

Petrological observations allowed the recognition of features typical of carbonate diagenesis, such as dissolution and secondary crystallization, or the presence of levels more susceptible to post-depositional fluid percolation, such as abrupt lithological contacts (e.g. siliciclastic *vs* carbonate facies). Cap carbonates are affected by dolomitization in Well 1 section, by intense recrystallization in Januária section, with spatic white carbonate layer immediately above the contact with basement, filled-fractures and fluid percolation features (Fig. 4.6I), while in Arcos section they exhibit frequent interbedding of siltstones and shales at the base (Fig. 4.2). The dolostone interval at the top of Arcos section also displays intense recrystallization, followed by a dissolution event, which resulted in vugular porosity (Fig. 4.6E; Caetano-Filho et al., 2019; Kuchenbecker et al., 2016). In Well 1 section, the EHST is composed of high frequency interbedding of green siltstones/mudstones and limestones (Fig. 4.6H) that are lithological contacts favorable to fluid percolation. Finally, the LHST stage of Well 1 unlike the other intervals discussed before does not present petrological evidence of pervasive post-depositional fluid percolation, being composed of carbonate rocks with well-preserved textures (e.g. Fig. 4.7B; Reis and Suss, 2016; Caetano-Filho et al., 2019) and almost completely free of a detrital component (Fig. 4.3; Table S1 – Appendix B).

Covariations between $\delta^{18}O_{carb}$ and $\delta^{13}C_{carb}$ have been widely used to track diagenetic overprint on both $\delta^{18}O_{carb}$ and $\delta^{13}C_{carb}$ (e.g. Jacobsen and Kaufman, 1999). In a $\delta^{18}O_{carb}$*vs* $\delta^{13}C_{carb}$ diagram no overall covariation can be seen for individual sections (Fig. 4.9A). Yet, if we consider only the samples with $\Delta^{13}C$ below 25‰, some intervals present positive trends (Fig. 4.9B). The cap carbonate intervals of all sections show a weak decrease of $\delta^{13}C_{carb}$ with $\delta^{18}O_{carb}$ following different trends. Notwithstanding, they present similar $\delta^{13}C_{carb}$ values for contrasting $\delta^{18}O_{carb}$ in each section, which suggests diagenetic alteration of $\delta^{13}C_{carb}$ was minor in these rocks, at least during diagenetic events responsible for the $\delta^{18}O_{carb}$ variability. The EHST and LHST of Well 1 both show positive $\delta^{13}C_{carb}$ and $\delta^{18}O_{carb}$ trends, with steep and gentle slopes, respectively (Fig. 4.9B). The diagenetic control of $\Delta^{13}C$ on these two segments of the Well 1 section can be further inspected with the $\Delta^{13}C$ *vs* $\delta^{13}C_{carb}$ diagram (Fig. 4.9C). A clear 1:1 slope is observed for EHST intimately associating $\Delta^{13}C$ below 25‰ to negative $\delta^{13}C_{carb}$ values, which strongly suggests a diagenetic overprint of the carbonate carbon isotope

compositions of this specific interval. In contrast, no correlation is observed for LHST. Therefore samples from LHST were further considered in our paleonvironmental analysis, whereas those from the EHST were discarded. Finally, the dolostone interval in Arcos section does not present a $\delta^{13}C_{carb}$ and $\delta^{18}O_{carb}$ positive covariation, but it displays the most positive $\delta^{18}O_{carb}$ values of all samples, suggesting an early diagenetic dolomitization related to saline brines (Caetano-Filho et al., 2019). Furthermore, occurrences of dissolution features associated with dolomitization in this interval (Fig. 4.6E) lead to a conservative assumption to avoid paleodepositional interpretations over the carbon isotope signatures of these rocks.

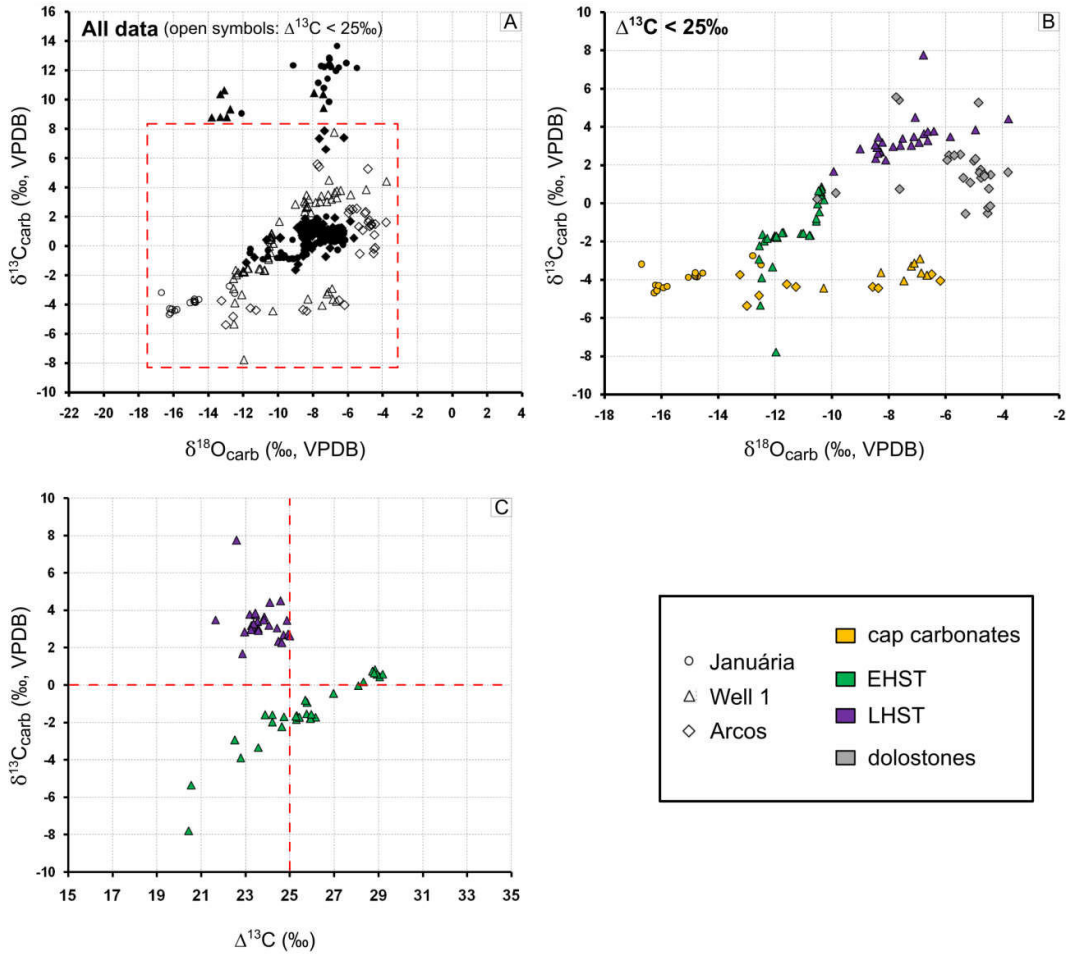

Figure 4.9: A) $\delta^{18}O_{carb}$ *vs* $\delta^{13}C_{carb}$ diagram for all the data. Open symbols represent those data with unusual $\Delta^{13}C$ < 25‰, whereas the filled points represent $\Delta^{13}C$ > 25‰. B) $\delta^{18}O_{carb}$ *vs* $\delta^{13}C_{carb}$ diagram with only data with $\Delta^{13}C$ < 25‰ (dashed rectangle in diagram A), distinguished per section and stratigraphic stage. C) $\Delta^{13}C$ *vs* $\delta^{13}C_{carb}$ diagram for EHST and LHST stage of the Well 1 section, note that negative $\delta^{13}C_{carb}$ values of the EHST stage is associated with $\Delta^{13}C$ < 25‰.

In sum, considering that their $\delta^{13}C_{carb}$ values are likely to have been overprinted during diagenesis none of the intervals with anomalously low $\Delta^{13}C$ were considered for further paleoenvironmental interpretation except for the LHST in Well 1 section. Nevertheless, omitting these intervals do not compromise the discussion concerning the MIBE, in which extreme positive $\delta^{13}C$ excursions (>10‰) occur, without significant changes in $\Delta^{13}C$ (<3‰ in magnitude; Fig. 4.5). In addition, although paired carbon isotope signatures from the cap carbonate interval are considered potentially altered in our sample screening, low $\Delta^{13}C$ values are typically described in other Ediacaran cap carbonate successions (e.g. Sansjofre et al., 2011). For this reason, the cap carbonate interval is discussed in a separate section before discussing the MIBE, considering they represent remarkable carbonate deposits in geological record and data presented here can be of interest for future studies on this topic.

4.6.2. Non facies-dependent and antithetical $\delta^{13}C_{carb}$ – $\delta^{13}C_{org}$ trends for the basal Sete Lagoas Formation: a typical cap carbonate $\Delta^{13}C$ excursion?

Low $\Delta^{13}C$ values are usually reported for Ediacaran cap carbonates (~19 to 24‰; Sansjofre et al., 2011 and references therein; and as low as 17‰ by this study; Januária section – Fig. 4.4), compared with the interglacial periods of late Neoproterozoic (28–32‰; Hayes et al., 1999). This results from decoupling and apparent inverse relationship between $\delta^{13}C_{carb}$ and $\delta^{13}C_{org}$ (e.g. Jiang et al., 2010; Sansjofre et al., 2011; Fig. 4.2, 4.3, 4.4 and 4.5). Changes in the photosynthetic fractionation factor (ε_p) (e.g. Hayes et al., 1999; Sansjofre et al., 2011), active uptake of HCO_3^- during photosynthesis (Jiang et al., 2010), diagenesis and allochthonous input of organic carbon (Jiang et al., 2012) were hypotheses proposed to explain such anomalously low values of $\Delta^{13}C$ in cap carbonate successions.

We report here that the new paired $\delta^{13}C$ data from Bambuí Group cap carbonates, from shallow to deep domains of the carbonate ramp (Fig. 4.5), show that major carbon isotope trends are not facies-dependent. These trends are equally recorded in intraclastic grainstones (Fig. 4.6A), rudstones and calcilutites in Arcos section, microbial limestones and calcimudstones bearing aragonite crystal fans in Arcos and Januária sections (Fig. 4.6B and 4.I, respectively), and microbial dolostones followed by distal black shales in Well 1 section (Fig. 4.3 and 4.6F) (Caetano-Filho et al., 2019). Thus, detrital organic matter influence can be discarded in our case, especially considering the dominantly pure carbonate facies usually associated with this interval (Table S1 – Appendix B). Given the clear stratigraphic control over these excursions and the fact that the different sections likely experienced different burial

rates (graben and paleohighs), late diagenesis is also not likely. Therefore, a primary or very early diagenetic origin for the mirrored $\delta^{13}C_{carb}$–$\delta^{13}C_{org}$ trends observed here remains possible (e.g. Knauth and Kennedy, 2009; Jiang et al., 2010; Sansjofre et al., 2011).

4.6.3. Extreme positive $\delta^{13}C$ excursion in the late Ediacaran-Cambrian Bambuí Group: a methanogenic-dominated basin?

When omitting the samples possibly affected by post-depositional perturbations, our paired $\delta^{13}C$ data show that the extreme positive $\delta^{13}C_{carb}$ excursion (MIBE) is nicely coupled to the $\delta^{13}C_{org}$ with a very strong positive correlation for all the studied sections (correlation coefficients of 0.90, 0.83 and 0.99 for Arcos, Well 1 and Januária sections, respectively, $p(\alpha) < 0.01$; Fig. 4.10). The $\Delta^{13}C$ patterns of each section show a maximum increase of 3‰ in the MIBE (Well 1 section) compared with the underlying intervals, in spite of a 10‰ $\delta^{13}C_{carb}$ isotope excursion (Fig. 4.5). Together with a range of $\Delta^{13}C$ values compatible with carbonates and organic matter acquiring their isotope value from the same DIC reservoir (Hayes et al., 1999), this suggests that the MIBE was driven by extreme increase in the $\delta^{13}C_{DIC}$ value of seawater through the whole basin, from shallow to deeper environments.

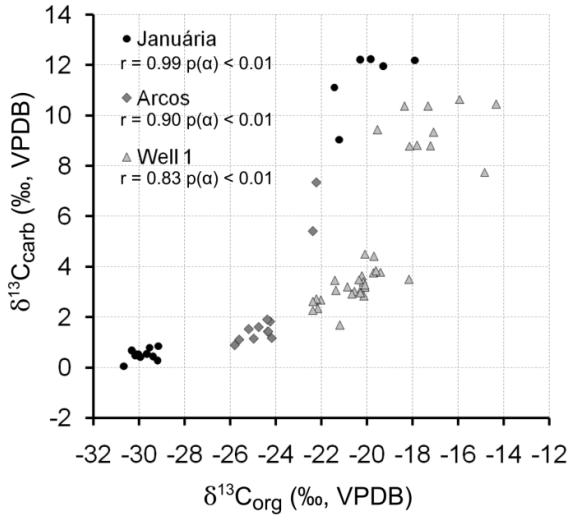

Figure 4.10: $\delta^{13}C_{org}$ *vs* $\delta^{13}C_{carb}$ diagram for data through LHST and overlying sequence. The MIBE presents very strong correlation coefficient for all the studied sections, attesting that these isotope excursions represent the same DIC reservoir.

The MIBE seems to have been strongly controlled by the tectonic evolution of the basin, as indicated by its relationship with the basal 2nd-order sequence boundary in the

Bambuí foreland system. This basal sequence boundary is accompanied by a drastic change in provenance data with relatively young zircon grains in the second sequence, indicating the advance of the mountain belts surrounding the São Francisco Craton during late Ediacaran-Cambrian (Reis et al., 2016; Paula-Santos et al., 2015). Geochemical inferences for a progressively restricted and isolated basin come from a basin-scale increase in Sr/Ca ratios preceding the MIBE, interpreted as a more alkaline, aragonitic, and/or hypersalinity conditions (Caetano-Filho et al., 2019), and from a drop in the $^{87}Sr/^{86}Sr$ ratios to 0.7075-0.7077, mismatching late Ediacaran-Cambrian global values (Paula-Santos et al., 2017). All of these arguments strongly suggest that the carbon cycle in the basin was also affected by the basin isolation in Gondwana interior and, therefore, the MIBE is here considered a local signal decoupled from the global carbon budget. This assumption is also supported by the fact that the MIBE presents values significantly higher than other upper Ediacaran–lower Cambrian successions, usually below 6‰ (e.g. Zhou and Xiao, 2007; Fike and Grotzinger, 2008; Halverson et al., 2010; and references therein), even considering other West Gondwana domains (Corumbá Group – $\delta^{13}C_{carb}$< 5‰, Boggiani et al., 2010; Arroyo del Soldado Group – $\delta^{13}C_{carb}$< 4‰; Gaucher et al., 2003). Similar heavy $\delta^{13}C_{carb}$ values (> 10‰) are reported from coeval carbonate successions of São Francisco-Congo craton for carbonate units within orogenic belts surrounding Bambuí Group (Uhlein et al., 2019 and references therein), and from the Hüttenberg Formation, Otavi Group (Cui et al., 2018), which are assigned to the same restricted geotectonic scenario of West Gondwana assembly.

As previously discussed by Paula-Santos et al. (2017) and Uhlein et al. (2019), this positive $\delta^{13}C$ excursion would require unrealistic scenarios under steady-state mass balance assumptions, where the ocean and atmosphere are in isotope equilibrium ($\delta^{13}C_{input} = (1-f_{org})$ x $\delta^{13}C_{carb} + f_{org}$ x $\delta^{13}C_{org}$; e.g. Hayes et al., 1999). The coupled carbon excursions presented here, reaching up to +14 and −14‰ for $\delta^{13}C_{carb}$ and $\delta^{13}C_{org}$ respectively, would require a fraction of organic carbon buried (f_{org}) higher than 50% or increased $\delta^{13}C_{input}$ above +4‰, more than 9‰ above the bulk value of −5‰. On the other hand, the MIBE might not fit time-dependent non-steady state scenarios, in which a decreased DIC reservoir leads to higher sensitivity of the marine carbon isotope system (i.e. extreme isotope excursions would not require dramatic changes in f_{org} and $\delta^{13}C_{input}$, e.g. Bartley and Kah, 2004). Carbonate rocks from the Bambuí Group towards the MIBE are usually carbonate-pure and accompanied by geochemical inferences of enhanced alkalinity (higher Sr/Ca ratios and higher HREE/LREE fractionation, i.e. higher carbonate alkalinity; Caetano-Filho et al., 2019; Paula-Santos et al., 2020) compared to the carbonate rocks deposited below this interval. Also, the MIBE

corresponds to a rapid excursion to a plateau of extreme and relatively stable high $\delta^{13}C_{carb}$ values (> 10‰) through hundreds of meters (Uhlein et al., 2019), which is also in disagreement with a decreased DIC reservoir that would lead to a higher variability of $\delta^{13}C_{DIC}$.

We thus want to explore the possibility that the MIBE is of local extent and of long duration, (i.e. spanning the 2nd-order sequence timescale in hundreds of meters in the stratigraphy, Uhlein et al., 2019) and results from a process which could have promoted a long-term isotope disequilibrium between the basin's DIC and the global atmospheric CO_2. In other words, to keep such anomalously high $\delta^{13}C_{DIC}$ values compared to coeval global seawater in the time-scale of million years, the regional carbon cycle in the Ediacaran-Cambrian Bambuí sea must have been dynamically maintained by a mechanism with a rate exceeding that of isotope equilibration between the DIC and the atmospheric CO_2, which is achieved in hundreds to thousands of years in continental water masses (e.g. Benson et al., 1996). In this case, the isotope mass balance equations used to model the steady-state global carbon cycle based on the hypothesis that ocean and atmosphere are in isotope equilibrium are not appropriate (e.g. Hayes et al., 1999; Schrag et al., 2013). We therefore revisit the hypotheses previously proposed for the mechanism responsible for the MIBE, namely (i) the increase in organic carbon burial, (ii) an increase in authigenic carbon precipitation, (iii) changes in isotope composition of the dissolved carbon input into the basin, and (iv) the methanogenesis coupled to methane loss to the atmosphere (e.g. Iyer et al., 1995; Paula-Santos et al., 2017; Uhlein et al., 2019).

In the modern carbon cycle the fluxes of carbon buried into sediments and the carbon delivered through riverine input into the oceans are three orders of magnitude lower than the exchange fluxes between the atmosphere and the oceans (less than 0.9 PgC yr^{-1} as opposed to 60 PgC yr^{-1}, respectively; Ciais et al., 2013). In contrast, the fluxes between surface ocean and marine biota, through photosynthesis and respiration, are of the same order of magnitude as those between the atmosphere and the ocean DIC reservoirs (37 to 50 PgC yr^{-1}; Ciais et al., 2013). On this basis, the increase in organic carbon burial and/or in authigenic carbon precipitation, and the change in the carbon isotope composition of dissolved carbon input by runoff into the basin are unlikely to explain the anomalous ^{13}C-enrichments found. Whether we consider equilibrium or disequilibrium scenarios between the Bambuí basin waters and the atmosphere, these fluxes should have been at least two to three orders of magnitude higher than the modern ones, for several million years in order to result in homogeneously high $\delta^{13}C$ values of MIBE interval, which is very unlikely.

Additional arguments can be invoked to rule out that this possible disequilibria condition between DIC and atmosphere was caused locally by the mechanisms usually envisaged for global positive $\delta^{13}C$ anomalies. No significant increase in TOC content is observed below and through the excursion anywhere in the basin that could support the hypothesis of a locally increased organic carbon burial. In Well 1 section, TOC increases after the positive $\delta^{13}C$ excursions, so it cannot be interpreted as a cause for the ^{13}C enrichments. In addition, trace element data through the Bambuí deposits suggest that bottom waters were predominantly anoxic before and after the positive $\delta^{13}C_{carb}$ excursion, compatible with a scenario of stagnant waters in an epicontinental basin (Paula-Santos et al., 2018; 2020; Hippertt et al., 2019). This stasis in the redox state of the water column is also incompatible with a major change in the organic burial rate, in the sense that enhanced organic burial is often associated with enhanced reducing conditions, whether associated with increased bioproductivity or not. Increases in precipitation and burial of ^{13}C-depleted authigenic carbonates (e.g. Schrag et al., 2013) can also be ruled out to account for the MIBE. For the restricted setting of the Bambuí sea an ^{13}C-enriched signal caused by authigenic carbonate precipitation would require both the identification of intervals rich in authigenic carbonates with very negative $\delta^{13}C_{carb}$ and the decoupling between carbonate and organic carbon isotope signatures. No significant event of ^{13}C-depleted authigenic carbonate deposition preceding MIBE has been identified so far. Apart from cap carbonates, the intervals identified as possibly diagenetic (section 4.6.1) are very local and lithologically-controlled rather than basin-wide occurrences. Uhlein et al. (2019) pointed to the occurrence of framboidal pyrite in carbonate facies from the Lagoa do Jacaré Formation as an evidence of sulfate-reduction activity known to result in authigenic carbonate precipitation. However, these carbonate rocks present extreme positive $\delta^{13}C_{carb}$ values (> 10‰). i.e., this unit belongs to the MIBE and cannot account for a ^{13}C-depleted authigenic precipitation event (Fig. 4.5). Finally, an increase in the $\delta^{13}C_{input}$ through riverine DIC to the basin has also been discussed for the MIBE (Uhlein et al., 2019). Because carbonates record the isotope composition of the DIC they precipitate from, the DIC generated through weathering on land and reaching the basin would need to present extremely positive $\delta^{13}C$ values to account for the MIBE. The values must have been even higher than those recorded in the excursion, since mixing with the water body DIC and ongoing isotopic exchange with the atmosphere would both tend to drive the $\delta^{13}C_{carb}$ to lower values.

Hence the only hypothesis we are left with is that of methanogenesis and methane loss to the atmosphere, representing an intrabasinal forcing on the carbon cycle as a result of

drastic paleoenvironmental changes through the basal Bambuí Group deposition. In a scenario of basin restriction, progressive marine sulfate distillation would ultimately lead to a methanogenic environment (Paula-Santos et al., 2017). In anoxic and sulfate-depleted environments, methanogenesis may take place as an important early diagenetic metabolism (e.g. Gu et al., 2004; Birgel et al., 2015). This metabolism produces two carbon compounds with very distinct carbon isotope composition: a very ^{13}C-depleted CH_4 and a ^{13}C-enriched CO_2 (Whiticar et al., 1986). Studies in modern marine and lacustrine methanogenic environments show that methanogenic ^{13}C-enriched CO_2 can influence $\delta^{13}C_{DIC}$ from pore waters (up to +26‰; Gu et al., 2004) and in restricted settings can even influence the DIC of the overlying water column (Gu et al., 2004; Assayag et al., 2008). In the Lake Apopka, Florida (USA), the $\delta^{13}C_{DIC}$ and $\delta^{13}C_{POC}$ from the water column are as high as +13‰ and −13‰, respectively (Gu et al., 2004). ^{13}C enrichment in the DIC of water column is associated with diffusion and advection of ^{13}C-enriched CO_2 from the methanogenic-dominated sediments ($\delta^{13}C_{DIC}$ of pore waters ~+26‰), coupled with methane ebullition. Photosynthetic carbon fixation of this ^{13}C-enriched DIC results in similar enrichments in POC. It is important to note here that in this case, methane loss to the atmosphere is required, otherwise its oxidation in the water column would buffer the $\delta^{13}C_{DIC}$ variations by adding very ^{13}C-depleted CO_2 from methane oxidation. Gu et al. (2004) suggested several factors are favoring the establishment of such unusual conditions of highly ^{13}C-enriched DIC. Bottom water anoxia, limited sulfate availability and high bioproductivity lead to high rates of methanogenesis required to maintain a significant flux of methanogenic CO_2 to the water column. Shallow water environment and efficient wind mixing are favoring methane loss to the atmosphere, preventing its oxidation in the water column. Such scenario was proposed by Birgel et al. (2015) for the extreme ^{13}C enrichments found in stromatolites from Lagoa Salgada, a coastal lagoon located in SE Brazil. Although these ^{13}C enrichments are not present in the DIC today, the authors proposed that methanogenesis coupled to methane escape to the atmosphere strongly affected the DIC during times of stromatolite formation, under more arid and sulfate-limited conditions in Lagoa Salgada. Anoxic and sulfate-depleted bottom conditions associated with a shallow water column would be responsible for preventing methane oxidation in the water column and rapid escape to the atmosphere.

For the MIBE, the enhanced restriction of the Bambuí sea driven by the advance of the orogenic fronts over the basin may have led to its complete disconnection from the marginal seas and to sulfate exhaustion through bacterial sulfate reduction and pyrite burial during the deposition of the basal sequence (Fig. 4.11). This would have resulted in an expansion of the

methanogenic zone to shallow depths within the sediment and even in the water column, increasing the methane concentration and its escape to the atmosphere. Methane escape to the atmosphere would have been favored by: (i) limited oxidation in a predominantly anoxic and sulfate-limited basin (e.g. Paula-Santos et al., 2017; 2020; Hippertt et al., 2019); (ii) a shallow chemocline, which would decrease the thickness of the methane oxidation zone (oxic layer), considering the absence of negative Ce anomalies from shallow to deep environments of the carbonate ramp (data from Januária and Arcos sections; Paula-Santos et al., 2020) (Fig. 4.11); and (iii) hypersalinity and decreased methane solubility, considering the high $\delta^{18}O_{carb}$ values in early diagenetic dolostones associated with the sequence boundary (Caetano-Filho et al., 2019). These favorable conditions for methane bypass to the atmosphere and the shallow chemocline would result in a surface marine DIC progressively enriched in ^{13}C by methanogenic CO_2, through mixing between the thin upper oxic layer and the thick anoxic bottom layer. In this scenario, the redox stratification attributed to the Bambuí sea would not imply in a divided DIC pool. Consequently, primary organic biomass produced through photosynthesis would also present heavy carbon isotope compositions (e.g. Gu et al., 2004), represented by the coupled $\delta^{13}C_{carb}$ and $\delta^{13}C_{org}$ high values through the MIBE (Fig. 4.11).

Recent iron speciation data from Hippertt et al. (2019) show an increasing trend from euxinic to more ferruginous conditions through the MIBE. Although the authors assigned this redox change to the higher detrital input, and so, higher reactive Fe availability, these data still support a sulfate-limited condition during the excursion. This redox change through the MIBE may also explain the increase in total sulfur content in this interval (Uhlein et al., 2019), when higher reactive Fe availability favored precipitation of iron sulfides from previous euxinic waters. Therefore, sulfur isotope compositions and further iron speciation data are still required to put constraints on the sulfate availability through the MIBE and, most important, to test the scenario here proposed.

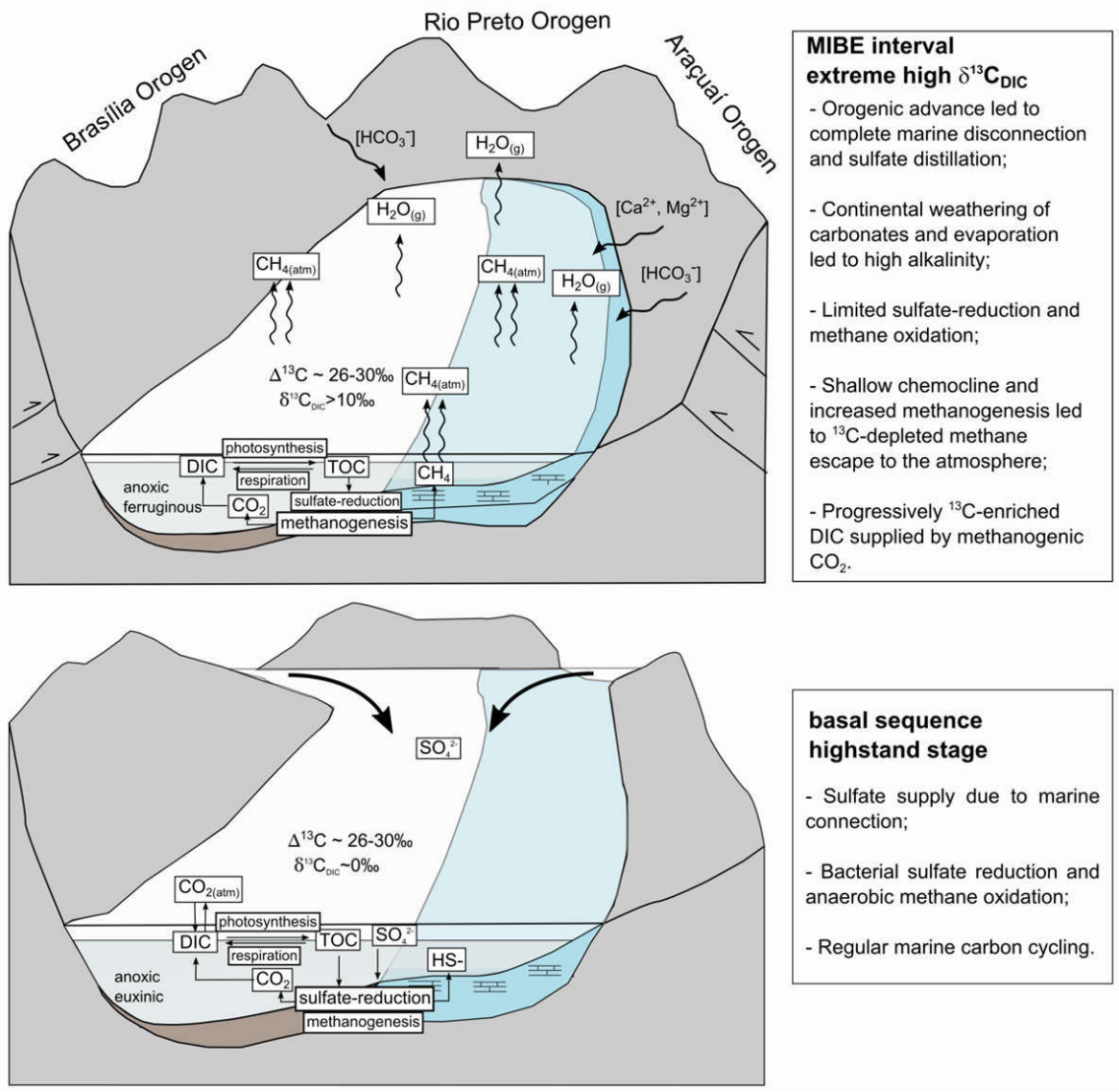

Figure 4.11: Conceptual model for the marine carbon cycle disturbance between basal and overlying 2nd-order sequences from the Bambuí Group. The Middle Bambuí Excursion would represent a transition for a methanogenic dominated basin after sulfate exhaustion and limited sulfate-reduction due to orogenic build-up and marine disconnection. A shallow chemocline would decrease methane oxidation in the Bambuí sea and favors methane escape to the atmosphere (based on data from Hippertt et al., 2019 and Paula-Santos et al., 2020). A thick anoxic bottom layer would have reached photic zone in which ^{13}C-enriched methanogenic-CO_2 influenced DIC available for photosynthetic primary production, resulting in equally heavy organic and carbonate-carbon isotope compositions.

At the same time, methanogenesis would lead to acidic conditions due to massive CO_2 production, being therefore unfavorable for carbonate precipitation (e.g. Birgel et al., 2015). This would require some processes to buffer the seawater pH to explain microbial limestones

and calcimudstones that dominate MIBE interval (Fig. 4.4F and 4.4G; Table S1 – Appendix B). One possibility would be an increase in alkalinity resulting from the marginal orogenic uplift and decreased continental weathering intensity due to higher denudation rates, therefore favoring weathering of carbonates and congruent silicate weathering. This was already inferred for middle Bambuí Group through unradiogenic $^{87}Sr/^{86}Sr$ ratios and enhanced rare earth elements fractionation recorded in carbonates at this stage (Paula-Santos et al., 2018; 2020). In this case, sea-level fall and/or orogenic reworking and uplift would result in a large flux of ions to the basin, especially Ca^{2+} and Mg^{2+} derived from carbonate weathering (Fig. 4.6). Sulfate may also have been produced through oxidative weathering of pyrites and sulfate minerals from the orogens and supplied to the basin, although not in quantities large enough to counter balance a previous sulfate distillation event. Even considering a sulfate amount in the Neoproteroic oceans 10 times lower than in the modern ocean (i.e. 1.3 x 10^{20} g S), a connection to the ocean would still supply much more sulfate to the Bambuí basin than the riverine sulfate input from major river systems (i.e. lower than the contemporaneous flux of 10^{14} g S yr^{-1}; Bottrell and Newton, 2006 and references therein). Therefore, a marine disconnection would critically reduce the sulfate supply to Bambuí sea. Finally, hypersalinity could also be an important factor for carbonate saturation (e.g. Birgel et al., 2015) in the scenario discussed above (Caetano-Filho et al., 2019). The isolation of the Bambuí basin in the very core of the Gondwana supercontinent might have resulted in arid conditions and negative hydrologic balance due to inefficient humidity transfer to the continent interior in times of absence of land vegetation.

4.6.4. The late Ediacaran-Cambrian Gondwana basin restriction: implications for the marine environment and climate

The extreme positive $\delta^{13}C$ anomaly from the middle Bambuí Group if associated to methanogenic environments would imply carbon isotope non-equilibrium between the marine DIC and the atmospheric CO_2 in a closed basin, resulting ultimately from the Gondwana assembly. Increased fluxes of methanogenic-derived CO_2 to the water column and methane escape to the atmosphere are combined requirements to maintain a ^{13}C-enriched DIC. Consequently, this has implications for metazoan colonization and regional climate in the West Gondwana interior during the late Ediacaran-Cambrian transition. The scenario of predominantly anoxic, sulfate-depleted, presence of free H_2S, methane-rich, and hypersaline conditions would imply in extreme environments for animal colonization (e.g. Bell, 2012;

Hippert et al., 2019). The large surface covered by the Bambuí basin (>350.000 km^2) would also represent a significant amount of methane emission to the atmosphere.

Links between the metazoan evolution and colonization and well-oxygenated environments have been extensively debated. The geochemical record of late Ediacaran successions bearing macroscopic metazoan assemblages is contradictory and points to well-oxygenated (e.g. Tostevin et al., 2016) or to predominantly anoxic conditions (e.g. Johnston et al., 2013), with the relationship between oxygenation and animal colonization remaining unsettled (Butterfield, 2009). The paleoenvironmental changes reported here for the middle Bambuí Group seem to have prevented widespread colonization of the basin, considering the lack of macrofossils at this stage so far, and are beyond the oxygen availability discussion. More favorable conditions would have been developed in other areas where coeval basins connected to the global ocean present a rich fossil record (Corumbá Group, Southern Paraguay Belt, and Arroyo del Soldado Group, Uruguay; e.g. Gaucher et al., 2003; Nama Group; Namibia; e.g. Tostevin et al., 2016). Besides oxygen depletion, the combination of other factors that characterize extreme environments, such as the presence of toxic free-H_2S in bottom waters as a result of a possible sulfate-distillation event driven by microbial sulfate reduction, could have precluded animal colonization in the Bambuí basin during the Ediacaran-Cambrian transition (e.g. Hippertt et al., 2019). Furthermore, the large methanogenic emissions from the Bambuí basin would result in high inputs of methane to the atmosphere. If similar environments existed in West Gondwana, it would imply in huge methane inputs to the atmosphere with potential impact over the global climate dynamics in the beginning of the Phanerozoic Eon.

4.7. Conclusions

The paired $\delta^{13}C$ evolution for the basal Bambuí Group illustrates the particular marine carbon cycling within epicontinental settings in terminal Neoproterozoic/early Paleozoic. At the base, a cap carbonate interval shows mirrored $\delta^{13}C_{carb}$ and $\delta^{13}C_{org}$ excursions, resulting in great variation in $\Delta^{13}C$, also recorded in other Ediacaran cap carbonates and Ediacaran-Cambrian successions. Upwards, the positive $\delta^{13}C$ excursion of the middle Bambuí Group presents a coupled and basin-wide behavior, from shallower to deeper paleodepositional systems, attesting to the change in DIC isotope composition linked to the progressive foreland-related restriction of the basin at the late Ediacaran-Cambrian transition. Our results show that the classical interpretation of enhanced organic carbon burial, as well as other

forcing controls (changes in $\delta^{13}C_{input}$ and fraction of authigenic carbonate buried), are unlikely to explain the extremely heavy carbon isotope compositions in a local marine carbon cycling. An intrabasinal and long-lived control may have caused significant disturbances in the marine carbon cycle in response to the West Gondwana assembly. We propose a scenario with a progressively methanogenic-dominated basin developed after a sulfate distillation event in an isolated marine setting, barred from sulfate recharge from the marginal seas. In this scenario, the extremely positive $\delta^{13}C_{DIC}$ values of Bambuí basin instead of being of global significance, would represent a regional disequilibria between atmospheric CO_2 and the DIC reservoir in a large restricted basin in the very core of West Gondwana landmass. Anoxic and sulfate depleted conditions hampered methane oxidation and, together with possibly hypersalinity and dominant shallow chemocline, allowed methane to escape to the atmosphere. This would result in ^{13}C-enriched DIC derived from methanogenic CO_2, with carbonates and primary organic matter equally enriched in ^{13}C.

Paleogeographic isolation and local paleoenvironmental conditions (anoxic, sulfate-depleted, presence of free-H_2S, methane rich, hypersaline) may have created extreme conditions and an ultimate challenge to metazoan migration and colonization of marine settings in the supercontinent interior. If reproducible in other coeval epicontinental basins, the proposed methanogenic scenario although resulting from local mechanisms, could affect the global carbon cycle and the climate system globally through an increased flux of methane to the atmosphere. Importantly, our proposed scenario is testable through different approaches, including investigations of the sulfur and iron cycles, the weathering regime, and the paleontological record of the Bambuí basin, especially throughout the whole MIBE interval, as well as in equivalent intracratonic basins within the West Gondwana. Further studies concerning these areas are required to improve the understanding of such extreme positive $\delta^{13}C$ excursions in the geological record.

4.8. Acknowledgements

This study was funded by the São Paulo Research Foundation (FAPESP) thematic project grant #2016/06114-6 and Brazilian Research Council project grant #400764/2016-4. We acknowledge to Lhoist and Petra Energia S.A. for providing drill core samples, and to Pôle de Spectométrie Océan staff, University of Western Brittany, for the technical support in data acquisition. Sergio Caetano Filho holds a FAPESP scholarship grant #2016/11496-5. Gustavo Paula-Santos holds a FAPESP post-doc grant #2017/00399-1. Marly Babinski,

Ricardo Trindade and Matheus Kuchenbecker are fellows of the Brazilian Research Council (#307563/2013-8, #206997/2014-0 and #309106/2017-6, respectively). This study contributes to the IdEx Université de Paris ANR-18-IDEX-0001 and to the LabexMER ANR-10-LABX-19. IPGP contribution N° 4103. Finally, we thank to Prof. Dr. Linda Kah and Prof. Dr. Gabriel Uhlein for their helpful and constructive reviews which improved this manuscript, and to the Prof. Dr. Richard Damian Nance for the careful editorial handling.

4.9. References

Ader, M., Javoy, M., 1998. Diagenese précoce en milieu sulfuré réducteur: une étude isotopique dans le Jurassique basal du Bassin parisien. Comptes Rendus de l'Académie des Sciences, Paris, Sciences de la Terre et des Planètes 327, 803-809.

Ader, M., Macouin, M., Trindade, R.I.F., Hadrien, M.H., Yang, Z., Sun, Z., Besse, J., 2009. A multi layered water column in the Ediacaran Yangtze platform? Insights from carbonate and organic matter paired $\delta^{13}C$. Earth and Planetary Science Letters 288, 213–227.

Alkmim, F.F., Marshak, S., Pedrosa-Soares, A.C., Peres, G.G., Cruz, S.C., Whittington, A., 2006. Kinematic evolution of the Araçuaí–West Congo orogen in Brazil and Africa: nutcracker tectonics during the Neoproterozoic assembly of Gondwana. Precambrian Research 149, 43–63.

Amthor, J.E., Grotzinger, J.P., Schröder, S., Bowring, S.A., Ramezani, J., Martin, M.W., Matter, A., 2003. Extinction of *Cloudina* and *Namacalathus* at the Precambrian-Cambrian boundary in Oman. Geology, 31, 431–434.

Assayag, N., Jezequel, D., Ader, M., Michard, G., Viollier, E., Prevot, F., Agrinier, P., 2008. Hydrological budget, carbon sources and biogeochemical processes in Lac Pavin (France): Constraints from $\delta^{18}O$ and $\delta^{13}C$ of dissolved inorganic carbon. Applied Geochemistry 23(10), 2800−2816.

Babinski, M., Vieira, L.C., Trindade, R.I.F., 2007. Direct dating of the Sete Lagoas cap carbonate (Bambuí Group, Brazil) and implications for the Neoproterozoic glacial events. Terra Nova 19, 401–406.

Bartley, J.K., Kah, L.C., 2004. Marine carbon reservoir, C_{org}-C_{carb} coupling, and the evolution of the Proterozoic carbon cycle. Geology 32(2), 129–132.

Bell, E., 2012. Life at Extremes: Environments, Organisms and Strategies for Survival. CABI, Wallingford, 576 pp.

Benson, L., White, L.D., Rye, R., 1996. Carbonate deposition, Pyramid Lake Subbasin, Nevada: 4. Comparison of the stable isotope values of carbonate deposits (tufas) and the Lahontan lake-level record. Palaeogeography, Palaeoclimatology, Palaeoecology 122, 45–76.

Birgel, D., Meister, P., Lundberg, R., Horath, T.D., Bontognali, T.R.R., Bahniuk, A.M., Rezende, C.E., Vasconcelos, C., McKenzie, J.A., 2015. Methanogenesis produces strong 13C enrichment in stromatolites of Lagoa Salgada, Brazil: a modern analogue for Paleo-/Neoproterozoic stromatolites? Geobiology 13, 245–266.

Boggiani, P.C., Gaucher, C., Sial, A.N., Babinski, M., Simon, C.M., Riccomini, C., Ferreira, V.P., Fairchild, T.R., 2010. Chemostratigraphy of the Tamengo Formation (Corumbá Group, Brazil): a contribution to the calibration of the Ediacaran carbon-isotope curve. Precambrian Research 182, 382–401.

Bottrell, S.H., Newton, R.J., 2006. Reconstruction of changes in global sulfur cycling from marine sulfate isotopes. Earth-Science Reviews 75, 59– 83.

Butterfield, N.J., 2009. Oxygen, animals and oceanic ventilation: an alternative view. Geobiology 7, 1–7.

Caetano-Filho, S., Paula-Santos, G.M., Guacaneme, C., Babinski, M., Bedoya-Rueda, C., Peloso, M., Amorim, K., Afonso, J., Kuchenbecker, M., Reis, H.L.S., Trindade, R.I.F., 2019. Sequence stratigraphy and chemostratigraphy of an Ediacaran-Cambrian foreland-related carbonate ramp (Bambuí Group, Brazil). Precambrian Research 331, 105365.

Caxito, F.A., Frei, R., Uhlein, G.J., Dias, T.G., Árting, T.B., Uhlein, A, 2018. Multiproxy geochemical and isotope stratigraphy records of a Neoproterozoic Oxygenation Event in the Ediacaran Sete Lagoas cap carbonate, Bambuí Group, Brazil. Chemical Geology 481, 119–132.

Ciais, P., Sabine, C., Bala, G., Bopp, L., Brovkin, V., Canadell, J., Chhabra, A., DeFries, R., Galloway, J., Heimann, M., Jones, C., Le Quéré, C., Myneni, R.B., Piao, S., Thornton, P., 2013. Carbon and Other Biogeochemical Cycles. In: Stocker, T.F., Qin, D., Plattner, G.-K., Tignor, M., Allen, S.K., Boschung, J., Nauels, A., Xia, Y., Bex, V., Midgley, P.M. (eds.). Climate Change 2013: The Physical Science Basis. Contribution of Working Group I to the Fifth Assessment Report of the Intergovernmental Panel on Climate Change. Cambridge University Press, Cambridge, United Kingdom and New York, NY, USA. 106 pp.

Crockford, P.W., Wing, B.A., Paytan, Hodgskiss, M.S.W., Mayfield, K.K., Hayles, J.A., Middleton, J.E., Ahm, A.S.C., Johnston, D.T., Caxito, F., Uhlein, G.J., Halverson, G.P.,

Eickmann, B., Torres, M., Horner, T.J., 2019. Barium-isotopic constraints on the origin of post-Marinoan barites. Earth and Planetary Science Letters 519, 234–244.

Cui, H., Kaufman, A.J., Peng, Y., Liu, X.M., Plummer, R.E., Lee, E.I., 2018. The Neoproterozoic Hüttenberg $\delta^{13}C$ anomaly: Genesis and global implications. Precambrian Research 313, 242–262.

Derry, L.A., 2010. A burial diagenesis origin for the Ediacaran Shuram–Wonoka carbon isotope anomaly. Earth and Planetary Science Letters 294 (1–2), 152–162.

Fanton, K.C., Holmden, C., 2007. Sea-level forcing of carbon isotope excursions in epeiric seas: Implications for chemostratigraphy. Canadian Journal of Earth Sciences 44, 807–818.

Fike, D.A., Grotzinger, J.P., 2008.A paired sulfate-pyrite $\delta^{34}S$ approach to understanding the evolution of the Ediacaran–Cambrian sulfur cycle. Geochimica et Cosmochimica Acta 72, 2636–2648.

Galimov, E.M., 2004. The pattern of δ13Corg versus HI/OI relation in recent sediments as an indicator of geochemical regime in marine basins: comparison of the Black Sea, Kara Sea, and Cariaco Trench. Chemical Geology 204, 287–301.

Gaucher, C., Boggiani, P.C., Sprechmann, P., Sial, A.N., Fairchild, T.R., 2003. Integrated correlation of the Vendian to Cambrian Arroyo del Soldado and Corumbá groups (Uruguay and Brazil): Palaeogeographic, palaeoclimatic and palaeobiologic implications. Precambrian Research 120, 241–278.

Geyman, E.C., Maloof, A.C., 2019. A diurnal carbon engine explains ^{13}C-enriched carbonates without increasing the global production of oxygen. Proceedings of the National Academy of Sciences 116(49), 24433–24439.

Grotzinger, J.P., Waters, W.A., Knoll, A.H., 2000. Calcified metazoans in thrombolite stromatolite reefs of the terminal Proterozoic Nama Group, Namibia. Paleobiology 26 (3), 334–359.

Gu, B., Schelske, C.L., Hodell, D.A., 2004. Extreme 13C enrichments in a shallow hypereutrophic lake: implications for carbon cycling. Limnology and Oceanography 49, 1152–1159.

Halverson, G., Hoffman, P., Schrag, D., Maloof, A., Rice, A., 2005. Towards a Neoproterozoic composite carbon isotope record. Geological Society of America Bulletin 117, 1181–1207.

Halverson, G.P., Hurtgen, M.T., Porter, S.M., Collins, A.S., 2009. Chapter 10 Neoproterozoic-Cambrian Biogeochemical Evolution, Developments in Precambrian Geology. Elsevier. https://doi.org/10.1016/S0166-2635(09)01625-9

Halverson, G.P., Wade, B.P., Hurtgen, M.T., Barovich, K.M., 2010. Neoproterozoic chemostratigraphy. Precambrian Research 182 (4), 337–350.

Hayes, J.M., Strauss, H., Kaufman, A.J., 1999. The abundance of 13C in marine organic matter and isotopic fractionation in the global biogeochemical cycle of carbon during the past 800 Ma. Chemical Geology 161, 103–125.

Heilbron, M., Cordani, U.G., Alkmim, F.F. São Francisco Craton, Eastern Brazil: Tectonic Genealogy of a Miniature Continent. Springer, Switzerland, 2017. 331p.

Hippertt, J.P. Caxito, F.A. Uhlein, G.J. Nalini, H.A. Sial, A.N. Abreu, A.T., Nogueira, L.B., 2019. The fate of a Neoproterozoic intracratonic marine basin: Trace elements, TOC and IRON speciation geochemistry of the Bambuí Basin, Brazil. Precambrian Research, 330, 101–120.

Iyer, S.S., Babinski, M., Krouse, H.L., Chemale, F., 1995. Highly ^{13}C enriched carbonate and organic matter in the Neoproterozoic sediments of the Bambuí Group, Brazil. Precambrian Research 73, 271–282.

Jacobsen, S.B., Kaufman, A.J., 1999. The Sr, C and O isotopic evolution of Neoproterozoic seawater. Chemical Geology 161, 37–57.

Jiang, G.Q., Wang, X.Q., Shi, X.Y., Zhang, S.H., Xiao, S.H., Dong, J., 2010. Organic carbon isotope constraints on the dissolved organic carbon (DOC) reservoir at the Cryogenian-Ediacaran transition. Earth and Planetary Science Letters 299, 159–168.

Jiang, G., Wang, X., Shi, X., Xiao, S., Zhang, S., Dong, J., 2012. The origin of decoupled carbonate and organic carbon isotope signatures in the early Cambrian (ca. 542–520 Ma) Yangtze platform. Earth and Planetary Science Letters 317-318, 96–110.

Johnston, D.T., Poulton, S.W., Tosca, N.J., O'Brien, T., Halverson, G.P.,Schrag, D.P., Macdonald, F.A., 2013. Searching for an oxygenation event in the fossiliferous Ediacaran of northwestern Canada. Chemical Geology 362, 273–286.

Knauth, L.P., Kennedy, M.J., 2009. The late Precambrian greening of the Earth. Nature 460, 728–732.

Kuchenbecker, M., Babinski, M., Pedrosa-Soares, A.C., Lopes-Silva, L., Pimenta, F., 2016. Chemostratigraphy of the lower Bambuí Group, southwestern São Francisco Craton, Brazil: insights on Gondwana paleoenvironments. Brazilian Journal of Geology 46(1), 145–162.

Lehmann, M.F., Bernasconi, S.M., Barbieri, A., Mckenzie, J.A., 2002. Preservation of organic matter and alteration of its carbon and nitrogen isotope composition during

simulated and in situ early sedimentary diagenesis. Geochimica et Cosmochimica Acta 66, 3573–3584.

Macko, S.A., Engel, M.H., Qian, Y., 1994. Early diagenesis and organic matter preservation -- a molecular stable carbon isotope perspective. Chemical Geology 114, 365–379.

McKirdy, D.M., Powell, T.G., 1974. Metamorphic Alteration of Carbon Isotopic Composition in Ancient Sedimentary Organic Matter: New Evidence from Australia and South Africa. Geology 2, 591–595.

Och, L.M., Shields-Zhou, G.A., 2012. The Neoproterozoic oxygenation event: environmental perturbations and biogeochemical cycling. Earth-Sciences Reviews 110, 26–57.

Okubo, J., Muscente, A.D., Luvizotto, G.L., Uhlein, G.J., Warren, L.V., 2018. Phosphogenesis, aragonite fan formation and seafloor environments following the Marinoan glaciation. Precambrian Research 311, 24–36.

Pasquier, V., Sansjofre, P., Lebeau, O., Liorzou, C., Rabineau, M., 2018. Acid digestion on river influenced shelf sediment organic matter: Carbon and Nitrogen contents and isotopic ratios. Rapid Communications in Mass Spectrometry 32, 86–92.

Paula-Santos, G.M., Babinski, M., Kuchenbecker, M., Caetano-Filho, S., Trindade, R.I.F., Pedrosa-Soares, A.C., 2015. New evidence of an Ediacaran age for the Bambuí Group in southern São Francisco craton (eastern Brazil) from zircon U-Pb data and isotope chemostratigraphy. Gondwana Research 28, 702–720.

Paula-Santos, G.M., Caetano-Filho, S., Babinski, B., Enzweiler, J., 2018. Rare earth elements of carbonate rocks from the Bambuí Group, southern São Francisco Basin, Brazil, and their significance as paleoenvironmental proxies. Precambrian Research 305, 327−340.

Paula-Santos, G.M., Caetano-Filho, S., Babinski, M., Trindade, R.I.F, Guacaneme, C., 2017. Tracking connection and restriction of West Gondwana São Francisco Basin through isotope chemostratigraphy. Gondwana Research 42, 280−305.

Paula-Santos, G., Caetano-Filho, S., Enzweiler, J., Navarro, M., Babinski, M., Guacaneme, C., Kuchenbecker, M., Reis, H., Trindade, R.I.F., 2020. Rare earth elements in the terminal Ediacaran Bambuí Group carbonate rocks (Brazil): evidence for high seawater alkalinity during rise of early animals. Precambrian Research 336, 105506.

Reis, H.L.S., Alkmim, F.F., Fonseca, R.C.S., Nascimento, T.C., Suss, J.F., Prevatti, L.D., 2016. The São Francisco Basin. In: Heilbron, M., Cordani, U.G., Alkmim, F.F. (Eds.), São Francisco Craton, Eastern Brazil, Regional Geology Reviews. Springer, Switzerland, pp. 117–143.

Reis, H.L.S., Suss, J.F., 2016. Mixed carbonate-siliciclastic sedimentation in forebulge grabens: an example from the Ediacaran Bambuí Group, São Francisco Basin, Brazil. Sedimentary Geology 339, 83–103.

Reis, H.L.S., Suss, J.F., Fonseca, R.C.S., Alkmim, F.F., 2017. Ediacaran forebulge grabens of the southern São Francisco basin, SE Brazil: Craton interior dynamics during West Gondwana assembly. Precambrian Research 302, 150–170.

Rothman, D.H., Hayes, J.M., Summons, R.E., 2003. Dynamics of the Neoproterozoic carbon cycle. Proceedings of the National Academy of Sciences of the United States of America 100 (14), 8124–8129.

Sansjofre, P., Ader, M., Trindade, R.I.F., Elie, M., Lyons, J., Cartigny, P., Nogueira, A.C.R., 2011. A carbon isotope challenge to the snowball Earth. Nature 478, 93–96.

Santos, R.V., Alvarenga, C.J.S., Babinski, M., Ramos, M.L.S., Cukrov, N., Fonseca, M.A., Sial, A.N., Dardenne, M.A., Noce, C.M., 2004. Carbon isotopes of Mesoproterozoic-Neoproterozoic sequences from southern São Francisco craton and Araçuaí Belt, Brazil: Paleogeographic implications. Journal of South America Earth Sciences 18, 27–39.

Schrag, D.P., Higgins, J.A., Macdonald, F.A., Johnston, D.T., 2013. Authigenic carbonate and the history of the global carbon cycle : Why diagenesis matters even more . Sci. Adv. 339, 2223.

Simoneit, B.R.T., Peters, K.E., Rohrback, B.G., Brenner, S., Kaplan, I.R., 2004. Thermal alteration of Cretaceous black shale from the Eastern Atlantic. III: Laboratory simulations. In: Hill, R.J., Leventhal, J., Aizenshtat, Z., Baedecker, M.J., Claypool, G., Eganhouse, R., Goldhaber, M., Peters, K. (Eds). Geochemical Investigations in Earth and Space Science: A Tribute to Isaac R. Kaplan. The Geochemical Society No. 9, 321-340.

Swart, P.K., 2008. Global synchronous changes in the carbon isotopic composition of carbonate sediments unrelated to changes in the global carbon cycle. Proceedings of the National Academy of Sciences 105(37), 13741–13745.

Tohver, E., D'Agrella Filho, M.S., Trindade, R.I.F., 2006. Paleomagnetic record of Africa and South America for the 1200-500 Ma interval, and evaluation of Rodinia and Gondwana assemblies. Precambrian Research 147, 193−222.

Tostevin R., Wood, R.A., Shields, G.A., Poulton, S.W., Guilbaud, R., Bowyer, F., Penny, A.M., He, T., Curtis, A., Hoffmann, K.H., Clarkson, M.O., 2016. Low-oxygen waters limited habitable space for early animals. Nature Communications 7, 1−9.

Uhlein, G.J., Uhlein, A., Pereira, E., Caxito, F.A., Okubo, J., Warren, L.V., Sial, A.N., 2019. Ediacaran paleoenvironmental changes recorded in the mixed carbonate-siliciclastic Bambuí Basin, Brazil. Palaeogeography, Palaeoclimatology, Palaeoecology 517, 39–51.

Vieira, L.C., Trindade, R.I.F, Nogueira, A.C.R., Ader, M. 2007. Identification of a Sturtian cap carbonate in the Neoproterozoic Sete Lagoas carbonate plataform, Bambuí Group, Brazil. Comptes Rendus Geoscience 339, 240−258.

Warren, L.V., Quaglio, F., Riccomini, C., Simões, M.G., Poiré, D.G., Strikis, N.M., Anelli, L.E., Strikis, P.C., 2014. The puzzle assembled: Ediacaran guide fossil Cloudina reveals an old proto-Gondwana seaway. Geology 42(5), 391−394.

Whiticar, M.J., Faber, E., Schoell, M., 1986. Biogenic methane formation in marine and freshwater environments: CO2 reduction versus acetate fermentation? Isotope evidence. Geochimica et Cosmochimica Acta 50, 693–709.

Yamaguchi, K.E., Oguri, K., Ogawa, N.O., Sakai, S., Hirano, S., Kitazato, H., Ohkouchi, N., 2010. Geochemistry of modern carbonaceous sediments overlain by a water mass showing photic zone anoxia in the saline meromictic Lake Kai-ike, southwest Japan: I. Early diagenesis of organic carbon, nitrogen, and phosphorus. Palaeogeography, Palaeoclimatology, Palaeoecology 294, 72–82.

Zhou, C., Xiao, S., 2007. Ediacaran $\delta^{13}C$ chemostratigraphy of South China. Chemical Geology 237, 89–108.

5. PAIRED CARBON ISOTOPE AND EARLY DIAGENESIS SIGNATURES SUGGEST COMPLEX OXYGENATION IN LATE EDIACARAN BENTHIC MARINE ENVIRONMENTS

Sergio Caetano-Filho, Gustavo M. Paula-Santos, Pierre Sansjofre, Magali Ader, Juan C. Gómez-Gutierrez, Laura C.M. Rivero; Kamilla B. Amorim, Jhon W.L. Afonso, Marly Babinski, Juliana M. Leme, Guilherme R. Romero, Paulo C. Boggiani, Ricardo I.F. Trindade

5.1. Abstract

Despite discussion concerning the relationship between bottom water oxygenation and early metazoan evolution during the Ediacaran, biomineralization of skeletal parts is believed to require sufficient amounts of oxygen in benthic environments. Bottom water oxygenation was apparently complex and could occurr within specific environments even in predominantly anoxic continental platforms during the late Ediacaran-early Cambrian. To better address the distribution and possible causes for these occurrences, spatially-distributed investigations of geochemical proxies are required. We present paired carbon isotope analyses from three sections representing proximal to distal parts of a late Ediacaran carbonate ramp – the Tamengo Formation, central-west Brazil. Unusual behavior of $\delta^{13}C$ curves occurs in the distal-mid ramp domain, deviating from stable $\delta^{13}C_{carb}$ and $\Delta^{13}C$ values from both inner and outer ramp. Substantial $\delta^{13}C_{carb}$-$\delta^{13}C_{org}$ excursions (up to 5 and 7‰ in magnitude, respectively) match parasequence cyclicity, suggesting local disturbances in DIC within distal mid ramp environments. These cycles also also contain both accumulations of the skeletal *Cloudina* fossil and early Fe-oxyhydroxide cements. We propose that an enhanced oxic organic carbon mineralization, probably associated with the more oxygenated environments inhabited by these metazoans, resulted in a heterogeneous DIC reservoir between surface and bottom layers. A similar paleoredox reconstruction has been proposed for coeval deposits from the Nama Group, in which ecological complexity shows a direct relationship with more oxygenated environments in the mid ramp. This supports a probable complex oxygenation of late Ediacaran platforms, which is independent of paleobathymetry. We thus envisage two scenarios: i) optimum balance between bioproductivity *vs* respiration in mid ramp, preventing eutrophication and allowing benthic oxygenation, and ii) an ecological relationship between *Cloudina* and cyanobacteria communities, in which these animals harvested oxygen from a benthic source, resulting in a dependence on favorable sedimentary environments for the

development of oxygen-producing microbial mats, such as low energy and benthic sunlight incidence.

5.2. Introduction

The Ediacaran Period records a striking coincidence between the first complex metazoans assemblages and geochemical signatures for ocean oxidation events in the long-term scale (e.g. Fike et al., 2006; Narbonne et al., 2012). This fuels an extrinsic hypothesis in which oceanic oxygenation could have had great impact over life evolution (e.g. Fike et al., 2006; Canfield et al., 2007; Och and Shields-Zhou, 2012), despite other discussions concerning intrinsic ecological forces or the possible low-oxygen requirement of early complex animals, which also attracted attention in the past years (e.g. Mills et al., 2014; Butterfield, 2009). However, after the appearance of first metazoan biota, biological innovations such as skeletal biomineralization during late Ediacaran would have resulted from competition and predation in more complex ecological nets (Bengtson and Zhao, 1992; Cai et al., 2014) and would require sufficient levels of oxygen to keep such metabolisms (Rhoads and Morse, 1971; Wood et al., 2015).

Despite geochemical indications for marine oxygenation in Ediacaran successions, anoxic conditions were probably dominant in the continental platforms from Ediacaran-early Cambrian, wherein bottom oxygenation may have represented only pulsed events (e.g. Goldberg et al., 2007; Canfield et al., 2008; Sahoo et al., 2016). To explore the distribution of such environments, studies have been developed in high stratigraphic and spatial resolution to test the relationship between benthic oxygenation and metazoan colonization. Some of these studies provided solid spatial-stratigraphic association between permanently well-oxygenated to intermittently oxygenated conditions with colonization of early skeletal metazoans. For example, elemental geochemical redox proxies from the Nama Group (Fe speciation, REE data; Wood et al., 2015; Tostevin et al., 2016) suggest a direct relationship between oxygen availability and biodiversity and ecological complexity, similar to that observed in modern marine environments (Diaz and Rosemberg, 1995). Additionally, Wood et al. (2015) also demonstrated that such oxygenation of bottom environments in late Ediacaran was not controlled by simple paleobathymetric variation, being distributed in specific environments of the carbonate ramp and even during specific stages of an eustatic cycle.

Within the carbon isotope record, most studies focus on the well-known long-term and global scale anomalies, usually associated with possible major oxidation events (The early

Ediacaran Maieberg and the mid to late Ediacaran Shuram/Wonoka $\delta^{13}C_{carb}$ anomalies; e.g. Halverson and Shields-Zhou, 2011 and references therein).These studies, however, do not provide the resolution needed to investigate relationships between metazoan habitable spaces and local process within the continental platforms. The present study therefore focuses on the high-resolution investigation of paired carbon isotope evolution ($\delta^{13}C_{carb}$ and $\delta^{13}C_{org}$) along a basin transect of the late Ediacaran Tamengo mixed ramp. Three sections, representing inner, mid, and outer ramp domains, were analyzed. Occurrences of the first skeletal carbonate-biomineralizing metazoan from *Cloudina* genus occur together with *Corumbella werneri* fossils preserved within silty-shale facies. Reconstruction of local marine carbon cycling and its relationship with distribution of early skeletal animals along Ediacaran carbonate platforms allows for a better comprehension of the biogeochemical dynamic and the complex redox architecture of these habitable marine benthic environments.

5.3. Geological Setting

5.3.1. The Neoproterozoic Southern Paraguay Belt, Corumbá Group and Tamengo Formation

The Paraguay Belt is an arc-shaped Brasiliano-Panafrican fold and thrust belt located in central-west Brazil which was developed during the terminal Neoproterozoic Gondwana assembly (Fig. 5.1; Almeida, 1984; Alvarenga and Trompette, 1993; Boggiani and Alvarenga, 2004). It is divided into two domains: i) the Northern Paraguay Belt, in a NE-SW trend, limited by the Neoproterozoic Amazonian Craton and the superimposed Paleozoic Parecis Basin at northwest, and by the Paleozoic Paraná Basin at southeast; and ii) the Southern Paraguay Belt, in a N-S trend, limited by Rio Apa Block at west and by the Paleozoic deposits from the Paraná Basin at east. Quaternary fluvial sediments from the Pantanal Basin cover the area between these two domains (Fig. 5.1).

The tectono-sedimentary evolution of the Southern Paraguay Belt starts with deposition of the Jacadigo Group (Fig. 5.2A), representing early to late rift stage along NE-SW grabens (Freitas et al., 2011 and references therein). At the end of Cryogenian Era, the Puga Formation, represents Marinoan glacial deposits from low-latitudes based on investigations in the northern domain of Paraguay Belt (Nogueira et al., 2003; Trindade et al., 2003; Alvarenga et al., 2011). Overlying the Jacadigo Group and the Puga Formation, carbonate platforms from a post-rift stage dominate the sedimentary record of the Corumbá

Group, represented by the Bocaina and Tamengo formations (Gaucher et al., 2003; Boggiani et al., 2010; Freitas et al., 2011; Fig. 5.2A). Siliciclastic lithostratigraphic units of minor geographic expression, the Cadiueus and Cerradinho formations (Almeida, 1984; Boggiani, 1998), are associated with the base of Corumbá Group, still representing a rift stage before the onset of carbonate deposition (Boggiani et al., 2010). The Bocaina Formation encompasses shallow-water limestone and dolostone, as well as associated boundstone and phosphorite deposits (Boggiani, 1998; Freitas et al., 2011). This carbonate deposition represents a rimmed carbonate platform during the immediate to late post-rift stage. Regarding age constraints, Parry et al. (2017) recently provided an age of 550 ± 0.3 Ma for volcanic ashes interbedded within shallow water dolostones of the Bocaina Formation. Previously, paleontological occurrences of *Titanotheca coimbrae*, a precursor of agglutinated foraminifers, were described in phosphorites of the Bocaina Formation (Gaucher et al., 2003) and were assigned to the late Ediacaran based on the other occurrences within Gondwana areas (~570-550; e.g. Gaucher and Germs, 2009).

In the middle to the upper part of the Corumbá Group, the Tamengo Formation represents more complex carbonate distribution, that preserves a rich paleontological record related to the late Ediacaran (Walde et al., 1982; Zaine and Fairchild, 1985; Gaucher et al., 2003; Babcock et al., 2005; Pacheco et al., 2015; Adorno et al., 2017). A polymictic breccia occurs at the base of the unit, composed of clasts of granite-gneiss basement rocks and dolomite, chert, and phosphorite from Bocaina Formation, suggesting an erosional unconformity between these two carbonate units from Corumbá Group (Boggiani, 1998; Boggiani et al., 2010; Amorim et al., 2020). The Tamengo Formation presents a variety of carbonate facies from inner to outer ramp, including dark-colored oolitic grainstone, wackestone-mudstone couplets with TOC reaching up to 1% (Spangenberg et al., 2014), cycles of bioclastic grainstone, packstone, wackestone and mudstone with wavy-lamination and cross bedding (e.g. hummocky) intercalated with marlstones and siltstones-mudstones in a more distal storm-dominated environment (Boggiani et al., 2010; Amorim et al., 2020). The Tamengo Formation is conformably overlain by fine-grained siliciclastic strata of the Guaicurus Formation in the area of Corumbá city (Boggiani et al., 2004; Boggiani et al., 2010).

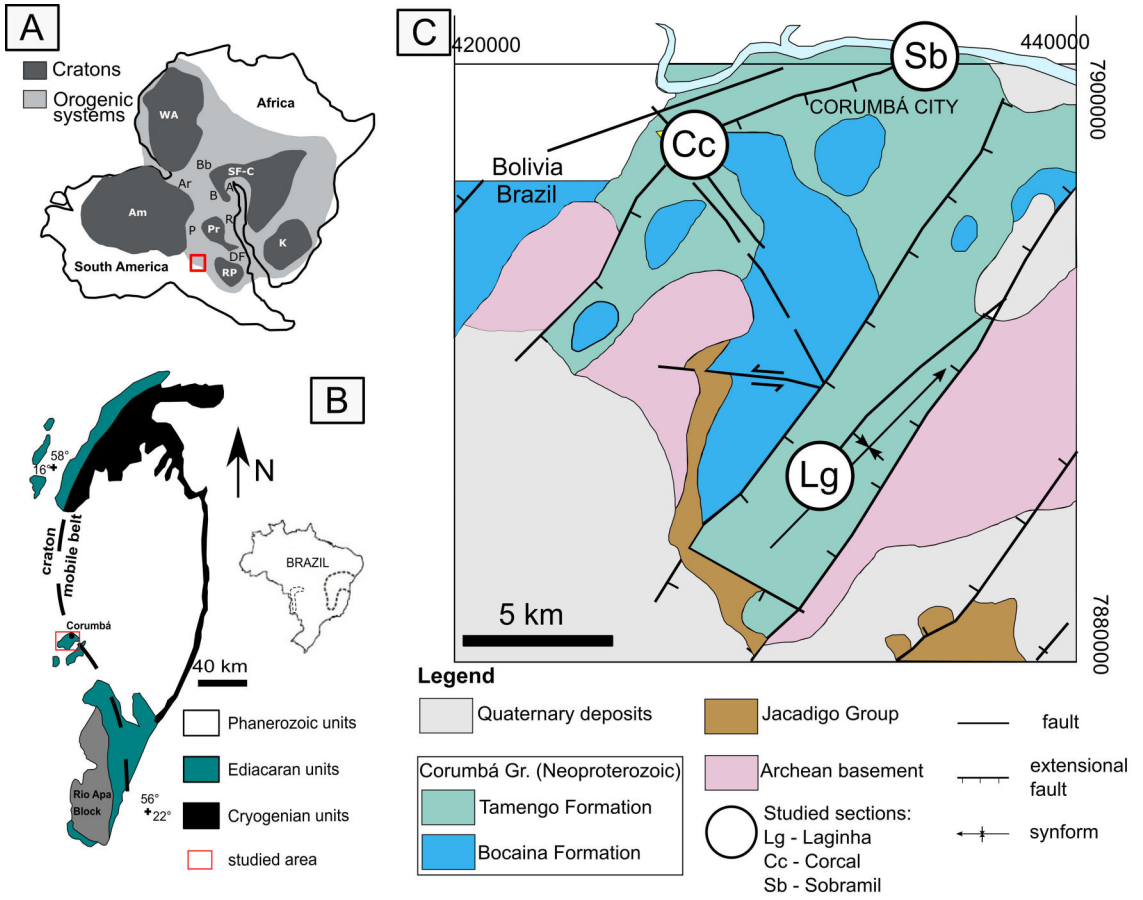

Figure 5.1: a) Paleogeographic reconstruction for the late Neoproterozoic West Gondwana. The red square marks the studied area (modified from Alkmim et al., 2006). b) Geological map of the Paraguay Belt, central-west Brazil. The red square marks the Corumbá city area (modified from Boggiani et al., 2010). c) Geological map of the Corumbá city area (modified from Mello and Godoi, 2001).

A rich fossil record is documented within the Tamengo Formation, and includes shell-beds containing the skeletal metazoan *Cloudina lucianoi* (Zaine and Fairchild, 1985; Gaucher et al., 2003; Adorno et al., 2017; Becker-Kerber et al., 2017), and the scyphozoan cnidarian *Corumbella werneri* that is well-preserved within silt-shale intercalations (Walde et al., 1982; Babcock et al., 2005; Pacheco et al., 2015). An acritarch assemblage dominated by *Bavlinella faveolata* as well as Vendotaenid algae also occur in the Tamengo and Guaicurus formations (Gaucher et al., 2003). U-Pb ID-TIMS ages of 542.37 ± 0.28 Ma and 541.85 ± 0.75 Ma (Parry et al., 2017) from zircon grains retrieved in volcanic ash beds in the upper Tamengo Formation supports deposition of Tamengo Formation during the late Ediacaran, similar to other *Cloudina* occurrences (549-541 Ma; Grotzinger et al., 2000; Amthor et al., 2003). A

$\delta^{13}C_{carb}$ chemostratigraphy was presented for the Tamengo Formation by Boggiani et al. (2010). The basal breccia interval starts with negative $\delta^{13}C_{carb}$ values, down to −3.5‰, with a recover to values between +5 and +6‰. The interval bearing *Cloudina* sp. and *Corumbella werneri* fossils are marked by a plateau between +3 and +5‰, with negative excursions down to +2‰. The pristine $^{87}Sr/^{86}Sr$ ratios vary between 0.7086 and 0.7088 within Tamengo Formation, which align with that proposed for the late Ediacaran Sr isotope stratigraphy (Babinski et al. 2008).

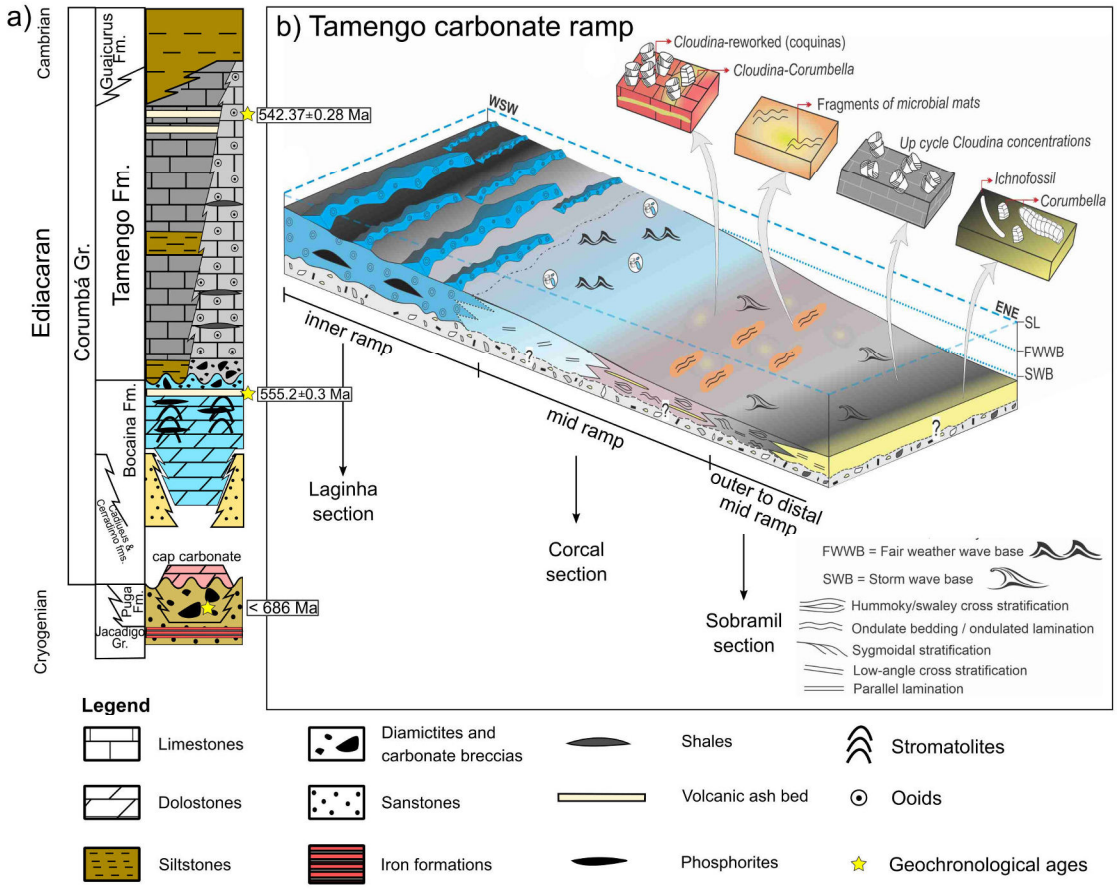

Figure 5.2: a) Stratigraphy of the Southern Paraguay Belt (after Boggiani et al., 2010 and Freitas et al., 2011). Geochronological ages for Puga Formation from McGee et al. (2018), U-Pb dating in zircon grains from volcanic ash beds from Parry et al. (2017). b) Paleoenvironmental reconstruction for the Tamengo Formation from Amorim et al. (2020), with the position of the studied sections along the mixed siliciclastic-carbonate ramp.

5.3.2. Studied sections

Here we investigate three sections distributed from proximal to distal environments of the Tamengo ramp. Sedimentologic and stratigraphic aspects of these sections were presented in detail by Amorim et al. (2020). We assume the depositional model presented by these authors (Fig. 5.2B), in which the Laginha section (Fig. 5.3) represents shallow environments of the inner ramp, as oolitic banks and interbank lagoons; the Corcal section (Fig. 5.4) encompasses intraclastic and bioclastic deposits from mid ramp, deposited between fair weather and storm wave base; and the Sobramil section (Fig. 5.5) comprises the most distal deposits from distal mid ramp to outer ramp, deposited below storm wave base.

The Laginha section (Fig. 5.3) is a ~140 m-thick carbonate succession dominated by oolitic limestone. At the base, a carbonate breccia (Fig. 5.6A) lies unconformably over the Bocaina Formation and bears clasts of basement rock, as well as carbonate rock and phosphorite from the underlying Bocaina Formation (Boggiani et al 2010). This carbonate breccia is overlain by dolomitized oolitic grainstone to packstone (Fig. 5.6B). Mid part of the section is dominated by interbedded wackestone and shaly calcimudstone (Fig. 5.6C) forming a meter-scale rhythmic succession that marks deposition within interbank lagoons. These deposits are erosionally overlain by oolitic grainstone, forming a sand shoal complex. At the top of the section, siltstone and mudstone of the Guaicurus Formation mark a major transgression over the carbonate ramp and the upper limit of the Tamengo Formation.

The Corcal section (Fig. 5.4) is a 52 m-thick succession composed of two shallowing-upward cycles. The basal cycle consists of higher ranked cycles composed of dark grey calcimudstone and silty-shale facies of the outer ramp that grade to intraclastic/bioclastic wackestone, packstone and grainstone of the mid ramp domain. These cycles bear remarkable accumulations of *Cloudina* shell beds (Fig. 5.6D and 5.6D), and silty-shale intercalations record well-preserved *Corumbella werneri* specimens (Fig. 5.6F). *Cloudina*-grainstone and packstone usually contain Fe-oxyhydroxide cements (Fig. 5.6F; e.g. Becker-Kerber et al., 2017). The upper cycle also contain higher-order cycles associated with a more proximal mid ramp domain, starting with a siltstone-calcimudstone interval that grades to intraclastic wackestone, packstone and grainstone. These cycles have more rare occurrences of bioclasts, but abundant microbial mats fragments compared with the basal cycle (Fig. 5.6H). Volcanic ash beds are frequent in the upper part of the section, with zircon grains that yielded U-Pb ID-TIMS ages of 542.37 ± 0.28 Ma and 541.85 ± 0.75 Ma (Parry et al., 2017; Fig. 5.4).

The Sobramil section (Fig. 5.5) is a 23 m-thick succession and comprises mixed deposits representing distal outer ramp environments. This section record three cycles containing higher order shallowing-upward cycles. These cycles contain calcimudstone at the base and intraclastic/bioclastic wackestone at the top. *Cloudina* bioclasts are less abundant compared to mid ramp deposits from the Corcal section. In the mid and upper part of the section, intercalated shale and siltstone mark minor oscillations in water depth during an overall transgressive event. These siltstone layers contain numerous occurrences of well-preserved *Corumbella werneri*.

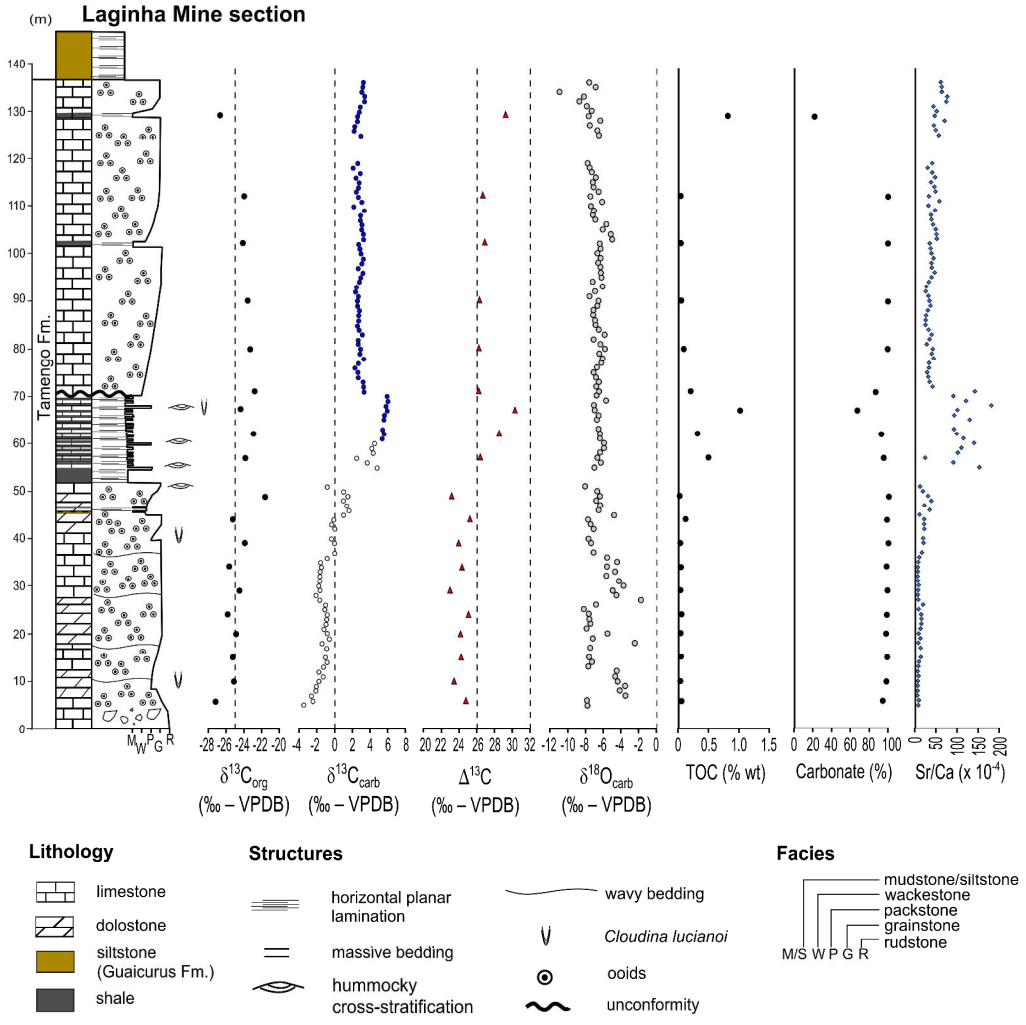

Figure 5.3: The Laginha section – facies, paired carbon isotope data, $\delta^{18}O_{carb}$, TOC and carbonate contents and Sr/Ca ratios.

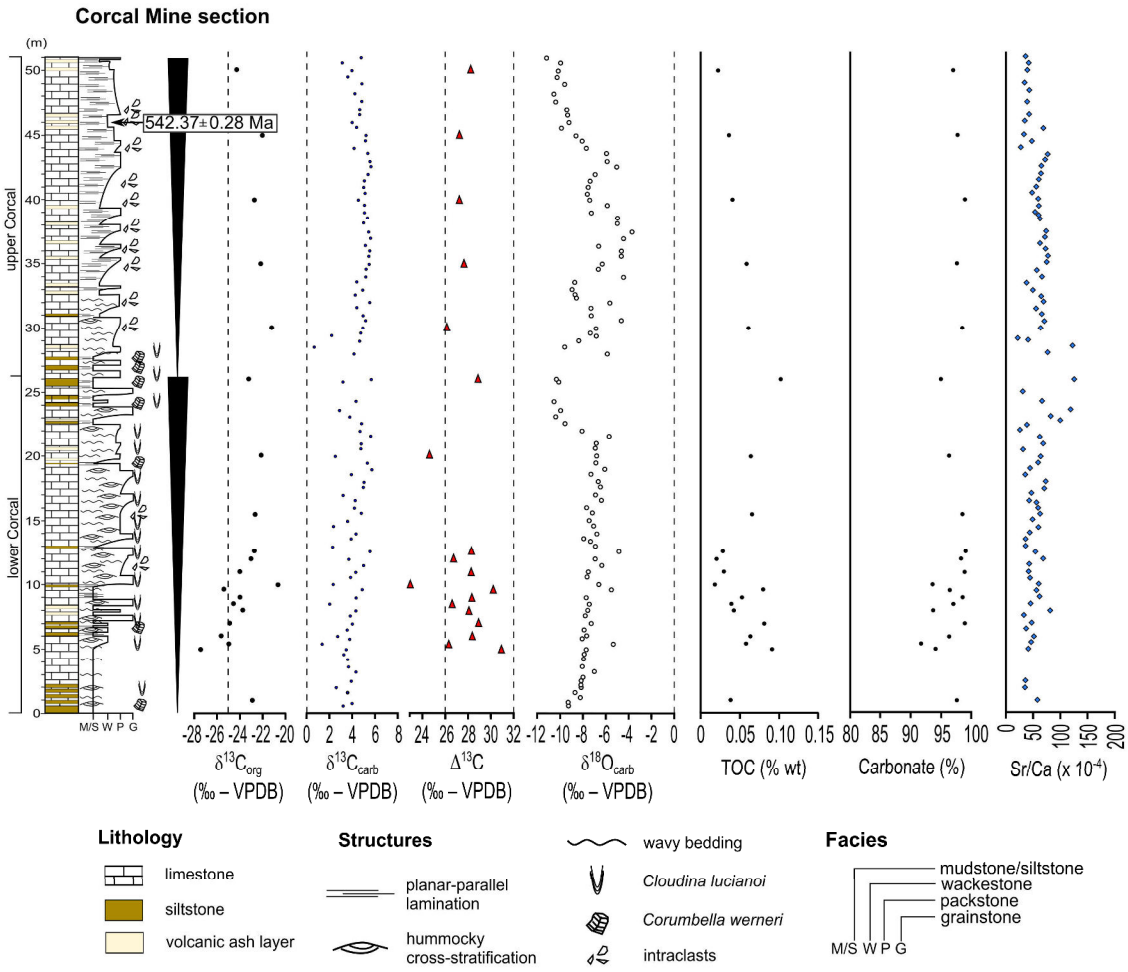

Figure 5.4: The Corcal section – facies, paired carbon isotope data, $\delta^{18}O_{carb}$, TOC and carbonate contents and Sr/Ca ratios. U-Pb age from zircon grains retrieved in volcanic ash beds from Parry et al. (2017).

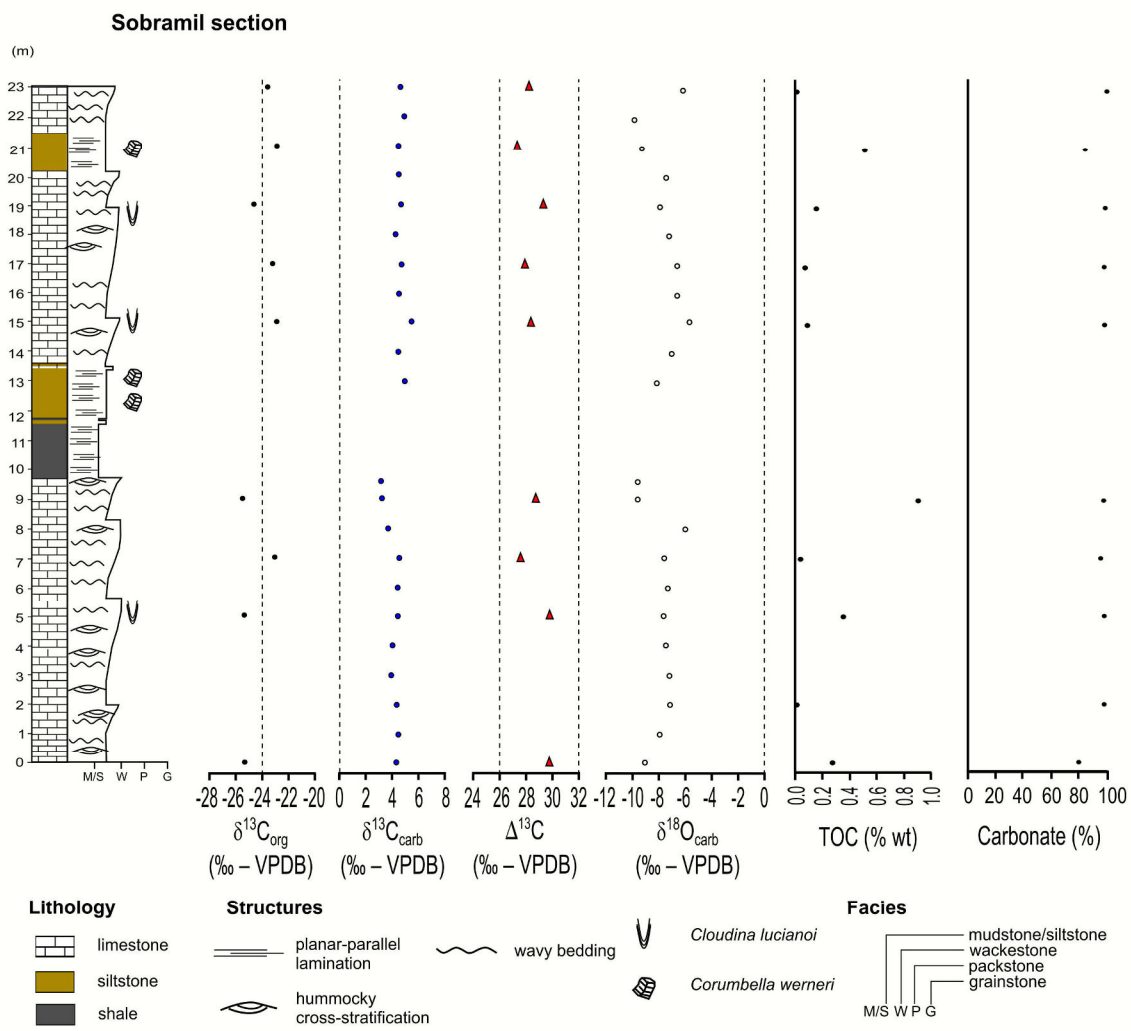

Figure 5.5: The Sobramil section – facies, paired carbon isotope data, $\delta^{18}O_{carb}$, TOC and carbonate contents.

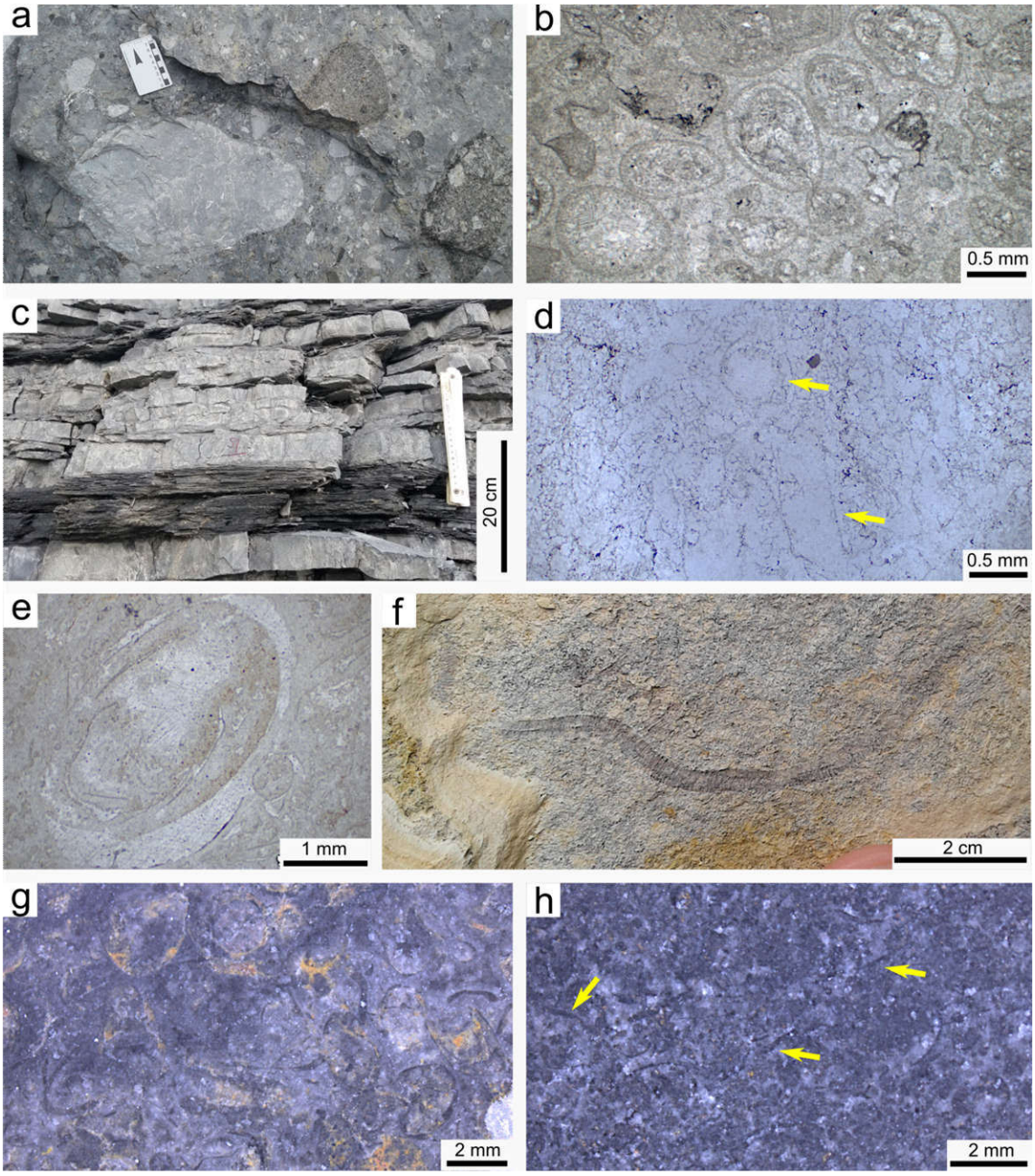

Figure 5.6: Sedimentary facies from the Tamengo Formation. a) Carbonate breccia from the base of unit at the Laginha section (scale has 5 cm). b) Photomicrography of dolomitized oolitic grainstone from the base of Laginha section. c) Interval of shale-limestone interbedding at the mid part of Laginha section. d) Photomicrography of bioclastic wackestone from the lower Corcal section. Arrows show perpendicular and transverse sections of *Cloudina* specimens. e) Photomicrography of bioclastic grainstone from the lower Corcal section, detail for perpendicular section of *Cloudina* shell, showing funnel-in-funnel structure. f) *Corumbella werneri* preserved within siltstone from the Sobramil section. g) Bioclastic-*Cloudina* grainstone from distal-mid ramp deposits of the lower Corcal section with widespread oxyhydroxide cementation (orange color). h) Intraclastic grainstone from proximal mid-ramp deposits of the upper Corcal section, arrows point to abundant microbial mat fragments.

5.4. Materials and Methods

5.4.1. Elemental geochemistry

Calcium and strontium content were analyzed for 210 samples of carbonate rocks through a portable XRF device Thermo Scientific Niton XL3t, provided by the Geological Survey of Brazil (CPRM). This technique was applied in polished slabs, aiming to analyze carbonate-rich layers of each sample, avoiding terrigenous laminations and a facies-related bias. A pure SiO_2 blank and the reference material QC 180-673 (Thermo, Germany) were run each 30 sample analyses. The blank material presented Sr content below the limit of detection for the device in all analyses, whereas the reference material presented an average standard error of ± 1 μg/g. Ca measurements of the blank were below 0.1% (wt) and the reference material presented an average standard error of ± 0.1%. A correlation coefficient of +0.91 ($p(\alpha) < 0.01$) between Sr/Ca ratio measured by XRF and ICP-MS techniques gives support to the use of the Sr/Ca ratios obtained by portable XRF device in this high-resolution chemostratigraphic approach (Table S1 – Supplementary Material; Appendix C).

Twenty six samples were selected from the Laginha and Corcal sections for major and trace element analyses of the carbonate fraction through ICP-MS technique. These samples were selected as representative of different carbonate facies from the Tamengo Formation. Ca, Mg, Mn, Fe, and Sr concentrations are used in this study to track post-depositional alterations of carbon isotope record. Leaching of the carbonate fraction of samples was conducted using a two-step procedure described by Paula-Santos et al. (2020). Measurements of Ca, Sr and Mg were performed on a quadrupole X-Series ICP-MS (Thermo, Germany), whereas other elements were measured on a sector field ICP-MS Element XR (Thermo Fisher, Germany), both at the Institute of Geosciences of the University of Campinas, Brazil. The limestone reference material CAL-S (CRPG, France) was measured during mass spectrometry procedures and the obtained mean values for this RM were: Mg = 2268 μg/g, U = 0.76 μg/g and Sr = 243 μg/g (n=4), which are in good agreement with values available at the GeoReM database (Mg = 2358 μg/g, U = 0.77 μg/g and Sr = 255 μg/g, 30th march, http://georem.mpch-mainz.gwdg.de). Additionally, four samples were measured in duplicates and the relative difference between pairs of results ranged from 3.52% to 12.15% with a median value of 7.71%.

5.4.2. SEM/EDS analysis

A sample of *Cloudina* grainstone from the base of Corcal section (CC-10; Table S1 – Appendix C) was selected for the characterization of cementation that commonly fills up the shells (Fig. 5.6g). SEM/EDS analysis was performed on a platinum-coated polished slab in a Thermo QUANTA FEG 650 scanning electron microscope with an attached Bruker XFlash 4030 energy dispersive X-ray detector at the Laboratory of Mineralogical Characterization of the University of São Paulo (LCT-USP).

5.4.3. Carbon and oxygen stable isotopes, carbonate content and TOC

About 10 mg of carbonate powder was obtained by microdrilling carbonate matrix from 242 samples for carbon and oxygen stable isotope analysis, avoiding areas of fractures, terrigenous components or any late diagenetic carbonate features. Carbonate powders were dissolved with orthophosphoric acid at 72 ºC followed by extraction of the released CO_2 through a continuous flow in a Thermo Finnigan Gas Bench II. C and O isotope compositions from carbonates were determined in a Delta V Advantage IRMS at the Stable Isotope Laboratory of the Center for Geochronological Research, University of São Paulo (CPGeo-USP). The analytical precision was better than ±0.07‰ and ±0.05‰ for $\delta^{18}O_{carb}$ and $\delta^{13}C_{carb}$, respectively.

For organic carbon isotope analyses, samples were powdered in a tungsten mill. A total of 49 samples were analyzed for organic carbon isotope compositions, in which 23 samples were analyzed at the Institut de Physique du Globe de Paris (IPGP) and 26 samples at the Laboratoire Domaines Océaniques from the University of Western Brittany, Brest, France. About 3 to 5 g of carbonate rock powder were dissolved with 25 mL of HCl 5N for 12h at 25°C, and then heated at 80°C for 2h. Residues were rinsed three times in distilled water and dried in an oven at 50-60 ºC. Insoluble residues from decarbonatation were weighted and the carbonate content was calculated. For $\delta^{13}C_{org}$ and TOC analyses, about 0.3 to 36.5 mg of the decarbonated powder were weighted in tin capsules and analyzed on an a Flash EA1112 elemental analyzer coupled to a Thermo Finnigan Deltaplus XP mass-spectrometer via a Conflo IV interface under a helium continuous flow, at the IPGP, and on an elemental analyzer Thermo Scientific EA Flash 2000 coupled to a Thermo Scientific Delta V+ mass-spectrometer at the Laboratoire Domaines Océaniques, University of Western Brittany. $\delta^{13}C_{org}$ uncertainty calculated based on measurements of internal standards was better than 0.2‰. The reproducibility of the $\delta^{13}C_{org}$ analyses based on duplicate measurements is ± 0.2‰.

The isotope compositions are reported in the delta notation against the Vienna Pee-Dee Belemnite standard (V-PDB – ‰). Simplified carbon isotope fractionation ($\Delta^{13}C$) was calculated as the difference between $\delta^{13}C_{carb}$ and $\delta^{13}C_{org}$ (e.g. Hayes et al., 1999).

5.5. Results

5.5.1. Elemental geochemistry, TOC and carbonate content

All geochemical data are present in Table S1 (Appendix C). From XRF analyses, samples from the Laginha section presented Ca content varying from 11 to 42% and Sr from 179 to 5044 ppm. Sr/Ca ratios vary from 0.001 to 0.018, with the lower values associated with dolostones (Fig. 5.3). From ICP-MS analyses, carbonate samples displayed Mn concentration from 5.3 to 73.9 μg/g; Fe from 44.6 to 967.5 μg/g; Ca from 338,288 to 424,774 μg/g; Mg from 1105 to 5900 μg/g; and Sr from 540.1 to 6269.3 μg/g. From these results, Mn/Sr ratios vary from 0.002 to 0.081; Fe/Sr from 0.016 to 0.476; Mg/Sr from 0.356 to 7.838; Sr/Ca from 0.002 to 0.016; and Mg/Ca from 32 to 174. Carbonate content range from 21.1 to 99.8%, with average of 91.5% and low values associated with silty-shaly levels interbedded with the thick limestone layers. TOC values are between 0.01 and 1.01%, with average of 0.17%. The highest values are most associated with the shaly interval at the mid part of the section, and also with a shale occurrence at the top of the section (Fig. 5.3).

The Corcal section displays Ca and Sr contents from 24 to 42% and from 915 to 5000 ppm, respectively, from XRF analyses. Sr/Ca ratios vary from 0.002 to 0.013 (Fig. 5.4). Carbonate fraction from selected samples for ICP-MS presented Mn concentrations from 13.2 to 507.3 μg/g; Fe from 96.0 to 1612.1 μg/g; Ca from 398,761.9 to 434,467.9 μg/g; Mg from 1910.1 to 4768.8 μg/g; Sr from 1410.8 to 4917.2 μg/g. Elemental ratios range from: Mn/Sr from 0.004 to 0.153; Fe/Sr from 0.034 to 1.143; Mg/Sr from 0.543 to 2.902; Sr/Ca from 0.003 to 0.012; and Mg/Ca 46 to 115. Carbonate content is homogeneously high, varying from 91.7 to 99.1%, with average of 96.7%. TOC values are very low and range from 0.02 to 0.10%, with average of 0.05%.

The Sobramil section presents carbonate content varying from 79.5 to 99.8%, with average of 94.6%. TOC values range from 0.01 to 0.90%, with average of 0.24% (Fig. 5.5).

5.5.2. SEM/EDS analysis of *Cloudina* bioaccumulations

The sample of *Cloudina* grainstone from the base of Corcal section presents a white to orange cementation filling up the shells (Fig. 5.7A). SEM/EDS analysis shows that these shells are partially silicified (Fig. 5.7B) and presents a concentration of very fine Fe-oxides in the interior of the shells (< 10 um; Fig. 5.7B-D). Previously, Becker-Kerber et al. (2017) also described Fe-oxide cementation associated with *Cloudina* skeletal flanges which may indicate oxidizing conditions during early diagenesis.

5.2.3. Stable isotope geochemistry

In the proximal Laginha section, $\delta^{13}C_{carb}$ varies from −3.51 to 6.02‰, $\delta^{13}C_{org}$ from −27.17 to −21.61‰, $\Delta^{13}C$ from 22.86 to 30.29‰, and $\delta^{18}O_{carb}$ from −10.91 to −1.79‰ (Fig. 5.3; Table S1 – Appendix C). Negative $\delta^{13}C_{carb}$ values are associated with the lower part of the section, intensively affected by dolomitization. In the first 50 m of section, the $\delta^{13}C_{carb}$ profile starts with values around −3.5‰ in a positive excursion up to values around 2‰. $\delta^{13}C_{org}$ presents small variation of values around −25‰, with $\Delta^{13}C$ varying from ~ 23 to 25‰. The $\delta^{18}O_{carb}$ profile display intense scattering of values in this lower part, varying from −8 to −2‰ and reaching highest values among studied sections. In the shaly interval at the mid part of the section, $\delta^{13}C_{carb}$ values continue to increase up to 6‰, with $\delta^{13}C_{org}$ more stable ranging from −24 to −22‰. These results show an increasing trend for $\Delta^{13}C$ from 26 to 30 ‰. $\delta^{18}O_{carb}$ data are relatively stable in this shaly interval, around −6 to −7‰. After the unconformity at the top of the mid shaly interval to the top of the Tamengo Formation, $\delta^{13}C_{carb}$ and $\delta^{13}C_{org}$ values vary less, around 3‰ and −24‰, respectively, resulting in a $\Delta^{13}C$ around 26‰. $\delta^{18}O_{carb}$ values are also relatively stable at this upper part of the section, between −7 and −6‰ (Fig. 5.3).

In the Corcal section, $\delta^{13}C_{carb}$ varies from 0.66 to 5.75‰, $\delta^{13}C_{org}$ from −27.47 to −20.66‰, $\Delta^{13}C$ from 24.63 to 30.96‰, and $\delta^{18}O_{carb}$ values range from −11.23 to −3.66‰ (Fig. 5.4; Table S1 – Appendix C). Regarding carbon isotopes, this section presents two different behaviors between its lower and upper part, which match two major shallowing-upward cycles (Amorim et al., 2020). At the lower cycle in the first ~30 m of section, representing outer to distal-mid ramp marked by bioclastic deposits mainly composed by *Cloudina* shells, $\delta^{13}C_{carb}$ and $\delta^{13}C_{org}$ values are highly variable and match higher rank stratigraphic cycles (parasequences). Aiming to investigate this variation, the interval between

5 and 13 m was analyzed in a higher resolution for $\delta^{13}C_{org}$. In these higher rank cycles, $\delta^{13}C_{carb}$ and $\delta^{13}C_{org}$ vary from ~1 to 6‰ and from ~−27 to −20‰, respectively (Fig. 5.4). These significant carbon isotope variation is not perfectly coupled between $\delta^{13}C_{carb}$ and $\delta^{13}C_{org}$, resulting in a variable $\Delta^{13}C$ between 26 and 31‰. $\delta^{18}O_{carb}$ profile presents a slightly positive excursion from values around −10 to −7‰. In the upper cycle of the Corcal section, composed mainly by intraclastic deposits from proximal-mid ramp, $\delta^{13}C_{carb}$ and $\delta^{13}C_{org}$ profiles are more stable, ranging from ~4 and 5‰ and ~−22 and −24‰, respectively. Consequently, $\Delta^{13}C$ is also more stable, varying from 26 to 28‰. $\delta^{18}O_{carb}$ profile presents higher variation in this upper part, ranging from −11 to −3‰.

The Sobramil section represents most distal domains of the Tamengo carbonate ramp and presents lower isotope variability through the whole section compared with the others, with $\delta^{13}C_{carb}$ varying from ~3 to 5‰, $\delta^{13}C_{org}$ from ~−25 to−23‰, $\Delta^{13}C$ from ~27 to 30‰, and $\delta^{18}O_{carb}$ from ~−10 to −6‰ (Fig. 5.5; Table S1 – Appendix C).

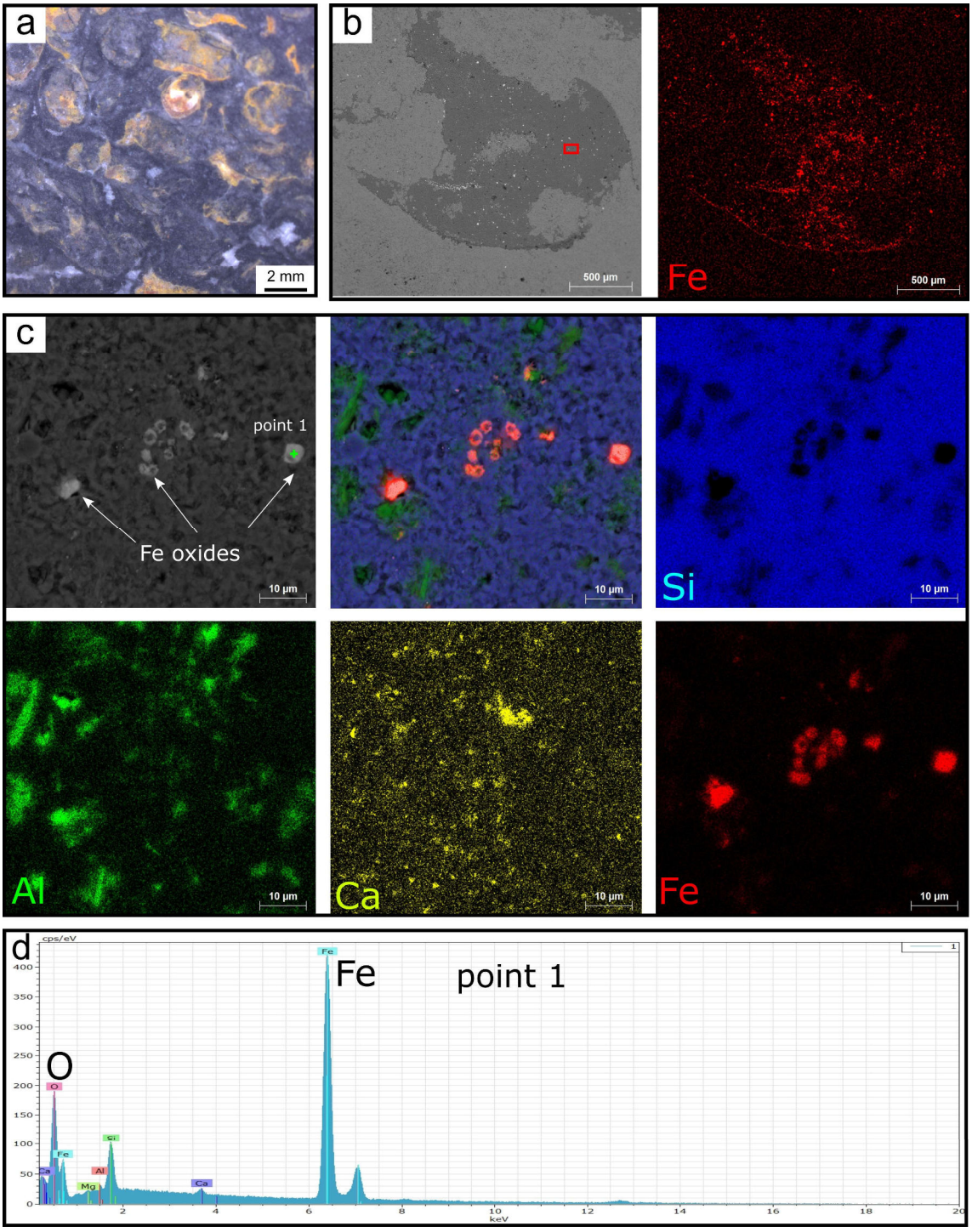

Figure 5.7: a) Polished slabe of *Cloudina* grainstone from the basal Corcal section (distal-mid ramp) presenting white-orange cementation of the shells. b) SEM backscattered electrons image and Fe EDS mapping of a selected Cloudina shell presenting partial silicification (dark-gray area in the backscattered image) and Fe oxides concentrated in the interior of the shell (bright red dots). c) SEM backscattered electrons and EDS mapping images in detail of the shell interior (red rectangle in "b"), showing very fine Fe-oxide crystals within the silicified area. d) EDS spectrum from a punctual analysis of the Fe-oxide crystal shoed in "c".

5.6. Discussion

5.6.1. Post-depositional assessment of the carbon isotope record

Before infer about the paleoenvironmental significance of carbon isotope compositions from both carbonates and organic matter from the Tamengo Formation, first we need to assess the potential alteration of these proxies by post-depositional processes capable to overcome primary signatures. These processes can occur from the early to late diagenesis, as well as during metamorphic events. Here we integrate petrographic, geochemical and isotope signatures to screen samples that potentially had their carbon isotope compositions altered. Effects of metamorphism over both $\delta^{13}C_{carb}$ and $\delta^{13}C_{org}$ signatures are dimmed considering that sedimentary sucessions from Tamengo Formation present very well-preserved sedimentological structures and depositional textures, besides the lack of any metamorphic paragenesis within the studied rocks (e.g. Fig. 5.6; section 5.3.2).

Regarding organic carbon isotope compositions, the main processes capable to modify primary signatures are microbial degradation in the sedimentary environment and thermal maturation of kerogen. However, experimental studies and observations in modern natural environments show that these processes can reach a maximum magnitude of alteration of ± 2‰ (e.g. Galimov, 2004; Lehmann et al., 2002; Macko et al., 1994; McKirdy and Powell, 1974; Simoneit et al., 2004; Yamaguchi et al., 2010). In this case, $\delta^{13}C_{org}$ variations in the studied sections, especially in the lower Corcal section in which $\delta^{13}C_{org}$ excursions reach up to ~7‰ of magnitude (Fig. 5.4), cannot be accounted for these processes. In addition, TOC *vs* $\delta^{13}C_{org}$ diagram (Fig. 5.8A) does not show a correlation between these parameters, therefore, the alteration of $\delta^{13}C_{org}$ by post-depositional process of organic matter degradation is not conclusive.

In contrast to organic carbon, carbon isotope compositions from carbonates are more susceptible to post-depositional alteration, especially during early diagenesis. Processes most capable to change depositional $\delta^{13}C_{carb}$ signatures are related to meteoric diagenesis, dolomitization, and authigenic carbonate precipitation influenced by microbial degradation processes (e.g. Hudson, 1977; Veizer et al., 1999). Burial diagenesis presents a minor potential to alter these signatures considering that processes acting in this diagenetic environment usually occur under low fluid/rock conditions due to intense chemical and physical compaction. Furthermore, pure carbonate sedimentary successions tend to be

carbonate-buffered compared to the burial diagenetic fluid, with a minor potential of $\delta^{13}C_{carb}$ alteration during neomorphism in these conditions (e.g. Hudson, 1977; Renard, 1986).

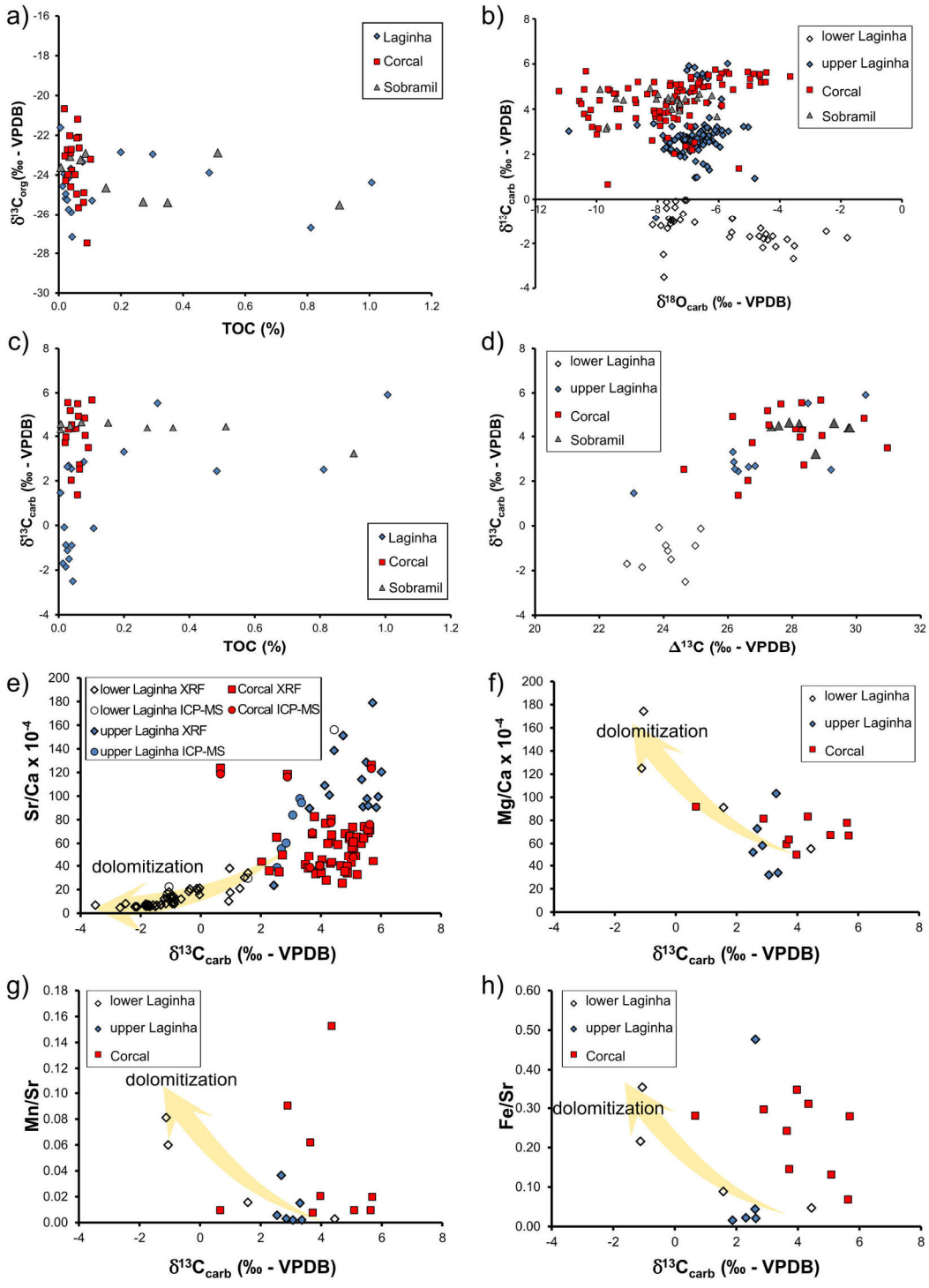

Figure 5.8: Geochemical diagrams for assessment of post-depositional alterations of carbon isotope data.

In terms of petrological aspects, regardless moderate recrystallization degree of carbonate components of the Tamengo Formation, only the base of Laginha section (0 to 60 m) presents neomorphism features marked by dolomitization process (Fig. 5.3 and 5.6B) which might have altered $\delta^{13}C_{carb}$ values. Not surprisingly, these first 60 m of the Laginha section present negative $\delta^{13}C_{carb}$ values in a positive excursion from negative to positive values, along with the demise of these diagenetic features. Another geochemical feature associated with this interval is the lowest Sr mass fractions (~400 μg/g) and Sr/Ca ratios (~0.001) among the studied sections, which can be interpreted as loss of Sr during dolomitization in proximal areas. Above 55 m of the Laginha section and in the Corcal section, Sr content and Sr/Ca ratios are usually high with averages of 1969 μg/g and 0.006, respectively, associated with well-preserved calcitic depositional textures (Fig. 5.6). These high Sr mass fractions and Sr/Ca ratios are frequent geochemical signatures in late Ediacaran carbonate successions, probably deposited in times of more alkaline seas (e.g. Cui et al., 2016; Wood et al., 2017; Caetano-Filho et al., 2019; Paula-Santos et al., 2020).

Despite these post-depositional features suggesting altered $\delta^{13}C_{carb}$ signatures at the base of the Laginha section, the classical evaluation through the $\delta^{18}O_{carb}$ *vs* $\delta^{13}C_{carb}$ diagram does not show any positive trend for the studied section, including the lower Laginha interval (Fig. 5.8B). Contrary to expected for meteoric diagenesis, which would influence neoformed carbonates with light carbon and oxygen isotope compositions, the lower dolomitized Laginha interval present heavier $\delta^{18}O_{carb}$ values associated with the lighter (and negative) $\delta^{13}C_{carb}$ values. This can be interpreted as an isotope influence of pervasive early dolomitization in these carbonate rocks possible associated with an evaporative fluid, whereas $\delta^{13}C_{carb}$ values may have been influenced by both meteoric and dolomitization fluids. Additionally, TOC *vs* $\delta^{13}C_{carb}$ diagram (Fig. 5.8C) does not show any trends for the studied sections, suggesting lack of influence of post-depositional organic matter degradation over $\delta^{13}C_{carb}$ signatures (i.e. organic diagenesis; Ader and Javoy, 1998; Ader et al., 2009).

Another approach to infer about post-depositional alteration of $\delta^{13}C_{carb}$ is the use of the $\Delta^{13}C$ parameter (e.g. Ader et al., 2009). Usual carbon isotope fractionation between carbonate carbon and organic carbon driven by photosynthetic carbon fixation ranges between 26 and 32‰, considering they were originated from the same DIC reservoir (e.g. Hayes et al., 1999). Although $\Delta^{13}C$ values out of this range could imply in carbonates and organic carbon originated from different DIC reservoirs and not necessarily altered, there is a clear positive trend in the $\Delta^{13}C$ *vs* $\delta^{13}C_{carb}$ diagram (Fig. 5.8D) for the lower Laginha samples, showing that $\Delta^{13}C < 26‰$ are mostly associated with the negative $\delta^{13}C_{carb}$ values. This trend coupled with

the petrological and geochemical features discussed earlier strongly suggests that $\delta^{13}C_{carb}$ of the lower Laginha were altered during post-depositional processes.

Finally, additional $\delta^{13}C_{carb}$ *vs* geochemical ratios relationships illustrate that dolomitization probably was the ultimate process responsible for $\delta^{13}C_{carb}$ alteration of the lower Laginha carbonates. A clear increasing trend between $\delta^{13}C_{carb}$ and Sr/Ca is developed for the Laginha section (Fig. 5.8E), illustrating loss of Sr during dolomitization at the base of the section coupled with lighter carbonate carbon isotope compositions. Negative trends are present in Mg/Ca, Mn/Sr and Fe/Sr *vs* $\delta^{13}C_{carb}$ diagrams (Figs. 5.8F, 5.8G and 5.8H), showing the relationship between decreases in Mg, Mn and Fe contents, and therefore decrease of dolomitization degree, with the heavier and probably primary $\delta^{13}C_{carb}$ values. The Corcal section data do not show any trend for these diagrams (Fig. 5.8) and accompany the data spreading field of the upper and non-dolomitized Laginha section. Therefore, taking aside the lower Laginha section from 0 to 60 m, $\delta^{13}C_{carb}$ results are considered to record primary signals from the Tamengo Formation paleodepositional environments.

5.6.2. Marine carbon cycling in the Tamengo carbonate ramp: intense oxic organic carbon remineralization associated with *Cloudina* bioaccumulations in mid ramp environments

Aside from the $\delta^{13}C_{carb}$ values of lower Laginha section (Fig. 5.3), carbonate rocks from the Tamengo Formation present $\delta^{13}C_{carb}$ varying from 0.7 to 6.0‰, with both average and median of 3.9‰, whereas $\delta^{13}C_{org}$ values vary from −27.5 to −20.7‰, with both average and median of −24.0‰. Considering the plateaus of $\delta^{13}C_{carb}$ values for most parts of the analyzed sections, from inner to outer domains of the carbonate ramp (Fig. 5.9), we assume that $\delta^{13}C_{DIC}$ from surface waters of the Tamengo carbonate ramp may have fluctuate around 4‰, a $\delta^{13}C_{carb}$ value usually found in late Ediacaran successions (e.g. Tahata et al., 2013; Wood et al., 2015). The carbon isotope fractionation between carbonate and organic carbon reservoirs mostly varies within the range between 26 and 30‰, as expected for photosynthetic carbon fixation (e.g. Hayes et al., 1999), suggesting that carbonate and organic carbon components from most part of these environments derived from the same DIC reservoir. However, an exceptional behavior is noticed in the basal shallowing-upward cycle of the Corcal section, representing distal-mid ramp domains of the Tamengo ramp and referred here as the lower Corcal section. This basal cycle encompasses a remarkable high variability for both $\delta^{13}C_{carb}$ and $\delta^{13}C_{org}$, varying from 0.7 to 5.7‰ and from −27.5 to −20.7‰, respectively.

These variations constitute higher frequency cycles of positive excursions which apparently match higher-rank stratigraphic cycles, illustrated by the selected interval for higher resolution paired analyses (Fig. 5.9). Considering that this chemostratigraphic-stratigraphic cyclicity is observed in carbonate facies representing the most concentrated bioaccumulations of the benthic biomineralizing *Cloudina* fossil fragments among the studied sections, we further explore the possible association between these isotope disturbances and biogeochemical processes occurring in the environments inhabited by this skeletal metazoan.

These short-term cycles in both $\delta^{13}C_{carb}$ and $\delta^{13}C_{org}$ record from the lower Corcal section suggest a heterogeneous DIC isotope composition in outer mid ramp domains, considering that post-depositional alteration within the sediment pile is not capable to explain such a magnitude of variation for both reservoirs (~5‰ for $\delta^{13}C_{carb}$ and ~7‰ for $\delta^{13}C_{org}$; Fig. 5.9). Additionally, they are linked to the parasequence cyclicity which supports a paleoenvironmental control (i.e. facies control) over these signatures. We also do not consider the possibility of higher isotope sensibility in response to a small DIC reservoir due to the fact that Tamengo Formation is mostly constituted by pure carbonate rocks with high Sr/Ca ratios (Fig. 5.4), suggesting high carbonate alkalinity in the system. This scenario is well documented in several Ediacaran successions, especially high Sr/Ca ratios, interpreted as a time of enhanced alkalinity which may have favored the development of carbonate biomineralization by these early skeletal metazoans, remarkably represented by *Cloudina* genus (e.g. Cui et al., 2016; Wood et al., 2018; Caetano-Filho et al., 2019; Paula-Santos et al., 2020).

The detailed interval between 5.0 to 12.6 m of the Corcal section presents decoupled $\delta^{13}C_{carb}$– $\delta^{13}C_{org}$ trends which results in a more scattered $\Delta^{13}C$ compared with the upper Corcal and other sections. This interval also presents two $\Delta^{13}C$ values below the range expected for photosynthetic isotope fractionation between carbonates and organic carbon formed in the same DIC reservoir ($\Delta^{13}C$ < 26‰; Fig. 5.4 and 5.8). The most probable explanation for such decoupling is the existence of different DIC sources for carbonate precipitation and carbon fixation by primary producers. Considering the significant magnitude of isotope variation, we thus access here the classical scenario of isotopically stratified DIC in response of enhanced organic carbon remineralization and consequent ^{13}C-depleted bottom waters.

A crucial point to be explored is what would have caused an enhanced organic carbon remineralization in the distal-mid ramp domain, compared with the inner and outer domains of the Tamengo carbonate ramp, to account for a disturbed DIC in such specific

environments. The degree of organic carbon remineralization may be related to the efficiency of metabolisms degrading organic matter, which relies on the available source of oxidants (i.e. electron acceptors; e.g. Aller, 2014). In a marine sedimentary environment under well-oxygenated water column, the classical sequence of biogeochemical redox reactions is developed with increasing depth in sediments, from most efficient to less efficient metabolism: aerobic respiration; nitrate-, manganese-, and iron-reduction; sulfate-reduction and methanogenesis (e.g. Canfield and Thadrump, 2009). The presence and thickness of each biogeochemical zone depends on the availability of reagents required by each metabolism and the velocity that they are exhausted (i.e. O_2, NO_3^-,Mn- and Fe-oxyhydroxides, SO_4^{2-}, CO_2). In the Tamengo carbonate ramp, chemical and lithological aspects suggest differences in the bottom redox conditions between the studied sections which could be an indicator of different metabolic dominance, and so, the efficiency of organic matter remineralization through the sedimentary environments.

The Corcal section presents the lowest TOC contents, with average values of 0.05% and maximum value of 0.10%, compared to Laginha and Sobramil TOC contents, with averages of 0.17% and 0.24% and substantially high maximum values of 1.01% and 0.90%, respectively. This is the first aspect suggesting that both inner and outer ramp domains had more favorable conditions to preserve organic matter compared with mid ramp environments, which could be related to a higher bioproductivity and/or oxygen-depleted conditions in bottom environments. An additional and more direct evidence for a distinct redox condition in the lower Corcal section is the remarkable presence of Fe-oxyhydroxide cementation in the *Cloudina* grainstones and packstones which compose the parasequences with high $\delta^{13}C_{carb}$-$\delta^{13}C_{org}$ variability (Fig. 5.6G and 5.7). Goethite cements were already identified from *in situ* and reworked *Cloudina* deposits of the Tamengo Formation (Becker-Kerber et al., 2017). This type of cement was associated with sparry calcite in the skeletal flanges of *Cloudina*, as a result of cyanobacteria activity in microbial mat environments inhabited by these skeletal metazoans (Becker-Kerber et al., 2017). The ecological association of *Cloudina* with microbial mats bearing oxygenic photoautotrophs also suggests higher oxygen levels in the benthic environment, potentially exploted by these epibenthic sessile animals (Gingras et al., 2011; Cai et al., 2014; Becker-Kerber et al., 2017). In the light of the described ecological relationship commonly reported for *Cloudina* habitats, including those from the Tamengo Formation, we interpret the presence of iron-oxyhydroxide cementation in *Cloudina* deposits from the lower Corcal section as a potential product of oxic Fe^{2+} oxidation, either by inorganic or metabolic-driven pathways (chemolithoautotrophs, chemoheterotrophs;

Konhauser and Riding, 2012). Therefore, more oxygenated conditions in the distal-mid ramp bottom environments may have been responsible for a thicker and more efficient organic carbon remineralization zone resulting in more ^{13}C-depleted DIC in bottom waters. Anoxic bottom layers in both inner and outer ramp domains would represent decreased organic carbon remineralization zones allowing for isotope homogeneity of DIC reservoir through mixing between a thinner surface oxic and the bottom anoxic layers (Fig. 5.10A).

Despite *Cloudina*-bearing carbonate facies from the lower Corcal section represent re-worked deposits, we assume a relatively proximity of the environments inhabited by this organism. This is depicted from the stratigraphic evolution of this lower cycle, grading from mudstones and wackestones with few *Cloudina* specimens (Fig. 5.6D) to grainstones and packstones essentially composed by *Cloudina* fragments, including well-preserved *cone-in-cone* structures (Fig. 5.6E), which would represent a short time (i.e. distance) of transport from the living environments. Thus, the presence of the higher variability of both $\delta^{13}C_{carb}$ and $\delta^{13}C_{org}$ within this interval, with lighter carbon isotope compositions compared with both inner and outer ramp domains, led us to the paleoceanographic reconstruction of a bottom ^{13}C-depleted DIC in the proximity of the *Cloudina* and probably *Corumbella werneri* living environments in mid ramp, which would have resulted from enhanced oxic degradation of organic matter (Fig. 5.10A). Although the later organism is preserved within silty-shale facies (Fig. 5.4 and 5.6F) not allowing for paired $\delta^{13}C$ analyses, well-preserved *Corumbella werneri* specimens were observed in siltstones-mudstones interbedded with *Cloudina*-bearing facies in the described parasequences (Fig. 5.4).

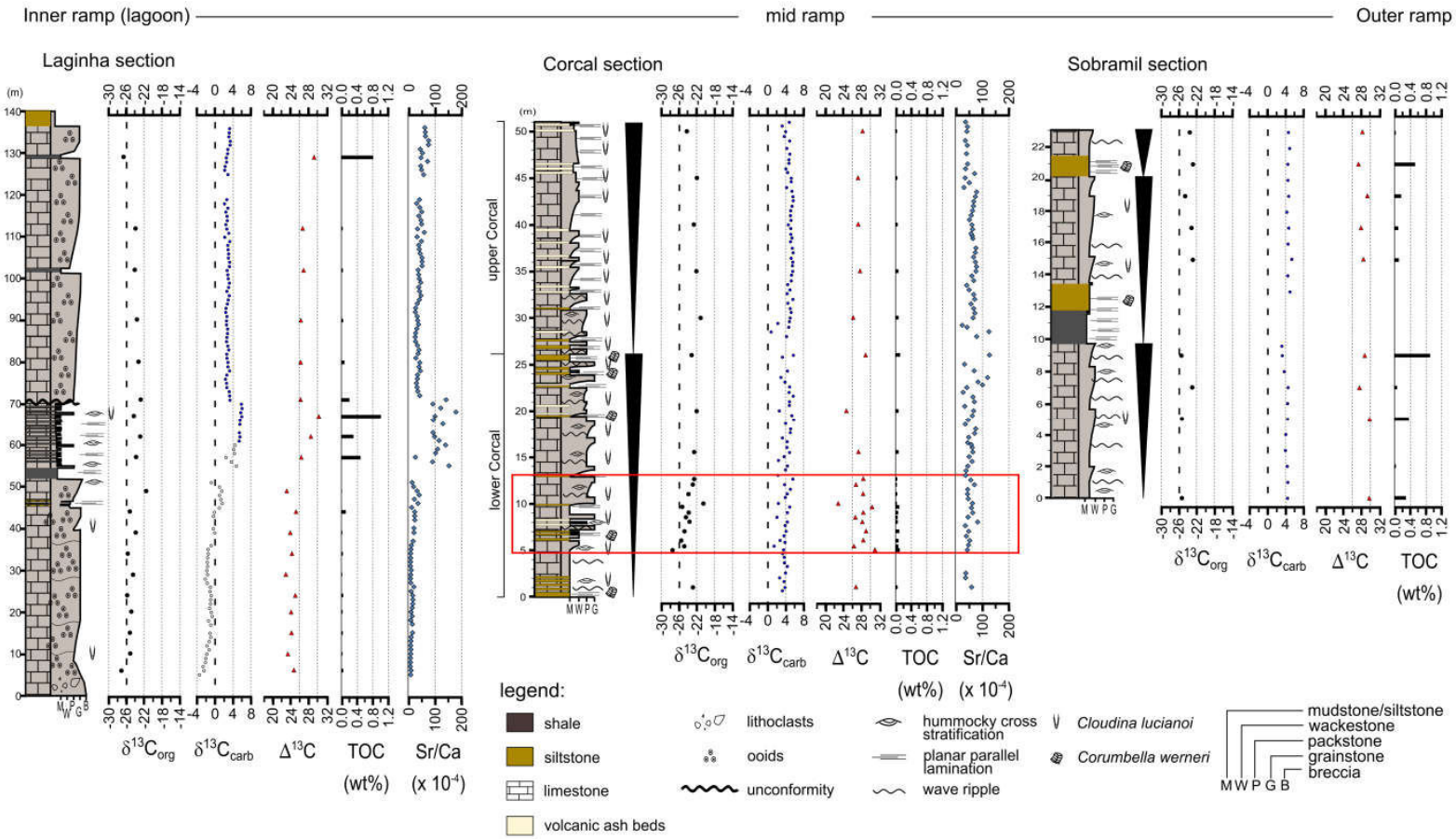

Figure 5.9: Comparison between studied sections, from inner to outer ramp. Red rectangle marks the interval of the lower Corcal section in which paired $\delta^{13}C$ analyses were performed in a higher resolution within the parasequences and presents a higher isotope variability.

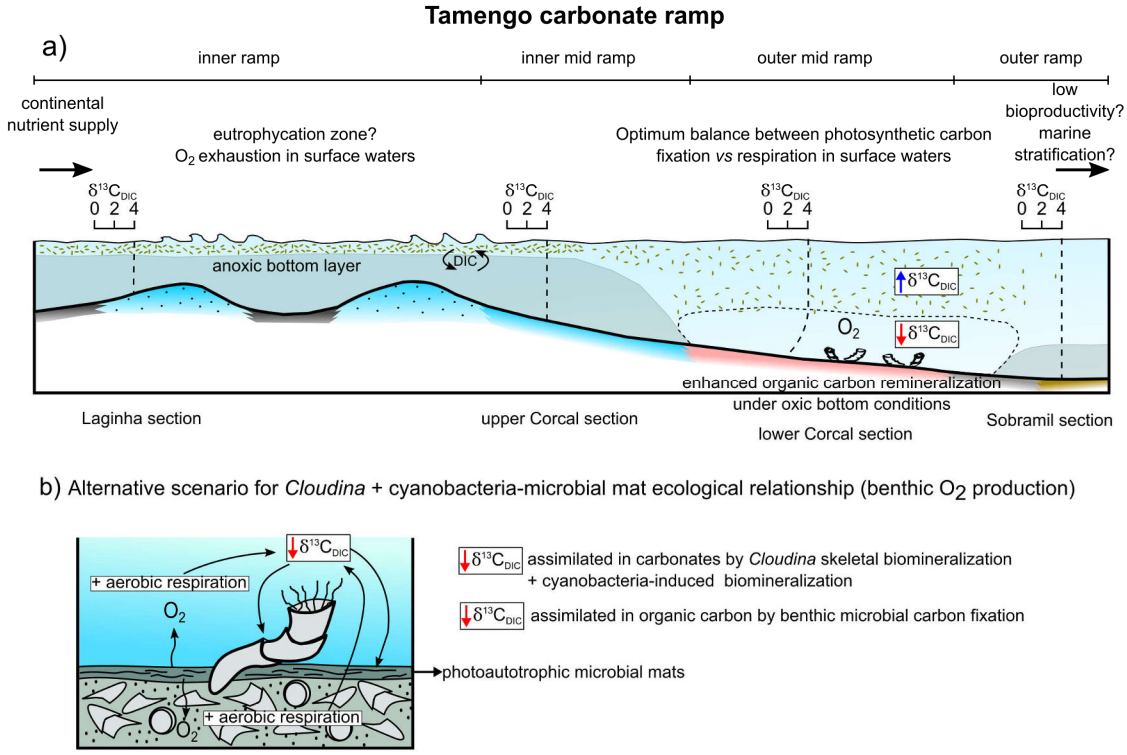

Figure 5.10: Proposed paleoredox architecture for the Tamengo carbonate ramp (Amorim et al., 2020) and DIC isotope disturbances in the distal mid ramp environments. a) Scenario of benthic oxygenation due to favorable balance between nutrients, bioproductivity and respiration in surface layers, allowing for oxygen to reach bottom waters and resulting in enhanced organic carbon remineralization within the sediments. DIC in these environments would be ^{13}C-depleted constrasting with surface layers whereas both inner and outer ramp waters would be homogeneized due to a thinner oxic surface layer. b) Alternative scenario for benthic oxygenation in *Cloudina* habitats, depending on the relationship between these animals and oxygen-producers' microbial mats. In this case, *Cloudina* would harvest oxygen from the bottom (e.g. Gingras et al., 2011) and inhabited spaces would depend on favorable sedimentary environments for development of photoautotrophic microbial mats. Nevertheless, the isotope influence over bottom DIC in this case would be similar to the proposed in scenario 'a'.

5.6.3. An additional piece for reconstructing complex oxygenation of benthic environments inhabited by early skeletal metazoans

The causal relationship between bottom ocean oxygenation and appearance of complex animals seems to be a never ending discussion. This is due to the long-term coincidence between the first metazoan assemblages and geochemical anomalies suggesting enhanced oxidation in the Ediacaran Period (e.g. Fike et al., 2006; Canfield et al., 2007), but at the same time the difficulty in assembly such geochemical disturbances with the fossil

record in the fine scale, either in time and space. Extended discussions concerning the minimum oxygen requirements by complex animals and intrinsic evolutionary forces driving life diversification and oxic signatures add more complexity to this coincidence of the geological record (e.g. Mills et al, 2014; Butterfield, 2009). However, in regards specifically to the advent of biomineralization by these early animals, it is interpreted that such innovation would require sufficient amounts of free oxygen (Rhoads and Morse, 1971; Wood et al., 2015). Indeed, oxic conditions were tracked in close association with *Cloudina* living habitats from the Nama Group in which a complex oxygen distribution through benthic environments seem to control both occurrence and ecological complexity of the system (Wood et al., 2015; 2018; Tostevin et al., 2016).

Wood et al. (2015) provided the paleoredox architecture based on iron speciation data for the Nama Group carbonate ramp where permanent oxic conditions would have been developed in deeper inner to mid ramp environments, especially during transgressions. On the other hand, shallower environments retrieved signals of intermittently oxygenated bottom waters whereas distal environments from outer ramp would have been predominantly anoxic. This redox architecture represents a complex distribution of oxic benthic environments, which would not have been controlled by paleobathymetry. In regards to fossil distribution within this model, Wood et al. (2015) described a direct relationship between ecological complexity and oxygen availability, similar to observed in modern environments (Diaz and Rosemberg, 1995). Skeletal organisms living in permanently oxic mid ramp environments were part of a more complex ecological net, with higher biodiversity (*C. hartmanne* and *Namacalathus*), larger bodies and in association with large thrombolites (Penny et al., 2014). Shallower environments from inner ramp which would have experienced intermittent oxygenation present a fossil record marked by monospecific communities, formed by small *C. riemkeae* probably representing short-lived and opportunistic organisms. Later, Tostevin et al. (2016) integrated REE systematic with iron speciation data in a basin transect of the Nama Group, demonstrating that skeletal communities and complex ecosystems did not occupy poorly oxygenated and narrow transient zones from well-oxygenated to fully anoxic conditions, suggesting a minimum oxygen demand for these communities (~>10 μM).

The same complex redox architecture would be present in our paleoenvironmental reconstruction for Tamengo Formation, in the sense that more oxic conditions would not have been controlled by depth. Disturbances in the high-resolution paired carbon isotope record from distal-mid ramp deposits composed by *Cloudina* bioaccumulations would have been a product of enhanced oxic degradation of organic matter compared to both inner and outer

ramp environments, influencing bottom waters ^{13}C-depleted DIC in these environments (Fig. 5.10A). Minor differences between Nama Group and Tamengo Formation can be discussed through analysis of $\delta^{13}C_{carb}$ and the biodiversity of fossil record. Wood et al. (2015) reported variations from 2 to 5‰ for inner ramp deposits from the Nama Group interpreted as intermittent oxic environments. This range of variations is very close to the parasequence $\delta^{13}C_{carb}$- $\delta^{13}C_{org}$ cycles from the lower Corcal section representing mid ramp deposits from the Tamengo Formation. Despite representing different parts of the respective carbonate ramps, this isotope behavior is assigned to facies presenting minor ecological complexity and biodiversity in both basins, here reported for the lower Corcal section in which *Cloudina* bioaccumulations seem to have a monospecific character formed by small organisms. This could represent more unstable redox conditions in mid ramp domains from the Tamengo Formation compared with mid ramp domains from the Nama Group, approaching more the intermittently oxygenated conditions reported for inner ramp environments of the later unit.

If this scenario holds, it adds a higher complexity for future investigations between the relationship of well-oxygenated benthic environments and metazoan colonization. Such complex redox distribution proposed for late Ediacaran carbonate ramps from Nama Group and Tamengo Formation suggests that bottom ocean oxygenation were not controlled by a simplistic paleobathymetry variation. Thus what would have controlled these specific well-oxygenated benthic environments in mid ramp domains? We envisage that an optimum balance between carbon fixation *vs* respiration of the biological pump could have impacted the oxygen availability for benthic environments and, therefore, the habitable environments for early skeletal metazoans (Fig. 5.10A). Li isotope data for the carbonates of Tamengo Formation strongly suggest that the continent was the main source of nutrients via chemical weathering, with enhanced fluxes influencing at least proximal and mid ramp areas (Paula-Santos et al., in prep.). Proximal environments could have been highly productive (eutrophic) due to this high nutrient discharge in shallow and intermittently lagoon confined environments, fatally resulting in oxygen exhaustion for less ventilated benthic environments, which could be the case for the Laginha section bearing some organic-rich intervals and lacking *Cloudina* bioaccumulations. On the other hand, the most distal Sobramil section, although presenting some facies bearing *Cloudina* and *Corumbella* specimens, would represent a portion more distant from nutrient source with minor bioproductivity and carbon remineralization and/or decreased bottom water oxygenation due to stratification. In these most proximal and distal environments, DIC reservoir would be easily homogenized between a thinner surface oxic and a thicker bottom anoxic layers (Fig. 5.10A). This water

stratification could be eventually disrupted during transgressions, when a better connection with the ocean would drive deep-water ventilation (e.g. Wood et al., 2015), enabling life on deeper environments and justifying the presence of benthic organisms (*Corumbella*) and burrows in fine siliclastic facies (Parry et al., 2017). A perfect imbalance could have been present in mid ramp domains, with sufficient nutrient input and primary bioproductivity but not high enough to cause an oxygen exhaustion (eutrophication) through the water column. An efficient bottom oxygenation would result in benthic nutrient recycling through enhanced organic matter degradation allowing for a higher complexity in these bottom habitats.

On the other hand, an alternative scenario to be considered is a possible commensalim relationship between oxygen-producers benthic microbial communities and skeletal metazoans, with the latter ones harvesting oxygen oases created by microbial mats (e.g. Gingras et al., 2011; Berker-Kerber et al., 2017; Fig. 5.10B). This could also result in the same bottom isotope DIC disturbance discussed earlier in a more oxygenated bottom environment, but representing a local microbial benthic oxygen input in a predominantly anoxic carbonate ramp. Although this scenario would not fit for the pelitic facies bearing *Corumbella werneri*, it could be explored for the usual faciological relationship described for *Cloudina* occurrences (e.g. Cai et al., 2014; Berker-Kerber et al., 2017), in which the habitable space for these metazoans could have been controlled by favorable environments for oxygenic photoautotrophic microbial mats (cyanobacterias), such as low hydrodynamic energy and sunlight incidence in bottom environments.

We stress that our proposed paleoenvironmental redox reconstruction and consequent hypothesized scenarios, although finding support on petrographical features (iron oxyhydroxide cementation) and similar redox architecture proposed for coeval basins, must be tested through other geochemical proxies. Studies relying on trace metal data, iron speciation coupled to paleontological investigations are strongly recommended for the Tamengo Formation to better understand the distribution and causes of this high frequency $\delta^{13}C$ cyclicity and its relationship with more oxygenated environments and metazoan habitats.

5.7. Conclusions

High resolution paired carbon isotope analyses from three sections distributed along a the Tamengo Formation carbonate ramp showed that most part of the domains presented homogeneous $\delta^{13}C_{carb}$ around 4‰, a common value for the late Ediacaran, whereas carbon isotope fractionation between carbonates and organic matter mostly ranges between 26 and

30‰, as expected for photosynthetic carbon fixation. However, a distinct behavior was observed in distal-mid ramp domains, in which high-frequency decoupled $\delta^{13}C_{carb}$ and $\delta^{13}C_{org}$ variations of substantial magnitude (5 and 7‰, respectively) are coupled with parasequences. This suggests disturbances in DIC within these environments compared with inner and outer ramp domains of the carbonate ramp. Such carbon isotope deviations are present in carbonate facies bearing fragmented to moderately preserved fossils of the early skeletal metazoan from *Cloudina* genus, suggesting a relationship between these isotope anomalies and the habitats colonized by these animals. Lower TOC values and presence of early diagenetic iron oxyhydroxide cements in these facies led to the interpretation of enhanced organic carbon remineralization under more oxygenated conditions. Oxic bottom conditions in mid ramp bottom environments could have been responsible for ^{13}C-depleted DIC, which in turn may have influenced primary carbon fixation and carbonate precipitation, at shallow water depths or even in benthic environments, leading to the observed negative spikes in both $\delta^{13}C_{carb}$ and $\delta^{13}C_{org}$. More oxygenated conditions in benthic mid ramp domains mimic the same complex paleoredox architecture reconstructed for the Nama Group based on iron speciation data, where oxygen availability seems to have controlled distribution of early metazoan habitats as well as the degree of ecological complexity.

Next steps should focus on the probable causes for such complex redox distribution of benthic environments from these late Ediacaran carbonate ramps. We envisage a scenario where an optimum balance between carbon fixation *vs* respiration is present in the mid ramp, with sufficient nutrient supply and bioproductivity in surface waters, but not high enough to promote eutrophication and oxygen exhaustion in bottom waters. A more efficient organic matter oxidation in bottom environments would also promote nutrient recycling for an active benthic ecosystem inhabited by these early skeletal metazoans. An alternative scenario is the possible commensalism relationship between oxygenic photoautotrophic microbial benthic communities and *Cloudina*, as a usually reported in literature, in which the latter organism could harvest oxygen from this benthic oxygen oases. Both scenarios would fit the stratigraphic-chemostratigraphic $\delta^{13}C_{carb}$–$\delta^{13}C_{org}$ cycles resulting from a bottom ^{13}C-depleted DIC derived from enhanced oxic organic carbon remineralization. Further studies focusing on paleoredox geochemical proxies are strongly recommended along the Tamengo carbonate ramp to test the proposed scenarios and to provide more constrains on the relationship between the $\delta^{13}C$ cyclicity in mid ramp environments and early metazoans habitats.

5.8. Acknowledgements

This study was funded by the São Paulo Research Foundation (FAPESP) thematic project grant #2016/06114-6. We are thankful to the technical teams from the Pôle de Spectométrie Océan, University of Western Brittany, the Stable Isotope Geochemistry Group, Institute de Physique du Globe de Paris, and the Stable Isotope Laboratory from the Geochronological Research Center, University of São Paulo, for the support during data acquisition. Sergio Caetano Filho holds a FAPESP scholarship grant #2016/11496-5 and part of the data was acquired during his BEPE/FAPESP project #2018/19302-0. Gustavo Paula-Santos holds a FAPESP post-doc grant #2017/00399-1. Marly Babinski and Ricardo Trindade and are fellows of the Brazilian Research Council (#307563/2013-8 and #206997/2014-0, respectively). This study contributes to the IdEx Université de Paris ANR-18-IDEX-0001 and to the LabexMER ANR-10-LABX-19.

5.9. References

Ader, M., Javoy, M., 1998. Diagenese précoce en milieu sulfuré réducteur: une étude isotopique dans le Jurassique basal du Bassin parisien. Comptes Rendus de l'Académie des Sciences, Paris, Sciences de la Terre et des Planètes 327, 803-809.

Ader, M., Macouin, M., Trindade, R.I.F., Hadrien, M.H., Yang, Z., Sun, Z., Besse, J., 2009. A multi layered water column in the Ediacaran Yangtze platform? Insights from carbonate and organic matter paired $\delta^{13}C$. Earth and Planetary Science Letters 288, 213–227.

Adorno, R.R., Carmo, D.A., Germs, G., Walde, D.H.G., Denezine, M., Boggiani, P.C., Silva, S.C.S., Vasconcelos, J.R., Tobias, T.C., Guimarães, E.M., Vieira, L.C., Figueiredo, M.F., Moraes, R., Caminha, S.A., Suarez, P.A.Z., Rodrigues, C.V., Caixeta, G.M., Pinho, D., Schneider, G., Ralph Muyamba, R., 2017. *Cloudina lucianoi* (Beurlen & Sommer, 1957), Tamengo Formation, Ediacaran, Brazil: Taxonomy, analysis of stratigraphic distribution and biostratigraphy. Precambrian Research 301, 19−35.

Alkmim, F.F., Marshak, S., Pedrosa-Soares, A.C., Peres, G.G., Cruz, S.C., Whittington, A., 2006. Kinematic evolution of the Araçuaí–West Congo orogen in Brazil and Africa: nutcracker tectonics during the Neoproterozoic assembly of Gondwana. Precambrian Research 149, 43–63.

Aller, R.C., 2014. Sedimentary Diagenesis, Depositional Environments, and Benthic Fluxes. In: Mottl, M. and Elderfield, H. (Eds.), The Oceans and Marine Geochemistry – Treatise on Geochemistry. Elsevier. 42 p.

Almeida, F.F.M., 1984. Província Tocantins, setor Sudoeste. In: Almeida, F.F.M., Hasui, Y. (Eds.), O Pré-Cambriano do Brasil. Edgard Blücher, São Paulo, pp. 265–281.

Alvarenga, C.J.S., Boggiani, P.C., Babinski, M., Dardenne, M.A., Figueiredo, M.F., Dantas, E.L., Uhlein, A., Santos, R.V., Sial, A.N., Trompette, R., 2011. Glacially influenced sedimentation of the Puga Formation, Cuiabá Group and Jacadigo Group, and associated carbonates of the Araras and Corumbá groups, Paraguay Belt, Brazil. In: Arnaud, E., Halverson, G. P., Shields-Zhou, G. (Eds.), The Geological Record of Neoproterozoic Glaciations. Geological Society, London, 36, pp. 487–497.

Alvarenga, C.J.S., Trompette, R., 1993. Evolução Tectônica da Faixa Paraguai: A Estruturação da Região de Cuiabá. Revista Brasileira de Geociências 23 (1), 18–30.

Amorim, K.B., Afonso, J.W.L., Leme, J.M., Diniz, C.Q.C., Rivera, L.C.M., Gómez-Gutiérrez, J.C., Boggiani, P.C., Trindade, R.I.F., 2020. Sedimentary facies, fossil distribution and depositional setting of the late Ediacaran Tamengo Formation (Brazil). Sedimentology. https://doi.org/10.1111/sed.12749

Babcock, L.E., Grunow, A.M., Sadowski, G.R., Leslie, S.A., 2005. Corumbella, an Ediacaran-grade organism from the Late Neoproterozoic of Brazil. Palaeogeography, Palaeoclimatology, Palaeoecology 220, 7–18.

Becker-Kerber, B., Pacheco, M.L.A.F., Rudnitzki, I.D., Galante, D., Rodrigues, F., Leme, J.M., 2017. Ecological interactions in *Cloudina* from the Ediacaran of Brazil:implications for the rise of animalbiomineralization. Scientific Reports 7:5482.

Bengtson, S., Zhao, Y., 1992. Predatorial borings in late precambrian mineralized exoskeletons. Science 257, 367–369.

Boggiani, P.C., 1998. Análise estratigráfica da Bacia Corumbá (Neoproterozoico)- Mato Grosso do Sul (Ph.D. Dissertation). University of São Paulo, Brazil, 181 pp.

Boggiani, P.C., Alvarenga, C.J.S., 2004. Faixa Paraguai. In: Matesso-Neto, V., Bartorelli, A., Carneiro, C.D.R., Brito-Neves, B.B. (Eds.), Geologia do Continente Sul-Americano. Beca, São Paulo 1, pp. 113-118.

Boggiani, P.C., Fairchild, T.R., Riccomini, C., 2004. New level of diamictites in the Corumbá Group (Ediacaran), Paraguay Belt, South America. Symposium on Neoproterozoic-Early Palaeozoic Events in SW-Gondwana, 1, São Paulo, Brazil, Extended Abstracts, pp. 10–12.

Boggiani, P.C., Gaucher, C., Sial, A.N., Babinski, M., Simon, C.M., Riccomini, C., Ferreira, V.P., Fairchild, T.R., 2010. Chemostratigraphy of the Tamengo Formation (Corumbá Group, Brazil): a contribution to the calibration of the Ediacaran carbon-isotope curve. Precambrian Research 182, 382–401. http://dx.doi.org/10.1016/j.precamres.2010.06.003.

Butterfield, N.J., 2009. Oxygen, animals and oceanic ventilation: an alternative view. Geobiology 7, 1–7.

Caetano-Filho, S., Paula-Santos, G.M., Guacaneme, C., Babinski, M., Bedoya-Rueda, C., Peloso, M., Amorim, K., Afonso, J., Kuchenbecker, M., Reis, H.L.S., Trindade, R.I.F., 2019. Sequence stratigraphy and chemostratigraphy of an Ediacaran-Cambrian foreland-related carbonate ramp (Bambuí Group, Brazil). Precambr. Res. 331, 105365.

Cai, Y., Hua, H., Schiffbauer, J.D., Sun, B., Yuan, X., 2014. Tube growth patterns and microbial mat-related lifestyles in the Ediacaran fossil Cloudina, Gaojiashan Lagerstätte, South China. Gondwana Res. 25, 1008–1018. http://dx.doi.org/10.1016/j.gr.2012.12.027.

Canfield, D., Thamdrup, B., 2009. Towards a consistent classification scheme for geochemical environments, or, why we wish the term 'suboxic' would go away. Geobiology 7, 385–392.

Canfield, D.E., Poulton, S.W., Knoll, A.H., Narbonne, G.M., Ross, G., Goldberg, T., Strauss, H., 2008. Ferruginous conditions dominated later Neoproterozoic deep- water chemistry. Science 321, 949–952.

Canfield, D.E., Poulton, S.W., Narbonne, G.M., 2007. Late-Neoproterozoic deep-ocean oxygenation and the rise of animal life. Science 315, 92–94.

Cui, H., Kaufman, A.J., Xiao, S., Peek, S., Cao, H.,Min, X., Cai, Y., Siegel, Z., Liu, X.M., Peng, Y., Schiffbauer, J.D., Martin, A.J., 2016. Environmental context for the terminal Ediacaran biomineralization of animals. Geobiology 14, 344–363.

Diaz, R.J., Rosenberg, R., 1995. Marine benthic hypoxia: a review of its ecologicaleffects and the behavioural responses of benthic macrofauna. Oceanography and Marine Biology: an Annual Review 33, 245–303.

Fike, D.A., Grotzinger, J.P., Pratt, L.M., Summons, R.E., 2006. Oxidation of the Ediacaran Ocean. Nature 444, 744–747.

Freitas, B.T., Warren, L.V., Boggiani, P.C., Almeida, R.P., Piacentini, T., 2011, Tectono-sedimentary evolution of the Neoproterozoic BIF-bearing Jacadigo Group, SW-Brazil. Sedimentary Geology 238, 48–70.

Galimov, E.M., 2004. The pattern of $\delta^{13}C_{org}$ versus HI/OI relation in recent sediments as an indicator of geochemical regime in marine basins: comparison of the Black Sea, Kara Sea, and Cariaco Trench. Chemical Geology 204, 287–301.

Gaucher, C., Boggiani, P.C., Sprechmann, P., Sial, A.N., Fairchild, T.R., 2003. Integrated correlation of the Vendian to Cambrian Arroyo del Soldado and Corumbá groups (Uruguay and Brazil): Palaeogeographic, palaeoclimatic and palaeobiologic implications. Precambrian Research 120, 241–278.

Gaucher, C., Germs, G.J.B., 2009. Skeletonised metazoans and protists. Neoproterozoic–Cambrian biota. In: Gaucher, C., Sial, A.N., Halverson, G.P., Frimmel, H.E. (Eds.), Neoproterozoic–Cambrian Tectonics, Global Change and Evolution: A Focus on Southwestern Gondwana. Developments in Precambrian Geology 16. Elsevier, Oxford, pp. 327–338.

Gingras, M., Hagadorn, J.W., Seilacher, A., Lalonde, S.V., Pecoits, E., Petrash, D., Konhauser, K.O., 2011. Possible evolution of mobile animals in association with microbial mats. Nature Geosciences 4, 372–375.

Goldberg, T., Strauss, H., Guo, Q., Liu, C., 2007. Reconstructing marine redox conditions for the early Cambrian Yangtze Platform: Evidence from biogenic sulphur and organic carbon isotopes. Palaeogeography, Palaeoclimatology, Palaeoecology 254, 175–193.

Halverson, G.P., Shields-Zhou, G., 2011. Chemostratigraphy and the Neoproterozoic glaciations. In: Arnaud, E., Halverson, G.P., Shields-Zhou, G. (Eds.), The Geological Record of Neoproterozoic Glaciations. Geological Society, London, Geological Society Memoir 36, pp. 51–66.

Hasui, Y., Almeida, F.F.M., 1970. Geocronologia do Centro-Oeste brasileiro. Boletim da Sociedade Brasileira de Geologia 19 (1), 5–26.

Hayes, J.M., Strauss, H., Kaufman, A.J., 1999. The abundance of ^{13}C in marine organic matter and isotopic fractionation in the global biogeochemical cycle of carbon during the past 800 Ma. Chemical Geology 161, 103–125.

Hudson, J.D., 1977. Stable isotopes and limestone lithification.Journal of Geological Society 133(6), 637−660.

Konhauser, K., Riding, R., 2012. Bacterial biomineralization. In: Knoll, A.H., Canfield, D.E., Konhauser, K.O. (Eds.), Fundamentals of Geobiology, First Edition. Blackwell Publishing Ltd, Oxford, pp. 105–130.

Lehmann, M.F., Bernasconi, S.M., Barbieri, A., Mckenzie, J.A., 2002. Preservation of organic matter and alteration of its carbon and nitrogen isotope composition during

simulated and in situ early sedimentary diagenesis. Geochimica et Cosmochimica Acta 66, 3573–3584.

Macko, S.A., Engel, M.H., Qian, Y., 1994. Early diagenesis and organic matter preservation -- a molecular stable carbon isotope perspective. Chemical Geology 114, 365–379.

McKirdy, D.M., Powell, T.G., 1974. Metamorphic Alteration of Carbon Isotopic Composition in Ancient Sedimentary Organic Matter: New Evidence from Australia and South Africa. Geology 2, 591–595.

Mello, J.C.R., Godoi, J.O., 2001. Mapa geológico da Folha Corumbá (SE.21-Y-D), escala 1:250.000. Programa Levantamentos Geológicos Básicos do Brasil. CPRM – Serviço Geológico do Brasil.

Mills, D.B., Ward, L.M., Jones, C.A., Sweeten, B., Forth, M., Treusch, A.H., Canfield, D.E., 2014. Oxygen requirements of the earliest animals. Proceedings of the National Academy of Sciences of the United States of America 111(11), 4168–4172.

Narbonne, G.M., Xiao, S., Shields, G.H., Gehling, J.G., 2012. The Ediacaran Period. In: Gradstein, F.M., Ogg, J.G., Schmitz, M., Ogg, G., (Coordinators), The Geologic Time Scale 2012. Elsevier Publisher, Oxford, pp. 413–435.

Nogueira, A.C.R., Riccomini, C., Sial, A.N., Moura, C.A.V., Fairchild, T.R., 2003. Soft-sediment deformation at the base of Neoproterozoic Puga cap carbonate (southwestern Amazon craton, Brazil): confirmation of rapid icehouse to greenhouse transition in snowball Earth. Geology 31, 613–616.

Och, L.M., Shields-Zhou, G.A., 2012. The Neoproterozoic oxygenation event: environmental perturbations and biogeochemical cycling. Earth-Sciences Reviews 110, 26–57.

Pacheco, M.L.A.F., Galante, D., Rodrigues, F., Leme, J.M., Bidola, P., Hagadorn, W., Stockmar, M., Herzen, J., Rudnitzki, I.D., Pfeiffer, F., Marques, A.C., 2015. Insights into the skeletonization, lifestyle, and affinity of the unusual Ediacaran fossil Corumbella. PLoS ONE 10(3), 1−19.

Parry, L.A., Boggiani, P.C., Condon, D.J., Garwood, R.J., Leme, J.M., McIlroy, D., Brasier, M.D., Trindade, R.I.F., Campanha, G.A.C., Pacheco, M.L.A.F., Diniz, C.Q.C., Liu, A.G., 2017. Ichnological evidence for meiofaunal bilaterians from the terminal Ediacaran and earliest Cambrian of Brazil. Nature Ecology & Evolution 1, 1455−1464.

Paula-Santos, G., Caetano-Filho, S., Enzweiler, J., Navarro, M., Babinski, M., Guacaneme, C., Kuchenbecker, M., Reis, H., Trindade, R.I.F., 2020. Rare earth elements in the terminal Ediacaran Bambuí Group carbonate rocks (Brazil): evidence for high seawater alkalinity during rise of early animals. Precambrian Research 336, 105506.

Paula-Santos, G.M., Gramcianinov, C.B., Kasemann, S.A., Wilckens, F.K., Caetano-Filho, S. Navarro, M.S., Marteleto, T.P., Enzweiler, J., Romero, G.R., Leme, J.M., Babinski, M., Trindade. R.I.F., Weathering-driven biomineralization in Late Ediacaran seas. In preparation.

Penny, A.M., Wood, R., Curtis, A., Bowyer, F., Tostevin, R., Hoffman, K.-H., 2014. Ediacaran metazoan reefs from the Nama Group, Namibia. Science 344, 1504–1506.

Piacentini, T., Vasconcelos, P.M., Farley, K.A., 2013. $^{40}Ar/^{39}Ar$ constraints on the age and thermal history of the Urucum Neoproterozoic banded iron-formation, Brazil. Precambrian Research 248, 48–62.

Renard, M., 1986. Pelagic carbonate chemostratigraphy (Sr, Mg, O-18, C-13). Marine Micropaleontology 10, 117−164.

Rhoads, D.C., Morse, J.W., 1971. Evolutionary and ecologic significance of oxygen-deficient basins. Lethaia 4, 413–428.

Sahoo, S.K., Planavsky, N.J., Jiang, G., Kendall, B., Owens, D., Wang, X., Shi, X., Anbar, A.D., Lyons, T.W., 2016. Oceanic oxygenation events in the anoxic Ediacaran ocean. Geobiology 14, 457−468.

Simoneit, B.R.T., Peters, K.E., Rohrback, B.G., Brenner, S., Kaplan, I.R., 2004. Thermal alteration of Cretaceous black shale from the Eastern Atlantic. III: Laboratory simulations. In: Hill, R.J., Leventhal, J., Aizenshtat, Z., Baedecker, M.J., Claypool, G., Eganhouse, R., Goldhaber, M., Peters, K. (Eds). Geochemical Investigations in Earth and Space Science: A Tribute to Isaac R. Kaplan. The Geochemical Society No. 9, 321-340.

Spangenberg, J.E., Bagnoud-Velásquez, M., Boggiani, P.C., Gaucher, C., 2014. Redox variations and bioproductivity in the Ediacaran: Evidence from inorganic and organic geochemistry of the Corumbá Group, Brazil. Gondwana Research 26, 1186−1207.

Tahata, M., Ueno, Y., Ishikawa, T., Sawaki, Y., Murakami, K., Han, J., Shu, D., Li, Y., Guo, J., Yoshida, N., Komiya, T, 2013. Carbon and oxygen isotope chemostratigraphies of the Yangtze platform, South China: Decoding temperature and environmental changes through the Ediacaran. Gondwana Research 23, 333–353.

Tostevin R., Wood, R.A., Shields, G.A., Poulton, S.W., Guilbaud, R., Bowyer, F., Penny, A.M., He, T., Curtis, A., Hoffmann, K.H., Clarkson, M.O., 2016. Low-oxygen waters limited habitable space for early animals. Nature Communications 7, 1−9.

Trindade, R.I.F., Font, E., D'Agrella-Filho, M.S., Nogueira, A.C.R., Riccomini, C., 2003. Low-latitude and multiple geomagnetic reversals in the Neoproterozoic Puga cap carbonate of Amazonia. Terra Nova 15, 441–446.

Veizer, J., Ala, D., Azmy, K., Bruckschen, P., Buhl, D., Bruhn F., Carden, G.A.F., Diener, A., Ebneth, S., Godderis, Y., Jasper, T., Korte, C., Pawellek, F., Podlaha, O.G., Strauss, H., 1999. $^{87}Sr/^{86}Sr$, $\delta^{13}C$ and $\delta^{18}O$ evolution of Phanerozoic seawater. Chemical Geology 161, 59−88.

Walde, D.H.G., Leonardos, O.H., Hahn, G., Pflug, H.D., 1982. The first pre-Cambrian megafossils from South America, *Corumbella werneri*. Anais da Academia Brasileira de Ciências 54, 461.

Wood, R., Bowyer, F., Penny, A., Poulton, S.W., 2018. Did anoxia terminate Ediacaran benthic communities? Evidence from early diagenesis. Precambrian Research 313, 134−147.

Wood, R., Ivantsov, A.Y., Zhuralev, A.Y., 2017. First macrobiota biomineralization was environmentally triggered. Proceedings of the Royal Society B: Biological Sciences 284.

Wood, R.A., Poulton, S.W., Prave, A.R., Hoffmann, K.H., Clarkson, M.O., Guilbaud, R., Lyne, J.W., Tostevin, R., Bowyer, F., Penny, A.M., Curtis, A., Kasemann, S.A., 2015. Dynamic redox conditions control late Ediacaran ecosystems in the Nama Group, Namibia. Precambrian Research 261, 252−271.

Yamaguchi, K.E., Oguri, K., Ogawa, N.O., Sakai, S., Hirano, S., Kitazato, H., Ohkouchi, N., 2010. Geochemistry of modern carbonaceous sediments overlain by a water mass showing photic zone anoxia in the saline meromictic Lake Kai-ike, southwest Japan: I. Early diagenesis of organic carbon, nitrogen, and phosphorus. Palaeogeography, Palaeoclimatology, Palaeoecology 294, 72–82.

Zaine, M.F., Fairchild, T.R., 1985. Comparison of Aulophycus lucianoi Beurlen and Sommer from Ladário (MS) and the genus *Cloudina* Germs. Ediacaran of Namibia. Anais da Academia Brasileira de Ciências 57, 130.

6. MULTIPLE SULFUR ISOTOPE CONSTRAINTS IN MARGINAL AND EPICONTINENTAL LATE EDIACARAN-CAMBRIAN MARINE SETTINGS: SUPERHEAVY $\delta^{34}S$ PYRITE TRENDS, SULFATE-DISTILLATION CYCLES AND IMPLICATIONS FOR EARLY ANIMAL COLONIZATION

Sergio Caetano-Filho, Pierre Sansjofre, Gustavo M. Paula-Santos, Pierre Cartigny, Magali Ader, Cristian Guacaneme, Marly Babinski, Matheus Kuchenbecker, Humberto L.S. Reis, Ricardo I.F. Trindade

6.1. Abstract

The terminal Ediacaran record encompasses frequent occurrences of the so-called superheavy pyrites, presenting extremely ^{34}S-enriched isotope compositions which can surpass the coexisting sulfate isotope values. These unusual sulfur isotope signatures challenge the known kinetic isotope fractionation effect during microbial sulfate reduction and have been interpreted either in terms of primary to early diagenetic genesis as well as a product of late diagenesis. Deciphering whether these anomalies represent disturbances in the marine sulfur cycle is important to reconstruct conditions in which biological innovations and animal colonization operated at the end of Neoproterozoic. We present here the pyrite multiple sulfur isotope record for two distinct geotectonic settings along the late Ediacaran-early Cambrian West Gondwana, aiming to constraint spatial and temporal distribution of superheavy pyrites. The Tamengo Formation represents a mixed carbonate-siliciclastic ramp at the continental margin, whereas the Bambuí Group records deposition in an epicontinental setting within the core of this supercontinent. Positive $\delta^{34}S_{py}$ excursions reaching superheavy values (>40‰) match regressive tendencies in both basins, whereas negative $\delta^{34}S_{py}$ excursions are recorded along transgressions. Multiple sulfur isotope distributions match Rayleigh distillation predictions, in which pyrite data follow pooled sulfide pathways towards initial sulfate values. We propose a scenario of sulfate-distillation cycles in bottom waters throughout regressions, forced by enhanced stratification and inefficient circulation, whereas transgressive events could recharge bottom environments with sulfate by incursion of more concentrated waters and/or through water mixing. Dynamics proposed here would help to explain the reason for such anomalous sulfur isotope signals being rare in the geological record, depending upon specific continental configurations favoring restricted basins with inefficient circulation, allied to low marine sulfate conditions, as envisaged for the terminal

Neoproterozoic West Gondwana. Additionally, negative $\Delta^{33}S_{py}$ values reached at the superheavy pyrite interval of the Bambuí Group suggest almost complete exhaustion of sulfate reservoir, representing enhanced anoxic sulfidic and toxic conditions for benthic metazoan colonization in epicontinental settings, compared with marginal seas. Sulfate-exhaustion in this isolated setting also supports the scenario of methanogenic-dominated basin proposed for the extreme positive $\delta^{13}C$ excursions succeeding the superheavy pyrite excursion in the Bambuí Group. If reproducible in coeval epicontinental basins, this scenario would represent large methane fluxes to the atmosphere which could have driven Earth out from Neoproterozoic glaciations towards more warm and favorable conditions for the Cambrian explosion of life.

6.2. Introduction

The Ediacaran Period encompasses one of the intervals of the geological record bearing frequent occurrences of unusually ^{34}S-enriched pyrites, the so-called superheavy pyrites (Ries et al., 2009). $\delta^{34}S$ values from these pyrites are usually are higher than +25‰ and may surpass the values for coexisting sulfate, challenging the kinetic effects of sulfur isotope fractionation during microbial sulfate reduction (e.g. Habicht and Canfield, 2001). Several hypothesis suggesting a paleodepositional origin for these anomalous signals have been proposed, such as: (i) before appearance of fecal pellets, the slow sinking of organic matter represented increased demand for oxidants in the water column, with planktonic bacterial sulfate-reduction activity and consequently existence of ^{34}S-enriched sulfate minimum zones in shallow platforms (Logan et al., 1995); (ii) overall low dissolved sulfate in the Neoproterozoic oceans in which pyrite burial would lead to enhanced Rayleigh distillation effects, especially in times of high Fe flux into the basins (Liu et al., 2006); (iii) basin stratification and decoupled sulfate reservoir, with pyrite as a product from sulfate-reduction in anoxic and sulfate-depleted bottom waters progressively enriched in ^{34}S, whereas sulfates derived from surface and more oxygenated waters (Shen et al., 2008); (iv) microbial sulfate reduction with minimal fractionation in a low sulfate environment, coupled with sulfide reoxidation, resulting in a more ^{34}S-depleted sulfate and progressively ^{34}S-enriched sulfide through Rayleigh distillation (Ries et al., 2009); and (v) contribution of ^{34}S-enriched H_2S from hydrothermal vents in a previously ^{34}S-enriched marine environment with low sulfate concentrations (Wang et al., 2019).

In spite of some intervals through the Ediacaran with more widespread $\delta^{34}S_{sulfate}$ trends suggesting growth of the marine reservoir (e.g. Hurtgen et al., 2002; Fike et al., 2006; Halverson and Hurtgen, 2007; Cui et al., 2015), much lower sulfate concentrations are envisaged for marine environments from the terminal Neoproterozoic compared with modern ones, due to high values and high variability of $\delta^{34}S$ recorded in both sulfate and sulfides (Kah et al., 2004; Hurtgen et al., 2006; Loyd et al., 2013; Tostevin et al., 2017). This major scenario of widespread low sulfate concentrations, probably as a result of inefficient oxygenation of marine environments, sustains most part of the hypothesis proposed for superheavy pyrite genesis, most of them grounded in the concept of sulfate-distillation in limited-sulfate environment. However, the mechanisms controlling sulfate availability and specific conditions driving extreme ^{34}S-enrichment in Neoproterozoic superheavy pyrites remain unsettled.

Ries et al. (2009) reported the widespread occurrence of superheavy pyrites in the late Ediacaran interval from the Nama Group, presenting $\delta^{34}S_{py} > 40‰$ and usually negative $\Delta^{34}S_{sulfate\text{-}sulfide}$. The authors suggested a scenario of minimal fractionation during microbial sulfate reduction under sulfate-limited conditions and ^{34}S-enrichment due to Rayleigh distillation effect, driven by sulfide re-oxidation to produce ^{34}S-depleted sulfates compared with reactant H_2S. Later, Tostevin et al. (2017) re-evaluated $\delta^{34}S_{CAS}$ signatures from the same interval of the Nama Group suggesting that $\delta^{34}S_{py} > \delta^{34}S_{CAS}$ condition is not as widespread as previously thought. These authors proposed that low $\Delta^{34}S_{CAS\text{-}py}$ values from the Nama Group (< 6.6‰), far below $\Delta^{34}S$ values from coeval strata from Oman and China (Fike and Grozinger, 2008; Cui et al., 2016) would be a product of microbial sulfate reduction under low sulfate concentrations and/or high sulfate reduction rates (i.e. minimal fractionation), allied to locally unfavorable conditions to preserve true $\Delta^{34}S$ resembling microbial sulfate reduction (e.g. Gomes and Hurtgen, 2015).

It is observed that modern shallow sedimentary environments may present equally ^{34}S-enriched $\delta^{34}S_{py}$ values surpassing $\delta^{34}S$ signatures of overlying seawater sulfate (~+21‰), as a result of local sedimentary conditions without necessarily imply in low sulfate concentrations in the coeval overlying seawater (Fike et al., 2015 and references therein). From a late diagenetic perspective, superheavy pyrites from Cryogenian and late Devonian deposits from China were associated with late hydrothermal mineralizations within Mn-rich carbonate rocks, as a product of Rayleigh distillation during Thermochemical Sulfate-Reduction (TSR; Cui et al., 2018; Yan et al., 2020). However, there are still pertinent questions to solve. What would be the reason for these ^{34}S-enriched pyrites being rare through geological record if they

can be ascribed to common early to late diagenetic processes? In the same sense, why are these occurrences so common and concentrated for such specific intervals, such as during the late Ediacaran (e.g. Bottomley et al., 1992; Ries et al., 2009)?

Aiming to distinguish local from regional major controls over sulfur cycling through the late Ediacaran, we examine here the multiple sulfur isotope record ($\delta^{34}S$, $\Delta^{33}S$ and $\Delta^{36}S$) from two distinct settings from the late Ediacaran-early Cambrian West Gondwana (Fig. 6.1) bearing $\delta^{34}S_{py}$ higher than +40‰. The Tamengo Formation, Southern Paraguay Belt, represents a mixed carbonate-siliciclastic ramp in the continental margin, whereas the Bambuí Group, São Francisco Basin, records deposition in an epicontinental sea in the very core of West Gondwana. Sulfur isotope record provided here is coupled with a well-established stratigraphic framework allowing investigations of lateral and temporal variability whereas the multiple sulfur isotope approach gives constraints on isotope effects through superheavy pyrite trends. Our approach improves discussions concerning the relationship between sulfur cycling and the animal colonization in the terminal Neoproterozoic, by considering remarkable differences of biota distribution in these settings. Additionally, we discuss the link between superheavy pyrites and equally rare superheavy carbon isotope compositions present in the Bambuí Group.

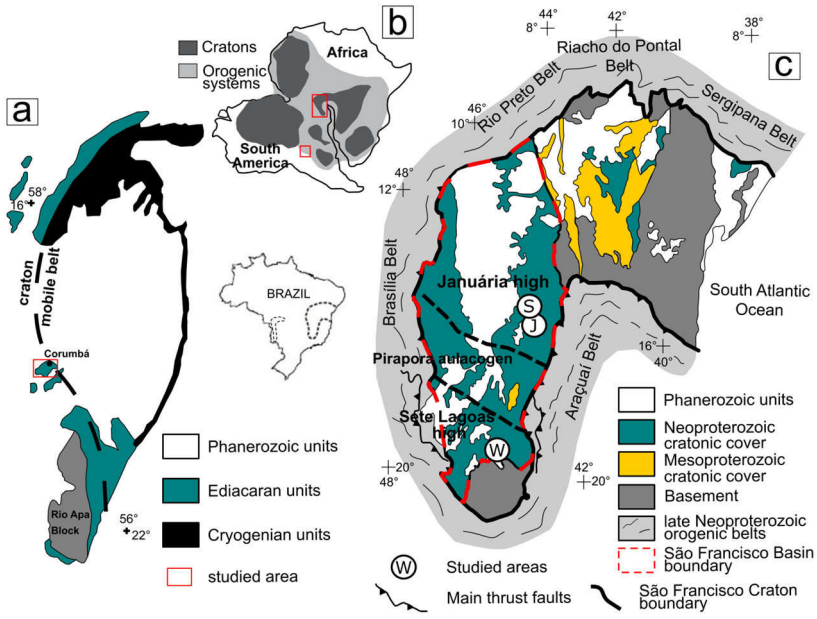

Figure 6.1: Location of the two studied units in the West Gondwana during late Ediacaran-early Cambrian. a) Geological map of the Paraguay Belt (modified from Boggiani et al., 2010). b) Paleogeographic reconstruction for the the West Gondwana during late Ediacaran-early Cambrian (modified from Alkmim et al., 2006). Geological map of the São Francisco Basin within the homonymous craton (modified from Reis et al., 2016).

6.3. Geological Setting

6.3.1. The late Ediacaran Tamengo Formation, Corumbá Group, Southern Paraguay Belt: a mixed carbonate-siliciclastic ramp in the West Gondwana margin

The Paraguay Belt is an arc-shaped Brasiliano-Panafrican fold and thrust belt developed during the terminal Neoproterozoic Gondwana assembly in the central-west Brazil (Fig. 6.1A; Boggiani and Alvarenga, 2004). The Corumbá Group represents the Ediacaran record within the Southern Paraguay Belt, exposed in a N-S trend limited by Rio Apa Block to the west and by the Paleozoic deposits from the Paraná Basin to the east. This unit is dominated by carbonate rocks and overlies the glacio-related Puga Formation, representing Marinoan glacial deposits from low-latitudes at the Northern Paraguay Belt (Nogueira et al., 2003; Trindade et al., 2003; Freitas et al., 2011).

The deposition of the Corumbá Group started with siliciclastic sediments which compose lithostratigraphic units of minor geographic expression, the Cadiueus and Cerradinho formations, still representing a rift stage (Fig. 6.2A; Boggiani et al., 2010). This early stage is overlain by shallow-water limestones and dolostones, as well as associated boundstones and phosphorite deposits from the Bocaina Formation, in a rimmed carbonate platform system developed in a post-rift stage at the border of West Gondwana continent (Freitas et al., 2011 Fig. 6.1B). In the middle to the upper part of the Corumbá Group, the Tamengo Formation represents a more complex carbonate facies distribution, presenting a rich paleontological record related to the late Ediacaran (e.g. Gaucher et al., 2003; Adorno et al., 2017; Fig. 6.2A). The basal contact with the Bocaina Formation is erosive, marked by a polymictic breccia composed of clasts of granite-gneiss basement rocks and rocks from the Bocaina Formation (Boggiani et al., 2010; Amorim et al., 2020). The Tamengo Formation is conformably overlain by fine-grained siliciclastics from the Guaicurus Formation in the area of Corumbá city (Boggiani et al., 2010).

The Tamengo Formation represents a mixed siliciclastic-carbonate ramp with a variety of carbonate facies from inner to outer ramp, represented by the three sections studied here and described previously by Amorim et al. (2020) (section 6.4.1.1). Regarding age constraints, the Tamengo Formation is well positioned in the late Ediacaran interval by U-Pb ID-TIMS ages from zircon grains retrieved in volcanic ash beds throughout the Corumbá

Group (Fig. 6.2A): the basal limit is marked by an age of 555 ± 0.3 Ma in the top of Bocaina Formation and the upper limit is set by an age of 542.37 ± 0.28 Ma in the upper Corcal Section, upper Tamengo Formation (Parry et al., 2017). A rich fossil record is documented within the Tamengo Formation, with remarkable occurrences of shell-beds containing the skeletal metazoan *Cloudina lucianoi* (Gaucher et al., 2003; Adorno et al., 2017; Becker-Kerber et al., 2017), and the scyphozoan cnidarian *Corumbella werneri* well-preserved within pelitic intercalations (Babcock et al., 2005; Pacheco et al., 2015). An acritarch assemblage dominated by *Bavlinella faveolata* as well as Vendotaenid algaes also occur in the Tamengo and Guaicurus formations (Gaucher et al., 2003).

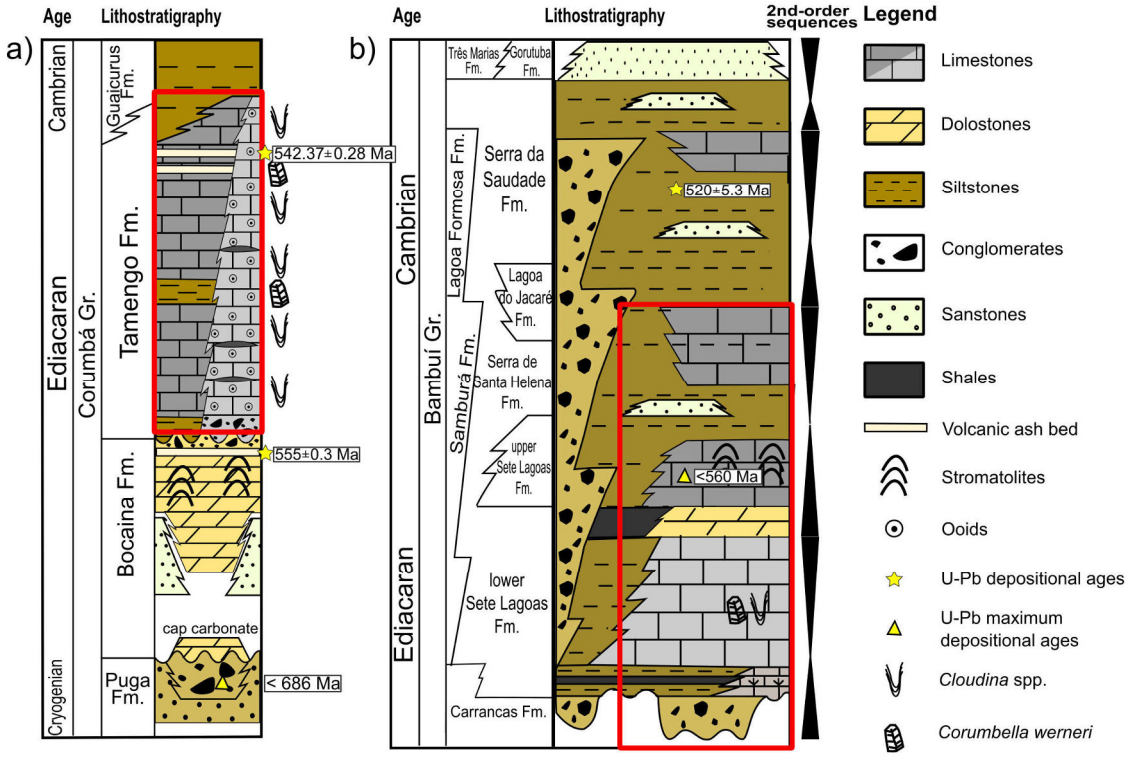

Figure 6.2: a) Stratigraphy of the Southern Paraguay Belt (after Boggiani et al., 2010 and Freitas et al., 2011). Geochronological ages from U-Pb dating in zircon grains from volcanic ash beds from Parry et al. (2017). b) Stratigraphic chart from the Bambuí Group (after Reis et al., 2016). Fossil occurrence from Warren et al. (2014); Maximum depositional age for the upper Sete Lagoas Formation from Paula-Santos et al. (2015) and U-Pb depositional age for volcanoclastic deposits from Serra da Saudade Formation from Moreira et al. (2020). Red rectangles represent studied intervals from both units.

6.3.2. The late Ediacaran-Cambrian Bambuí Group, São Francisco Basin: an epicontinental marine setting in the core of West Gondwana

In western South America, São Francisco craton represents one of the inner and stable continental parts involved in the assembly of Gondwana, by the end of Neoproterozoic Era (e.g. Heilbron et al. 2017). During these diachronous collisional events, several orogenic belts evolved around the craton, giving rise to a complex foreland system in its interior, represented by the Bambuí Group as the sedimentary record of an epicontinental sea in the very core of West Gondwana (e.g. Reis et al. 2016; Caetano-Filho et al., 2020). The foreland-related nature of the Bambuí Group and its progressive restriction through time are supported by paleogeographic reconstructions (e.g. Tohver et al., 2006), the tectono-sedimentary filling pattern of the basin as constrained by seismic and drill core data (Reis and Suss, 2016; Reis et al., 2017), and by drastic changes in detrital provenance at the transition between the two basal sequences (Paula-Santos et al., 2015).

The Bambuí Group deposition started with the siliciclastic sediments of the Carrancas Formation, which is overlain by mixed carbonate-siliciclastic deposits from Sete Lagoas, Serra de Santa Helena, Lagoa do Jacaré, Serra da Saudade and Três Marias formations (Dardenne, 1978; Fig. 6.2B). These lithostratigraphic units constitute 2nd-order sequences in the 1st-order foreland basin cycle (for a detailed review see Reis et al., 2016). Our focus is on the lower to middle sedimentary successions of the Bambuí Group, represented by the Carrancas, Sete Lagoas, Serra de Santa Helena and Lagoa do Jacaré formations, which will be detailed in the studied section description (section 6.4.1.2).

U-Pb ages and local occurrences of late Ediacaran metazoan fossils in the basal Sete Lagoas Formation suggest that deposition of the Bambuí basin cycle occurred along the late Ediacaran-Cambrian interval. *Cloudina* sp. and *Corumbella werneri* (549-541 Ma; Grotzinger et al., 2000; Amthor et al., 2003) were reported in the middle Sete Lagoas Formation (~40 to 50 m from the basement; Warren et al., 2014; Perrella Jr. et al., 2017). U-Pb ages for detrital zircon grains provide a maximum depositional age of 560 Ma for the overlying sequence, in the upper Sete Lagoas Formation (Paula-Santos et al., 2015), corroborating the age suggested by the fossil occurrences in the underlying interval. A U-Pb age of 520 ± 5.3 Ma obtained from zircon grains from a volcanoclastic layer within the Serra da Saudade Formation, in the upper Bambuí Group, confirms that deposition in the basin spanned the early Paleozoic (Moreira et al., 2020). Despite contrasting Pb-Pb isochron ages for the cap carbonate interval at the base of Bambuí Group (740 ± 22 Ma, Babinski et al., 2007; 608 ± 19 Ma, Caxito et al.,

2018), no stratigraphical evidence has been found so far to support the possible existence of condensation levels or hiatuses in the corresponding interval to fit early and late Ediacaran ages within the basal Sete Lagoas Formation (Reis and Suss, 2016; Kuchenbecker et al., 2016; Caetano-Filho et al., 2019; Fig. 6.2).

6.4. Materials and Methods

6.4.1. Studied sections: stratigraphic and chemostratigraphic background

6.4.1.1. Tamengo Formation, Southern Paraguay Belt

Three sections from the Tamengo Formation were analyzed and represent proximal to distal environments of the Tamengo mixed siliciclastic-carbonate ramp. Amorim et al. (2020) presented the paleoenvironmental reconstruction for the Tamengo Formation based on detailed sedimentological and stratigraphic aspects for these sections (Fig. 6.3), whereas oxygen and carbon isotope data, carbonate and TOC contents and Sr/Ca ratios used in this study were provided by Caetano-Filho et al. (in prep.); (Table S1 – Supplementary Materials; Appendix C).

The Laginha section (Fig. 6.3) is a ~140 m-thick carbonate succession and represents shallow environments of the inner ramp, as oolitic banks and interbank lagoons. Carbonate rocks from the Tamengo Formation unconformably overlain the Bocaina Formation, marked by an erosive contact with deposition of a carbonate breccia interval. This carbonate breccia layer grades into intensively dolomitized oolitic grainstones to packstones, followed by a high frequency interbedding of wackestones and shaly-calcimudstones at the mid part of the section, representing deposition on interbank lagoons. These deposits end in an erosional unconformity and are overlain by oolitic grainstones, forming coarsening-upward cycles with subordinated occurrences of black shaly calcimudstones. At the top of the section, siltstones and mudstones of the Guaicurus Formation mark a major transgression over the carbonate ramp and the upper limit of the Tamengo Formation. $\delta^{13}C_{carb}$ profile starts with negative values close to −4‰ at the base in a positive excursion to values around +6‰. Negative values in the first 55m of the section are associated with dolomitization and were not taken as primary values (Caetano-Filho et al., in prep). Above the unconformity at the mid part of the section, $\delta^{13}C_{carb}$ are very stable around +3‰. $\delta^{13}C_{org}$ data present a small variation through the section, with values usually between −26 to −24‰. TOC contents are low, with average of 0.17%, but reach values up to 1% in the shaly interval at the mid section (Fig. 6.3).

The Corcal section is a 52 m-thick succession composed of two major shallowing-upward cycles representing mid ramp domains. The basal cycle starts with dark grey calcimudstones and siltstones grading to intraclastic/bioclastic wackestones, packstones and grainstones from mid ramp domain, representing higher rank shallowing-upward cycles (parasequences). These deposits bear remarkable bioaccumulations of *Cloudina* shell beds from the Tamengo Formation, whereas siliciclastic facies present well-preserved *Corumbella werneri* specimens. The upper cycle starts with a siltstone-calcimudstone interval which grades to more intraclastic wackestones, packstones and grainstones, also constituting minor shallowing-upward cycles, however, with minor occurrence of bioclasts compared with the basal cycle and abundant microbial mat fragments. Volcanic ash beds are frequent in the upper part of the section, presenting U-Pb ID-TIMS ages of 542.37 ± 0.28 Ma and 541.85 ± 0.75 Ma (Parry et al., 2017; Fig. 6.3). This section presents two different behaviors for $\delta^{13}C$ between its lower and upper major shallowing-upward cycles. The lower cycle encompasses higher variation of $\delta^{13}C_{carb}$ and $\delta^{13}C_{org}$, from +1 to +6‰ and from −27 to −20‰, respectively. These variations match parasequence cycles and were interpreted as a result of local heterogeneity in the DIC developed by enhanced oxic remineralization of organic carbon, associated with the bioaccumulations of *Cloudina* sp. (Caetano-Filho et al., in prep). In the upper cycle, $\delta^{13}C_{carb}$ and $\delta^{13}C_{org}$ profiles are more stable, ranging from +4 and +5‰ and −22 and −24‰, respectively. TOC values are very low and range from 0.02 to 0.10%, with average of 0.05%.

The Sobramil section is a 23 m-thick succession and represents the most distal deposits from distal mid ramp to outer mid ramp, deposited below the storm wave base level. This section records three shallowing-upward cycles, from calcimudstones at the base to intraclastic/bioclastic wackestones at the top, in which *Cloudina* bioclasts are rare. Shales and siltstones mark transgressions and the start of major shallowing-upward cycles. These siltstone layers present frequent occurrences of well-preserved *Corumbella werneri*. $\delta^{13}C_{carb}$ and $\delta^{13}C_{org}$ are very homogeneous, varying from +3 to +5‰ and from −25 to−23‰, respectively. TOC content varies from 0.01 to 0.90%, with average of 0.24%.

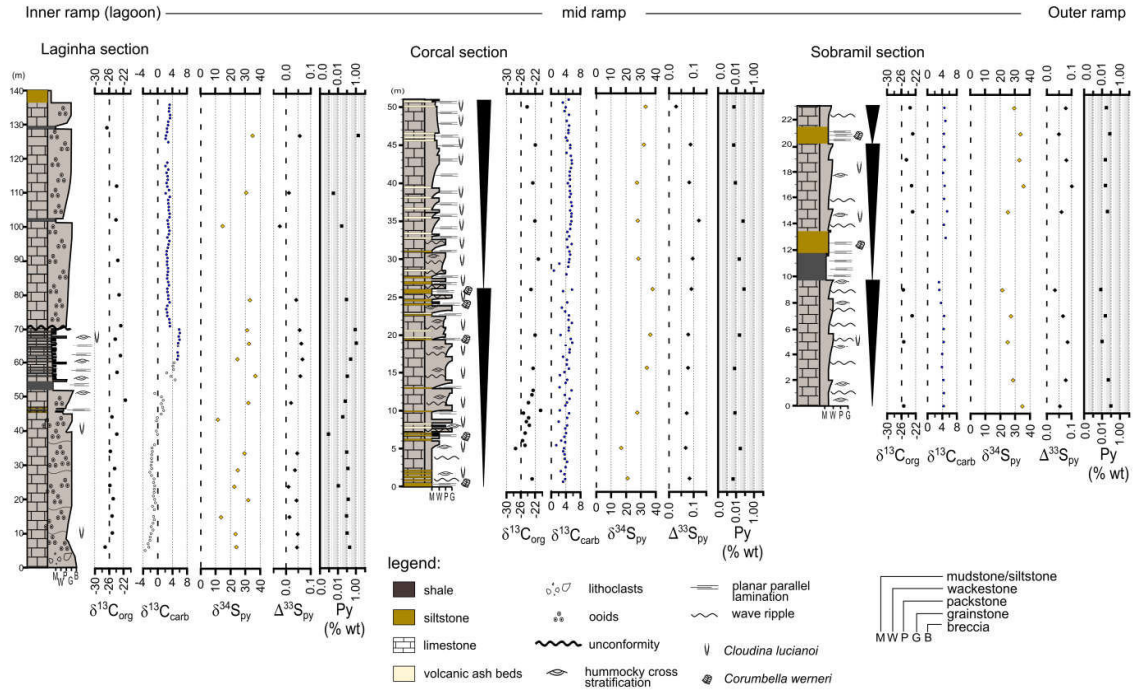

Figure 6.3: Studied sections from the Tamengo Formation and isotope chemostratigraphy. Detailed sedimentological and stratigraphic aspects accompanied by depositional model for the Tamengo mixed ramp were provided by Amorim et al. (2020). Paired carbon isotope data from Caetano-Filho et al. (in prep) given in ‰ (VPDB). $\delta^{34}S$ data given in ‰ (VCDT).

6.4.1.2. Bambuí Group, São Francisco Basin

The three sections analyzed in the Bambuí Group encompass the two lowermost sequences of the unit and represent different sectors of the epicontinental basin. The Well 1 section is a drillcore sampled at the southern Sete Lagoas basement high (Fig. 6.4) and record a syn-tectonic deposition within a forebulge graben (Reis and Suss, 2016). Januária and Santa Maria da Vitória sections are outcrop sections located at the northern Januária basement high, representing deposition in the paleohighs of the basin (Caetano-Filho et al., 2019). Detailed sedimentological/stratigraphic description, paired $\delta^{13}C$ data and TOC contents used in this study were provided previously by Reis and Suss (2016) and Caetano-Filho et al. (2019; 2020), and are summarized below. Stratigraphic correlation between the studied sections considered the 2nd-order stacking patterns and correlative surfaces (e.g. Reis and Suss, 2016; Caetano-Filho et al., 2019 and references therein; Fig. 6.4). The highstand systems tract was divided in early and late highstand systems tracts (EHST and LHST, respectively), based on a basin-wide increase in Sr/Ca ratios observed in these sections (Caetano-Filho et al., 2019).

Carbonate content, $\delta^{18}O_{carb}$ and Sr/Ca ratios used for post-depositional alteration assessment of sulfur isotope compositions (section 6.6.1; Table S1 –Appendix D) were presented previously by Caetano-Filho et al. (2019; 2020).

The Well 1 section is a 430 m-thick mixed siliciclastic-carbonate succession, encompassing deeper environments within a forebulge graben domain (Reis and Suss, 2016). The basal transgressive systems tract (TST) encompasses a thin layer of polymictic diamictite of the Carrancas Formation, which grades upward into microbial dolostones of the basal Sete Lagoas Formation (Fig. 6.4) and thick organic-rich black shales, marking the 2nd-order maximum flooding surface (MFS). The early highstand systems tract (EHST) starts with greenish siltstones interbedded with light gray limestones deposited in outer to mid-carbonate ramp setting. These strata grade upward into mid- to inner-carbonate ramp successions composed of dark-colored and detrital-lean intraclastic grainstones to packstones, mudstones oolitic grainstones and microbial limestones, representing the late highstand systems tract (LHST). A 2nd-order erosional surface recorded within supratidal carbonate deposits sets the sequence boundary (SB; Fig. 6.4). In the overlying 2nd-order sequence, dark gray microbial limestones of the upper Sete Lagoas Formation grade into fine-grained siliciclastics of the Serra de Santa Helena Formation and define the new transgressive systems tract (Fig. 6.4).

The Januária section is a ~140 m-thick carbonate-dominated succession located in a paleohigh domain. At the base, a cap carbonate succession of the lower Sete Lagoas Formation unconformably overlies Archean/ Paleoproterozoic basement. The cap carbonate is characterized by massive layers of calcimudstones and microbial limestones with aragonite pseudomorph crystal fans, which grade to reddish to pinkish calcimudstones to microbial limestones. The maximum flooding surface is set within an interval of more frequent pelitic layers interbedded in these limestones. The EHST comprises pinkish to light gray calcimudstones with hummocky cross-stratifications and abundant terrigenous clay laminae grading to dark gray microbial limestones deposited in mid ramp environments from the LHST. The end of LHST is dominated by flat-pebble intraclastic carbonate breccias, as products of exposure and reworking of inner ramp strata (Perrella Jr. et al., 2017; Caetano-Filho et al., 2019). Sequence boundary is set at the base of an overlying intertidal dolostone interval, at the top of Sete Lagoas Formation. Siltstones from the Serra de Santa Helena Formation represent the new transgression in the overlying sequence, followed by deposition of shallow water carbonate facies from the Lagoa do Jacaré Formation, as laminated calcimudstones, intraclastic grainstones and layers of carbonate breccias.

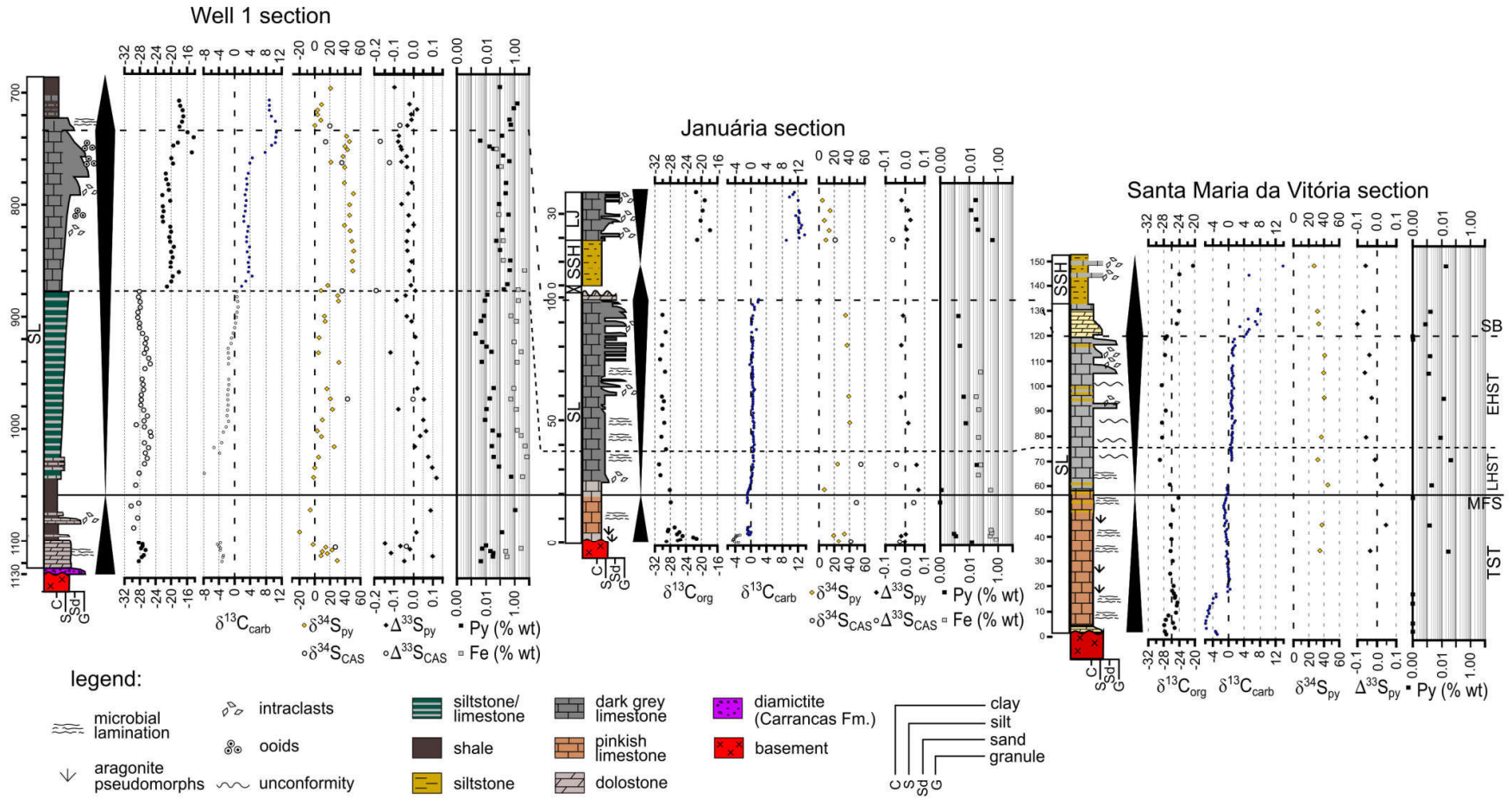

Figure 6.4: Studied sections from the basal Bambuí Group and chemostratigraphy. Detailed sedimentological, stratigraphic aspects and stratigraphic correlation for the sections were provided by Reis and Suss (2016) and Caetano-Filho et al. (2019). Paired carbon isotope data from Caetano-Filho et al. (2019; 2020) given in ‰ (VPDB). $\delta^{34}S$ data given in ‰ (VCDT). Lithostratigraphic units: SL – Sete Lagoas Formation; SSH – Serra de Santa Helena Formation; LJ – Lagoa do Jacaré Formation.

The Santa Maria da Vitória section is a ~150 m-thick carbonate dominated succession which records the shallowest facies among the studied sections. The basal sequence is represented by the lower Sete Lagoas Formation, starting with beige dolostones unconformably overlying the Paleoproterozoic basement. These dolostones grade to pinkish to reddish calcimudstones to microbial limestones, with occasional occurrences of aragonite pseudomorph crystal fans. The maximum flooding surface is represented by an interval of more frequent pelitic intercalations. Deposits from the EHST start with dark grey calcimudstones from mid ramp which grade upward to intraclastic grainstones and flat-pebble carbonate breccias from inner ramp domains representing the LHST, very similar to the Januária section. The sequence boundary is represented by a thin layer of a paleosol, followed by a new transgression represented by intertidal dolostone facies, as dolograinstones with cross-stratications and columnar stromatolites. This dolostone interval grades into light gray calcimudstones followed by a thick interval of siltstones and mudstones from the Serra de Santa Helena Formation, presenting carbonate lenses of intraclastic grainstones.

The paired $\delta^{13}C$ evolution of the basal Bambuí Group is in a good agreement with the 2^{nd}-order stratigraphic trends in the basin-scale (Caetano-Filho et al., 2019; 2020), and can be described in terms of the systems tract:

(i) The transgressive systems tract is represented by the basal Sete Lagoas Formation and is characterized by the cap carbonate excursions, with $\delta^{13}C_{carb}$ in a negative excursion to values around −5‰ followed by increases upward to values around 0‰ with the $\delta^{13}C_{org}$ in an antithetical behavior, starting with a $\delta^{13}C_{org}$ increase from about −29‰ to about −25‰, but with a highest value of ~ −21‰ in Januária section, followed by a decline to values of about −30‰ (Fig. 6.4).

(ii) The highstand systems tract, at the middle of the Sete Lagoas Formation, present $\delta^{13}C_{carb}$ plateaus around 0‰, except for Well 1 section (Fig. 6.4). $\delta^{13}C_{org}$ profiles also form plateaus at values in between −30‰ and −25‰. Well 1 section shows a distinct pattern for this interval. $\delta^{13}C_{carb}$ varies from around −2‰ in the mixed siliciclastic-carbonate EHST interval at the beginning of regression, to +4‰ in the carbonate-dominated LHST interval. A similar shift is also observed in the $\delta^{13}C_{org}$ which increases from −27‰ to −21‰. This lithological control over isotope shifts within HST interval of the Well 1 led to the dismissing of isotope compositions from the EHST in terms of primary signals. High amounts of siliciclastic represent more favorable conditions to post-depositional alteration of both $\delta^{13}C_{carb}$ and $\delta^{13}C_{org}$ (Caetano-Filho et al., 2020).

(iii) At the end of the highstand systems tract in Well 1 section and through the overlying sequence in all section, a coupled $\delta^{13}C$ positive excursion is observed and reaches extremely heavy isotope compositions (up to +14‰ for $\delta^{13}C_{carb}$ and to −14‰ for $\delta^{13}C_{org}$; Fig. 6.4; Caetano-Filho et al., 2020). This positive $\delta^{13}C$ excursion was named as the Middle Bambuí Isotope Excursion (Uhlein et al., 2019) and represents extreme paleoenvironmental disturbances in the basin carbon cycle, probably driven by enhanced restriction due to late Neoproterozoic orogen build-ups surrounding the basin (Paula-Santos et al., 2017; Uhlein et al., 2019; Caetano-Filho et al., 2020).

6.4.2. Multiple sulfur isotope analyses from sulfides and sulfates

Sulfides were recovered for multiple sulfur isotope analysis through the Chromium-Reducible Sulfide extraction protocol (CRS; Canfield et al., 1986) at the Sulfur Laboratory from the Institut de Physique du Globe de Paris (IPGP), France. About 1 to 15 g of whole-rock powder was initially acidified with 5 to 50 mL of HCl 6 N, at sub-boiling temperature during ~2h, to remove Acid Volatile Sulfides (AVS fraction, e.g. monosulfides). After this, about 20 mL of the CRS solution, obtained by reaction of 60 mg of granular Zn with 104 g of $CrCl_3$ and 250 mL of HCl 0.6 N, was added to the samples at sub-boiling temperature. H_2S liberated from the sample was reacted with $AgNO_3$ solution for conversion into Ag_2S precipitates, representing mostly pyrite fraction of the sample. In the carbonate facies, pyrite occurs as framboids clusters to small subhedral crystals (10 to 70 μm) distributed within the matrix associated with organic matter (Fig. 6.5). In black shales from Well 1 section, there are very fine framboidal pyrites (10 to 50 μm) concentrated in thin laminae and also larger subhedral to euhedral crystals (up to 3 mm).

The sulfate fraction analyzed corresponds to the Carbonate Associate Sulfate (CAS; e.g. Kampschulte and Strauss, 2004), as trace amounts of sulfate present in the lattice of carbonate minerals. The extraction of $BaSO_4$ from the carbonate samples was carried out at the Laboratoire Domaines Océaniques from the University of Western Brittany, in Brest, France. About 65 to 225 g of whole-rock powders were rinsed three times with 700 mL of 10% NaCl solution, aiming to remove soluble sulfates. After this first rinsing, samples were rinsed three times with deionized water. Then, samples were dissolved with 5N HCl. For a complete dissolution of the carbonate fraction, samples were left in a magnetic stir plate overnight. Dissolved samples were filtered in a 0.45-mm nitrocellulose paper and $BaCl_2$ was added in excess to the leachate. $BaSO_4$ precipitates were recovered after three days of

reaction. Finally, $BaSO_4$ precipitates were reacted with Thode reagent (Thode et al., 1961) at the IPGP Sulfur Laboratory and the released H_2S was converted in Ag_2S by reaction with $AgNO_3$. CAS and pyrite contents were calculated by stoichiometric conversion of $BaSO_4$ and Ag_2S recovered, respectively, compared to whole-rock.

Multiple sulfur isotope compositions ($^{33}S/^{32}S$, $^{34}S/^{32}S$ and $^{36}S/^{32}S$) were measured through the fluorination technique at the Sulfur Laboratory of the IPGP. First step consists in converting about 1.5 mg of Ag_2S in SF_6 by heating in nickel bombs at ~350 ºC overnight. The SF_6 produced is separated through cryogenic technique in a vacuum line followed by gas chromatography. Multiple sulfur isotope compositions from SF_6 molecules were determined in the Thermo Finnigan MAT 253 isotope ratio mass spectrometer.

Sulfur isotope compositions are presented in standard delta notation, with $\delta^{34}S$ reported against Vienna Cañon Diablo Troilite standard (V-CDT). $\Delta^{33}S$ and $\Delta^{36}S$ were calculated following the equation (e.g. Farquhar and Wing, 2003):

$$\Delta^{3x}S = \delta^{3x}S - 1000 \times [(1 + \delta^{34}S/1000)^{3x\lambda} - 1]$$

where, $^{3x}\lambda$ is the fractionation relationship for mass-dependent processes ($^{33}\lambda = 0.515$ and $^{36}\lambda = 1.89$). $\delta^{34}S_{VCDT}$, $\Delta^{33}S$ and $\Delta^{36}S$ results presented analytical reproducibility of 0.5‰, 0.01‰ and 0.3‰, respectively, based on duplicate analyses. Uncertainties for $\delta^{34}S_{VCDT}$, $\Delta^{33}S$ and $\Delta^{36}S$ values are 0.1‰, 0.01‰ and 0.1‰, respectively, based on the analyses of IAEA-S-1 standard (n = 20).

Rayleigh equations applied for sulfate distillation model are given in terms of isotope ratios ($R = {}^{3x}S/^{32}S$): $^{3x}R_{res} = {}^{3x}R_{initial} \times F^{(3x\alpha-1)}$, for residual sulfate; $^{3x}R_{ip} = {}^{3x}\alpha \times {}^{3x}R_{initial} \times F^{(3x\alpha-1)}$) for the instantaneous sulfide; and $^{3x}R_{pp} = [{}^{3x}R_{initial} \times (1-F^{3x\alpha})] / (1 - F)$ for the pooled sulfide (e.g. Canfield, 2001; Sansjofre et al., 2016). F is the fraction of residual sulfate and $^{3x}\alpha$ represents the isotope fractionation between sulfate and sulfide, in which $^{3x}\alpha = {}^{34}\alpha^{3x\lambda}$. Isotope ratios were converted in deltas by $\delta = (R - 1) \times 1000$. Mixing lines between $\delta^{3x}S_{res}$ and $\delta^{3x}S_{pp}$ follows the prediction $\delta^{3x}S_{mix} = f_{mix} \times \delta^{3x}S_{res} + (1-f_{mix}) \times \delta^{3x}S_{pp}$, in which f_{mix} is the fraction of $\delta^{3x}S_{res}$ in the mixing and $\delta^{3x}S_{mix}$, $\delta^{3x}S_{res}$ and $\delta^{3x}S_{pp}$ are the isotope composition of mixing product, residual sulfate and pooled sulfide, respectively, for a given F. Rayleigh parameters are presented in Table S2 and S3 – Supplementary materials; Appendix D).

6.4.3. Fe concentrations

Fe concentrations from 38 samples from the Bambuí Group were analyzed in the ALS Global laboratories, by using a combination of nitric, perchloric, hydrofluoric, and

hydrochloric acid aiming to promote complete digestion of ~0.25 g rock powders to be measured by ICP-MS technique. Average reproducibility was 0.02% by measuring duplicates.

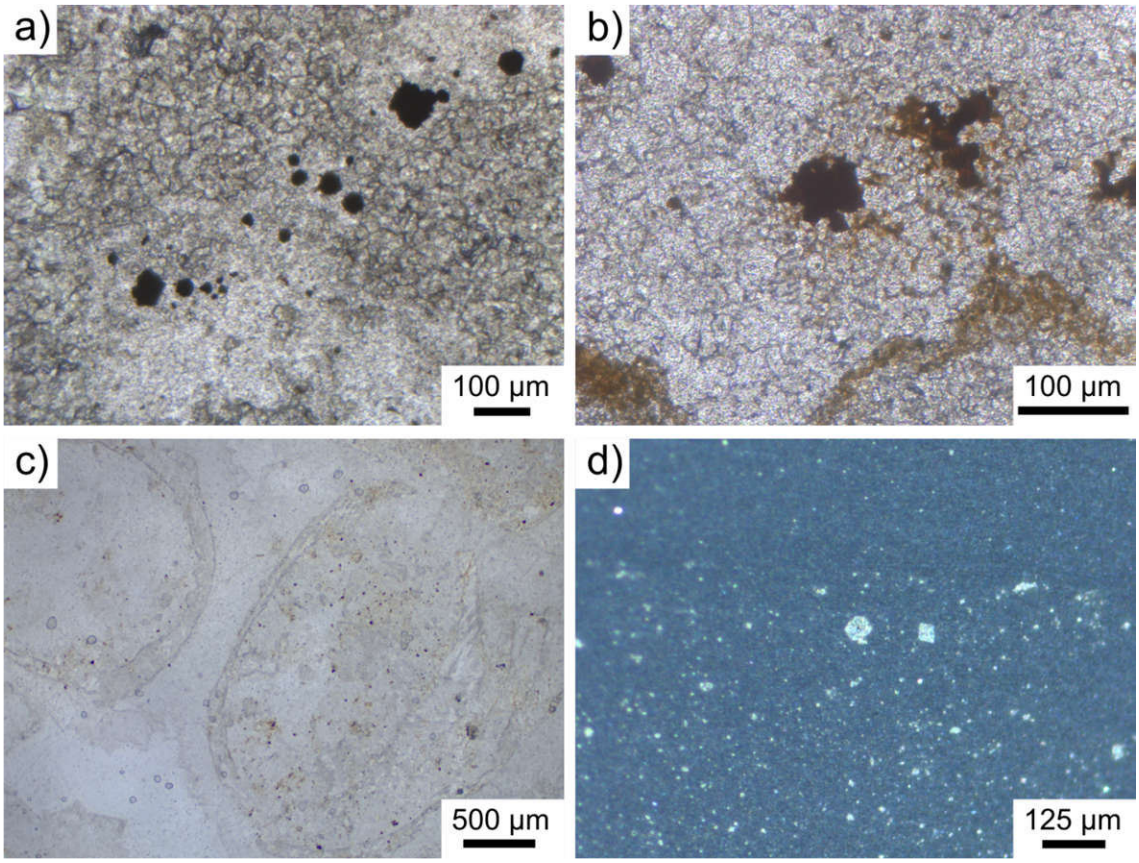

Figure 6.5: Pyrite textures within studied rocks. a) and b) Pyrite framboids within carbonate matrix from carbonate rocks of the Bambuí Group. c) Overview of a bioclastic grainstone with *Cloudina* fragments from the Corcal section, Tamengo Formation. Fine framboidal pyrites are dispersed through the matrix. d) Framboidal and cubic pyrites in black shales from Well 1 section, Bambuí Group.

6.5. Results

Seventy six samples from the Bambuí Group had their multiple sulfur isotope compositions analyzed for pyrite fraction, whereas 10 samples had their CAS recovered and analyzed (Table S1 – Appendix D). Pyrite content in the samples ranges between 0.0 to 1.5%, with average of 0.1%. Sulfur isotope compositions from pyrite vary between: $\delta^{34}S_{py(VCDT)}$ from −19.9 to +51.2‰; $\Delta^{33}S_{py}$ from −0.43 to +0.12‰; and $\Delta^{36}S_{py}$ from −1.4 to +0.7‰. Pyrite samples provided a $\Delta^{36}S/\Delta^{33}S$ slope of −6.71 (Fig. 6.6). Four samples from the base of Well 1 section presenting high deviations of $\Delta^{33}S_{py}$ (0.10‰; −0.12‰; −0.43‰; and −0.15‰) were

taken as outliers, strongly deviating from $\Delta^{36}S/\Delta^{33}S$ slope for mass-dependent fractionation processes (e.g. Ono et al., 2006). These samples are few meters above lithological contact with Archean basement (Reis and Suss, 2016) and may have assumed mass-independent (MIF) signatures from these rocks during late diagenesis processes. CAS content from the Bambuí Group samples are very low, varying from 0 to 30 ppm, with average of 5 ppm (n=19). Sulfur isotope analyses from recovered CAS fractions vary from: +14.2 to +54.6‰ for $\delta^{34}S_{CAS(VCDT)}$; −0.19 to +0.05‰ for $\Delta^{33}S$; and 0.0 to +0.1 for $\Delta^{36}S$. Bambuí Group sulfur isotope data present mass-dependent fractionation relationships of $^{33}\lambda = 0.512$ and $^{36}\lambda = 1.894$ (Fig. S1 – Appendix D). $\Delta^{34}S_{CAS\text{-}py}$ varies significantly from −31.5 to +30.2‰, with average of +13.7‰ (n=9). Fe concentrations vary from 0.03 to 6.25%, with average of 1.09% (n=38).

Regarding sulfur chemostratigraphy in the basal Bambuí Group, sulfur isotope trends are coupled with the basinal stratigraphic evolution established for these sections, from shallow to deep domains of the basin (Fig. 6.4). For the Well 1 and Januária sections, $\delta^{34}S_{py(VCDT)}$ presents a negative excursion through the initial transgression at the base of the Sete Lagoas Formation, reaching −20‰ in the Well 1 section, whereas in the Santa Maria da Vitória section samples from the basal TST interval did not provide pyrite for measurements, probably due to the paleodepositional oxidizing conditions proposed for this interval (Fig. 6.4; Caxito et al., 2018). The regressive stage (HST) is marked by a positive excursion reaching superheavy pyrite values (> +40‰) towards the top of all sections. The new transgression in the overlying sequence is marked by a new negative excursion to values close to 0‰, except for the Santa Maria section in which values do not decrease below +20‰. $\Delta^{33}S_{py}$ profiles seem to present in antithetical behavior compared to $\delta^{34}S_{py(VCDT)}$, increasing during the initial transgression in Januária and Well 1 section, and decreasing to negative values throughout the regressive stage. The second transgressive stage in the overlying sequence is marked by a new increase of $\Delta^{33}S_{py}$ values. Fe concentrations obtained for the basal sequence shows an increase during the initial transgression followed by a decrease to very low concentrations throughout the regressive stage in both sections (Fig. 6.4).

In the Tamengo Formation, 38 samples had their pyrite fraction analyzed for multiple sulfur isotope compositions (Table S1 – Appendix D). Pyrite contents vary between 0.0 and 1.8%. $\delta^{34}S_{py(VCDT)}$ ranged from +11.5 to +37.8‰; $\Delta^{33}S_{py}$ from −0.03 to +0.12‰; and $\Delta^{36}S_{py}$ from −0.8 to 0.0‰. Sulfur isotope data present mass-dependent fractionation relationships of $^{33}\lambda = 0.515$ and $^{36}\lambda = 1.892$ (Fig. S1 – Appendix D), with a $\Delta^{36}S_{py}/\Delta^{33}S_{py}$ slope of −4.84 (Fig. 6.6). Regarding chemostratigraphy, the Tamengo Formation did not show common trends between the sections, as observed in the Bambuí Group (Fig. 6.3). In the most proximal

Laginha section, $\delta^{34}S_{py(VCDT)}$ are scattered between +10 and +40‰, and roughly resemble to minor positive excursions associated with coarsening-upward cycles. The most distal Sobramil section show a decreasing $\delta^{34}S_{py(VCDT)}$ trend from +40 to +20‰ in the basal shallowing-upward cycle, followed by a positive excursion to values around +30‰ in the upper cycles. Finally, the mid ramp Corcal section presents more clear $\delta^{34}S_{py(VCDT)}$ trends coupled to the two major shallowing-upward cycles, similar to the observed for all the sections analyzed in the Bambuí Group (Fig. 6.4). In the basal cycle, $\delta^{34}S_{py(VCDT)}$ values increase from about +20 to +40‰, with a slightly decrease through the overlying cycle, reaching values around +30‰ followed by a new positive excursion to values close to +40‰ in the top of the second shallowing-upward cycle (Fig. 6.3). $\Delta^{33}S_{py}$ profiles do not show a typical trend for all the sections, and varies between 0.00 to +0.01‰, lacking negative values observed in the Bambuí Group.

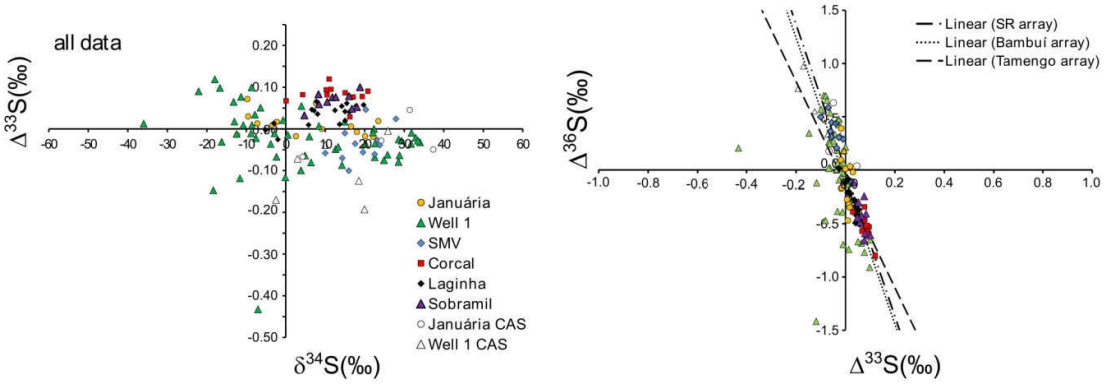

Figure 6.6: Multiple sulfur isotope data for the Tamengo Formation and Bambuí Group. Sulfate-reduction slope (SR array) of −6.85 plotted in the $\Delta^{33}S$ *vs* $\Delta^{36}S$ diagram from Ono et al. (2006).

6.6. Discussion

6.6.1. Assessment of primary sulfur isotope compositions

6.6.1.1. CAS

Past studies have discussed about the potential influence of early to late diagenesis over CAS concentrations and sulfur isotope compositions (e.g. Staud and Schoonen, 1995; Gill et al., 2008; Fichtner et al., 2017). It is relatively well established that increasing burial leads to decreasing CAS content, which prevents the interpretation of these values as a direct proxy of marine sulfate concentrations. On the other hand, $\delta^{34}S_{CAS}$ seems to be relatively

robust face to CAS loss during burial, with no correlation between $\delta^{34}S_{CAS}$ and [CAS] in the literature (e.g. Staud and Schoonen, 1995; Fichtner et al., 2017). This is also observed from our samples analyzed in the Well 1 and Januária sections, Bambuí Group, in which there is no clear trend for [CAS] *vs* $\delta^{34}S_{CAS}$ relationship (Fig. 6.7A). Considering effects of meteoric diagenesis at any stage of the geological evolution of the sections, despite meteoric fluids have low sulfate concentrations resulting in a CAS decrease in neoformed carbonates, Gill et al. (2008) demonstrated that Pleistocene carbonate rocks under severe meteoric influence kept their primary $\delta^{34}S_{CAS}$ signatures close to the coeval seawater. By analyzing the $\delta^{34}S_{CAS}$ relationship with Sr/Ca and $\delta^{18}O_{carb}$ (Fig. 6.7B and C, respectively), there is no clear influence of low Sr/Ca ratios and low $\delta^{18}O_{carb}$ values over $\delta^{34}S_{CAS}$ to argue for an alteration driven by meteoric diagenesis.

During early diagenesis, neomorphism (e.g. dolomitization) and authigenesis can be responsible for $\delta^{34}S_{CAS}$ signatures that differ from marine conditions. Precambrian dolostones usually present higher $\delta^{34}S_{CAS}$ compared with coeval limestones, which is ascribed to influence of ^{34}S-enriched sulfate derived from microbial sulfate reduction in pore water, representing a close system under distillation (e.g. Kah et al., 2004; Hurtgen et al., 2006). Sr/Ca *vs* $\delta^{34}S_{CAS}$ diagram (Fig. 6.7A) shows the predominantly calcitic nature of the samples analyzed with high Sr/Ca ratios, and no negative trend is observed to suggest the association of high $\delta^{34}S_{CAS}$ values with low Sr/Ca ratios which accompany dolostone samples (Caetano-Filho et al., 2019; in prep). Authigenic influence over CAS isotope signatures derives from both sulfide oxidation and sulfate reduction in the sedimentary environments (e.g. Kampschulte and Strauss, 2004; Gill et al., 2008). Microbial sulfate reduction would drive $\delta^{34}S_{CAS}$ to positive values due to Rayleigh distillation effect on the pore water system, whereas sulfide oxidation would result in a negative trend due to oxidation of ^{34}S-depleted sulfide produced by microbial sulfate reduction. Considering that both metabolisms can be related to the pyrite precipitation, pyrite content *vs* $\delta^{34}S_{CAS}$ diagram (Fig. 6.7D) does not exhibit any trend to account for the influence of these early diagenetic reactions over $\delta^{34}S_{CAS}$. We therefore interpret the Bambuí Group $\delta^{34}S_{CAS}$ data as derived from the environments where carbonate minerals were precipitated.

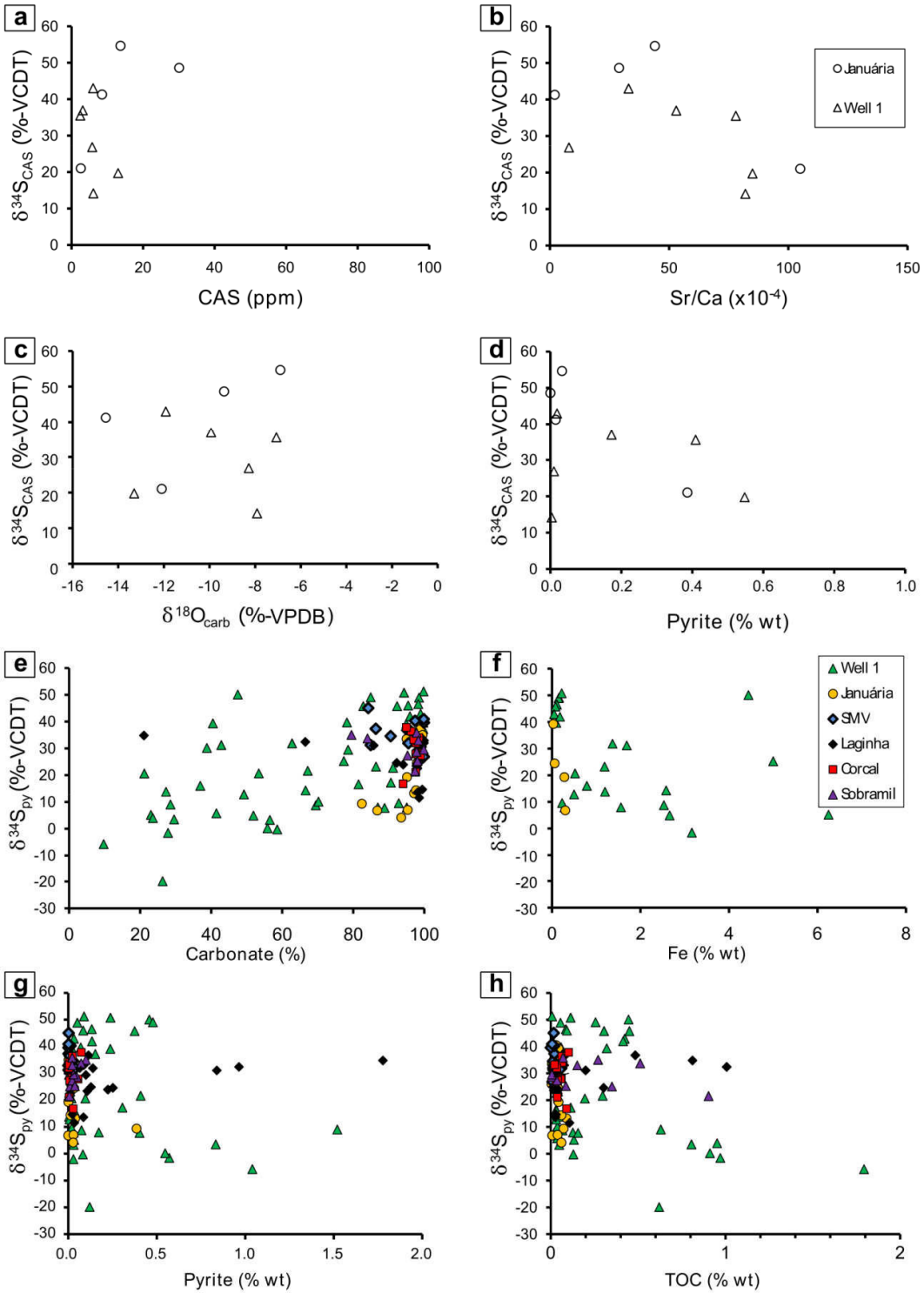

Figure 6.7: Geochemical diagrams for assessment of post-depositional alteration over sulfur isotope compositions from CAS and pyrites.

6.6.1.2. Sulfides

Despite sulfur isotope compositions from pyrites being highly influenced by local conditions in the sedimentary environments, mainly related to controls operating microbial sulfate reduction (e.g. sulfate and organic substrate availability, rate of sulfate reduction; Canfield, 2001), $\delta^{34}S_{py}$ would be less sensitive to post-depositional alterations compared with sulfates. Isotope heterogeneities would occur in the early diagenetic environment due to distillation effects over sulfate reservoir in the pore water system, leading to heavier sulfur isotope compositions from the core to the border of pyrite cumulates (e.g. Kohn et al., 1998). Regarding anomalous superheavy pyrites, they commonly present $\delta^{34}S_{py}$ values higher than the coexisting sulfate, which challenge the knowledge about sulfur isotope fractionation driven by microbial sulfate reducing communities. Recent studies based on $\delta^{34}S_{py}$ SIMS analyses showed the association of superheavy pyrites with hydrothermal features in Cryogenian and late Devonian strata from China, leading to the inference that these isotope signatures would be a product of Thermochemical Sulfate Reduction (TSR) during late diagenesis (Cui et al., 2018; Yan et al., 2020). Therefore, it is important to discuss and compare our data in face of these recent observations from China before interpreting the observed trends.

Cui et al. (2018) reported homogeneous superheavy $\delta^{34}S_{py}$ values of +56 to +60‰ in late diagenetic framboidal to lacy pyrites from Mn-rich carbonate rocks of the Cryogenian Datangpo Formation in South China, through *in situ* SIMS analyses. The authors argue that the occurrences of superheavy pyrites in the Datangpo Formation do not present a basin wide lateral correlation and are more related to carbonate successions accompanied by several features of pervasive hydrothermal events of sulfate-rich fluids. In this sense, these extreme isotope signatures would be a result of Rayleigh distillation during TSR. Besides the fact that these superheavy pyrites overgrowth late mineralization of rhodochrosite and illite, these successions are close to zone of ancient faults and present gypsum and barite-filled veins, supporting a late diagenetic origin. Additionally, they suggest that the common negative correlation between Fe content *vs* $\delta^{34}S_{py}$ observed in the Datangpo Formation would be a result of the Rayleigh distillation effect over pyrite precipitation during TSR. Lower $\delta^{34}S_{py}$ values associated with higher pyrite content (and so Fe content) would represent the early TSR stage and superheavy $\delta^{34}S_{py}$ values coupled with lower pyrite content would result from low Fe availability during late stages of TSR.

Considering this robust data supporting a TSR genesis for superheavy pyrites from the Cryogenian strata in China, we present the main features from our samples to argue for a primary to early diagenetic genesis for the continental-scale superheavy pyrite trends observed in both West Gondwana basins:

(i) Regarding the clear relationship between superheavy pyrites from Cryogenian and late Devonian carbonate rocks from China with post-depositional hydrothermal mineralizations, our samples do not present any late diagenetic paragenesis. Although carbonate rocks from the Bambuí Group and Tamengo Formation present some degree of recrystalization, pyrite are mixed within the predominantly calcite carbonate matrix, varying from small framboids to subhedral crystals (Fig. 6.5).

(ii) In the major scale, especially considering the intracratonic Bambuí Group, the sections are not related to major fault systems or any evidence of pervasive hydrothermal events in this stable portion of the continent since Neoproterozoic Era. Different from the Datangpo Formation, the Bambuí Group presents solid basin-wide $\delta^{34}S_{py}$ trends associated with the 2nd-order regressive cycle within the basal sequence through different sectors of the basin (Fig. 6.4). Thicknesses from these trends vary accompanying different sedimentary rates from each domain of the basin (graben *vs* paleohighs), supporting a paleoenvironmental evolution of the basinal sulfur system.

(iii) Besides basin scale $\delta^{34}S_{py}$ excursions from Bambuí Group, our samples do not show a carbonate facies-bias for superheavy pyrite values (Fig. 6.7E), represented by positive $\delta^{34}S_{py}$ excursions in both carbonate-dominated Januária section and in the mixed carbonate-siliciclastic Well 1 section (Fig. 6.4E).

(iv) The association between negative [Fe] *vs* $\delta^{34}S_{py}$ correlations with decreasing pyrite content and increasing $\delta^{34}S_{py}$ values does not hold for our data. First, although it is observed a decrease in Fe content in the superheavy $\delta^{34}S_{py}$ interval in the end of the regression at the basal Bambuí Group (Fig. 6.4), there are no significant correlations for Fe and pyrite content *vs* $\delta^{34}S_{py}$ in our samples (Fig. 6.7F and G, respectively). Furthermore, Fe content cannot be directly associated with pyrite content, as it is observed for the Well 1 section. Although Fe concentrations decreases throughout the regressive stage, mixed carbonate-siliciclastic deposits from the Well 1 at the initial regression have a higher Fe content and lower pyrite occurrence whereas detrital-lean carbonate rocks from the late regressive stage presents higher pyrite occurrence and lower Fe concentrations (Fig. 6.4).

In sum, the most important feature observed from the Bambuí Group and Tamengo Formation is the striking coincidence between positive $\delta^{34}S_{py}$ excursions to superheavy values

with shallowing upward cycles (i.e. regressions) in both basins. They are not facies-biased and match variable thicknesses for the identified systems tract, i.e. isotope trends follows specific sedimentary rates from different depositional environments. Apart the lack of evidence for hydrothermal influence over studied samples, this stratigraphic-chemostratigraphic association makes a TSR influence over pyrite sulfur isotope signatures unlikely in our case of study. Our sections were subject to different burial conditions, i.e. different geothermal gradient. In the Bambuí Group, Well 1 section represents a thick succession buried in a forebulge graben setting, whereas Januária and Santa Maria da Vitória sections represents outcrops from paleohighs (Reis et al., 2016; Reis and Suss, 2016; Caetano-Filho et al., 2019). On the other hand, sections from the Tamengo Formation in the Paraguay Belt were rapidly deformed after deposition by a late Ediacaran-Cambrian orogeny in the Western Gondwana. Therefore, it is very unlikely that similar burial conditions operated in these distinct settings to account for homogeneous TSR-derived isotope trends.

Additionally, TSR would depend on both organic matter and sulfate availability. Studied units are depleted in CAS (Table S1 – Appendix D) and no sulfate-rich unit is recognized so far in the surroundings of studied areas to supply sulfate rich fluids for a homogeneous TSR influence. Regarding the organic matter content, TOC *vs* $\delta^{34}S_{py}$ diagram does not show any direct correlation to account for enhanced effect of a TSR-driven Rayleigh distillation effect over $\delta^{34}S_{py}$ values in organic rich intervals (Fig. 6.7H). In fact, organic rich intervals from the Well 1 section presents the lighter sulfur isotope compositions, associated with maximum flooding surfaces (Fig. 6.4). Finally, we do not dismiss the possible TSR influence over superheavy $\delta^{34}S_{py}$ values from Chinese deposits (Cui et al., 2018a; Yan et al., 2020), however, it does not seem to be applicable in our case which represents continental scale trends through late Ediacaran strata. Important to stress that several geochemical proxies present the same stratigraphic-chemostratigraphic coupling in the Bambuí Group, e.g. REE patterns (Paula-Santos et al., 2020), $^{87}Sr/^{86}Sr$ ratios (Paula-Santos et al., 2017; Caetano-Filho et al., 2019; Guacaneme et al., under review), and Li isotopes (Paula-Santos et al., in prep.a, b), supporting a paleodepositional and relative sea-level control over seawater chemistry.

6.6.2. Superheavy pyrite trends and sulfate distillation through regressive cycles in shallow platforms and restricted seas: insights from multiple sulfur isotope data

Superheavy pyrites are characterized by extremely ^{34}S-enriched isotope compositions which are usually higher than the coexisting sulfate ($\delta^{34}S_{py} > \delta^{34}S_{CAS}$). In the late Ediacaran interval from the Nama Group, Ries et al. (2009) reported highly variable $\delta^{34}S_{py}$ values reaching up to +80‰, in an interval of low CAS concentrations, which led to the interpretations of low sulfate conditions. On the other hand, the average $\Delta^{34}S_{CAS\text{-}py}$ of −8‰ reported by these authors was ascribed to low sulfate conditions and minor isotope fractionation during microbial sulfate reduction coupled to sulfide reoxidation, leading to ^{34}S-depleted sulfate compared with the parental ^{34}S-enriched sulfide. Later, Tostevin et al. (2017) interpreted that high $\delta^{34}S_{CAS}$ (30 to 38‰) and $\delta^{34}S_{py}$ values in the late Ediacaran Nama Group would be a product of low sulfate concentrations and/or high rates of microbial sulfate reduction (i.e. decreased isotope fractionation). Additionally, they suggested that low $\Delta^{34}S_{CAS\text{-}py}$ values (< +6.6‰) could have been compromised by early diagenesis processes (sulfate-poor closed-systems; e.g. Gomes and Hurtgen, 2015) and that different redox conditions and variable re-oxidation of sulfide would explain the large difference between low $\Delta^{34}S$ from the Nama Group and high $\Delta^{34}S$ values from late Ediacaran deposits from Oman and China (e.g. Fike and Grotzinger, 2008; Cui et al., 2016). However, apart discussion concerning the $\delta^{34}S_{py} > \delta^{34}S_{CAS}$ condition for superheavy pyrites and anomalous $\Delta^{34}S_{CAS\text{-}py}$ values, the mechanisms behind the unusual ^{34}S-enrichment remain unsettled (e.g. Canfield, 2004; Tostevin et al., 2017).

Despite pyrite-sulfur isotope signatures being strongly controlled by local processes mainly related to sulfate reduction conditions, our data reinforce that $\delta^{34}S_{py} >$ +40‰ is a very common feature throughout the late Ediacaran-early Cambrian interval from West Gondwana basins (Tamengo Formation and Bambuí Group, Brazil; this study; and Nama Group; Namibia; Ries et al., 2009). Equally ^{34}S-enriched CAS isotope compositions found here are compatible with late Ediacaran $\delta^{34}S_{sulfate}$ data worldwide (Halverson and Hurtgen, 2007; Fike and Grotzinger, 2008; Cui et al., 2016; Tostevin et al., 2017). Low CAS concentrations also seems to be another characteristic within West Gondwana basins (average of 5 ppm, n = 19, for this study, and 69 ppm for the late Ediacaran strata from Nama Group; Tostevin et al., 2017). These observations allied to a high variability of $\delta^{34}S_{CAS}$ in the late Ediacaran support

a scenario of low concentrations and low residence times for sulfate in these environments which will be explored below (e.g. Tostevin et al., 2017).

The Bambuí Group present solid lateral correlation for the trends throughout the basin, with a negative $\delta^{34}S_{py}$ excursion in the initial transgressive systems tract, followed by a long positive excursion reaching superheavy $\delta^{34}S_{py}$ values in the end of the regressive stage ($\delta^{34}S_{py}$ up to +51‰; Fig. 6.4). The second transgression in the overlying sequence is accompanied by a negative $\delta^{34}S_{py}$ excursion reaching low values close to 0‰ in the Well 1 and Januária sections, suggesting a control from relative sea-level change over $\delta^{34}S_{py}$ trends. This is also observed in the two major shallowing upward cycles which compose the Corcal section in the Tamengo Formation, representing mid ramp domains (Amorim et al., 2020) with $\delta^{34}S_{py}$ positive excursions reaching values around +40‰ at the end of each cycle. The Laginha section also seems to present short positive $\delta^{34}S_{py}$ excursions in minor oolitic-dominated shallowing-upward cycles, whereas the most distal Sobramil section does not present a clear trend (Fig. 6.3). It could be related to higher sedimentary rates in the inner ramp lagoon (Laginha section) and lower sedimentary rates in the outer ramp (Sobramil section) which may hinder the observation of these cycles due to sampling-resolution. In this case, the mid ramp Corcal section would represent more favorable resolution for the analysis of similar trends described in the Bambuí Group.

Multiple sulfur isotope data presented here provide further inferences on the causes of possible sulfate-depletion events linked to superheavy pyrite trends throughout the regressive cycles from West Gondwana basins. To explore the isotope effect expected for a scenario of sulfate distillation during regressive cycles, the obtained data were plotted in the $\delta^{34}S$ *vs* $\Delta^{33}S$ diagrams with predictions for the residual sulfate, instantaneous sulfide and pooled sulfide, following Rayleigh equations (section 6.4.2). A $^{33}\lambda$ of 0.512 was used for the Bambuí Group (Fig. 6.8A), whereas a $^{33}\lambda$ of 0.515 was applied for the Tamengo Formation (Fig. 6.8B), following respective mass-dependent fractionation relationships obtained for each unit (Table S1 – Appendix D). $\delta^{34}S$ values for the initial sulfate were set as +35‰ and +30‰, whereas $^{34}\alpha_{sulfate\text{-}sulfide}$ were set as 0.945 and 0.955, for the Bambuí Group and Tamengo Formation, respectively. The goal is to qualitatively illustrate multiple sulfur isotope evolution through decreasing fractions of the residual sulfate as a result of microbial sulfate reduction followed by pyrite burial in a sulfate-limited reservoir. Considering high variability of $\delta^{34}S_{CAS}$ and $\Delta^{34}S_{sulfate\text{-}sulfide}$ in the terminal Neoproterozoic, the chosen $\delta^{34}S_{initial\ sulfate}$ and $^{34}\alpha_{sulfate\text{-}sulfide}$ were set arbitrarily to fit the data spreading in each case. Nevertheless, these values are within the range considering $\delta^{34}S_{sulfate}$ data for other late Ediacaran basins (e.g. Tostevin et al., 2017 and

references therein) and isotope fractionation effect driven by microbial sulfate reduction, accompanied or not by sulfur disproportionation (e.g. Canfield, 2001). We assume that pyrite analyzed from bulk samples would represent a product from a pooled sulfide reservoir within the basins.

For the Bambuí Group, $\delta^{34}S$ *vs* $\Delta^{33}S$ diagram show a major tendency of the pyrite data migrating towards the initial sulfate field along the regressive cycle, from negative $\delta^{34}S_{py}$ and positive $\Delta^{33}S_{py}$ in the EHST towards highly positive $\delta^{34}S_{py}$ and negative $\Delta^{33}S_{py}$ in the LHST (Fig. 6.8A), supporting a distillation effect. Pyrite isotope compositions from the Tamengo Formation data fit very well to the pooled sulfide curve and also present a migration towards initial sulfate along the regressive cycles (Fig. 6.8B). Bambuí Group data show a considerably spreading below pooled sulfide curve and, for this reason, we combine a possible effect of mixing between a fraction of the residual sulfate direct to the pooled sulfide, for a time of a given fraction of residual sulfate (F) (Fig. 6.8A). The scenario envisaged here would represent an amount of sulfate being converted into sulfide through microbial sulfate-reduction with minimal fractional, by considering low sulfate concentrations. We consider that deviations between Rayleigh predictions and the measured data are expected due to the use of constant isotope fractionation ($^{34}\alpha$). When sulfate is distilled to critical values, this assumption would not hold for microbial sulfate reduction, by considering experimental studies with sulfate reducer communities under low sulfate concentrations (e.g. Canfield, 2001 and references therein). Nevertheless, even not perfectly coupled to the pooled sulfide curve, pyrite sulfur isotope data at the end of regression in the Bambuí Group (black symbols in Fig. 6.8A) would require minimal influence of this mixing scenario between residual sulfate and pooled sulfide and show a clear trend towards initial sulfate along the regression.

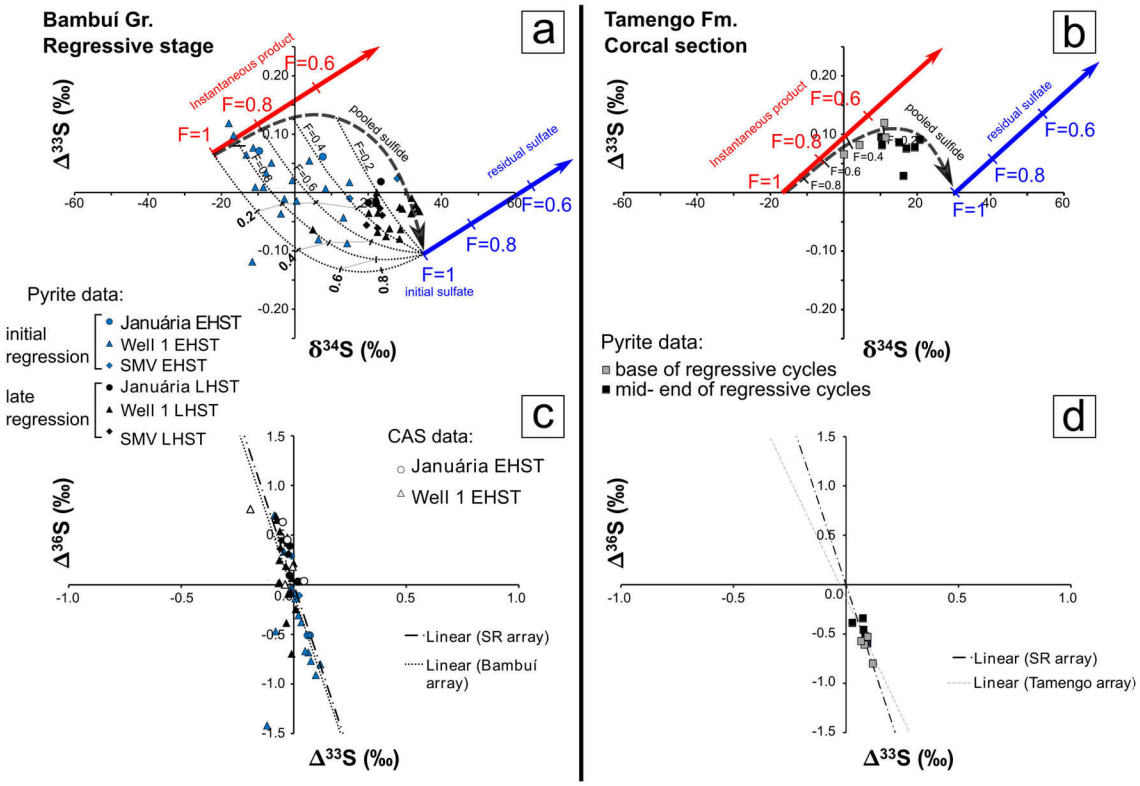

Figure 6.8: $\delta^{34}S$ *vs* $\Delta^{33}S$ and $\Delta^{33}S$ *vs* $\Delta^{36}S$ diagrams with samples from the regressive cycles from the basal Bambuí Group and Corcal section, Tamengo Formation. a) and b) present Rayleigh distillation trends for the residual sulfate, instantaneous sulfide and pooled sulfide. Parameters set were given in the text. In a) dotted lines represent mixing lines between residual sulfate and pooled sulfide for a given fraction of residual sulfate (F), by considering an amount of sulfate being converted into sulfide with minimal fractionation though microbial sulfate reduction under low sulfate concentrations. Fractions of mixing (f_{mix}) are given in bold numbers throughout mixing lines. See discussion through the text.

By analyzing $\Delta^{33}S$ *vs* $\Delta^{36}S$ diagram (Figs. 6.8C), the Bambuí Group data spread from the field of positive $\Delta^{33}S_{py}$ and negative $\Delta^{36}S_{py}$ values toward the field of negative $\Delta^{33}S_{py}$ and positive $\Delta^{36}S_{py}$ (sulfate field), whereas data from the Corcal section, Tamengo Formation (Fig. 6.8D) concentrates in the field of positive $\Delta^{33}S_{py}$ and negative $\Delta^{36}S_{py}$, however, with an apparent migration of the samples toward the field of sulfate along regressive cycles. Again, this turnover in the multiple sulfur isotope compositions from Bambuí Group pyrite data also matches the stratigraphic division of the samples from the early regressive stage (EHST) to the late regressive stage (LHST), in which the later group reaches the field of the CAS isotope signatures from the beginning of regression (Fig. 6.8C). This reinforces the scenario of a

sulfate distillation event through regressive cycles, as a nearly quantitative conversion of sulfate in sulfide along the relative sea-level fall.

Based on the multiple sulfur isotope trends presented coupled to regressive cycles, we propose a scenario of sulfate distillation events in sulfate-limited bottom environments of restricted basins and shallow platforms to explain superheavy pyrite occurrences on the late Ediacaran West Gondwana (Fig. 6.9; e.g. Logan et al., 1995; Canfield, 2004). Thus, we assume these signatures as a product of reservoir effect in which a significant part of available sulfate was converted to sulfide by microbial sulfate reduction, representing local but continentally representative sulfur cycling disturbances. This could be in part in agreement with the interpretation that superheavy pyrites would be a product of Rayleigh distillation in sulfate-poor pore water conditions of shallower sedimentary environments, which characterizes final regressive stages, rather than low sulfate concentrations of overlying seawater (e.g. Fike et al., 2015). However, the similar stratigraphic-chemostratigraphic dynamics affecting very different sedimentary environments in these two geotectonic domains of West Gondwana at the terminal Neoproterozoic points to a major sea-level control over these trends. The variety of carbonate facies bearing superheavy pyrites, such as microbial limestones, grainstones, packstones and wackestones argue against a pore-water effect. This suggests that the distillation of sulfate reservoir could have at least operated within bottom layers of enclosed basins and marginal shallow platforms. Negative $\delta^{34}S_{py}$ excursions during transgressive systems tracts, as clearly represented in the Bambuí Group sections (Fig. 6.4), imply that incursions of more sulfate-concentrated waters and/or a more efficient mixing between upper oxidized and bottom euxinic layers resulted in a sulfate recharge in bottom layers during transgressions (Fig. 6.9). After the maximum flooding and with the beginning of the regression, stratification would be favored in shallow platforms resulting in sulfate-limited bottom layers and sulfate distillation cycles. At the end of regression a major part of sulfate would be exhausted by conversion into sulfides through microbial sulfate reduction and pyrite burial, with extremely ^{34}S-enriched pyrites approaching initial sulfate set during the previous transgression (Fig. 6.9).

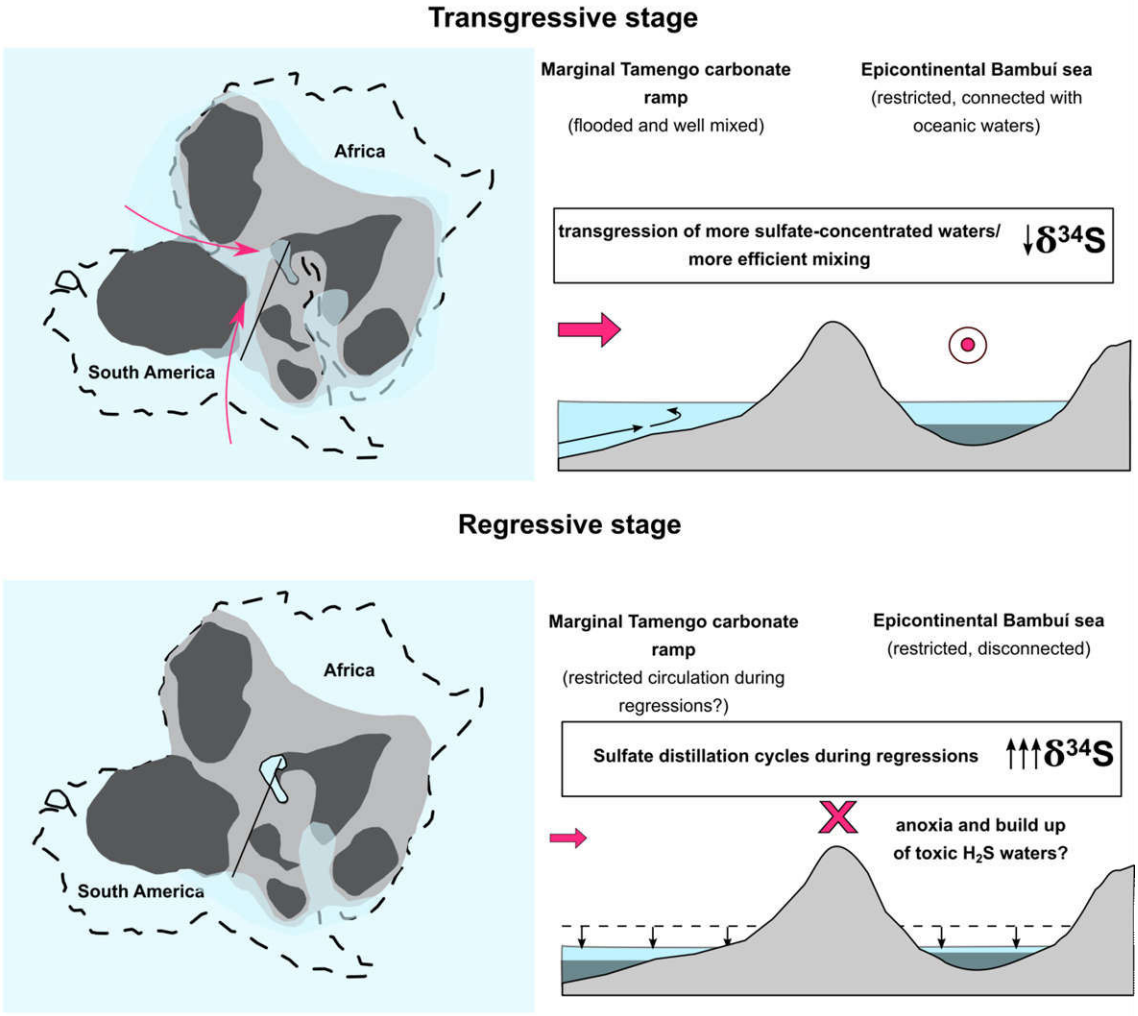

Figure 6.9: Paleoceanographic reconstruction for the eustatic control over superheavy pyrite trends. During transgressions shallow platforms would be ventilated and epicontinental basins connected with marginal seas and oceans, in which bottom waters would receive sulfate. Regressions would favor basin stratification and sulfate-distillation events, resulting in the positive excursions to superheavy pyrite values. Negative $\Delta^{33}S$ recorded during late regressive stage from the Bambuí Group suggest nearly sulfate exhaustion, resulting in enhanced euxinia in this isolated basin. This scenario also supports a biogeochemical turnover from a sulfate-reducing to methanogenic-dominated basin culminating in the extreme ^{13}C-enrichment in both carbonate and organic carbon succeeding superheavy pyrite excursion (MIBE excursion).

Despite presenting similar stratigraphic-chemostratigraphic patterns for $\delta^{34}S_{py}$, differences in multiple sulfur isotope signatures between the Bambuí Group and Tamengo Formation may be a result of distinct geotectonic settings they represent. The fact that Tamengo Formation data do not reach negative $\Delta^{33}S_{py}$ values (Fig. 6.8D) can be interpreted as a partial distillation event whereas the Bambuí Group records nearly complete conversion of

sulfate to sulfide, as a dramatic event of sulfate exhaustion. This would be expected in an intracontinental basin isolated in the very core of West Gondwana where regressions could represent a disconnection with open marine waters and ocean sulfate reservoir (Fig. 6.9). The parameters set for the Bambuí Group Rayleigh trends show that negative $\Delta^{33}S_{py}$ and $\delta^{34}S_{py}$ close to 40‰ would be reached when sulfate was almost entirely consumed in the late stage of regression (F close to zero; Fig. 6.10). On the other hand, the Tamengo Formation representing a carbonate ramp in the continental margin would be prone to exchange waters with open ocean and more efficient bottom ventilation preventing the fully exhaustion of sulfate in bottom waters. Important to stress that negative $\delta^{7}Li$ excursions recorded in the same regressive cycles from Tamengo Formation and Bambuí Group suggest less retention of ^{6}Li by clay formation and enhanced input of ions (nutrients) into these basins during late Ediacaran (Paula-Santos et al., in prep, a, b). This scenario of higher nutrient availability during terminal Ediacaran could also result in enhanced eutrophication in the enclosed Bambuí sea, boosting redox stratification of the basin and sulfate exhaustion (Paula-Santos et al., in prep,a).

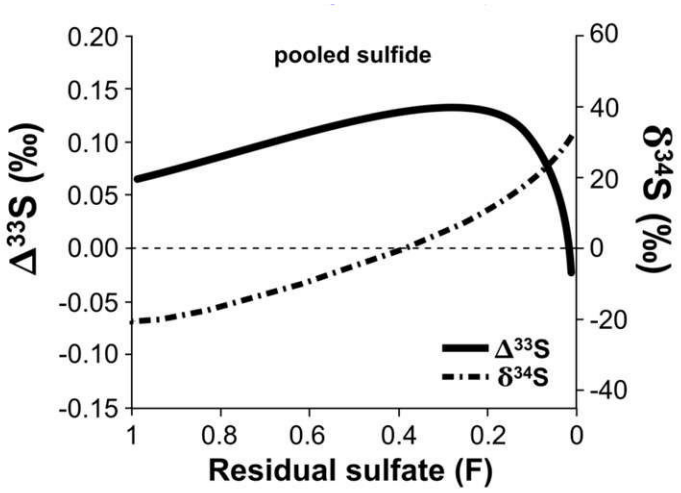

Figure 6.10: $\delta^{34}S$ and $\Delta^{33}S$ evolution for the pooled sulfide reservoir through the Rayleigh distillation scenario set for the Bambuí Group data (see details in text). Note that negative $\Delta^{33}S$ values would be reached when the residual sulfate is almost entirely consumed, suggesting a dramatic event in this epicontinental sea.

Although we do not present $\delta^{34}S_{CAS}$ in a proper resolution for a chemostratigraphic analysis, we do not consider $\Delta^{34}S_{CAS\text{-}py}$ from the Bambuí Group as a reliable primary paleodepositional proxy for the reconstructed scenario (e.g. Tostevin et al., 2017). A build-up

of euxinic waters during regressions could explain the variable $\Delta^{34}S_{CAS\text{-}py}$ observed in the Bambuí Group. Gomes and Hurtgen (2015) presented a compilation of $\Delta^{34}S$ data from modern euxinic environments and model results to show a positive correlation between $\Delta^{34}S$ values and sulfate concentrations, under low sulfate conditions (<8.5 mM). Under a sulfate concentration threshold (<5 mM), $\Delta^{34}S$ would not represent the isotope fractionation during microbial sulfate reduction due to the reservoir effect over pyrite signals, which represent euxinic bottom water/pore water conditions whereas sulfate records more superficial waters.

To conclude, dynamics proposed here suggest that a conjunction of factors, such as supercontinent configuration, inefficient circulation patterns, and stratified basins allied to low sulfate concentrations, would have resulted in dramatic sulfate distillation events and widespread conditions for precipitation of superheavy pyrites. This might explain the reason for these anomalous sulfur isotope signatures being rare in the geological record and frequent in the terminal Neoproterozoic strata, by considering a possible first-order tectonic control when supercontinent assembly represented favorable conditions to enhanced distillation effects of a decrease marine sulfate reservoir.

6.6.3. Sulfate distillation events challenging benthic colonization in the continent interior and driving epicontinental methanic basins

Late Ediacaran Tamengo Formation and the basal Bambuí Group present remarkable differences mainly concerning carbon isotope evolution and fossil distribution. The Tamengo Formation, representing a marginal carbonate ramp in the West Gondwana, has a rich fossil assemblage with abundant occurrences of benthic metazoans *Cloudina lucianoi* and *Corumbella werneri* (e.g. Pacheco et al., 2015; Becker-Kerber et al., 2017) distributed along mid to outer ramp domains. Carbon isotope evolution of the Tamengo Formation evolves in a relatively stability, with $\delta^{13}C_{carb}$ varying between +3 and +4‰ and $\delta^{13}C_{org}$ between −26 to −22‰, with no major excursions (Caetano-Filho et al., in prep.). On the other hand, the Bambuí Group represents an epicontinental sea in the core of West Gondwana at Ediacaran-Cambrian transition with very scarce fossil record, dominated by microbial limestones and with very rare occurrences of benthic metazoan *Cloudina* sp. (Warren et al., 2014; Perrella Jr. et al., 2017). The Bambuí Group carbon isotope evolution evolves dramatically, represented by a unique and extreme positive $\delta^{13}C_{carb}$ and $\delta^{13}C_{org}$ excursions reaching values as high as +16 and −14‰, respectively, occurring at the sequence boundary between the two lowermost 2nd-order sequences of the unit (Fig. 6.4; the Middle Bambuí Isotope Excursion – MIBE; Iyer

et al., 1995; Uhlein et al., 2019; Caetano-Filho et al., 2020). This carbon isotope excursion is commonly associated with enhanced restriction of the basin, however, with the main controls still discussed (Uhlein et al., 2019; Caetano-Filho et al., 2020). In the light of these discrepancies, our scenario of sulfate distillation cycles may have some implications over both biota occurrence and carbon isotope signatures of these distinct geotectonic settings during the late Ediacaran-early Cambrian transition.

It has been proposed that the Bambuí Group could have represented a more disturbed and unfavorable environment for animal colonization compared with marginal coeval seas, such as those represented by the Tamengo Formation and Nama Group, probably due to the more stratified and widespread anoxic conditions (Hippertt et al., 2019; Caetano-Filho et al., 2020). Negative $\Delta^{33}S_{py}$ values reached at the end of regressive cycle of the basal sequence of the Bambuí Group would represent virtually complete conversion of sulfate into sulfite (Fig. 6.10), i.e. a higher build-up of sulfidic bottom waters in the enclosed Bambuí sea, probably enhanced by lack of connection with surrounding seas (Fig. 6.9). Pyrite content decrease in the shallower sections (Januária and Santa Maria da Vitória; Fig. 6.4) was probably linked to the low ferruginous iron availability in this detrital-lean interval, resulting in free H_2S and euxinic conditions, as suggested by iron speciation data for this interval (Hippertt et al., 2019). This would represent a toxic environment for benthic metazoan colonization apart the simple oxygen availability discussion. Negative $\Delta^{33}S_{py}$ and positive $\delta^{34}S_{py}$ values were also described in the terminal Ediacaran strata from China (Xiaotan Section; Li et al., 2019) and were ascribed to a similar scenario in which upwelling of sulfidic waters led to extinction of Ediacara Biota. The authors suggested mixing between sulfidic deep waters of negative $\Delta^{33}S_{py}$ and positive $\Delta^{33}S_{py}$ with sulfide derived from nearly-quantitative sulfate reduction in shallow environments presenting positive $\Delta^{33}S_{py}$ and negative $\Delta^{33}S_{py}$. However, the $\delta^{34}S_{py}$ and $\Delta^{33}S_{py}$ trends from Xiaotan section are directly coupled in a negative excursion, different from multiple sulfur isotope patterns observed in the Bambuí Group. Furthermore, a paleoceanographic reconstruction of upwelling is not compatible with the epicontinental Bambuí sea. The basin wide occurrences of antithetical positive $\delta^{34}S_{py}$ and negative $\Delta^{33}S_{py}$ trends of the Bambuí Group support the build-up of a widespread euxinic bottom layer during sulfate-distillation regressive cycles.

In the marginal Tamengo ramp, the apparent less intense sulfate distillation event could be associated with the permanent connection with open ocean waters representing higher potential of mixing between surface and bottom layers, preventing formation of a widespred euxinic layer. Additionally, high frequency negative $\delta^{13}C_{carb}$–$\delta^{13}C_{org}$ excursions

recorded in parasequences from the basal Corcal section (Fig. 6.3) bearing *Cloudina* bioaccumulations and Fe-oxide cements would suggest enhanced organic carbon remineralization driven by unstable oxygenation of benthic environments (Caetano-Filho et al., in prep.). The proposed scenario matches a similar eustatic dynamic envisaged for the late Ediacaran interval from the Nama Group, in which more oxygenated mid ramp environments bearing complex benthic assemblages would be a result of bottom ventilation during high-energy transgressive events (Wood et al., 2015).

Regarding the MIBE, multiple sulfur isotope data presented here complement the scenario of methanic basin previously proposed to explain these anomalous carbon isotope signatures. Caetano-Filho et al. (2020) envisaged that the basin isolation in the very core of West Gondwana supercontinent would have enhanced bottom anoxia and sulfate-limited conditions, which would potentially result in sulfate exhaustion through microbial sulfate reduction and favored methanogenesis as an important metabolism in the basin. Subsequent increased methane production and ebullition to the atmosphere under limited oxidizing conditions in the water column would have created a disequilibrium condition between atmosphere and local marine DIC. The later reservoir would have been progressively influenced by a ^{13}C-enriched methanogenic CO_2, affecting both carbonates and organic carbon. The dramatic event of sulfate distillation throughout the regression at the basal sequence precedes the MIBE and corroborates the scenario of biogeochemical turnover in the basin, from a sulfate-reduction to methanogenic dominated environments. The progressive and possibly complete exhaustion of sulfate in the basal sequence would represent a retreat of the sulfate reduction and anaerobic oxidation of methane zones, favoring methane flux to the atmosphere and methanogenic-CO_2 assimilation in the marine DIC. Recent $\delta^{34}S_{py}$ data from Cui et al. (2020) shows that ^{34}S-enriched values persist through the MIBE in the upper Bambuí Group. Similar mechanisms in other epicontinental West Gondwana basins may have represented a large methane flux to the atmosphere with potential impact over global climate, perhaps driving the Earth out of Neoproterozoic glaciations to a more warm planet favorable to the fully development of life in the early Paleozoic.

Negative $\delta^{34}S_{py}$ excursions during the second transgression in the Bambuí Group might represent a sulfate recharge to bottom waters and an eventual rapid comeback from sulfate-reduction activity. In this case, the epicontinental sea condition might have played an important role over a disturbed local marine DIC reservoir. First, transgressions might have not represented the same high-energy event for an efficient mixing and ventilation of bottom layers in this enclosed sea compared with marginal basins. Second, if this epeiric water mass

experienced long times of marine disconnection during low sea level, as depicted from drastic decrease in $^{87}Sr/^{86}Sr$ ratios during the LHST (Caetano-Filho et al., 2019; Guacaneme et al., under review), transgressions may have represented faster events compared with regressions, being unable to recover a previous DIC massively influenced by methanogenic-CO_2. Furthermore, a new succeeding regression would favor another sulfate distillation cycle and sulfate-reduction zone retreat. In this sense, we recommend a similar sulfur chemostratigraphic approach in the overlying sequences throughout the MIBE to test this basinal marine geochemistry dynamic. In regards to increases in the pyrite content for some samples within the MIBE, it could be related to a higher Fe availability driven by massive detrital input represented by the Serra de Santa Helena Formation (Fig. 6.4; e.g. Hippertt et al., 2019). A previous euxinic and Fe-starved basin would be prone to pyrite precipitation in response to iron input, without necessarily representing sulfate-reduction under non-limited sulfate conditions. The fact that $\delta^{34}S_{py}$ negative excursions are more accentuated in the deep Well 1 section and virtually absent in the shallower Santa Maria da Vitória section during second transgression (Fig. 6.4) sustains the interpretation of sulfate input by marine connection rather than riverine input. This is in agreement with the modern sulfur cycle, in which ocean waters represent the final and more concentrated reservoir compared with major fluvial systems (Bottrell and Newton, 2006 and references therein).

Finally, we propose that homogeneous $\delta^{13}C$ signatures recorded in the Tamengo Formation, similar of other late Ediacaran successions worldwide (~4‰; Boggiani et al., 2010; Caetano-Filho et al., in prep), would be a result of permanent connection with open ocean waters, still under restricted circulation and sulfate distillation cycles during regressions. In this case, the marine DIC would represent an ocean-buffered reservoir against eventual increased methanogenic-CO_2 influence in the shallow platform. Additionally, occurrences of benthic metazoans associated with isotope and petrographic signatures for bottom ocean ventilation (Caetano-Filho et al., in prep.) would result in methane oxidation, preventing ebullition required for ^{13}C-enrichment in the DIC (Gu et al., 2004; Birgel et al., 2016).

6.7. Conclusions

Continental scale $\delta^{34}S_{py}$ isotope excursions coupled with stratigraphic cycles recorded within Tamengo Formation and Bambuí Group suggest an sea-level control over sulfur cycling through the West Gondwana marine environments during late Ediacaran-early

Cambrian. Superheavy $\delta^{34}S_{py}$ values (> 40‰) were reached along positive excursions during regressions recorded in both basins, whereas negative excursions are recorded through transgressive deposits. Multiple sulfur isotope constraints sustain a scenario of Rayleigh distillation cycles through regressions, in which $\delta^{34}S_{py}$ *vs* $\Delta^{33}S_{py}$ and $\Delta^{33}S_{py}$ *vs* $\Delta^{36}S_{py}$ relationships show isotope trends migrating towards initial sulfate values. Sulfate distillation cycles would be favored by basin stratification and sulfate-limited bottom waters during regressions, whereas transgressions would resupply sulfate by incursion of more concentrated waters and/or mixing between water layers.

Basin wide negative $\Delta^{33}S_{py}$ values found in the basal Bambuí Group point to a nearly quantitative conversion of sulfate to sulfide through microbial sulfate reduction in bottom environments, probably resulting from enhanced basin stratification and lack of marine connection during regressions in this epicontinental sea isolated in the very core of West Gondwana. On the other hand, the marginal Tamengo ramp does not present negative $\Delta^{33}S_{py}$, suggesting that sulfate consumption was not as intense as for the restricted Bambuí sea, probably due to permanent marine connection with open ocean and more efficient water layer mixing. Enhanced sulfate distillation cycles leading to nearly complete exhaustion of marine sulfate in epicontinental basins would represent build-up of toxic sulfidic bottom environments, challenging early metazoan colonization in the continental interior. On the other hand, these conditions would support a biogeochemical turnover from a sulfate-reduction to methanogenic-dominated basin, as previously suggested to explain extremely heavy carbon isotope compositions from the middle Bambuí Group ($\delta^{13}C_{DIC}$ > +10‰), succeeding the basal positive $\delta^{34}S_{py}$ excursion to superheavy values. If reproducible in other coeval epicontinental basins, increased methane flux to the atmosphere could have resulted in enhanced greenhouse conditions, driving the Earth out from the glacial Neoproterozoic Era towards more warm conditions favorable to the Cambrian explosion of life.

The proposed scenario helps to explain the reason for these unusual isotope sulfur anomalies being rare in the geological record. Superheavy pyrites would be a result of a conjunction of factors including specific tectonic configuration, restricted settings and inefficient circulation, allied to low concentrations of marine sulfate. In this sense, terminal Neoproterozoic presents all the requirements to justify frequent occurrences of extremely ^{34}S-enriched pyrites. Similar stratigraphic-chemostratigraphic analyses through superheavy pyrite-bearing successions, coupled to a paleogeographic assessment of the geotectonic setting, would help to test this hypothesis proposed for late Ediacaran-early Cambrian West Gondwana basins.

6.8. Acknowledgements

Funding for this study was provided by the São Paulo Research Foundation (FAPESP) thematic project grant #2016/06114-6 and Brazilian Research Council project grant #400764/2016-4. We acknowledge to Petra Energia S.A. for providing drill core samples, and to technical staff from the Stable Isotope Geochemistry Group from the Institut de Physique du Globe de Paris, for the technical support during data acquisition. Sergio Caetano Filho holds a FAPESP scholarship grant #2016/11496-5 and sulfur isotope data were acquired during the BEPE/FAPESP project #2018/19302-0. Gustavo Paula-Santos holds a FAPESP post-doc grant #2017/00399-1. Marly Babinski, Ricardo Trindade and Matheus Kuchenbecker are fellows of the Brazilian Research Council (#307563/2013-8, #206997/2014-0 and #309106/2017-6, respectively). This study contributes to the IdEx Université de Paris ANR-18-IDEX-0001 and to the LabexMER ANR-10-LABX-19.

6.9. References

Adorno, R.R., Carmo, D.A., Germs, G., Walde, D.H.G., Denezine, M., Boggiani, P.C., Silva, S.C.S., Vasconcelos, J.R., Tobias, T.C., Guimarães, E.M., Vieira, L.C., Figueiredo, M.F., Moraes, R., Caminha, S.A., Suarez, P.A.Z., Rodrigues, C.V., Caixeta, G.M., Pinho, D., Schneider, G., Ralph Muyamba, R., 2017. *Cloudina lucianoi* (Beurlen & Sommer, 1957), Tamengo Formation, Ediacaran, Brazil: Taxonomy, analysis of stratigraphic distribution and biostratigraphy. Precambrian Research 301, 19−35.

Alkmim, F.F., Marshak, S., Pedrosa-Soares, A.C., Peres, G.G., Cruz, S.C., Whittington, A., 2006. Kinematic evolution of the Araçuaí–West Congo orogen in Brazil and Africa: nutcracker tectonics during the Neoproterozoic assembly of Gondwana. Precambrian Research 149, 43–63.

Amorim, K.B., Afonso, J.W.L., Leme, J.M., Diniz, C.Q.C., Rivera, L.C.M., Gómez-Gutiérrez, J.C., Boggiani, P.C., Trindade, R.I.F., 2020. Sedimentary facies, fossil distribution and depositional setting of the late Ediacaran Tamengo Formation (Brazil). Sedimentology. https://doi.org/10.1111/sed.12749

Amthor, J.E., Grotzinger, J.P., Schröder, S., Bowring, S.A., Ramezani, J., Martin, M.W., Matter, A., 2003. Extinction of *Cloudina* and *Namacalathus* at the Precambrian-Cambrian boundary in Oman. Geology, 31, 431–434.

Babcock, L.E., Grunow, A.M., Sadowski, G.R., Leslie, S.A., 2005. *Corumbella*, an Ediacaran-grade organism from the Late Neoproterozoic of Brazil. Palaeogeography, Palaeoclimatology, Palaeoecology 220, 7–18.

Babinski, M., Boggiani, P.C., Fanning, M., Simon, C.M., Sial, A.N., 2008. U–Pb SHRIMP geochronology and isotope chemostratigraphy (C, O, Sr) of the Tamengo Formation, southern Paraguay belt, Brazil. South American Symposium on Isotope Geology, 6, San Carlos de Bariloche, Argentina, Proceedings, p. 160.

Babinski, M., Vieira, L.C., Trindade, R.I.F., 2007. Direct dating of the Sete Lagoas cap carbonate (Bambuí Group, Brazil) and implications for the Neoproterozoic glacial events. Terra Nova 19, 401–406.

Becker-Kerber, B., Pacheco, M.L.A.F., Rudnitzki, I.D., Galante, D., Rodrigues, F., Leme, J.M., 2017. Ecological interactions in *Cloudina* from the Ediacaran of Brazil:implications for the rise of animalbiomineralization. Scientific Reports 7:5482.

Birgel, D., Meister, P., Lundberg, R., Horath, T.D., Bontognali, T.R.R., Bahniuk, A.M., Rezende, C.E., Vasconcelos, C., McKenzie, J.A., 2015. Methanogenesis produces strong ^{13}C enrichment in stromatolites of Lagoa Salgada, Brazil: a modern analogue for Paleo-/Neoproterozoic stromatolites? Geobiology 13, 245–266.

Boggiani, P.C., Alvarenga, C.J.S., 2004. Faixa Paraguai. In: Matesso-Neto, V., Bartorelli, A., Carneiro, C.D.R., Brito-Neves, B.B. (Eds.), Geologia do Continente Sul-Americano. Beca, São Paulo 1, pp. 113-118.

Boggiani, P.C., Gaucher, C., Sial, A.N., Babinski, M., Simon, C.M., Riccomini, C., Ferreira, V.P., Fairchild, T.R., 2010. Chemostratigraphy of the Tamengo Formation (Corumbá Group, Brazil): a contribution to the calibration of the Ediacaran carbon-isotope curve. Precambrian Research 182, 382–401.

Bottomley, D.J., Veizer, J., Nielsen, H., Moczydlowska, M., 1992. Isotopic composition of disseminated sulfur in Precambrian sedimentary rocks. Geochimica et Cosmochimica Acta 56, 3311–3322.

Bottrell, S.H., Newton, R.J., 2006. Reconstruction of changes in global sulfur cycling from marine sulfate isotopes. Earth-Science Reviews 75, 59– 83.

Caetano-Filho, S., Paula-Santos, G.M., Guacaneme, C., Babinski, M., Bedoya-Rueda, C., Peloso, M., Amorim, K., Afonso, J., Kuchenbecker, M., Reis, H.L.S., Trindade, R.I.F., 2019. Sequence stratigraphy and chemostratigraphy of an Ediacaran-Cambrian foreland-related carbonate ramp (Bambuí Group, Brazil). Precambrian Research 331, 105365.

Caetano-Filho, S., Paula-Santos, G.M., Sansjofre, P., Ader, M., Gómez-Gutierrez, J.C., Rivero; L.C.M., Amorim, K.B., Afonso, J.W.L., Babinski, M., Leme, J.M., Boggiani, P.C., Trindade, RI.F. Paired carbon isotope and early diagenesis signatures suggest complex oxygenation in late Ediacaran benthic marine environments. In preparation.

Caetano-Filho, S., Sansjofre, P., Ader, M., Paula-Santos, G.M., Guacaneme, C., Babinski, M., Bedoya-Rueda, C., Kuchenbecker, M., Reis, H.L.S., Trindade, R.I.F., 2020. A large epeiric methanogenic Bambuí sea in the core of Gondwana supercontinent? Geoscience Frontiers https://doi.org/10.1016/j.gsf.2020.04.005

Canfield, D.E., 2001. Biogeochemistry of sulfur isotopes. Reviews in Mineralogy and Geochemistry 43(1), 607–636.

Canfield, D.E., 2004. The evolution of the Earth surface sulfur reservoir. American Journal of Science 304(10), 839–861.

Canfield, D.E., Raiswell, R., Westrich, J.T., Reaves, C.M., Berner, R.A., 1986. The use of chromium reduction in the analysis of reduced inorganic sulfur in sediments and shales. Chemical Geology 54, 149–155.

Caxito, F.A., Frei, R., Uhlein, G.J., Dias, T.G., Árting, T.B., Uhlein, A., 2018. Multiproxy geochemical and isotope stratigraphy records of a Neoproterozoic Oxygenation Event in the Ediacaran Sete Lagoas cap carbonate, Bambuí Group, Brazil. Chemical Geology 481, 119–132.

Cui, H., Kaufman, A.J., Xiao, S., Peek, S., Cao, H.,Min, X., Cai, Y., Siegel, Z., Liu, X.M., Peng, Y., Schiffbauer, J.D., Martin, A.J., 2016. Environmental context for the terminal Ediacaran biomineralization of animals. Geobiology 14, 344–363.

Cui, H., Kaufman, A.J., Xiao, S., Zhu, M., Zhou, C., Liu, X.M., 2015. Redox architecture of an Ediacaran ocean margin: integrated chemostratigraphic ($\delta^{13}C$–$\delta^{34}S$–$^{87}Sr/^{86}Sr$–Ce/Ce*) correlation of the Doushantuo Formation, South China. Chemical Geology 405, 48–62.

Cui, H., Kitajima, K., Spicuzza, M.J., Fournelle, J.H., Denny, A., Ishida, A., Zhang, F.F., Valley, J.W., 2018. Questioning the biogenicity of Neoproterozoic superheavy pyrite by SIMS. American Mineralogist 103(9), 1362−1400.

Cui, H., Warren, L.V., Uhlein, G.J., Okubo, J., Liu, X.M., Plummer, R.E., Baele, J.M., Goderis, S., Claeys, P., Li, F., 2020. Global or regional? Constraining the origins of the middle Bambuí carbon cycle anomaly in Brazil. Precambrian Research 348, 105861.

Dardenne, M.A., 1978. Síntese sobre a estratigrafia do Grupo Bambuí no Brasil Central. Congresso Brasileiro de Geologia, 30, Recife, Brazil, Proceedings 2, 507–610 pp.

Farquhar, J., Wing, B.A., 2003. Multiple sulfur isotopes and the evolution of the atmosphere. Earth and Planetary Science Letters 213 (1–2), 1–13.

Fichtner, V., Strauss, H., Immenhauser, A., Buhl, D., Neuser, R.D., Niedermayr, A., 2017. Diagenesis of carbonate associated sulfate. Chemical Geology 463, 61−75.

Fike, D.A., Bradley, A.S., and Rose, C.V., 2015. Rethinking the ancient sulfur cycle. Annual Review of Earth and Planetary Sciences, 43, 593–622.

Fike, D.A., Grotzinger, J.P., 2008. A paired sulfate–pyrite $\delta^{34}S$ approach to understanding the evolution of the Ediacaran-Cambrian sulfur cycle. Geochimica et Cosmochimica Acta 72, 2636–2648.

Fike, D.A., Grotzinger, J.P., Pratt, L.M., Summons, R.E., 2006. Oxidation of the Ediacaran Ocean. Nature 444, 744–747.

Freitas, B.T., Warren, L.V., Boggiani, P.C., Almeida, R.P., Piacentini, T., 2011. Tectono-sedimentary evolution of the Neoproterozoic BIF-bearing Jacadigo Group, SW-Brazil. Sedimentary Geology 238, 48–70.

Gaucher, C., Boggiani, P.C., Sprechmann, P., Sial, A.N., Fairchild, T.R., 2003. Integrated correlation of the Vendian to Cambrian Arroyo del Soldado and Corumbá groups (Uruguay and Brazil): Palaeogeographic, palaeoclimatic and palaeobiologic implications. Precambrian Research 120, 241–278.

Gill, B.C., Lyons, T.W., Frank, T.D., 2008. Behavior of carbonate-associated sulfate during meteoric diagenesis and implications for the sulfur isotope paleoproxy. Geochimica et Cosmochimica Acta 72, 4699–4711.

Gomes, M.L., Hurtgen, M.T., 2015. Sulfur isotope fractionation in modern euxinic systems: Implications for paleoenvironmental reconstructions of paired sulfate–sulfide isotope records. Geochimica et Cosmochimica Acta, 157, 39–55.

Grotzinger, J.P., Waters, W.A., Knoll, A.H., 2000. Calcified metazoans in thrombolite stromatolite reefs of the terminal Proterozoic Nama Group, Namibia. Paleobiology 26(3), 334–359.

Gu, B., Schelske, C.L., Hodell, D.A., 2004. Extreme ^{13}C enrichments in a shallow hypereutrophic lake: implications for carbon cycling. Limnology and Oceanography 49, 1152–1159.

Guacaneme, C., Babinski, M., Bedoya-Rueda, C., Paula-Santos, G.M., Caetano-Filho, S., Kuchenbecker, M., Reis, H.L.S., Trindade, R.I.F. Tectonically-induced strontium isotope changes in ancient restricted seas: the case of the Ediacaran-Cambrian Bambuí foreland basin system, east Brazil. Under review (Gondwana Research).

Habicht, K.S., Canfield, D.E., 2001. Isotope fractionation by sulfate-reducing natural populations and the isotopic composition of sulfide in marine sediments. Geology 29, 555–558.

Halverson, G.P., Hurtgen, M.T., 2007. Ediacaran growth of the marine sulfate reservoir. Earth and Planetary Science Letters 263, 32–44.

Heilbron, M., Cordani, U.G., Alkmim, F.F, 2017.. São Francisco Craton, Eastern Brazil: Tectonic Genealogy of a Miniature Continent. Springer, Switzerland, 331p.

Hippertt, J.P. Caxito, F.A. Uhlein, G.J. Nalini, H.A. Sial, A.N. Abreu, A.T., Nogueira, L.B., 2019. The fate of a Neoproterozoic intracratonic marine basin: Trace elements, TOC and IRON speciation geochemistry of the Bambuí Basin, Brazil. Precambrian Research 330, 101–120.

Hurtgen, M.T., Arthur, M.A., Suits, N., Kaufman, A.J., 2002. The sulfur isotopic composition of Neoproterozoic seawater sulfate: implications for snowball Earth? Earth and Planetary Science Letters 203, 413–429.

Hurtgen, M.T., Halverson, G.P., Arthur, M.A., Hoffman, P.F., 2006. Sulfur cycling in the aftermath of a Neoproterozoic (Marinoan) snowball glaciation: Evidence for a syn-glacial sulfidic deep ocean. Earth and Planetary Science Letters 245, 551–570.

Iyer, S.S., Babinski, M., Krouse, H.L., Chemale, F., 1995. Highly ^{13}C enriched carbonate and organic matter in the Neoproterozoic sediments of the Bambuí Group, Brazil. Precambrian Research 73, 271–282.

Johnston, D.T. 2011. Multiple sulfur isotopes and the evolution of Earth's surface sulfur cycle. Earth-Science Reviews 106, 161–183.

Kah, L.C., Lyons, T.W., Frank, T.D., 2004. Low marine sulphate and protracted oxygenation of the Proterozoic biosphere. Nature 431(7010), 834–838.

Kampschulte, A., Strauss, H., 2004. The sulfur isotopic evolution of Phanerozoic seawater based on the analysis of structurally substituted sulfate in carbonates. Chemical Geology 204, 255–286.

Kohn, M.J., Riciputi, L.R., Stakes, D., Orange, D.L., 1998. Sulfur isotope variability in biogenic pyrite: Reflections of heterogeneous bacterial colonization? American Mineralogist 83, 1454–1468.

Kuchenbecker, M., Babinski, M., Pedrosa-Soares, A.C., Lopes-Silva, L., Pimenta, F., 2016. Chemostratigraphy of the lower Bambuí Group, southwestern São Francisco Craton, Brazil: insights on Gondwana paleoenvironments. Brazilian Journal of Geology 46(1), 145–162.

Li, D., Zhang, X., Hu, D., Li, D., Zhang, G., Zhang, X., Ling, H-.F., Xu., Y., Shen, Y., 2019. Multiple S-isotopic constraints on paleo-redox and sulfate concentrations across the Ediacaran-Cambrian transition in South China. Precambrian Research 105500.

Liu, T.-B., Maynard, J.B., Alten, J., 2006. Superheavy S isotopes from glacier-associated sediments of the Neoproterozoic of south China: Oceanic anoxia or sulfate limitation? Geological Society of America Memoirs, 198, 205–222.

Logan, G.A., Hayes, J., Hieshima, G.B., Summons, R.E., 1995. Terminal Proterozoic reorganization of biogeochemical cycles. Nature 376, 53–56.

Loyd, S.J., Marenco, P.M., Hagadorn, J.W., Lyons, T.W., Kaufman, A.J., Sour-Tovar, F.,Corsetti, F.A., 2013. Local $\delta^{34}S$ variability in ~580 Ma carbonates of northwestern Mexico and the Neoproterozoic marine sulfate reservoir. Precambrian Research 224, 551–569.

Moreira, D.S., Uhlein, A., Dussin, I.A., Uhlein, G.J., Pimentel Misuzaki, A.M., 2020. A Cambrian age for the upper Bambuí Group, Brazil, supported by the first U-Pb dating of volcaniclastic bed. Journal of South American Earth Sciences 99, 102503.

Nogueira, A.C.R., Riccomini, C., Sial, A.N., Moura, C.A.V., Fairchild, T.R., 2003. Soft-sediment deformation at the base of Neoproterozoic Puga cap carbonate (southwestern Amazon craton, Brazil): confirmation of rapid icehouse to greenhouse transition in snowball Earth. Geology 31, 613–616.

Ono, S., Wing, B., Johnston, D., Farquhar, J., Rumble, D., 2006. Mass-dependent fractionation of quadruple stable sulfur isotope system as a new tracer of sulfur biogeochemical cycles. Geochimica et Cosmochimica Acta 70(9), 2238–2252.

Pacheco, M.L.A.F., Galante, D., Rodrigues, F., Leme, J.M., Bidola, P., Hagadorn, W., Stockmar, M., Herzen, J., Rudnitzki, I.D., Pfeiffer, F., Marques, A.C., 2015. Insights into the skeletonization, lifestyle, and affinity of the unusual ediacaran fossil *Corumbella*. PLoS ONE 10(3), 1−19.

Parry, L.A., Boggiani, P.C., Condon, D.J., Garwood, R.J., Leme, J.M., McIlroy, D., Brasier, M.D., Trindade, R.I.F., Campanha, G.A.C., Pacheco, M.L.A.F., Diniz, C.Q.C., Liu, A.G., 2017. Ichnological evidence for meiofaunal bilaterians from the terminal Ediacaran and earliest Cambrian of Brazil. Nature Ecology & Evolution 1, 1455−1464.

Paula-Santos, G., Caetano-Filho, S., Enzweiler, J., Navarro, M., Babinski, M., Guacaneme, C., Kuchenbecker, M., Reis, H., Trindade, R.I.F., 2020. Rare earth elements in the terminal Ediacaran Bambuí Group carbonate rocks (Brazil): evidence for high seawater alkalinity during rise of early animals. Precambrian Research 336, 105506.

Paula-Santos, G.M., Caetano-Filho, S., Babinski, M., Trindade, R.I.F, Guacaneme, C., 2017. Tracking connection and restriction of West Gondwana São Francisco Basin through isotope chemostratigraphy. Gondwana Research 42, 280−305.

Paula-Santos, G.M., Babinski, M., Kuchenbecker, M., Caetano-Filho, S., Trindade, R.I.F., Pedrosa-Soares, A.C., 2015. New evidence of an Ediacaran age for the Bambuí Group in southern São Francisco craton (eastern Brazil) from zircon U-Pb data and isotope chemostratigraphy. Gondwana Research 28, 702–720.

Paula-Santos, G.M., Caetano-Filho, S., Guacaneme, C., Bedoya-Rueda, C., Gramcianinov. C.B., Babinski, M., Kasemann, S.A., Kuchenbecker, M., Navarro, M.S., Marteleto, T.P., Enzweiler, J., Trindade, R.I.F. The biological response to increased weathering fluxes at the Late Ediacaran: the case of the Sete Lagoas Formation, Brazil. In preparation (a).

Paula-Santos, G.M., Gramcianinov, C.B., Kasemann, S.A., Wilckens, F.K., Caetano-Filho, S. Navarro, M.S., Marteleto, T.P., Enzweiler, J., Romero, G.R., Leme, J.M., Babinski, M., Trindade. R.I.F., Weathering-driven biomineralization in Late Ediacaran seas. In preparation (b).

Perrella Jr., P., Uhlein, A., Uhlein, G.J., Sial, A.N., Pedrosa-Soares, A.C., Lima, O.N.B., 2017. Facies analysis, sequence stratigraphy and chemostratigraphy of the Sete Lagoas Formation (Bambuí Group), northern Minas Gerais State, Brazil: evidence of a cap carbonate deposited on the Januária basement high. Brazilian Journal of Geology 47, 59−77.

Reis, H.L.S., Alkmim, F.F., Fonseca, R.C.S., Nascimento, T.C., Suss, J.F., Prevatti, L.D., 2016. The São Francisco Basin. In: Heilbron, M., Cordani, U.G., Alkmim, F.F. (Eds.), São Francisco Craton, Eastern Brazil, Regional Geology Reviews. Springer, Switzerland, pp. 117–143.

Reis, H.L.S., Suss, J.F., 2016. Mixed carbonate-siliciclastic sedimentation in forebulge grabens: an example from the Ediacaran Bambuí Group, São Francisco Basin, Brazil. Sedimentary Geology 339, 83–103.

Reis, H.L.S., Suss, J.F., Fonseca, R.C.S., Alkmim, F.F., 2017. Ediacaran forebulge grabens of the southern São Francisco basin, SE Brazil: Craton interior dynamics during West Gondwana assembly. Precambrian Research 302, 150–170.

Ries, J.B., Fike, D.A., Pratt, L.M., Lyons, T.W., and Grotzinger, J.P., 2009. Superheavy pyrite (δ34Spyr >δ34SCAS) in the terminal Proterozoic Nama Group, southern Namibia: A consequence of low seawater sulfate at the dawn of animal life. Geology 37, 743–746.

Sansjofre, P., Cartigny, P., Trindade, R.I.F., Nogueira, A.C.R., Agrinier, P., Ader, M., 2016. Multiple sulfur isotope evidence for massive oceanic sulfate depletion in the aftermath of Snowball Earth. Nature Communications 7, 1−8.

Shen, B., Xiao, S., Kaufman, A.J., Bao, H., Zhou, C., Wang, H., 2008. Stratification and mixing of a post-glacial Neoproterozoic ocean: Evidence from carbon and sulfur isotopes in a cap dolostone from northwest China. Earth and Planetary Science Letters 265, 209–228.

Staudt, W.J., Schoonen, M.A., 1995. Sulfate incorporation into sedimentary carbonates. In: Vairavamurthy, A., Schoonen, M.A.A. (Eds.), Geochemical Transformation of Sedimentary Sulfur. American Chemical Society Symposium Series 612, 332–347.

Thode, H.G., Monster, J., Dunford, H.B., 1961. Sulphur isotope geochemistry. Geochimica et Cosmochimica Acta 25, 159–174.

Tohver, E., D'Agrella Filho, M.S., Trindade, R.I.F., 2006. Paleomagnetic record of Africa and South America for the 1200-500 Ma interval, and evaluation of Rodinia and Gondwana assemblies. Precambrian Research 147, 193−222.

Tostevin, R., He, T., Turchyn, A.V., Wood, R.A., Penny, A.M., Bowyer, F., Antler, G., Shields, G.A., 2017. Constraints on the late Ediacaran sulfur cycle from carbonate associated sulfate. Precambrian Research 290, 113–125.

Trindade, R.I.F., Font, E., D'Agrella-Filho, M.S., Nogueira, A.C.R., Riccomini, C., 2003. Low-latitude and multiple geomagnetic reversals in the Neoproterozoic Puga cap carbonate of Amazonia. Terra Nova 15, 441–446.

Uhlein, G.J., Uhlein, A., Pereira, E., Caxito, F.A., Okubo, J., Warren, L.V., Sial, A.N., 2019. Ediacaran paleoenvironmental changes recorded in the mixed carbonate-siliciclastic Bambuí Basin, Brazil. Palaeogeography, Palaeoclimatology, Palaeoecology 517, 39–51.

Wang, P., Algeo, .J., Du, Y., Yu, W., Zhou, Q., Qin, Y., Xu, Y., Yuan, L., Pan, W., 2019. Large accumulations of ^{34}S-enriched pyrite in a low-sulfate marine basin: the Sturtian Nanhua Basin, South China. Precambrian Research 335, 105504.

Warren, L.V., Quaglio, F., Riccomini, C., Simões, M.G., Poiré, D.G., Strikis, N.M., Anelli, L.E., Strikis, P.C., 2014. The puzzle assembled: Ediacaran guide fossil Cloudina reveals an old proto-Gondwana seaway. Geology 42(5), 391−394.

Wood, R.A., Poulton, S.W., Prave, A.R., Hoffmann, K.H., Clarkson, M.O., Guilbaud, R., Lyne, J.W., Tostevin, R., Bowyer, F., Penny, A.M., Curtis, A., Kasemann, S.A., 2015. Dynamic redox conditions control late Ediacaran ecosystems in the Nama Group, Namibia. Precambrian Research 261, 252−271.

Yan, H., Pi, D., Jiang, S-Y., Hao, W., Cui, H., Robbins, L.J., Mänd, K., Li, L., Planavsky, N.J., Konhauser, K.O., 2020. Hydrothermally induced ^{34}S enrichment in pyrite as an alternative explanation of the Late-Devonian sulfur isotope excursion in South China. Geochimica et Cosmochimica Acta, in press, doi: https://doi.org/10.1016/j.gca.2020.05.017.

7. INTEGRATIVE DISCUSSION AND CONCLUDING REMARKS

Discussions developed through chapters 3 to 6 succeeded in order to reconstruct marine geochemistry dynamics within the two distinct geotectonic scenarios studied in the context of late Ediacaran-early Cambrian West Gondwana. Chapter 4 provided a stratigraphic framework and correlation for the studied sections in the Bambuí Group. It demonstrates that $\delta^{13}C_{carb}$ evolution is in a good agreement with stratigraphic division of the basal Bambuí Group and that the well-known extreme positive $\delta^{13}C$ excursion is coupled with the basal sequence boundary all over the basin, as an important paleoenvironmental disturbance probably driven by enhanced basin restriction during West Gondwana assembly. For the Tamengo Formation, the studied sections were considered in the depositional model proposed by Amorim et al. (2020), representing inner to outer ramp environments. Thus, carbon and sulfur isotope evolution were grounded in well-established depositional models, properly assessing geotectonic settings for each basin.

Regarding the carbon cycling in these two basins, Chapter 4 discussed the unique carbon isotope evolution of the Bambuí Group through Ediacaran-Cambrian transition. Paired $\delta^{13}C$ results, first time presented in stratigraphic continuity and in the basin scale, attested that the positive $\delta^{13}C$ excursion is perfectly coupled between carbonate and organic carbon, encompassing the highest values recorded in late Ediacaran successions. This confirms that disturbances affected the marine DIC and primary carbon fixation and strongly suggests that the basin carbon cycle was decoupled from the global one, by considering $\delta^{13}C$ values far higher compared with coeval sections. Such high $\delta^{13}C_{carb}$ and $\delta^{13}C_{org}$ would require unrealistic values for both changes in the fraction of organic carbon burial and $\delta^{13}C_{input}$ for a long interval, making these assumptions unlikely. By considering similar values in modern methanogenic environments and related environmental conditions, we proposed a scenario of methanogenic basin for the Bambuí sea. Enhanced basin restriction led to anoxic and sulfate limited conditions, resulting in a biogeochemical turnover from a sulfate-reducing to methanogenic-dominated basin through sulfate consumption by microbial sulfate reduction preceding the extreme $\delta^{13}C$ excursions. The hypothesis of sulfate-limitationand anoxia would prevent oxidation of ^{13}C-depleted methane in the water column, resulting in ebullition to the atmosphere. As a consequence, marine DIC would be influenced by ^{13}C-enriched methanogenic CO_2. This scenario has implications for colonization of benthic environments by the early metazoans as well as for climate changes, considering a significant area of

methane emissions. Nevertheless, this hypothesis needed to be tested through sulfur isotope systematics to sustain sulfate-limited conditions in this basin.

On the other hand, Chapter 5 presented paired carbon isotope compositions throughout different domains of the Tamengo Formation. As reported by previous studies in this unit, carbon isotope record does not present large excursions such as those reported for the Bambuí Group, with $\delta^{13}C_{carb}$ values usually reported for the late Ediacaran. In turn, paired carbon isotope data show a distinct pattern within mid ramp domains of the Tamengo ramp, associated with lower-rank shallowing upward cycles bearing *Cloudina* bioclasts. These deposits presents negative spikes of $\delta^{13}C_{carb}$ and $\delta^{13}C_{org}$ and also occurrences of oxide cementation, suggesting enhanced organic carbon remineralization in more oxygenated environments related to *Cloudina* occurrences. This suggested paleoredox structure based on paired $\delta^{13}C$ data for the Tamengo ramp mimics those proposed for the coeval interval of the Nama Group, in which more oxygenated conditions were depicted from iron speciation data in mid ramp domains associated with more complex ecological nets. Therefore, early benthic metazoans seem to have occupied more oxygenated environments disposed in a complex redox architecture throughout shallow platforms.

Finally, Chapter 6 provided sulfur isotope evolution for both units, focusing on the occurrences of superheavy pyrites. The observation of positive $\delta^{34}S_{py}$ excursions coupled to regressive cycles and negative excursions associated with transgressive stages led to the interpretation of a major control of the relative sea level over sulfur isotope compositions recorded in pyrites. Considering that most part of these rocks lack CAS fractions (and did not allowed for a systematic chemostratigraphic study of sulfate fractions), allied with the common low CAS concentrations and limited sulfate conditions proposed for superheavy pyrite intervals in other late Ediacaran successions, the scenario of Rayleigh distillation effect in these basins was tested. Pyrite-sulfur data from both units fit trends envisaged for the pooled sulfide, which migrates towards initial sulfate along the regressions. In the Bambuí Group, $\Delta^{33}S$ and $\Delta^{36}S$ values from superheavy pyrites reached the field of few sulfates samples analysed for the interval representing the beginning of regressive cycles, suggesting nearly complete conversion of sulfate in sulfides throughout regression. Furthermore, negative $\Delta^{33}S$ reported in this unit would be reached in the Rayleigh distillation scenario when residual sulfate approaches zero. Based on this multiple sulfur isotope investigation coupled to well-stablished stratigraphic framework, a scenario of continental-scale control of relative sea-level (probably associated with tectonoeustasy) was proposed, in which transgressions would supply sulfate for the bottom environments whereas regressions would force

stratification, especially in the epicontinental sea where connection with surrounding seas could have been closed. Dramatic distillation events in epicontinental settings, as suggested by Bambuí Group data, would result in enhanced euxinia, representing toxic environments for metazoan colonization, besides oxygen depletion. A nearly complete sulfate exhaustion also supports the scenario of methanic basin envisaged in the Chapter 4, implying that if similar basins coexisted in this time of supercontinent assembly, massive methane emissions to the atmosphere could have helped Earth to live the Neoproterozoic Era of massive glaciations towards a more warm and favorable planet for the fully development of life.

For future research in these units and/or concerning carbon and sulfur cycles in the Ediacaran-Cambrian interval, it is recommended application of independent proxies to constrain redox conditions and a similar stratigraphic approach to test all the scenarios proposed by this work. In the Tamengo Formation, main questions should concern about what would be a cause for such complex bottom oxygenation pattern, apparently independent of paleobathymetry. In this sense, geochemical proxies concerning bioproductivity, nutrient availability and redox conditions should be applied along different domains of the Tamengo ramp. For the Bambuí Group, the same is valid to better characterize possible intervals of euxinia following superheavy pyrite trends and the possible scenario of enhanced eutrophication and exhaustion of oxidants. A similar approach of carbon and sulfur investigations towards the top of the unit, as well as towards deeper domains of the basin, is required to address the entire MIBE interval bearing ^{13}C-enriched carbonates and organic matter. The dynamics proposed for superheavy pyrite trends will be supported if reproducible for the overlying 2nd-order sequences and in coeval basins bearing these anomalous signatures.

REFERENCES

Ader, M., Sansjofre, P., Halverson, G.P., Busigny, V., Trindade, R.I.F., Kunzmann, M., Nogueira, A.C.R., 2014. Ocean redox structure across the Late Neoproterozoic Oxygenation Event: A nitrogen isotope perspective. Earth and Planetary Science Letters 396, 1−13.

Ader, M., Macouin, M., Trindade, R.I.F., Hadrien, M.H., Yang, Z., Sun, Z., Besse, J., 2009. A multi layered water column in the Ediacaran Yangtze platform? Insights from carbonate and organic matter paired $\delta^{13}C$. Earth and Planetary Science Letters 288, 213–227.

Amorim, K.B., Afonso, J.W.L., Leme, J.M., Diniz, C.Q.C., Rivera, L.C.M., Gómez-Gutiérrez, J.C., Boggiani, P.C., Trindade, R.I.F., 2020. Sedimentary facies, fossil distribution and depositional setting of the late Ediacaran Tamengo Formation (Brazil). Sedimentology. https://doi.org/10.1111/sed.12749

Anbar, A.D., Knoll, A.H., 2002. Proterozoic ocean chemistry and evolution: a bioinorganic bridge? Science 297 (5584), 1137–1142.

Babcock, L.E., Grunow, A.M., Sadowski, G.R., Leslie, S.A., 2005. Corumbella, an Ediacaran-grade organism from the Late Neoproterozoic of Brazil. Palaeogeography, Palaeoclimatology, Palaeoecology 220, 7–18.

Bjerrum, C.J., Canfield, D.E., 2011. Towards a quantitative understanding of the late Neoproterozoic carbon cycle. Proceedings of the National Academy of Sciences 108 (14), 5542–5547.

Boggiani, P.C., Gaucher, C., Sial, A.N., Babinski, M., Simon, C.M., Riccomini, C., Ferreira, V.P., Fairchild, T.R., 2010. Chemostratigraphy of the Tamengo Formation (Corumbá Group, Brazil): a contribution to the calibration of the Ediacaran carbon-isotope curve. Precambrian Research 182, 382–401. http://dx.doi.org/10.1016/j.precamres.2010.06.003.

Canfield, D.E., 2001. Biogeochemistry of sulfur isotopes. Reviews in Mineralogy and Geochemistry 43 (1), 607–636.

Canfield, D.E., 2004. The evolution of the Earth surface sulfur reservoir. American Journal of Science 304 (10), 839–861.

Canfield, D.E., 2005. The early history of atmospheric oxygen: homage to Robert M. Garrels. Annual Review of Earth and Planetary Sciences 33 (1), 1–36.

Canfield, D.E., Poulton, S.W., Knoll, A.H., Narbonne, G.M., Ross, G., Goldberg, T., Strauss, H., 2008. Ferruginous conditions dominated later Neoproterozoic deep- water chemistry. Science 321, 949–952.

Canfield, D.E., Poulton, S.W., Narbonne, G.M., 2007. Late-Neoproterozoic deep-ocean oxygenation and the rise of animal life. Science 315, 92–94.

Canfield, D.E., Teske, A., 1996. Late Proterozoic rise in atmospheric oxygen concentration inferred from phylogenetic and sulphur-isotope studies. Nature 382 (6587), 127–132.

Crockford, P.W., Cowie, B.R., Johnston, D.T., Hoffman, P.F., Sugiyama, I., Pellerin, A., Bui, T.H., Hayles, J., Halverson, G.P., Macdonald, F.M., Wing, B.A., 2016. Triple oxygen and multiple sulfur isotope constraints on the evolution of the post-Marinoan sulfur cycle. Earth and Planetary Science Letters 435, 74–83.

Cui, H., Kaufman, A.J., Xiao, S., Zhu, M., Zhou, C., Liu, X.M, 2015. Redox architecture of an Ediacaran ocean margin: integrated chemostratigraphic ($\delta^{13}C$–$\delta^{34}S$–$^{87}Sr/^{86}Sr$–Ce/Ce*) correlation of the Doushantuo Formation, South China. Chemical Geology 405, 48–62.

Cui, H., Kaufman, A.J., Xiao, S., Zhou, C., Liu, X.M., 2017. Was the Ediacaran Shuram Excursion a globally synchronized early diagenetic event? Insights from methane-derived authigenic carbonates in the uppermost Doushantuo Formation, South China. Chemical Geology 450, 59–80.

Cui, H., Kaufman, A.J., Xiao, S., Peek, S., Cao, H.,Min, X., Cai, Y., Siegel, Z., Liu, X.M., Peng, Y., Schiffbauer, J.D., Martin, A.J., 2016. Environmental context for the terminal Ediacaran biomineralization of animals. Geobiology 14, 344–363.

Farquhar, J., Bao, H., Thiemens, M., 2000. Atmospheric influence of Earth's earliest sulfur cycle. Science 289, 756–758.

Farquhar, J., Johnston, D.T., Wing, B.A., Habicht, K.S., Canfield, D.E., Airieau, S., Thiemens, M.H., 2003. Multiple sulphur isotopic interpretations of biosynthetic pathways: implications for biological signatures in the sulphur isotope record. Geobiology 1 (1), 27–36.

Farquhar, J., Peters, M., Johnston, D.T., Strauss, H., Masterson, A., Wiechert, U., Kaufman, A.J., 2007. Isotopic evidence for Mesoarchaean anoxia and changing atmospheric sulphur chemistry. Nature 449 (7163), 706–709.

Farquhar, J., Wing, B.A., 2003. Multiple sulfur isotopes and the evolution of the atmosphere. Earth and Planetary Science Letters 213 (1–2), 1–13.

Feng, L., Li, C., Huang, J., Chang, H., Chu, X., 2014. A sulfate control on marine mid-depth euxinia on the early Cambrian (ca. 529–521 Ma) Yangtze platform, South China. Precambrian Research 24, 123–133.

Fike, D.A., Grotzinger, J.P., 2008. A paired sulfate–pyrite $\delta^{34}S$ approach to understanding the evolution of the Ediacaran-Cambrian sulfur cycle. Geochimica et Cosmochimica Acta 72, 2636–2648.

Fike, D.A., Grotzinger, J.P., Pratt, L.M., Summons, R.E., 2006. Oxidation of the Ediacaran Ocean. Nature 444, 744–747.

Tostevin, R., He, T., Turchyn, A.V., Wood, R.A., Penny, A.M., Bowyer, F., Antler, G., Shields, G.A., 2017. Constraints on the late Ediacaran sulfur cycle from carbonate associated sulfate. Precambrian Research 290, 113–125.

Gaucher, C., Boggiani, P.C., Sprechmann, P., Sial, A.N., Fairchild, T.R., 2003. Integrated correlation of the Vendian to Cambrian Arroyo del Soldado and Corumbá groups (Uruguay and Brazil):

Palaeogeographic, palaeoclimatic and palaeobiologic implications. Precambrian Research 120, 241–278.

Goldberg, T., Strauss, H., Guo, Q., Liu, C., 2007. Reconstructing marine redox conditions for the early Cambrian Yangtze Platform: Evidence from biogenic sulphur and organic carbon isotopes. Palaeogeography, Palaeoclimatology, Palaeoecology 254, 175–193.

Goldberg, T., Poulton, S.W., Strauss, H., 2005. Sulphur and oxygen isotope signatures of late Neoproterozoic to early Cambrian sulphate, Yangtze Platform, China: Diagenetic constrains and seawater evolution. Precambrian Research 137, 223–241.

Grotzinger, J.P., Knoll, A.H., 1995. Anomalous carbonate precipitates: is the Precambrian the keyto the Permian? Palaios 10, 578–596.

Halverson, G.P., Hurtgen, M.T., 2007. Ediacaran growth of the marine sulfate reservoir. Earth and Planetary Science Letters 263, 32–44.

Halverson, G.P., Shields-Zhou, G., 2011. Chemostratigraphy and the Neoproterozoic glaciations. In: Arnaud, E., Halverson, G.P., Shields-Zhou, G. (Eds.), The Geological Record of Neoproterozoic Glaciations. Geological Society, London, Geological Society Memoir 36, pp. 51–66.

Hoffman, P.F., Kaufman, A.J., Halverson, G.P., Schrag, D.P., 1998. A Neoproterozoic snowball Earth. Science 281, 1342–1346.

Hoffman, P.F., Schrag, D.P., 2002. The snowball Earth hypothesis: testing the limits of global change. Terra Nova 14, 129–155.

Holland, H.D., 2006. The oxygenation of the atmosphere and oceans. Philosophical Transactions of the Royal Society B: Biological Sciences 361 (1470), 903–915.

Hulston, J.R., Thode, H.G., 1965. Variations in S33 S34 and S36 contents of meteorites and their relation to chemical and nuclear effects. Journal of Geophysical Research 70 (14), 3475–3484.

Hurtgen, M.T., Halverson, G.P., Arthur, M.A., Hoffman, P.F., 2006. Sulfur cycling in the aftermath of a Neoproterozoic (Marinoan) snowball glaciation: Evidence for a syn-glacial sulfidic deep ocean. Earth and Planetary Science Letters 245, 551–570.

Hurtgen, M.T., Arthur, M.A., Halverson, G.P., 2005. Neoproterozoic sulfur isotopes, the evolution of microbial sulfur species, and the burial efficiency of sulfide as sedimentary pyrite. Geology 33 (1), 41–44.

Hurtgen, M.T., Arthur, M.A., Suits, N., Kaufman, A.J., 2002. The sulfur isotopic composition of Neoproterozoic seawater sulfate: implications for snowball Earth? Earth and Planetary Science Letters 203, 413–429.

Ishikawa, T., Ueno, Y., Shu, D., Li, Y., Han, J., Guo J., Yoshida, N., Komiya, T., 2013. Irreversible change of the oceanic carbon cycle in the earliest Cambrian: High-resolution organic and inorganic carbon chemostratigraphy in the Three Gorges area, South China. Precambrian Research 225, 190–208.

Johnston, D.T. 2011. Multiple sulfur isotopes and the evolution of Earth's surface sulfur cycle. Earth-Science Reviews 106 (2011) 161–183.

Johnston, D.T., Farquhar, J., Wing, B.A., Kaufman, A., Canfield, D.E., Habicht, K.S., 2005a. Multiple sulfur isotope fractionations in biological systems: a case study with sulfate reducers and sulfur disproportionators. American Journal of Science 305 (6–8), 645–660.

Johnston, D.T., Wing, B.A., Farquhar, J., Kaufman, A.J., Strauss, H., Lyons, T.W., Kah, L.C., Canfield, D.E., 2005b. Active microbial sulfur disproportionation in the Mesoproterozoic. Science 310 (5753), 1477–1479.

Johnston, D.T., Farquhar, J., Canfield, D.E., 2007. Sulfur isotope insights into microbial sulfate reduction: when microbes meet models. Geochimica et Cosmochimica Acta 71 (16), 3929–3947.

Johnston, D.T., Farquhar, J., Habicht, K.S., Canfield, D.E., 2008a. Sulphur isotopes and the search for life: strategies for identifying sulphur metabolisms in the rock record and beyond. Geobiology 6 (5), 425–435.

Johnston, D.T., Farquhar, J., Summons, R.E., Shen, Y., Kaufman, A.J., Masterson, A.L., Canfield, D.E., 2008b. Sulfur isotope biogeochemistry of the Proterozoic McArthur Basin. Geochimica et Cosmochimica Acta 72 (17), 4278–4290.

Kah, L.C., Lyons, T.W., Frank, T.D., 2004. Low marine sulphate and protracted oxygenation of the Proterozoic biosphere. Nature 431 (7010), 834–838.

Kennedy, M., Mrofka, D., von der Borch, C., 2008. Snowball Earth termination by destabilization of equatorial permafrost methane clathrate. Nature 453, 642–645.

Kennedy, M.J., Christie-Blick, N., 2011. Condensation origin for Neoproterozoic cap carbonates during deglaciation. Geology 39, 319–322.

Knoll, A.H., Walter, M.R., Narbonne, G.M., Christie-Blick, N., 2006. The Ediacaran Period: a new addition to the geologic time scale. Lethaia 39, 13–30.

Kroopnick, P.M., The distribution of $\delta^{13}C$ of ΣCO_2 in the world oceans. Deep-Sea Research, Part A 32, 57–84.

Swart, P.K., 2008. Global synchronous changes in the carbon isotopic composition of carbonate sediments unrelated to changes in the global carbon cycle. Proceedings of the National Academy of Sciences 105(37), 13741–13745.

Geyman, E.C., Maloof, A.C., 2019. A diurnal carbon engine explains ^{13}C-enriched carbonates without increasing the global production of oxygen. Proceedings of the National Academy of Sciences 116(49), 24433–24439.

Lang X., Shen, B., Peng, Y., Huang, K., Lv, J., Ma, H., 2016. Ocean oxidation during the deposition of basal Ediacaran Doushantuo cap carbonates in the Yangtze Platform, South China. Precambrian Research 281, 253–268.

Loyd, S.J., Marenco, P.M., Hagadorn, J.W., Lyons, T.W., Kaufman, A.J., Sour-Tovar, F., Corsetti, F.A., 2012. Sustained low marine sulfate concentrations from the Neo-proterozoic to the

Cambrian: insights from carbonates of northwestern Mexicoand eastern California. Earth and Planetary Science Letters 339 (340), 79–94.

Loyd, S.J., Marenco, P.M., Hagadorn, J.W., Lyons, T.W., Kaufman, A.J., Sour-Tovar, F.,Corsetti, F.A., 2013. Local $\delta^{34}S$ variability in ~580 Ma carbonates of northwest-ern Mexico and the Neoproterozoic marine sulfate reservoir. Precambrian Research 224, 551–569.

Macdonald, F.A., Strauss, J.V., Sperling, E.A., Halverson, G.P., Narbonne, G.M., Johnston, D.T., Kunzmann, M., Schrag, D.P., Higgins, J.A., 2013. The stratigraphic relationship between the Shuram carbon isotope excursion, the oxygenation of Neoproterozoic oceans, and the first appearance of the Ediacara biota and bilaterian trace fossils in northwestern Canada. Chemical Geology 362, 250–272.

Martins, M., Lemos, V.B., 2007. Análise estratigráfica das sequências neoproterozoicas da Bacia do São Francisco. Revista Brasileira de Geociencias 37 (4), 156–167.

McFadden, K.A., Huang, J., Chu, X., Jiang, G., Kaufman, A.J., Zhou, C., Yuan, X., Xiao, S., 2008. Pulsed oxidation and biological evolution in the Ediacaran Doushantuo Formation. Proceedings of the National Academy of Sciences of the United States of America 105, 3197–3202.

Narbonne, G.M., 2005. The Ediacara Biota: Neoproterozoic origin of animals and their ecosystems. Annual Review of Earth and Planetary Sciences 33 (1), 421–442.

Narbonne, G.M., Xiao, S., Shields, G.H., Gehling, J.G., 2012. The Ediacaran Period. In: Gradstein, F.M., Ogg, J.G., Schmitz, M., Ogg, G., (Coordinators), The Geologic Time Scale 2012. Elsevier Publisher, Oxford, pp. 413–435.

Och, L.M., Shields-Zhou, G.A., 2012. The Neoproterozoic oxygenation event: environ- mental perturbations and biogeochemical cycling. Earth-Sciences Reviews 110, 26–57.

Ono, S., 2008. Multiple-sulphur isotope biosignatures. Space Science Reviews 135 (1–4), 203–220.

Ono, S., Wing, B., Johnston, D., Farquhar, J., Rumble, D., 2006. Mass-dependent fractionation of quadruple stable sulfur isotope system as a new tracer of sulfur biogeochemical cycles. Geochimica et Cosmochimica Acta 70 (9), 2238–2252.

Osburn, M.R., Owens, J., Bergmann, K.D., Lyons, T.W., Grotzinger, J.P., 2015. Dynamic changes in sulfate sulfur isotopes preceding the Ediacaran Shuram Excursion. Geochimica et Cosmochimica Acta 170, 204–224.

Pacheco, M.L.A.F., Galante, D., Rodrigues, F., Leme, J.M., Bidola, P., Hagadorn, W., Stockmar, M., Herzen, J., Rudnitzki, I.D., Pfeiffer, F., Marques, A.C., 2015. Insights into the skeletonization, lifestyle, and affinity of the unusual ediacaran fossil Corumbella. PLoS ONE 10(3), 1−19.

Paula-Santos, G.M., Caetano-Filho, S., Babinski, M., Trindade, R.I.F, Guacaneme, C., 2017. Tracking connection and restriction of West Gondwana São Francisco Basin through isotope chemostratigraphy. Gondwana Research 42, 280−305.

Paula-Santos, G.M., Babinski, M., Kuchenbecker, M., Caetano-Filho, S., Trindade, R.I.F., Pedrosa-Soares, A.C., 2015. New evidence of an Ediacaran age for the Bambuí Group in southern São

Francisco craton (eastern Brazil) from zircon U-Pb data and isotope chemostratigraphy. Gondwana Research 28, 702–720.

Reis, H.L.S., Alkmim, F.F., Fonseca, R.C.S., Nascimento, T.C., Suss, J.F., Prevatti, L.D., 2016. The São Francisco Basin. In: Heilbron, M., Cordani, U.G., Alkmim, F.F. (Eds.), São Francisco Craton, Eastern Brazil, Regional Geology Reviews. Springer, Switzerland, pp. 117–143.

Sahoo, S.K., Planavsky, N.J., Jiang, G., Kendall, B., Owens, D., Wang, X., Shi, X., Anbar, A.D., Lyons, T.W., 2016. Oceanic oxygenation events in the anoxic Ediacaran ocean. Geobiology 14, 457−468.

Sahoo, S.K., Planavsky, N.J., Kendall, B., Wang, X., Shi, X., Scott, C., Anbar, A.D., Lyons, T.W., Jiang, G., 2012. Ocean oxygenation in the wake of the Marinoan glaciation. Nature 489, 546–549.

Sansjofre, P., Cartigny, P., Trindade, R.I.F., Nogueira, A.C.R., Agrinier, P., Ader, M., 2016. Multiple sulfur isotope evidence for massive oceanic sulfate depletion in the aftermath of Snowball Earth. Nature Communications 7, 1−8.

Santos, R.V., Alvarenga, C.J.S., Babinski, M., Ramos, M.L.S., Cukrov, N., Fonseca, M.A., Sial, A.N., Dardenne, M.A., Noce, C.M., 2004. Carbon isotopes of Mesoproterozoic–Neoproterozoic sequences from southern São Francisco craton and Araçuaí Belt, Brazil: Paleogeographic implications. Journal of South American Earth Sciences 18, 27–39.

Shen, B., Xiao, S., Kaufman, A.J., Bao, H., Zhou, C., Wang, H., 2008. Stratification and mixing of a post-glacial Neoproterozoic ocean: Evidence from carbon and sulfur isotopes in a cap dolostone from northwest China: Earth and Planetary Science Letters 265, 209–228.

Ries, J.B., Fike, D.A., Pratt, L.M., Lyons, T.W., and Grotzinger, J.P., 2009. Superheavy pyrite (δ34Spyr >δ34SCAS) in the terminal Proterozoic Nama Group, southern Namibia: A consequence of low seawater sulfate at the dawn of animal life. Geology 37, 743–746.

Shields-Zhou, G., Och, L., 2011. The case for a Neoproterozoic oxygenation event: geochemical evidence and biological consequences. GSA Today 21 (3), 4–11.

Shields-Zhou, G., Zhu, M., 2013. Biogeochemical changes across the Ediacaran–Cambrian transition in South China. Precambrian Research 225, 1–6.

Tostevin R., Wood, R.A., Shields, G.A., Poulton, S.W., Guilbaud, R., Bowyer, F., Penny, A.M., He, T., Curtis, A., Hoffmann, K.H., Clarkson, M.O., 2016. Low-oxygen waters limited habitable space for early animals. Nature Communications 7, 1−9.

Urey, H.C., 1947. The thermodynamic properties of isotopic substances. Journal of the Chemical Society 0, 562–581.

Wang, J., Jiang, G., Xiao, S., Li, Q., Wei, Q., 2008. Carbon isotope evidence for widespread methane seeps in the ca. 635 Ma Doushantuo cap carbonate in south China. Geology 36, 347–350.

Wang, X., Jiang, G., Shi, X., Xiao, S., 2016. Paired carbonate and organic carbon isotope variations of the Ediacaran Doushantuo Formation from an upper slope section at Siduping, South China. Precambrian Research 273, 53–66.

Warren, L.V., Quaglio, F., Riccomini, C., Simões, M.G., Poiré, D.G., Strikis, N.M., Anelli, L.E., Strikis, P.C., 2014. The puzzle assembled: Ediacaran guide fossil Cloudina reveals an old proto-Gondwana seaway. Geology 42(5), 391−394.

Wood, R.A., Poulton, S.W., Prave, A.R., Hoffmann, K.H., Clarkson, M.O., Guilbaud, R., Lyne, J.W., Tostevin, R., Bowyer, F., Penny, A.M., Curtis, A., Kasemann, S.A., 2015. Dynamic redox conditions control late Ediacaran ecosystems in the Nama Group, Namibia. Precambrian Research 261, 252−271.

APPENDIX A – SUPPLEMENTARY MATERIALS: CHAPTER 3 – SEQUENCE STRATIGRAPHY AND CHEMOSTRATIGRAPHY OF AN EDIACARAN-CAMBRIAN FORELAND-RELATED CARBONATE RAMP (BAMBUÍ GROUP, BRAZIL)

Table S1: Sedimentary facies from the sections of the Januária High domain.

Facies	Facies Code	Description	Sedimentary structures	Sedimentary processes	Facies association	Lithostratigraphic unit
Crystalline dolomitic limestone	C1	White to beige dolomitic limestone with intense recrystallization and vugs filled with sparry calcite. Presence of oxidized sulfide minerals.	Massive layers with high amplitude wavy bedding.	Storm-related(?) oscillatory flow.	mid ramp?	Sete Lagoas Formation
Light grey calcimudstones with aragonite pseudomorph crystal fans	C2	Light grey limestones with micritic matrix and irregular laminations with abundant aragonite pseudomorphs. Oxidized sulfide grains are present.	Horizontal planar-parallel lamination.	suspension/particle settling.	outer ramp	Sete Lagoas Formation
Reddish laminated peloidal bindstone	C3	Microbial limestones varying from intense red to pinkish color, with peloidal matrix (20 to 30 um) and oxides within the matrix. Local occurrences of aragonite pseudomorphs crusts.	microbial lamination.	Biologically-related precipitation	outer to mid ramp	Sete Lagoas Formation
Pinkish to light grey laminated peloidal bindstone with argillaceous intercalations	C4	Pinkish to light grey microbial limestones with peloidal matrix (20 to 30 um) and oxides within the matrix. Frequent intercalations of brown to green argillaceous laminae and nodular fabrics developed by differential mechanical compaction. Abundant framboidal pyrite.	Irregular/planar-parallel lamination. Microbial limestones layers present sets of wavy bedding and hummocky cross-stratification.	Biologically induced/influenced. Periods of storm-driven oscillatory flows.	mid ramp	Sete Lagoas Formation

Facies	Facies Code	Description	Sedimentary structures	Sedimentary processes	Facies association	Lithostratigraphic unit
Dark-grey laminated peloidal calcimudstone	C5	Dark grey calcimudstones with peloidal matrix (20-30 um). Presence of dissolution seams. Framboidal pyrite are rare or absent.	Horizontal planar-parallel lamination. Sets of layers with wave ripples, planar cross-stratification, and hummocky cross-stratification.	Unidirectional flow / Oscillatory flow and storm-driven oscillatory flow.	mid ramp	Sete Lagoas and Lagoa do Jacaré formations
Dark-grey laminated peloidal bindstone	C6	Dark grey microbial limestones, with peloidal matrix (20 to 60 um). Ocassionaly nodular fabrics developed by different compaction between carbonates and insoluble laminations, and clotted fabrics (thrombolites?). Framboidal pyrite are very rare, usually absent. Local occurrences of reworked microbial mats, as intraclastic packstones. SEM analysis revealed honeycomb-like structures associated with EPS (extracellular polymeric substance).	Irregular/lamelar lamination and shrub-like microbial structures. Sets of layers with wave ripples, and hummocky cross-stratification.	Storm-driven oscillatory flow associated with biologically-related processes.	mid to inner ramp	Sete Lagoas Formation
Argillaceous dark grey laminated peloidal calcimudstone	C7	Dark grey calcimudstones with peloidal matrix (20-60 um). Presence of reddish clay laminations (1-5 mm) with oxide minerals. Local occurrences of intraclastic packstones laminations.	Horizontal planar-parallel lamination, ocassionally truncated laminations. Sets of layers with wave ripples and hummocky cross-stratification.	Oscillatory flow.	mid to inner ramp	Sete Lagoas Formation

Facies	Facies Code	Description	Sedimentary structures	Sedimentary processes	Facies association	Lithostratigraphic unit
Intraclastic rudtone	C8	Intraclastic rudstones (carbonate breccias) are clast-supported, poorly-sorted, and monomictic (limestones fragments) with imbricated flat pebbles to cobbles (2 to 10 cm) and subangular to subrounded peebles (0.5 to 2 cm) - Fig. 5J.	Sets of massive bedding, ocassionally imbricated clasts. Tabular layers from several hundreds of meters of lateral extension.	Unidirectional flow.	inner ramp	Sete Lagoas and Lagoa do Jacaré formations
Intraclastic dolograinstones	C9	Intraclastic dolostone with subrounded to subangular intraclasts (2-20 mm). It shows dissolution features, such as vugular porosity. A possible paleosol layer is associated with this facies at the Santa Maria da Vitória section.	Sets of planar to trough cross-stratification.	Channelized unidirectional flow associated with decelerate processes.	inner ramp	Sete Lagoas Formation
Dolobindstones	C10	Laminated to domical dolomitic stromatolites. Fine horizontal parallel to crinkled lamination and related subaerial exposure features, as teepees.	Fine biogenically-related lamination (<4 mm), teepees.	Biologically-related precipitation and subaerial exposure.	inner ramp	Sete Lagoas Formation
Oolitic/intraclastic grainstones	C11	Oolitic to intraclastic grainstones, moderately-sorted (fine to coarse sand) with open packing and early cementation. Presence of lamelar organic matter. Intraclastic rudestones (C8) and laminated calcimudstones (C5) locally occur associated with this facies.	Massive layers and lenses interbedded with pelites from S1.	Oscillatory flow (high energy).	inner ramp (high energy)	Lagoa do Jacaré Formation

Facies	Facies Code	Description	Sedimentary structures	Sedimentary processes	Facies association	Lithostratigraphic unit
Siliciclastic siltstones and mudstones	S1	Laminated to massive siltstones and mudstones	Fine lamination to massive layers (~1cm).	suspension/particle settling.	mid to outer ramp	Serra de Santa Helena Formation

Table S2: Carbon and oxygen isotope data, carbonate content, strontium concentrations and Sr/Ca ratios.

section	sample	m	stratigraphic interval	$\delta^{13}C$ (V-PDB - ‰)	error δ13C (V-PDB ‰)	$\delta^{18}O$ (V-PDB - ‰)	error $\delta^{18}O$ (V-PDB ‰)	Carbonate (%)	Sr (ppm)	Sr/Ca (x 10^{-4})
Januária	17-CM-01	0.15	TST	-3.17	0.03	-16.70	0.06		220	6
	17-CM-01a	0.35	TST	-3.64	0.05	-14.55	0.05	98.6	255	8
	17-CM-01b	0.55	TST	-4.28	0.04	-16.21	0.06		402	12
	17-CM-01c	0.75	TST	-4.67	0.07	-16.25	0.06	93.7	380	12
	17-CM-01d	0.95	TST	-4.55	0.08	-16.16	0.08		342	11
	17-CM-02	1.15	TST	-4.30	0.08	-16.10	0.09	92.0	290	9
	17-CM-02a	1.35	TST	-4.41	0.04	-15.93	0.06		181	5
	17-CM-02b	1.55	TST	-4.35	0.05	-15.80	0.05	92.6	268	8
	17-CM-02c	1.75	TST	-3.85	0.07	-14.75	0.06		316	12
	17-CM-02d	1.95	TST	-3.83	0.04	-14.74	0.05		304	10
	17-CM-03	2.15	TST	-3.81	0.04	-14.81	0.06	92.0	261	9
	17-CM-03a	2.35	TST	-3.86	0.04	-15.05	0.06		196	5
	17-CM-03b	2.55	TST	-3.74	0.03	-14.82	0.06		397	12
	17-CM-03c	2.75	TST	-3.64	0.06	-14.81	0.06	95.1	271	9
	17-CM-03d	2.95	TST	-3.22	0.03	-12.50	0.07		198	6
	17-CM-03e	3.25	TST	-2.73	0.07	-12.79	0.06		321	11
	17-CM-03f	3.45	TST	-0.49	0.03	-11.59	0.05	95.0	3197	
	17-CM-03g	3.60	TST	-0.23	0.04	-11.57	0.06		421	12
	17-CM-03h	3.87	TST	-0.89	0.05	-10.85	0.05	92.6	293	8
	17-CM-04	4.07	TST	-0.32	0.04	-10.58	0.05		328	9
	17-CM-04a	4.27	TST	-0.73	0.03	-10.59	0.05	94.2	342	10
	17-CM-04b	4.47	TST	0.06	0.07	-7.89	0.07		262	10
	17-CM-04c	4.67	TST	-0.47	0.03	-9.84	0.04	90.8	244	8
	17-CM-04d	4.87	TST	-0.68	0.04	-9.60	0.05		257	10
	17-CM-05	5.27	TST	-0.81	0.06	-9.89	0.08	92.4	252	8
	17-CM-05a	5.47	TST	-0.80	0.03	-10.03	0.04		219	6

section	sample	m	stratigraphic interval	$\delta^{13}C$ (V-PDB - ‰)	error δ13C (V-PDB ‰)	$\delta^{18}O$ (V-PDB - ‰)	error $\delta^{18}O$ (V-PDB ‰)	Carbonate (%)	Sr (ppm)	Sr/Ca (x 10^{-4})
	17-CM-06	6.27	TST	-0.80	0.05	-9.70	0.04	89.0	207	6
	17-CM-06a	6.47	TST	-0.60	0.03	-8.57	0.04		285	8
	17-CM-07	16.50	TST	-0.91	0.05	-9.36	0.08	91.5	320	10
	17-CM-08	17.50	TST	-0.82	0.06	-8.88	0.07		227	9
	17-CM-09	18.50	TST	-0.87	0.06	-9.20	0.04		238	12
	17-CM-10	19.50	TST	-0.91	0.05	-9.13	0.06		365	12
	17-CM-11	20.50	eHST	-0.87	0.06	-9.07	0.06		242	8
	17-CM-12	21.50	eHST	-0.59	0.06	-8.35	0.05	86.8	343	14
	17-CM-13	22.50	eHST	-0.32	0.05	-8.53	0.07		367	14
	17-CM-14	23.50	eHST	-0.18	0.07	-8.30	0.07		387	13
	17-CM-15	24.50	eHST	0.04	0.05	-8.55	0.04		379	11
	17-CM-16	25.50	eHST	0.13	0.08	-8.26	0.07		435	16
	17-CM-17	26.50	eHST	0.03	0.04	-8.46	0.05		708	20
	17-CM-18	27.50	eHST	0.30	0.04	-6.91	0.04	97.6	688	19
	17-CM-19	28.50	eHST	0.33	0.03	-6.98	0.06		542	16
	17-CM-20	29.90	eHST	0.37	0.08	-6.72	0.05		744	21
	17-CM-21	30.90	eHST	0.56	0.08	-6.45	0.06		698	20
	17-CM-22	31.90	eHST	0.47	0.05	-6.90	0.10	97.9	745	20
	17-CM-23	33.40	eHST	0.75	0.05	-7.20	0.08		754	22
	17-CM-24	34.70	eHST	0.60	0.08	-7.25	0.08		727	20
	17-CM-25	35.70	eHST	0.57	0.08	-7.01	0.05		958	24
	17-CM-26	37.10	eHST	0.55	0.07	-6.95	0.03		956	26
	17-CM-27	38.10	lHST	0.85	0.07	-6.32	0.05	98.6	2127	56
	17-CM-28	39.10	lHST	0.56	0.07	-6.85	0.04		937	26
	17-CM-29	40.10	lHST	0.83	0.09	-6.44	0.06		2111	51
	17-CM-30	41.10	lHST	0.68	0.08	-6.88	0.07		1390	39
	17-CM-31	42.10	lHST	0.62	0.08	-7.03	0.06		881	22
	17-CM-32	43.10	lHST	0.66	0.09	-6.88	0.06	98.5	689	21

section	sample	m	stratigraphic interval	$\delta^{13}C$ (V-PDB - ‰)	error δ13C (V-PDB ‰)	$\delta^{18}O$ (V-PDB - ‰)	error $\delta^{18}O$ (V-PDB ‰)	Carbonate (%)	Sr (ppm)	Sr/Ca (x 10^{-4})
	17-CM-33	44.10	lHST	0.50	0.09	-6.77	0.07		1309	35
	17-CM-34	45.10	lHST	0.50	0.07	-6.77	0.06		768	19
	17-CM-35	46.80	lHST	0.83	0.07	-6.21	0.05		2307	56
	17-CM-36	47.80	lHST	0.75	0.09	-6.26	0.07		1219	30
	17-CM-37	48.80	lHST	0.79	0.08	-6.33	0.06	99.3	1825	55
	17-CM-38	49.80	lHST	0.51	0.08	-6.78	0.05		1016	25
	17-CM-39	50.80	lHST	0.59	0.08	-6.70	0.13		970	27
	17-CM-40	51.80	lHST	0.44	0.03	-6.77	0.07		1031	28
	17-CM-41	52.80	lHST	0.56	0.07	-7.09	0.04		898	26
	17-CM-42	54.50	lHST	0.41	0.03	-6.88	0.06	99.1	1315	35
	17-CM-43	55.50	lHST	0.44	0.05	-6.55	0.07		1110	28
	17-CM-44	56.50	lHST	0.52	0.08	-6.78	0.06		909	25
	17-CM-45	57.50	lHST	0.52	0.06	-6.74	0.06	98.8	865	25
	17-BAR-09	58.50	lHST	0.56	0.04	-6.59	0.04		959	26
	17-BAR-10	59.50	lHST	0.53	0.05	-6.59	0.05	99.0	1143	28
	17-BAR-11	60.50	lHST	0.43	0.04	-6.77	0.05		759	21
	17-BAR-12	61.70	lHST	0.61	0.03	-6.47	0.08		1553	37
	17-BAR-13	62.40	lHST	0.98	0.03	-6.25	0.06		384	14
	17-BAR-14	63.30	lHST	0.59	0.03	-6.81	0.04		725	21
	17-BAR-15	64.30	lHST	0.44	0.07	-6.68	0.08	98.5	691	20
	17-BAR-16	65.30	lHST	0.44	0.02	-6.46	0.04		712	18
	17-BAR-17	66.50	lHST	0.41	0.07	-6.53	0.08		536	15
	17-BAR-18	67.50	lHST	0.52	0.07	-6.65	0.10		1207	39
	17-BAR-19	68.50	lHST	0.55	0.09	-6.28	0.07		2124	59
	17-BAR-20	69.50	lHST	0.42	0.07	-6.45	0.09	98.2	874	21
	17-BAR-21	70.50	lHST	0.48	0.09	-6.37	0.07		1829	45
	17-BAR-22	71.50	lHST	0.44	0.08	-6.29	0.09		1183	32
	17-BAR-23	72.50	lHST	-0.29	0.06	-6.55	0.06		1892	54

section	sample	m	stratigraphic interval	$\delta^{13}C$ (V-PDB - ‰)	error δ13C (V-PDB ‰)	$\delta^{18}O$ (V-PDB - ‰)	error $\delta^{18}O$ (V-PDB ‰)	Carbonate (%)	Sr (ppm)	Sr/Ca (x 10^{-4})
	17-BAR-24	73.50	lHST	0.18	0.09	-6.32	0.08		983	25
	17-BAR-25	74.50	lHST	0.06	0.05	-6.28	0.04	98.2	496	13
	17-BAR-26	75.50	lHST	0.39	0.03	-6.15	0.04		325	9
	17-BAR-27	76.50	lHST	0.36	0.04	-6.53	0.04		1895	47
	17-BAR-28	77.30	lHST	0.46	0.08	-6.83	0.08		1351	36
	17-BAR-29	79.10	lHST	0.35	0.07	-6.96	0.08		538	14
	17-BAR-30	80.30	lHST	0.46	0.03	-6.63	0.04	98.8	964	26
	17-BAR-31	81.30	lHST	0.47	0.07	-6.41	0.07		671	18
	17-BAR-32	81.70	lHST	0.28	0.08	-6.76	0.06		649	18
	17-BAR-33	82.30	lHST	0.55	0.06	-7.31	0.07		446	12
	17-BAR-34	83.50	lHST	0.38	0.08	-7.54	0.10		599	16
	17-BAR-35	85.70	lHST	0.26	0.07	-7.33	0.06	98.9	1064	26
	17-BAR-36	86.90	lHST	1.38	0.07	-8.57	0.07		133	5
	17-BAR-37	88.90	lHST	0.17	0.03	-7.58	0.06		566	15
	17-BAR-38	89.90	lHST	0.23	0.07	-7.81	0.06		315	11
	17-BAR-39	91.10	lHST	0.40	0.07	-7.57	0.07		460	16
	17-BAR-40	92.50	lHST	0.51	0.08	-7.41	0.06	99.5	351	10
	17-BAR-41	94.90	lHST	0.97	0.07	-7.83	0.06		211	8
	17-BAR-42	95.90	dolomites	0.92	0.07	-8.70	0.06		109	5
	17-BAR-43	96.90	dolomites	0.43	0.07	-9.18	0.06		405	10
	17-BAR-44	97.90	dolomites	1.88	0.04	-7.78	0.07		109	5
	17-BAR-45	98.90	dolomites	2.02	0.03	-7.24	0.06		79	4
	17-JL-01	150.00	2nd sequence	9.05	0.08	-12.10	0.06	82.4	731	28
	17-JL-02	151.00	2nd sequence	12.35	0.09	-9.12	0.07		572	21
	17-JL-03	152.00	2nd sequence	13.68	0.04	-6.62	0.06		1346	33
	17-JL-04	153.00	2nd sequence	12.28	0.08	-7.50	0.06		840	24
	17-JL-05	154.00	2nd sequence	12.20	0.08	-6.53	0.05	97.1	1140	32
	17-JL-06	155.00	2nd sequence	12.74	0.08	-7.03	0.04		909	24

section	sample	m	stratigraphic interval	$\delta^{13}C$ (V-PDB - ‰)	error δ13C (V-PDB ‰)	$\delta^{18}O$ (V-PDB - ‰)	error $\delta^{18}O$ (V-PDB ‰)	Carbonate (%)	Sr (ppm)	Sr/Ca (x 10^{-4})
	17-JL-07	156.00	2nd sequence	12.88	0.08	-7.06	0.05		878	25
	17-JL-08	157.00	2nd sequence	12.41	0.05	-7.03	0.06		821	23
	17-JL-09	158.00	2nd sequence	12.21	0.09	-6.96	0.05	95.3	786	24
	17-JL-10	159.00	2nd sequence	12.17	0.09	-5.48	0.05		1081	27
	17-JL-11	160.00	2nd sequence	11.44	0.08	-7.16	0.06		820	21
	17-JL-12	161.00	2nd sequence	12.48	0.08	-6.07	0.03		757	21
	17-JL-13	162.00	2nd sequence	12.22	0.08	-7.33	0.05	97.7	874	22
	17-JL-14	166.00	2nd sequence	11.96	0.07	-6.65	0.03	93.5	1200	36
	17-JL-15	167.45	2nd sequence	9.84	0.03	-7.06	0.05		663	22
	17-JL-16	168.45	2nd sequence	10.78	0.08	-7.35	0.05		868	27
	17-JL-17	169.45	2nd sequence	11.13	0.04	-7.68	0.05	78.9	751	30
Santa Maria da Vitória	18-COR-01	1.00	TST	-2.96	0.04	-5.18	0.04	88.0	74	4
	18-COR-02	1.50	TST	-3.23	0.04	-4.87	0.04		74	4
	18-COR-03	2.00	TST	-3.35	0.05	-5.72	0.03	91.2	84	5
	18-COR-04	3.50	TST	-5.67	0.04	-10.53	0.06	63.2	210	8
	18-COR-05	4.50	TST	-6.48	0.06	-7.83	0.05	53.6	158	7
	18-COR-06	5.50	TST	-5.95	0.05	-10.84	0.04	80.2	159	13
	18-COR-07	6.50	TST	-5.85	0.05	-10.96	0.04	86.7	212	6
	18-COR-08	8.30	TST	-5.54	0.05	-10.91	0.05	90.3	239	7
	18-COR-09	9.30	TST	-5.09	0.05	-10.38	0.04	85.1	240	7
	18-COR-10	10.30	TST	-5.25	0.05	-10.61	0.04	84.5	258	8
	18-COR-11	11.30	TST	-4.88	0.05	-10.19	0.05	80.6	185	9
	18-COR-12	12.30	TST	-4.81	0.05	-10.36	0.06	90.5	177	6
	18-COR-13	13.30	TST	-4.08	0.05	-8.46	0.06	85.9	186	8
	18-COR-14	15.30	TST	-3.94	0.06	-9.56	0.05	90.4	201	7
	18-COR-15	16.00	TST	-3.20	0.05	-8.68	0.04	88.7	244	9
	18-COR-16	17.00	TST	-3.28	0.04	-8.93	0.06	89.1	242	8
	18-COR-17	18.00	TST	-0.24	0.03	-8.42	0.03	90.5	312	10

section	sample	m	stratigraphic interval	$\delta^{13}C$ (V-PDB - ‰)	error δ13C (V-PDB ‰)	$\delta^{18}O$ (V-PDB - ‰)	error $\delta^{18}O$ (V-PDB ‰)	Carbonate (%)	Sr (ppm)	Sr/Ca (x 10^{-4})
	18-COR-18	19.00	TST	0.31	0.04	-6.62	0.07		301	13
	18-COR-19	20.00	TST	-0.20	0.04	-7.98	0.06	87.5	263	8
	18-COR-20	21.00	TST	-0.18	0.03	-8.00	0.05		327	11
	18-COR-21	22.00	TST	-0.01	0.04	-7.98	0.05		257	7
	18-COR-22	23.00	TST	0.23	0.04	-7.27	0.04		355	14
	18-COR-23	24.00	TST	-0.01	0.04	-7.78	0.04		305	9
	18-COR-24	25.00	TST	-0.01	0.03	-7.53	0.04	89.1	328	11
	18-COR-25	26.00	TST	-0.17	0.03	-7.63	0.05		276	9
	18-COR-26	27.00	TST	-0.06	0.04	-7.32	0.04		292	11
	18-COR-27	28.00	TST	-0.30	0.04	-7.36	0.05		307	11
	18-COR-28	29.00	TST	-0.41	0.03	-7.45	0.04		291	9
	18-COR-29	30.00	TST	-0.04	0.05	-6.50	0.04	90.5	264	9
	18-COR-30	31.00	TST	-0.23	0.04	-6.72	0.04		463	18
	18-ALD-01	32.00	TST	-0.64	0.07	-7.21	0.08		283	9
	18-ALD-02	33.00	TST	-0.40	0.07	-7.14	0.05		272	8
	18-ALD-03	34.00	TST	-0.53	0.10	-7.33	0.09	90.5	265	7
	18-ALD-04	37.00	eHST	-0.30	0.09	-6.71	0.09		270	8
	18-ALD-05	38.00	eHST	-0.71	0.07	-7.18	0.08		288	9
	18-ALD-06	39.00	eHST	-0.44	0.08	-6.05	0.09	89.6	308	11
	18-ALD-07	40.00	eHST	-0.64	0.06	-6.61	0.06		265	8
	18-ALD-08	41.00	eHST	-0.69	0.07	-6.61	0.08		301	10
	18-ALD-09	42.00	eHST	-0.93	0.10	-6.92	0.10		322	9
	18-ALD-10	43.00	eHST	-0.49	0.05	-5.61	0.04		355	13
	18-ALD-11	44.60	eHST	-1.14	0.04	-7.10	0.05	86.3	275	9
	18-ALD-12	45.60	eHST	-0.88	0.08	-6.73	0.08		289	9
	18-ALD-13	46.60	eHST	-0.53	0.09	-5.77	0.10		302	10
	18-ALD-14	47.60	eHST	-1.11	0.10	-6.91	0.11		304	10
	18-ALD-15	48.60	eHST	-1.06	0.11	-6.91	0.09		328	11

section	sample	m	stratigraphic interval	$\delta^{13}C$ (V-PDB - ‰)	error δ13C (V-PDB ‰)	$\delta^{18}O$ (V-PDB - ‰)	error $\delta^{18}O$ (V-PDB ‰)	Carbonate (%)	Sr (ppm)	Sr/Ca (x 10^{-4})
	18-ALD-16	49.60	eHST	-0.90	0.11	-6.53	0.11		335	9
	18-ALD-17	50.60	eHST	-0.97	0.07	-6.11	0.09	89.2	357	11
	18-ALD-18	51.60	eHST	-1.22	0.09	-6.75	0.09		324	10
	18-ALD-19	52.60	eHST	-1.24	0.06	-6.82	0.06		354	12
	18-ALD-20	53.60	eHST	-1.03	0.09	-6.91	0.11		305	11
	18-ALD-21	54.60	eHST	-0.81	0.08	-6.78	0.07		344	11
	18-ALD-22	55.60	eHST	-0.65	0.09	-6.16	0.10	86.1	351	11
	18-ALD-23	56.60	eHST	-0.66	0.09	-6.27	0.08		382	12
	18-ALD-24	57.60	eHST	-0.18	0.10	-6.09	0.11		293	12
	18-ALD-25	58.60	eHST	-0.34	0.08	-6.59	0.07		368	14
	18-ALD-26	59.60	eHST	-0.41	0.09	-6.75	0.10		269	12
	18-ALD-27	60.60	eHST	-0.26	0.09	-6.69	0.10	84.2	245	9
	18-ALD-28	70.60	eHST	0.74	0.08	-6.79	0.09	95.5	851	25
	18-ALD-29	71.60	eHST	0.85	0.03	-6.98	0.10		929	23
	18-ALD-30	72.60	eHST	0.77	0.05	-7.00	0.04		740	22
	18-ALD-31	73.60	eHST	0.78	0.08	-6.88	0.06		969	27
	18-ALD-32	74.60	eHST	0.59	0.10	-6.61	0.10		791	21
	18-ALD-33	75.60	eHST	0.82	0.10	-6.74	0.07	99.2	761	22
	18-ALD-34	76.60	eHST	0.47	0.09	-6.30	0.06		947	26
	18-ALD-35	77.60	lHST	0.74	0.05	-6.35	0.06		1339	41
	18-ALD-36	78.60	lHST	0.85	0.10	-6.34	0.06		1606	45
	18-ALD-37	79.60	lHST	0.94	0.05	-6.31	0.05	96.0	2451	59
	18-ALD-38	80.60	lHST	0.78	0.07	-6.46	0.06		1704	46
	18-ALD-39	81.60	lHST	1.07	0.07	-6.44	0.07		1943	53
	18-ALD-40	83.30	lHST	0.86	0.08	-6.58	0.06		1555	38
	18-ALD-41	84.30	lHST	0.99	0.06	-6.39	0.05		2102	57
	18-ALD-42	85.30	lHST	1.34	0.05	-5.62	0.06	99.7	2279	64
	18-ALD-43	86.30	lHST	1.72	0.03	-5.36	0.05		3243	81

section	sample	m	stratigraphic interval	$\delta^{13}C$ (V-PDB - ‰)	error δ13C (V-PDB ‰)	$\delta^{18}O$ (V-PDB - ‰)	error $\delta^{18}O$ (V-PDB ‰)	Carbonate (%)	Sr (ppm)	Sr/Ca (x 10^{-4})
	18-ALD-44	87.30	lHST	0.86	0.02	-6.27	0.04		1619	45
	18-ALD-45	88.30	lHST	0.98	0.10	-6.18	0.11		1140	28
	18-ALD-46	90.30	lHST	0.76	0.11	-6.32	0.11	99.8	783	20
	18-ALD-47	91.30	lHST	1.01	0.09	-5.60	0.10		1324	33
	18-ALD-48	92.30	lHST	0.73	0.10	-6.40	0.10		1702	47
	18-ALD-49	93.30	lHST	0.52	0.09	-6.38	0.07		1050	31
	18-ALD-50	94.30	lHST	0.62	0.07	-6.22	0.06		545	21
	18-ALD-51	95.30	lHST	0.79	0.06	-5.57	0.05	97.4	1670	47
	18-ALD-52	96.30	lHST	0.99	0.10	-6.35	0.11		2432	67
	18-ALD-53	97.30	lHST	0.77	0.08	-6.20	0.07		870	25
	18-ALD-54	98.30	lHST	0.86	0.09	-6.32	0.08		1216	30
	18-ALD-55	99.30	lHST	1.31	0.05	-5.82	0.05		2080	55
	18-ALD-56	100.30	lHST	0.95	0.09	-6.54	0.08	99.9	1507	43
	18-ALD-57	101.30	lHST	0.89	0.09	-6.59	0.10		1861	58
	18-ALD-58	102.30	lHST	0.66	0.07	-6.68	0.06		2259	57
	18-ALD-59	103.30	lHST	0.84	0.04	-6.68	0.05		1242	35
	18-ALD-60	104.30	lHST	1.22	0.09	-6.56	0.10		2544	63
	18-ALD-61	105.30	lHST	0.96	0.05	-6.69	0.06	99.9	2111	54
	18-ALD-62	106.30	lHST	0.91	0.07	-7.67	0.09		1154	36
	18-BA-13	107.30	lHST	0.80	0.10	-7.38	0.10		506	14
	18-BA-14	108.30	lHST	1.00	0.10	-7.24	0.10		1592	43
	18-BA-15	112.30	lHST	1.24	0.06	-7.96	0.06	99.8	1771	48
	18-BA-16	113.30	lHST	0.88	0.05	-7.31	0.05		2051	52
	18-BA-17	114.30	lHST	0.92	0.08	-7.10	0.08		1263	38
	18-BA-18	115.30	lHST	1.18	0.11	-6.69	0.10		1817	53
	18-BA-19	116.30	lHST	1.66	0.10	-7.30	0.09		229	9
	18-BA-20	117.80	lHST	1.11	0.07	-8.01	0.07		1171	36
	18-BA-21	118.80	lHST	1.50	0.08	-6.65	0.07	97.7	1853	51

section	sample	m	stratigraphic interval	$\delta^{13}C$ (V-PDB - ‰)	error δ13C (V-PDB ‰)	$\delta^{18}O$ (V-PDB - ‰)	error $\delta^{18}O$ (V-PDB ‰)	Carbonate (%)	Sr (ppm)	Sr/Ca (x 10^{-4})
	18-BA-22	119.80	dolomites	3.96	0.09	-7.38	0.07	99.8	158	8
	18-BA-23	120.80	dolomites	4.51	0.08	-6.80	0.10		113	6
	18-BA-24	121.80	dolomites	4.84	0.07	-5.86	0.07		83	5
	18-BA-25	122.80	dolomites	5.29	0.08	-4.73	0.07		80	4
	18-BA-26	123.80	dolomites	2.88	0.03	-5.06	0.04		75	3
	18-BA-27	124.80	dolomites	7.27	0.06	-1.66	0.06	99.5	100	5
	18-BA-28	125.80	dolomites	6.82	0.07	-2.19	0.06		67	4
	18-BA-29	126.80	dolomites	4.98	0.10	-2.37	0.10		109	5
	18-BA-30	128.80	dolomites	8.13	0.09	-3.08	0.06		138	8
	18-BA-31	129.80	2nd sequence	7.37	0.05	-1.98	0.06	84.9	88	6
	18-BA-32	130.80	2nd sequence	7.55	0.07	-2.92	0.08		128	7
	18-BA-33	144.30	2nd sequence	5.22	0.10	-3.28	0.11	76.2	515	28
	18-BA-34	148.30	2nd sequence	13.92	0.05	-5.29	0.05	99.9	1155	32
	18-BA-35	149.80	2nd sequence	13.03	0.06	-5.69	0.07		631	18
Well 1	WS-01	1122.08	TST	-3.28	0.10	-7.20	0.10	86.8	150	8
	WS-02	1118.54	TST	-3.13	0.08	-7.11	0.07	73.3	79	4
	WS-02a	1116.88	TST	-2.91	0.09	-6.90	0.10	78.6	83	5
	WS-02b	1112.34	TST	-3.77	0.07	-6.66	0.08	95.1	97	5
	WS-03a	1110.49	TST	-3.65	0.08	-6.86	0.08	81.5	68	5
	WS-03b	1108.66	TST	-4.06	0.07	-7.47	0.08	92.8	93	5
	WS-04	1107.09	TST	-4.44	0.09	-10.30	0.06	91.2	143	7
	WS-04a	1105.51	TST	-3.62	0.10	-8.28	0.10	66.6	180	10
	WS-04b	1102.98	TST						186	13
	WS-06	1097.05	TST						53	52
	WS-07	1091.99	TST					26.3	137	14
	WS-08	1087.80	TST						132	12
	WS-11	1072.28	TST					9.8	46	
	WS-16	1049.37	TST						149	27

section	sample	m	stratigraphic interval	$\delta^{13}C$ (V-PDB - ‰)	error δ13C (V-PDB ‰)	$\delta^{18}O$ (V-PDB - ‰)	error $\delta^{18}O$ (V-PDB ‰)	Carbonate (%)	Sr (ppm)	Sr/Ca (x 10^{-4})
	WS-18	1043.10	eHST	-7.78	0.10	-11.96	0.09	27.9	115	19
	WS-20	1034.57	eHST					58.6	556	19
	WS-21	1029.86	eHST					45.4	502	15
	WS-22	1025.10	eHST	-3.90	0.06	-12.48	0.07	23.1	539	27
	WS-23	1020.25	eHST	-5.34	0.08	-12.52	0.06	91.3	363	12
	WS-24	1015.84	eHST	-3.33	0.08	-12.09	0.07	77.4	585	35
	WS-25	1010.10	eHST					53.9	225	37
	WS-26	1006.63	eHST	-2.93	0.09	-12.56	0.09	69.5	463	15
	WS-27	1001.90	eHST	-2.23	0.07	-12.55	0.07	56.5	316	15
	WS-28	996.77	eHST	-1.64	0.06	-12.43	0.05	80.6	397	11
	WS-29	992.00	eHST	-1.97	0.09	-12.38	0.07	70.2	378	14
	WS-30	987.03	eHST	-1.83	0.08	-12.28	0.07	83.4	335	13
	WS-31	982.43	eHST	-1.71	0.05	-12.01	0.05	86.4	367	12
	WS-32	977.82	eHST	-1.77	0.06	-12.00	0.06	74.7	370	11
	WS-33	973.34	eHST	-1.79	0.05	-11.92	0.05	53.4	446	16
	WS-34	968.74	eHST	-1.73	0.05	-11.95	0.07	46.9	397	11
	WS-35	964.30	eHST	-1.53	0.08	-11.71	0.08	37.0	324	11
	WS-36	959.52	eHST	-1.55	0.09	-11.76	0.10	61.0	345	11
	WS-37	954.82	eHST	-1.62	0.08	-11.42	0.07			
	WS-38	950.09	eHST					48.5	89	
	WS-39	945.61	eHST	-1.58	0.08	-11.09	0.05	73.4	284	11
	WS-40	940.81	eHST	-1.57	0.08	-11.01	0.08	62.8	330	11
	WS-41	936.28	eHST	-1.67	0.09	-10.76	0.08	63.8	315	13
	WS-42	932.21	eHST	-1.69	0.08	-10.80	0.07	51.9	355	14
	WS-43	927.55	eHST	-0.93	0.04	-10.55	0.04	24.8	304	10
	WS-44	922.85	eHST	-0.81	0.05	-10.55	0.04	54.4	250	11
	WS-45	918.49	eHST	-0.45	0.09	-10.44	0.11	41.5	267	17
	WS-46	913.50	eHST	-0.02	0.07	-10.50	0.08	59.6	317	14

section	sample	m	stratigraphic interval	$\delta^{13}C$ (V-PDB - ‰)	error δ13C (V-PDB ‰)	$\delta^{18}O$ (V-PDB - ‰)	error $\delta^{18}O$ (V-PDB ‰)	Carbonate (%)	Sr (ppm)	Sr/Ca (x 10^{-4})
	WS-47	909.23	eHST	0.18	0.05	-10.28	0.06	52.1	341	12
	WS-48	904.28	eHST	0.44	0.08	-10.40	0.05	27.3	247	10
	WS-49	899.70	eHST	0.60	0.07	-10.38	0.09	49.2	274	10
	WS-50	895.12	eHST	0.85	0.10	-10.36	0.09	64.6	292	11
	WS-51	890.26	eHST	0.75	0.09	-10.37	0.07	65.7	417	20
	WS-52	886.04	eHST	0.59	0.08	-10.40	0.07	42.8	342	17
	WS-53	881.15	eHST	0.65	0.08	-10.48	0.07	38.8	504	16
	WS-54	876.74	lHST	1.68	0.05	-9.93	0.05	86.9	756	25
	WS-55	872.20	lHST	2.84	0.08	-9.01	0.10	90.6	1209	38
	WS-56	867.65	lHST	4.42	0.09	-3.78	0.06	41.2	1985	63
	WS-57	863.81	lHST	3.49	0.08	-7.11	0.08	99.8	1784	51
	WS-58	859.12	lHST	3.64	0.08	-6.76	0.09	47.5	423	29
	WS-59	854.56	lHST	3.40	0.06	-7.52	0.07	95.5	2253	65
	WS-60	850.11	lHST	3.76	0.07	-6.63	0.07	84.9	2551	64
	WS-61	845.24	lHST	3.19	0.08	-6.93	0.06	97.1	1937	53
	WS-62	840.74	lHST	3.79	0.07	-6.41	0.10	99.8	2320	66
	WS-63	836.14	lHST	3.02	0.07	-7.20	0.10	89.0	1954	60
	WS-64	832.03	lHST	3.02	0.09	-7.60	0.05	98.5	2142	62
	WS-65	827.07	lHST	3.28	0.07	-6.63	0.06	97.4	2186	64
	WS-66	822.75	lHST	3.49	0.09	-5.84	0.06	98.3	2494	69
	WS-67	818.14	lHST	2.34	0.09	-8.46	0.06	40.5	1664	44
	WS-68	813.70	lHST	2.27	0.10	-8.11	0.06	88.9	1868	54
	WS-69	809.01	lHST	2.68	0.06	-8.28	0.08	82.8	2213	67
	WS-70	804.41	lHST	2.72	0.09	-8.32	0.06	41.6	2023	56
	WS-71	799.41	lHST	2.97	0.07	-7.85	0.06	95.5	2113	54
	WS-72	794.52	lHST	2.62	0.07	-8.38	0.06	17.5	1804	54
	WS-73	789.86	lHST	2.92	0.07	-8.41	0.06	94.3	2255	57
	WS-74	784.93	lHST	3.20	0.07	-8.23	0.07	97.6	1301	38

section	sample	m	stratigraphic interval	$\delta^{13}C$ (V-PDB - ‰)	error δ13C (V-PDB ‰)	$\delta^{18}O$ (V-PDB - ‰)	error $\delta^{18}O$ (V-PDB ‰)	Carbonate (%)	Sr (ppm)	Sr/Ca (x 10^{-4})
	WS-75	780.16	lHST	3.06	0.10	-8.47	0.09	95.0	1770	51
	WS-76	775.42	lHST	3.46	0.07	-8.36	0.07	94.9	1697	50
	WS-78	766.36	lHST	3.84	0.06	-4.95	0.06	78.2	1314	40
	WS-79	761.63	lHST	4.50	0.06	-7.07	0.05	67.2	2130	60
	WS-80	756.70	lHST	7.76	0.04	-6.78	0.04	99.7	3081	76
	WS-81	750.45	lHST	9.44	0.06	-7.39	0.08	99.0	2154	55
	WS-82	747.94	lHST	10.38	0.04	-7.40	0.05	99.7	2393	66
	WS-83	743.31	lHST	10.45	0.06	-7.92	0.06	92.3	2548	78
	WS-84	738.61	lHST	10.64	0.05	-13.08	0.05	96.0	2998	77
	WS-85	733.93	2nd sequence					64.5	487	75
	WS-86	729.14	2nd sequence	10.38	0.08	-13.30	0.09	55.9	1872	
	WS-87	724.45	2nd sequence	9.34	0.07	-12.73	0.07	88.8	871	121
	WS-88	719.16	2nd sequence	8.80	0.07	-12.95	0.08	23.6	508	
	WS-89	715.00	2nd sequence	8.82	0.08	-13.31	0.09	29.6	853	
	WS-90	710.22	2nd sequence	8.79	0.08	-13.80	0.08	28.5	2386	
	WS-91	705.37	2nd sequence						329	
	WS-92	700.58	2nd sequence						505	
	WS-93	695.68	2nd sequence					21.2	311	21
Arcos	M3	590.90	TST	-3.72		-6.49		81.3	156	6
	M4	592.02	TST	-4.05		-6.18		75.0	307	16
	M5	593.02	TST	-4.38		-11.27		89.6	265	11
	M6	594.02	TST	-4.23		-11.59		87.7	100	5
	M7	595.02	TST	-4.37		-8.56		85.9	120	6
	M8	596.02	TST	-4.44		-8.37		64.1	227	14
	M9	596.60	TST	-5.38		-12.99		66.6	209	9
	M10	597.54	TST	-4.83		-12.57		68.1	317	13
	M11	598.62	TST						145	12
	M12	599.27	TST	-3.73		-13.24		89.1	355	10

section	sample	m	stratigraphic interval	$\delta^{13}C$ (V-PDB - ‰)	error δ13C (V-PDB ‰)	$\delta^{18}O$ (V-PDB - ‰)	error $\delta^{18}O$ (V-PDB ‰)	Carbonate (%)	Sr (ppm)	Sr/Ca (x 10^{-4})
	M13	600.17	TST	-1.64		-8.99		83.1	158	9
	M14	601.37	TST						51	26
	M15	601.72	TST	-0.73		-7.26		81.3	153	7
	M16	602.02	TST						58	22
	M17	602.62	TST	-0.71		-8.54		81.1	165	8
	M18	604.82	TST	0.15		-8.21		91.1	127	7
	M19	605.87	TST	0.39		-8.44		96.0	160	9
	M20	606.52	TST	-1.14		-11.81		91.1	275	8
	M21	606.92	TST	-0.19		-8.06		69.7	146	9
	M22	607.37	TST	-1.27		-8.84		79.4	430	12
	M23	607.52	TST						65	30
	K23a	608.17	TST						177	15
	K23b	609.17	TST						54	
	K23c	610.17	TST						189	14
	K23d	611.27	TST						115	31
	K23e	611.77	TST						100	27
	M24	612.02	TST	-0.80		-11.36		16.3	65	
	K24a	613.02	TST						413	20
	K24b	614.02	TST						62	
	K24c	614.77	TST						34	
	M25	616.77	TST	0.43		-10.65			84	
	M26	621.77	TST	0.56		-9.89			54	
	K26c	624.42	eHST						283	18
	M27	626.42	eHST	1.24		-7.90		57.3	271	11
	K27b	628.17	eHST	1.86	0.05	-8.45	0.04		167	7
	K27c	629.17	eHST	1.69	0.04	-5.83	0.05		157	10
	K27d	630.17	eHST	1.59	0.05	-7.86	0.04		170	8
	M28	631.17	eHST	0.93		-6.95			210	5

section	sample	m	stratigraphic interval	$\delta^{13}C$ (V-PDB - ‰)	error δ13C (V-PDB ‰)	$\delta^{18}O$ (V-PDB - ‰)	error $\delta^{18}O$ (V-PDB ‰)	Carbonate (%)	Sr (ppm)	Sr/Ca (x 10^{-4})
	K28a	632.17	eHST	0.84	0.05	-6.91	0.06	95.3	154	4
	K28b	633.02	eHST	0.38	0.05	-7.28	0.05		211	5
	K28c	634.02	eHST	0.88	0.06	-6.60	0.06		228	6
	K28d	635.02	eHST	0.91	0.05	-6.81	0.06		184	5
	M29	636.02	eHST	1.08		-6.84			239	6
	K29a	637.02	eHST	0.93	0.05	-6.74	0.05	97.6	261	7
	K29b	638.02	eHST	0.97	0.05	-6.93	0.05		274	7
	K29c	639.02	eHST	0.94	0.05	-6.94	0.04		178	4
	K29d	640.02	eHST	0.88	0.04	-7.18	0.05		199	5
	M30	641.02	eHST	0.75		-6.47			179	5
	K30a	642.02	eHST	1.14	0.04	-6.64	0.05	98.5	192	5
	K30b	643.02	eHST	1.00	0.04	-6.26	0.04		219	6
	K30c	644.02	eHST	1.23	0.05	-6.37	0.07		225	6
	K30d	645.02	eHST	1.16	0.05	-6.79	0.05		204	6
	M31	646.02	eHST	0.98		-6.40			226	6
	K31a	647.02	eHST	1.22	0.07	-6.48	0.08		186	5
	K31b	648.02	eHST	1.17	0.05	-6.73	0.06		139	4
	K31c	649.02	eHST	1.23	0.05	-6.32	0.04	98.7	222	6
	K31d	650.02	eHST	1.19	0.05	-6.56	0.05		213	5
	M32	651.02	eHST	1.27		-6.87			223	7
	K32a	652.02	eHST	1.09	0.06	-6.98	0.04		295	7
	K32b	653.02	eHST	1.01	0.05	-7.46	0.05		215	5
	K32c	654.02	eHST	1.09	0.04	-7.61	0.07		226	5
	K32d	655.02	eHST	1.07	0.05	-6.82	0.05	99.5	256	7
	M33	656.02	eHST	1.12		-6.97			267	6
	K33a	657.02	eHST	1.01	0.04	-7.30	0.06		307	8
	K33b	658.02	eHST	1.00	0.04	-6.70	0.05		274	7
	K33c	659.02	eHST	1.04	0.03	-7.89	0.05		267	7

section	sample	m	stratigraphic interval	$\delta^{13}C$ (V-PDB - ‰)	error δ13C (V-PDB ‰)	$\delta^{18}O$ (V-PDB - ‰)	error $\delta^{18}O$ (V-PDB ‰)	Carbonate (%)	Sr (ppm)	Sr/Ca (x 10^{-4})
	K33d	660.02	eHST	1.12	0.03	-7.14	0.05	99.7	239	6
	M34	661.02	eHST	1.10		-7.18			263	7
	K34a	662.02	eHST	1.06	0.05	-8.24	0.05		253	7
	K34b	663.17	eHST	1.04	0.03	-7.78	0.05		383	9
	K34c	664.17	eHST	1.05	0.03	-8.06	0.06	98.5	365	10
	K34d	665.17	eHST	1.06	0.04	-8.07	0.05		296	8
	M35	666.17	eHST	1.05		-8.06			249	7
	K35a	667.17	eHST	0.94	0.04	-7.72	0.04		258	7
	K35b	668.17	eHST	1.03	0.03	-8.01	0.04		274	7
	K35c	668.41	eHST	1.08	0.03	-6.30	0.06		632	18
	K35d	669.41	eHST	0.95	0.04	-6.89	0.06	96.0	676	18
	K35e	670.41	eHST	1.03	0.03	-8.44	0.05		379	10
	M36	671.41	eHST	0.77		-8.34			417	11
	K36a	672.41	eHST	1.08	0.07	-8.32	0.07		279	7
	K36b	673.41	eHST	1.17	0.04	-8.08	0.04		299	7
	K36c	674.41	eHST	1.01	0.03	-7.43	0.05	99.0	369	10
	K36d	675.41	eHST	1.04	0.05	-7.32	0.05		345	9
	M37	676.41	eHST	1.00		-7.44			383	10
	K37a	677.41	eHST	1.04	0.05	-8.31	0.05		467	11
	K37b	678.36	eHST	0.70	0.04	-8.56	0.06		536	14
	K37c	679.36	eHST	0.71	0.09	-8.15	0.08	97.3	829	20
	K37d	680.51	eHST	0.88	0.04	-8.07	0.05		952	25
	M38	681.51	eHST	0.98		-7.18			778	21
	K38a	682.61	lHST	1.23	0.03	-8.49	0.04		1865	51
	K38b	683.56	lHST	1.10	0.06	-7.98	0.06		1135	30
	K38c	684.41	lHST	1.18	0.04	-7.90	0.05	99.1	1771	48
	K38d	685.66	lHST	1.26	0.05	-7.80	0.05		1388	37
	M39	686.66	lHST	1.50		-7.40			3295	79

section	sample	m	stratigraphic interval	$\delta^{13}C$ (V-PDB - ‰)	error δ13C (V-PDB ‰)	$\delta^{18}O$ (V-PDB - ‰)	error $\delta^{18}O$ (V-PDB ‰)	Carbonate (%)	Sr (ppm)	Sr/Ca (x 10^{-4})
	K39a	687.66	lHST	1.58	0.03	-7.88	0.04		2234	54
	K39b	688.66	lHST	1.47	0.03	-8.08	0.05		1597	42
	K39c	689.76	lHST	1.36	0.06	-8.07	0.07		2345	62
	M40	690.90	lHST	1.52		-7.99		99.2	1724	46
	K40a	692.56	lHST	1.11	0.06	-7.34	0.07		1771	48
	K40b	693.71	lHST	1.09	0.05	-8.27	0.05		922	23
	K40c	694.66	lHST	1.07	0.04	-8.38	0.05		1274	34
	K40d	695.66	lHST	0.92	0.05	-7.28	0.08		1730	47
	M41	696.66	lHST	0.40		-6.63			190	7
	K41a	697.66	lHST	0.62	0.03	-8.17	0.05		739	18
	K41b	698.66	lHST	0.66	0.03	-8.04	0.06		553	15
	K41c	699.66	lHST	0.52	0.03	-5.66	0.04		1080	29
	K41d	700.66	lHST	1.19	0.04	-8.10	0.06		1337	36
	M42	701.66	lHST	1.11		-8.32		99.3	1091	29
	K42a	702.66	lHST	0.67	0.07	-7.55	0.11		1174	29
	K42b	703.41	lHST	1.08	0.04	-8.03	0.06		1523	41
	K42c	704.41	lHST	0.60	0.05	-8.50	0.07		561	15
	K42d	705.41	lHST	0.88	0.04	-8.10	0.06	99.2	1031	28
	M43	706.41	lHST	0.73		-8.61			741	20
	K43a	707.41	lHST	0.55	0.04	-8.56	0.06		717	19
	K43b	708.41	lHST	0.90	0.03	-8.66	0.05		739	18
	K43c	709.41	lHST	1.04	0.03	-8.67	0.06		1143	31
	K43d	710.41	lHST	1.24	0.04	-8.89	0.05		1592	43
	M44	711.41	lHST	1.14		-8.73		99.5	1750	42
	K44a	712.41	lHST	1.46	0.07	-8.70	0.07		1209	29
	K44b	713.41	lHST	1.22	0.05	-8.57	0.05		1878	50
	K44c	714.41	lHST	1.23	0.05	-8.46	0.05		1656	44
	K44d	715.41	lHST	1.32	0.04	-8.54	0.05		1488	35

section	sample	m	stratigraphic interval	$\delta^{13}C$ (V-PDB - ‰)	error δ13C (V-PDB ‰)	$\delta^{18}O$ (V-PDB - ‰)	error $\delta^{18}O$ (V-PDB ‰)	Carbonate (%)	Sr (ppm)	Sr/Ca (x 10^{-4})
	M45	716.41	lHST	1.43		-8.43		98.7	1326	36
	K45a	717.41	lHST	1.34	0.05	-8.28	0.07		1737	46
	K45b	718.41	lHST	1.45	0.04	-8.20	0.06		1509	36
	K45c	719.41	lHST	1.51	0.04	-8.10	0.06		1851	45
	K45d	720.41	lHST	1.53	0.05	-8.13	0.07		1945	47
	M46	721.41	lHST	1.61		-7.80		99.8	1001	24
	K46a	722.41	lHST	1.38	0.04	-8.10	0.06		1786	47
	K46b	723.41	lHST	1.44	0.04	-7.82	0.05		869	24
	K46c	724.41	lHST	-0.13	0.04	-7.01	0.06		545	15
	K46d	725.41	lHST	1.36	0.05	-8.23	0.07		1473	39
	M47	726.41	lHST	1.83		-7.73		99.8	1956	46
	K47a	727.41	lHST	1.59	0.04	-8.44	0.06		1570	41
	K47b	728.41	lHST	1.50	0.05	-8.21	0.06		2131	51
	K47c	729.41	lHST	1.59	0.05	-7.85	0.06		1918	51
	K47d	730.41	lHST	1.16	0.05	-8.22	0.08		1949	46
	M48	731.41	lHST	1.91		-6.74		99.6	3353	79
	K48a	732.41	lHST	1.62	0.04	-7.96	0.06		2014	48
	K48b	733.41	lHST	1.71	0.04	-7.75	0.06		2500	59
	K48c	734.41	lHST	1.64	0.04	-7.77	0.06		2422	57
	K48d	735.41	lHST	1.45	0.06	-7.88	0.07		2706	64
	M49	736.41	lHST	1.43		-7.66		98.9	2919	69
	K49a	737.41	lHST	1.36	0.04	-7.75	0.06		2949	78
	K49b	738.41	dolomites	0.54	0.05	-9.87	0.06		212	8
	K49c	738.91	dolomites	0.23	0.05	-10.52	0.07		75	4
	K49d	739.91	dolomites	0.74	0.05	-7.61	0.06		73	3
	K49e	740.91	dolomites	-0.51	0.05	-4.52	0.05		143	7
	M50	741.91	dolomites	0.77		-4.47		96.3	172	9
	K50a	743.16	dolomites	-0.22	0.05	-4.50	0.07		227	10

section	sample	m	stratigraphic interval	$\delta^{13}C$ (V-PDB - ‰)	error δ13C (V-PDB ‰)	$\delta^{18}O$ (V-PDB - ‰)	error $\delta^{18}O$ (V-PDB ‰)	Carbonate (%)	Sr (ppm)	Sr/Ca (x 10^{-4})
	K50b	744.16	dolomites	1.75	0.04	-4.76	0.06		209	9
	K50c	745.16	dolomites	2.50	0.05	-5.88	0.05		130	6
	K50d	746.16	dolomites	2.56	0.04	-5.49	0.07		100	5
	M51	747.16	dolomites	2.50		-5.70		99.2	132	6
	K51a	748.16	dolomites	2.27	0.05	-5.94	0.06		148	6
	K51b	749.16	dolomites	2.23	0.06	-5.02	0.06		132	6
	K51c	750.16	dolomites	2.32	0.05	-4.95	0.05		146	6
	K51d	751.16	dolomites	1.62	0.07	-3.81	0.07		145	6
	M52	752.16	dolomites	1.49		-4.42			145	7
	K52a	753.16	dolomites	1.34	0.06	-4.75	0.06	98.4	130	7
	K52b	754.16	dolomites	-0.55	0.05	-5.30	0.06		205	9
	K52c	755.16	dolomites	1.08	0.05	-5.13	0.05		119	5
	K52d	756.16	dolomites	1.61	0.04	-4.82	0.05		177	8
	M53	757.16	dolomites	1.50		-4.65		97.8	136	7
	MD1	758.16	dolomites	1.42	0.04	-4.63	0.05		117	8
	MD2	759.16	dolomites	1.33	0.04	-5.37	0.07		143	9
	MD3	760.16	dolomites	-0.13	0.04	-4.43	0.05		144	10
	MD4	761.16	dolomites	5.27	0.04	-4.84	0.06		169	11
	M54	762.16	dolomites	5.41	0.04	-7.64	0.06	91.7	132	6
	MD5	763.16	dolomites	5.57	0.04	-7.74	0.07		188	10
	MD6	764.16	2nd sequence	6.61	0.04	-7.25	0.05		1038	49
	MD7	765.16	2nd sequence	7.85	0.05	-7.33	0.07		598	26
	MD8	766.16	2nd sequence	7.38	0.05	-6.22	0.07		665	26
	M55	767.16	2nd sequence	7.34		-7.63		84.5	571	19

Analytical precision: δ13C - 0.05‰ and δ18O - 0.07‰

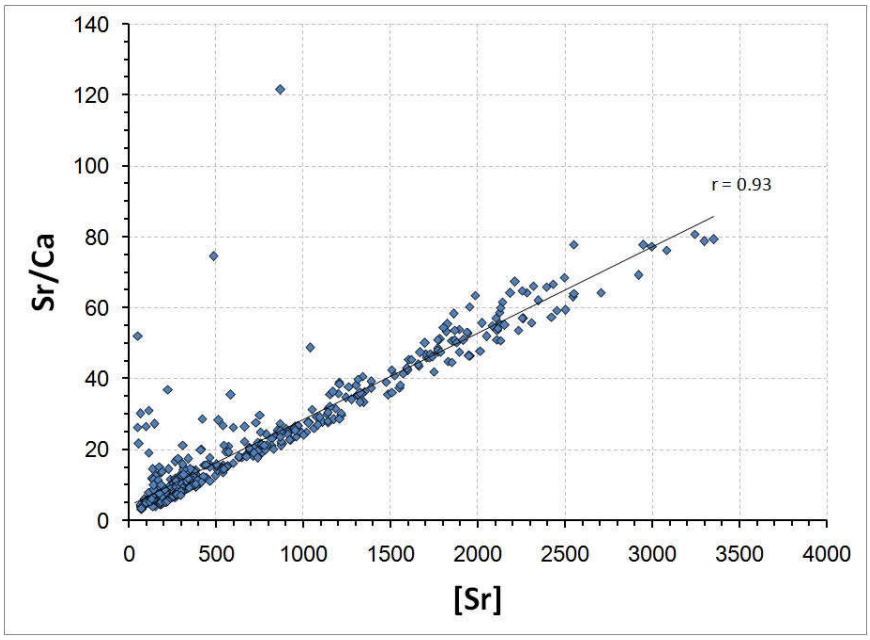

Figure S1: Sr concentrations *vs* Sr/Ca ratios.

APPENDIX B – SUPPLEMENTARY MATERIALS: CHAPTER 4 – A LARGE EPEIRIC METHANOGENIC BAMBUÍ SEA IN THE CORE OF GONDWANA SUPERCONTINENT?

Table S1: Paired carbon isotope data, carbonate, insoluble residue and TOC contents, and Sr/Ca ratios.

Section	Sample	m	Stage	$\delta^{13}C_{carb}$ (‰ - V-PDB)	error $\delta^{13}C_{carb}$ (‰)	$\delta^{18}O_{carb}$ (‰ - V-PDB)	error $\delta^{18}O_{carb}$ (‰)	$\delta^{13}C_{org}$ (‰ - V-PDB)	%C	$\Delta^{13}C$ (‰)	Carbonate (%)	IR (%)	TOC (%)	Sr/Ca (x 10^{-4})
Januária	17-CM-01	0.15	TST	-3.17	0.03	-16.70	0.06							6
	17-CM-01a	0.35	TST	-3.64	0.05	-14.55	0.05	-28.95	0.34	25.31	98.57	1.43	0.00	8
	17-CM-01b	0.55	TST	-4.28	0.04	-16.21	0.06							12
	17-CM-01c	0.75	TST	-4.67	0.07	-16.25	0.06	-26.13	0.13	21.46	93.68	6.32	0.01	12
	17-CM-01d	0.95	TST	-4.55	0.08	-16.16	0.08							11
	17-CM-02	1.15	TST	-4.30	0.08	-16.10	0.09	-25.44	0.12	21.14	91.98	8.02	0.01	9
	17-CM-02a	1.35	TST	-4.41	0.04	-15.93	0.06							5
	17-CM-02b	1.55	TST	-4.35	0.05	-15.80	0.05	-21.36	0.12	17.02	92.55	7.45	0.01	8
	17-CM-02c	1.75	TST	-3.85	0.07	-14.75	0.06							12
	17-CM-02d	1.95	TST	-3.83	0.04	-14.74	0.05							10
	17-CM-03	2.15	TST	-3.81	0.04	-14.81	0.06	-22.17	0.09	18.36	92.05	7.95	0.01	9
	17-CM-03a	2.35	TST	-3.86	0.04	-15.05	0.06							5
	17-CM-03b	2.55	TST	-3.74	0.03	-14.82	0.06							12
	17-CM-03c	2.75	TST	-3.64	0.06	-14.81	0.06	-24.90	0.92	21.26	95.12	4.88	0.04	9
	17-CM-03d	2.95	TST	-3.22	0.03	-12.50	0.07							6
	17-CM-03e	3.25	TST	-2.73	0.07	-12.79	0.06							11
	17-CM-03f	3.45	TST	-0.49	0.03	-11.59	0.05	-26.25	0.14	25.76	95.01	4.99	0.01	
	17-CM-03g	3.6	TST	-0.23	0.04	-11.57	0.06							12
	17-CM-03h	3.87	TST	-0.89	0.05	-10.85	0.05		0.09		92.64	7.36	0.01	8
	17-CM-04	4.07	TST	-0.32	0.04	-10.58	0.05							9
	17-CM-04a	4.27	TST	-0.73	0.03	-10.59	0.05	-25.71	0.05	24.98	94.21	5.79	0.00	10
	17-CM-04b	4.47	TST	0.06	0.07	-7.89	0.07							10
	17-CM-04c	4.67	TST	-0.47	0.03	-9.84	0.04	-28.68	0.06	28.21	90.76	9.24	0.01	8
	17-CM-04d	4.87	TST	-0.68	0.04	-9.60	0.05							10

Section	Sample	m	Stage	$\delta^{13}C_{carb}$ (‰ - V-PDB)	error $\delta^{13}C_{carb}$ (‰)	$\delta^{18}O_{carb}$ (‰ - V-PDB)	error $\delta^{18}O_{carb}$ (‰)	$\delta^{13}C_{org}$ (‰ - V-PDB)	%C	$\Delta^{13}C$ (‰)	Carbonate (%)	IR (%)	TOC (%)	Sr/Ca (x 10^{-4})
	17-CM-05	5.27	TST	-0.81	0.06	-9.89	0.08	-28.53	0.05	27.72	92.35	7.65	0.00	8
	17-CM-05a	5.47	TST	-0.80	0.03	-10.03	0.04							6
	17-CM-06	6.27	TST	-0.80	0.05	-9.70	0.04	-26.92	0.02	26.12	89.03	10.97	0.00	6
	17-CM-06a	6.47	TST	-0.60	0.03	-8.57	0.04							8
	17-CM-07	16.5	TST	-0.91	0.05	-9.36	0.08	-27.91	0.05	27.00	91.52	8.48	0.00	10
	17-CM-08	17.5	TST	-0.82	0.06	-8.88	0.07							9
	17-CM-09	18.5	TST	-0.87	0.06	-9.20	0.04							12
	17-CM-10	19.5	TST	-0.91	0.05	-9.13	0.06							12
	17-CM-11	20.5	EHST	-0.87	0.06	-9.07	0.06							8
	17-CM-12	21.5	EHST	-0.59	0.06	-8.35	0.05	-28.19	0.06	27.60	86.77	13.23	0.01	14
	17-CM-13	22.5	EHST	-0.32	0.05	-8.53	0.07							14
	17-CM-14	23.5	EHST	-0.18	0.07	-8.30	0.07							13
	17-CM-15	24.5	EHST	0.04	0.05	-8.55	0.04							11
	17-CM-16	25.5	EHST	0.13	0.08	-8.26	0.07							16
	17-CM-17	26.5	EHST	0.03	0.04	-8.46	0.05							20
	17-CM-18	27.5	EHST	0.30	0.04	-6.91	0.04	-30.50	1.59	30.80	97.61	2.39	0.04	19
	17-CM-19	28.5	EHST	0.33	0.03	-6.98	0.06							16
	17-CM-20	29.9	EHST	0.37	0.08	-6.72	0.05							21
	17-CM-21	30.9	EHST	0.56	0.08	-6.45	0.06							20
	17-CM-22	31.9	EHST	0.47	0.05	-6.90	0.10	-30.84	2.03	31.31	97.89	2.11	0.04	20
	17-CM-23	33.4	EHST	0.75	0.05	-7.20	0.08							22
	17-CM-24	34.7	EHST	0.60	0.08	-7.25	0.08							20
	17-CM-25	35.7	EHST	0.57	0.08	-7.01	0.05							24
	17-CM-26	37.1	EHST	0.55	0.07	-6.95	0.03							26
	17-CM-27	38.1	LHST	0.85	0.07	-6.32	0.05	-29.13	2.82	29.99	98.59	1.41	0.04	56

Section	Sample	m	Stage	$\delta^{13}C_{carb}$ (‰ - V-PDB)	error $\delta^{13}C_{carb}$ (‰)	$\delta^{18}O_{carb}$ (‰ - V-PDB)	error $\delta^{18}O_{carb}$ (‰)	$\delta^{13}C_{org}$ (‰ - V-PDB)	%C	$\Delta^{13}C$ (‰)	Carbonate (%)	IR (%)	TOC (%)	Sr/Ca (x 10^{-4})
	17-CM-28	39.1	LHST	0.56	0.07	-6.85	0.04							26
	17-CM-29	40.1	LHST	0.83	0.09	-6.44	0.06							51
	17-CM-30	41.1	LHST	0.68	0.08	-6.88	0.07							39
	17-CM-31	42.1	LHST	0.62	0.08	-7.03	0.06							22
	17-CM-32	43.1	LHST	0.66	0.09	-6.88	0.06	-30.29	2.94	30.95	98.51	1.49	0.04	21
	17-CM-33	44.1	LHST	0.50	0.09	-6.77	0.07							35
	17-CM-34	45.1	LHST	0.50	0.07	-6.77	0.06							19
	17-CM-35	46.8	LHST	0.83	0.07	-6.21	0.05							56
	17-CM-36	47.8	LHST	0.75	0.09	-6.26	0.07							30
	17-CM-37	48.8	LHST	0.79	0.08	-6.33	0.06	-29.54	4.63	30.33	99.34	0.66	0.03	55
	17-CM-38	49.8	LHST	0.51	0.08	-6.78	0.05							25
	17-CM-39	50.8	LHST	0.59	0.08	-6.70	0.13							27
	17-CM-40	51.8	LHST	0.44	0.03	-6.77	0.07							28
	17-CM-41	52.8	LHST	0.56	0.07	-7.09	0.04							26
	17-CM-42	54.5	LHST	0.41	0.03	-6.88	0.06	-29.92	3.79	30.33	99.10	0.90	0.03	35
	17-CM-43	55.5	LHST	0.44	0.05	-6.55	0.07							28
	17-CM-44	56.5	LHST	0.52	0.08	-6.78	0.06							25
	17-CM-45	57.5	LHST	0.52	0.06	-6.74	0.06	-29.64	1.32	30.16	98.75	1.25	0.02	25
	17-BAR-09	58.50	LHST	0.56	0.04	-6.59	0.04							26
	17-BAR-10	59.50	LHST	0.53	0.05	-6.59	0.05	-30.10	4.38	30.64	98.97	1.03	0.05	28
	17-BAR-11	60.50	LHST	0.43	0.04	-6.77	0.05							21
	17-BAR-12	61.70	LHST	0.61	0.03	-6.47	0.08							37
	17-BAR-13	62.40	LHST	0.98	0.03	-6.25	0.06							14
	17-BAR-14	63.30	LHST	0.59	0.03	-6.81	0.04							21
	17-BAR-15	64.30	LHST	0.44	0.07	-6.68	0.08		1.54		98.48	1.52	0.02	20

Section	Sample	m	Stage	$\delta^{13}C_{carb}$ (‰ - V-PDB)	error $\delta^{13}C_{carb}$ (‰)	$\delta^{18}O_{carb}$ (‰ - V-PDB)	error $\delta^{18}O_{carb}$ (‰)	$\delta^{13}C_{org}$ (‰ - V-PDB)	%C	$\Delta^{13}C$ (‰)	Carbonate (%)	IR (%)	TOC (%)	Sr/Ca (x 10^{-4})
	17-BAR-16	65.30	LHST	0.44	0.02	-6.46	0.04							18
	17-BAR-17	66.50	LHST	0.41	0.07	-6.53	0.08							15
	17-BAR-18	67.50	LHST	0.52	0.07	-6.65	0.10							39
	17-BAR-19	68.50	LHST	0.55	0.09	-6.28	0.07							59
	17-BAR-20	69.50	LHST	0.42	0.07	-6.45	0.09	-29.38	1.85	29.81	98.16	1.84	0.03	21
	17-BAR-21	70.50	LHST	0.48	0.09	-6.37	0.07							45
	17-BAR-22	71.50	LHST	0.44	0.08	-6.29	0.09							32
	17-BAR-23	72.50	LHST	-0.29	0.06	-6.55	0.06							54
	17-BAR-24	73.50	LHST	0.18	0.09	-6.32	0.08							25
	17-BAR-25	74.50	LHST	0.06	0.05	-6.28	0.04	-30.65	1.04	30.71	98.17	1.83	0.02	13
	17-BAR-26	75.50	LHST	0.39	0.03	-6.15	0.04							9
	17-BAR-27	76.50	LHST	0.36	0.04	-6.53	0.04							47
	17-BAR-28	77.30	LHST	0.46	0.08	-6.83	0.08							36
	17-BAR-29	79.10	LHST	0.35	0.07	-6.96	0.08							14
	17-BAR-30	80.30	LHST	0.46	0.03	-6.63	0.04	-30.14	1.96	30.60	98.85	1.15	0.02	26
	17-BAR-31	81.30	LHST	0.47	0.07	-6.41	0.07							18
	17-BAR-32	81.70	LHST	0.28	0.08	-6.76	0.06							18
	17-BAR-33	82.30	LHST	0.55	0.06	-7.31	0.07							12
	17-BAR-34	83.50	LHST	0.38	0.08	-7.54	0.10							16
	17-BAR-35	85.70	LHST	0.26	0.07	-7.33	0.06	-29.19	1.73	29.45	98.94	1.06	0.02	26
	17-BAR-36	86.90	LHST - dolomites	1.38	0.07	-8.57	0.07							5
	17-BAR-37	88.90	LHST - dolomites	0.17	0.03	-7.58	0.06							15
	17-BAR-38	89.90	LHST - dolomites	0.23	0.07	-7.81	0.06							11
	17-BAR-39	91.10	LHST - dolomites	0.40	0.07	-7.57	0.07							16
	17-BAR-40	92.50	LHST -	0.51	0.08	-7.41	0.06	-30.02	3.98	30.53	99.49	0.51	0.02	10

Section	Sample	m	Stage	$\delta^{13}C_{carb}$ (‰ - V-PDB)	error $\delta^{13}C_{carb}$ (‰)	$\delta^{18}O_{carb}$ (‰ - V-PDB)	error $\delta^{18}O_{carb}$ (‰)	$\delta^{13}C_{org}$ (‰ - V-PDB)	%C	$\Delta^{13}C$ (‰)	Carbonate (%)	IR (%)	TOC (%)	Sr/Ca (x 10^{-4})
			dolomites											
	17-BAR-41	94.90	LHST - dolomites	0.97	0.07	-7.83	0.06							8
	17-BAR-42	95.90	LHST - dolomites	0.92	0.07	-8.70	0.06							5
	17-BAR-43	96.90	LHST - dolomites	0.43	0.07	-9.18	0.06							10
	17-BAR-44	97.90	LHST - dolomites	1.88	0.04	-7.78	0.07							5
	17-BAR-45	98.90	LHST - dolomites	2.02	0.03	-7.24	0.06							4
	17-JL-01	150	2nd-sequence	9.05	0.08	-12.10	0.06	-21.19	0.42	30.24	82.43	17.57	0.07	28
	17-JL-02	151	2nd-sequence	12.35	0.09	-9.12	0.07							21
	17-JL-03	152	2nd-sequence	13.68	0.04	-6.62	0.06							33
	17-JL-04	153	2nd-sequence	12.28	0.08	-7.50	0.06							24
	17-JL-05	154	2nd-sequence	12.20	0.08	-6.53	0.05	-17.89	3.12	30.08	97.09	2.91	0.09	32
	17-JL-06	155	2nd-sequence	12.74	0.08	-7.03	0.04							24
	17-JL-07	156	2nd-sequence	12.88	0.08	-7.06	0.05							25
	17-JL-08	157	2nd-sequence	12.41	0.05	-7.03	0.06							23
	17-JL-09	158	2nd-sequence	12.21	0.09	-6.96	0.05	-20.27	0.85	32.48	95.33	4.67	0.04	24
	17-JL-10	159	2nd-sequence	12.17	0.09	-5.48	0.05							27
	17-JL-11	160	2nd-sequence	11.44	0.08	-7.16	0.06							21
	17-JL-12	161	2nd-sequence	12.48	0.08	-6.07	0.03							21
	17-JL-13	162	2nd-sequence	12.22	0.08	-7.33	0.05	-19.82	2.62	32.04	97.66	2.34	0.06	22
	17-JL-14	166	2nd-sequence	11.96	0.07	-6.65	0.03	-19.27	0.94	31.22	93.48	6.52	0.06	36
	17-JL-15	167.45	2nd-sequence	9.84	0.03	-7.06	0.05							22

Section	Sample	m	Stage	$\delta^{13}C_{carb}$ (‰ - V-PDB)	error $\delta^{13}C_{carb}$ (‰)	$\delta^{18}O_{carb}$ (‰ - V-PDB)	error $\delta^{18}O_{carb}$ (‰)	$\delta^{13}C_{org}$ (‰ - V-PDB)	%C	$\Delta^{13}C$ (‰)	Carbonate (%)	IR (%)	TOC (%)	Sr/Ca (x 10^{-4})
	17-JL-16	168.45	2nd-sequence	10.78	0.08	-7.35	0.05							27
	17-JL-17	169.45	2nd-sequence	11.13	0.04	-7.68	0.05	-21.43	0.29	32.56	78.94	21.06	0.06	30
Arcos	M3	590.9	TST	**-3.72**		**-6.49**		-27.57	0.01	23.85	81.28	18.72	0.00	6
	M4	592.02	TST	**-4.05**		**-6.18**					74.96	25.04		16
	M5	593.02	TST	**-4.38**		**-11.27**		-26.92	0.12	22.54	89.56	10.44	0.01	11
	M6	594.02	TST	**-4.23**		**-11.59**		-27.03	0.08	22.80	87.73	12.27	0.01	5
	M7	595.02	TST	**-4.37**		**-8.56**		-26.14	0.08	21.77	85.95	14.05	0.01	6
	M8	596.02	TST	**-4.44**		**-8.37**		-27.14	0.00	22.70	64.06	35.94	0.00	14
	M9	596.6	TST	**-5.38**		**-12.99**		-27.08	0.04	21.70	66.57	33.43	0.01	9
	M10	597.54	TST	**-4.83**		**-12.57**		-28.11	0.08	23.28	68.09	31.91	0.02	13
	M11	598.62	TST											12
	M12	599.27	TST	**-3.73**		**-13.24**		-27.83	0.28	24.10	89.08	10.92	0.03	10
	M13	600.17	TST	**-1.64**		**-8.99**		-30.72	0.64	29.08	83.09	16.91	0.11	9
	M14	601.37	TST										0.00	26
	M15	601.72	TST	**-0.73**		**-7.26**		-30.28	1.62	29.55	81.30	18.70	0.30	7
	M16	602.02	TST											22
	M17	602.62	TST	**-0.71**		**-8.54**		-27.33	0.08	26.62	81.05	18.95	0.02	8
	M18	604.82	TST	**0.15**		**-8.21**		-26.42	0.07	26.57	91.12	8.88	0.01	7
	M19	605.87	TST	**0.39**		**-8.44**					95.98	4.02		9
	M20	606.52	TST	**-1.14**		**-11.81**		-26.36	0.35	25.22	91.14	8.86	0.03	8
	M21	606.92	TST	**-0.19**		**-8.06**		-29.24	0.32	29.05	69.73	30.27	0.10	9
	M22	607.37	TST	**-1.27**		**-8.84**		-26.01	0.11	24.74	79.42	20.58	0.02	12
	M23	607.52	TST											30
	K23a	608.17	TST											15
	K23b	609.17	TST											

Section	Sample	m	Stage	$\delta^{13}C_{carb}$ (‰ - V-PDB)	error $\delta^{13}C_{carb}$ (‰)	$\delta^{18}O_{carb}$ (‰ - V-PDB)	error $\delta^{18}O_{carb}$ (‰)	$\delta^{13}C_{org}$ (‰ - V-PDB)	%C	$\Delta^{13}C$ (‰)	Carbonate (%)	IR (%)	TOC (%)	Sr/Ca (x 10^{-4})
	K23c	610.17	TST											14
	K23d	611.27	TST											31
	K23e	611.77	TST											27
	M24	612.02	TST	**-0.80**		**-11.36**		-26.61	0.03	25.81	16.31	83.69	0.02	
	K24a	613.02	TST											20
	K24b	614.02	TST											
	K24c	614.77	TST											
	K24d	615.77	TST											
	M25	616.77	TST	**0.43**		**-10.65**								
	K25a	617.77	TST											
	K25b	618.77	TST											
	K25c	619.77	TST											
	K25d	620.77	TST											
	M26	621.77	TST	**0.56**		**-9.89**								
	K26a	622.77	EHST											
	K26b	623.52	EHST											
	K26c	624.42	EHST											18
	K26d	625.42	EHST											
	M27	626.42	EHST	**1.24**		**-7.9**		-26.58	0.00	27.82	57.34	42.66	0.00	11
	K27a	627.42	EHST											
	K27b	628.17	EHST	1.86	0.05	-8.45	0.04							7
	K27c	629.17	EHST	1.69	0.04	-5.83	0.05							10
	K27d	630.17	EHST	1.59	0.05	-7.86	0.04							8
	M28	631.17	EHST	**0.93**		**-6.95**								5
	K28a	632.17	EHST	0.84	0.05	-6.91	0.06	-26.47	0.24	27.32	95.30	4.70	0.01	4

Section	Sample	m	Stage	$\delta^{13}C_{carb}$ (‰ - V-PDB)	error $\delta^{13}C_{carb}$ (‰)	$\delta^{18}O_{carb}$ (‰ - V-PDB)	error $\delta^{18}O_{carb}$ (‰)	$\delta^{13}C_{org}$ (‰ - V-PDB)	%C	$\Delta^{13}C$ (‰)	Carbonate (%)	IR (%)	TOC (%)	Sr/Ca (x 10^{-4})
	K28b	633.02	EHST	0.38	0.05	-7.28	0.05							5
	K28c	634.02	EHST	0.88	0.06	-6.60	0.06							6
	K28d	635.02	EHST	0.91	0.05	-6.81	0.06							5
	M29	636.02	EHST	**1.08**		**-6.84**								6
	K29a	637.02	EHST	0.93	0.05	-6.74	0.05	-26.31	0.39	27.24	97.59	2.41	0.01	7
	K29b	638.02	EHST	0.97	0.05	-6.93	0.05							7
	K29c	639.02	EHST	0.94	0.05	-6.94	0.04							4
	K29d	640.02	EHST	0.88	0.04	-7.18	0.05							5
	M30	641.02	EHST	**0.75**		**-6.47**								5
	K30a	642.02	EHST	1.14	0.04	-6.64	0.05	-26.20	0.58	27.34	98.54	1.46	0.01	5
	K30b	643.02	EHST	1.00	0.04	-6.26	0.04							6
	K30c	644.02	EHST	1.23	0.05	-6.37	0.07							6
	K30d	645.02	EHST	1.16	0.05	-6.79	0.05							6
	M31	646.02	EHST	**0.98**		**-6.4**								6
	K31a	647.02	EHST	1.22	0.07	-6.48	0.08							5
	K31b	648.02	EHST	1.17	0.05	-6.73	0.06							4
	K31c	649.02	EHST	1.23	0.05	-6.32	0.04				98.65	1.35		6
	K31d	650.02	EHST	1.19	0.05	-6.56	0.05							5
	M32	651.02	EHST	**1.27**		**-6.87**								7
	K32a	652.02	EHST	1.09	0.06	-6.98	0.04							7
	K32b	653.02	EHST	1.01	0.05	-7.46	0.05							5
	K32c	654.02	EHST	1.09	0.04	-7.61	0.07							5
	K32d	655.02	EHST	1.07	0.05	-6.82	0.05	-25.79	1.81	26.86	99.47	0.53	0.01	7
	M33	656.02	EHST	**1.12**		**-6.97**								6
	K33a	657.02	EHST	1.01	0.04	-7.30	0.06							8

Section	Sample	m	Stage	$\delta^{13}C_{carb}$ (‰ - V-PDB)	error $\delta^{13}C_{carb}$ (‰)	$\delta^{18}O_{carb}$ (‰ - V-PDB)	error $\delta^{18}O_{carb}$ (‰)	$\delta^{13}C_{org}$ (‰ - V-PDB)	%C	$\Delta^{13}C$ (‰)	Carbonate (%)	IR (%)	TOC (%)	Sr/Ca (x 10^{-4})
	K33b	658.02	EHST	1.00	0.04	-6.70	0.05							7
	K33c	659.02	EHST	1.04	0.03	-7.89	0.05							7
	K33d	660.02	EHST	1.12	0.03	-7.14	0.05				99.74	0.26		6
	M34	661.02	EHST	**1.10**		**-7.18**								7
	K34a	662.02	EHST	1.06	0.05	-8.24	0.05							7
	K34b	663.17	EHST	1.04	0.03	-7.78	0.05							9
	K34c	664.17	EHST	1.05	0.03	-8.06	0.06	-25.81	2.44	26.86	98.46	1.54	0.04	10
	K34d	665.17	EHST	1.06	0.04	-8.07	0.05							8
	M35	666.17	EHST	**1.05**		**-8.06**								7
	K35a	667.17	EHST	0.94	0.04	-7.72	0.04							7
	K35b	668.17	EHST	1.03	0.03	-8.01	0.04							7
	K35c	668.41	EHST	1.08	0.03	-6.30	0.06							18
	K35d	669.41	EHST	0.95	0.04	-6.89	0.06	-25.80	2.23	26.75	96.00	4.00	0.09	18
	K35e	670.41	EHST	1.03	0.03	-8.44	0.05							10
	M36	671.41	EHST	**0.77**		**-8.34**								11
	K36a	672.41	EHST	1.08	0.07	-8.32	0.07							7
	K36b	673.41	EHST	1.17	0.04	-8.08	0.04							7
	K36c	674.41	EHST	1.01	0.03	-7.43	0.05				99.01	0.99		10
	K36d	675.41	EHST	1.04	0.05	-7.32	0.05							9
	M37	676.41	EHST	**1.00**		**-7.44**								10
	K37a	677.41	EHST	1.04	0.05	-8.31	0.05							11
	K37b	678.36	EHST	0.70	0.04	-8.56	0.06							14
	K37c	679.36	EHST	0.71	0.09	-8.15	0.08	-25.51	3.38	26.22	97.26	2.74	0.09	20
	K37d	680.51	EHST	0.88	0.04	-8.07	0.05							25
	M38	681.51	EHST	**0.98**		**-7.18**								21

Section	Sample	m	Stage	$\delta^{13}C_{carb}$ (‰ - V-PDB)	error $\delta^{13}C_{carb}$ (‰)	$\delta^{18}O_{carb}$ (‰ - V-PDB)	error $\delta^{18}O_{carb}$ (‰)	$\delta^{13}C_{org}$ (‰ - V-PDB)	%C	$\Delta^{13}C$ (‰)	Carbonate (%)	IR (%)	TOC (%)	Sr/Ca (x 10^{-4})
	K38a	682.61	LHST	1.23	0.03	-8.49	0.04							51
	K38b	683.56	LHST	1.10	0.06	-7.98	0.06							30
	K38c	684.41	LHST	1.18	0.04	-7.90	0.05	-24.16	11.43	25.34	99.14	0.86	0.10	48
	K38d	685.66	LHST	1.26	0.05	-7.80	0.05							37
	M39	686.66	LHST	**1.50**		**-7.4**								79
	K39a	687.66	LHST	1.58	0.03	-7.88	0.04							54
	K39b	688.66	LHST	1.47	0.03	-8.08	0.05							42
	K39c	689.76	LHST	1.36	0.06	-8.07	0.07							62
	M40	690.9	LHST	**1.52**		**-7.99**		-25.17	12.38	26.69	99.17	0.83	0.10	46
	K40a	692.56	LHST	1.11	0.06	-7.34	0.07							48
	K40b	693.71	LHST	1.09	0.05	-8.27	0.05							23
	K40c	694.66	LHST	1.07	0.04	-8.38	0.05							34
	K40d	695.66	LHST	0.92	0.05	-7.28	0.08							47
	M41	696.66	LHST	**0.40**		**-6.63**								7
	K41a	697.66	LHST	0.62	0.03	-8.17	0.05							18
	K41b	698.66	LHST	0.66	0.03	-8.04	0.06							15
	K41c	699.66	LHST	0.52	0.03	-5.66	0.04							29
	K41d	700.66	LHST	1.19	0.04	-8.10	0.06							36
	M42	701.66	LHST	**1.11**		**-8.32**		-25.60	4.85	26.71	99.27	0.73	0.04	29
	K42a	702.66	LHST	0.67	0.07	-7.55	0.11							29
	K42b	703.41	LHST	1.08	0.04	-8.03	0.06							41
	K42c	704.41	LHST	0.60	0.05	-8.50	0.07							15
	K42d	705.41	LHST	0.88	0.04	-8.10	0.06	-25.79	9.42	26.67	99.23	0.77	0.07	28
	M43	706.41	LHST	**0.73**		**-8.61**								20
	K43a	707.41	LHST	0.55	0.04	-8.56	0.06							19

Section	Sample	m	Stage	$\delta^{13}C_{carb}$ (‰ - V-PDB)	error $\delta^{13}C_{carb}$ (‰)	$\delta^{18}O_{carb}$ (‰ - V-PDB)	error $\delta^{18}O_{carb}$ (‰)	$\delta^{13}C_{org}$ (‰ - V-PDB)	%C	$\Delta^{13}C$ (‰)	Carbonate (%)	IR (%)	TOC (%)	Sr/Ca (x 10^{-4})
	K43b	708.41	LHST	0.90	0.03	-8.66	0.05							18
	K43c	709.41	LHST	1.04	0.03	-8.67	0.06							31
	K43d	710.41	LHST	1.24	0.04	-8.89	0.05							43
	M44	711.41	LHST	**1.14**		**-8.73**		-24.96	14.89	26.10	99.51	0.49	0.07	42
	K44a	712.41	LHST	1.46	0.07	-8.70	0.07							29
	K44b	713.41	LHST	1.22	0.05	-8.57	0.05							50
	K44c	714.41	LHST	1.23	0.05	-8.46	0.05							44
	K44d	715.41	LHST	1.32	0.04	-8.54	0.05							35
	M45	716.41	LHST	**1.43**		**-8.43**		-24.35	4.05	25.78	98.70	1.30	0.05	36
	K45a	717.41	LHST	1.34	0.05	-8.28	0.07							46
	K45b	718.41	LHST	1.45	0.04	-8.20	0.06							36
	K45c	719.41	LHST	1.51	0.04	-8.10	0.06							45
	K45d	720.41	LHST	1.53	0.05	-8.13	0.07							47
	M46	721.41	LHST	**1.61**		**-7.8**		-24.74	10.14	26.35	99.81	0.19	0.02	24
	K46a	722.41	LHST	1.38	0.04	-8.10	0.06							47
	K46b	723.41	LHST	1.44	0.04	-7.82	0.05							24
	K46c	724.41	LHST	-0.13	0.04	-7.01	0.06							15
	K46d	725.41	LHST	1.36	0.05	-8.23	0.07							39
	M47	726.41	LHST	**1.83**		**-7.73**		-24.24	18.52	26.07	99.78	0.22	0.04	46
	K47a	727.41	LHST	1.59	0.04	-8.44	0.06							41
	K47b	728.41	LHST	1.50	0.05	-8.21	0.06							51
	K47c	729.41	LHST	1.59	0.05	-7.85	0.06							51
	K47d	730.41	LHST	1.16	0.05	-8.22	0.08							46
	M48	731.41	LHST	**1.91**		**-6.74**		-24.36	13.45	26.27	99.64	0.36	0.05	79
	K48a	732.41	LHST	1.62	0.04	-7.96	0.06							48

Section	Sample	m	Stage	$\delta^{13}C_{carb}$ (‰ - V-PDB)	error $\delta^{13}C_{carb}$ (‰)	$\delta^{18}O_{carb}$ (‰ - V-PDB)	error $\delta^{18}O_{carb}$ (‰)	$\delta^{13}C_{org}$ (‰ - V-PDB)	%C	$\Delta^{13}C$ (‰)	Carbonate (%)	IR (%)	TOC (%)	Sr/Ca (x 10^{-4})
	K48b	733.41	LHST	1.71	0.04	-7.75	0.06							59
	K48c	734.41	LHST	1.64	0.04	-7.77	0.06							57
	K48d	735.41	LHST	1.45	0.06	-7.88	0.07							64
	M49	736.41	LHST	**1.43**		**-7.66**		-24.31	3.52	25.74	98.89	1.11	0.04	69
	K49a	737.41	LHST	1.36	0.04	-7.75	0.06							78
	K49b	738.41	LHST-dolomites	0.54	0.05	-9.87	0.06							8
	K49c	738.91	LHST-dolomites	0.23	0.05	-10.52	0.07							4
	K49d	739.91	LHST-dolomites	0.74	0.05	-7.61	0.06							3
	K49e	740.91	LHST-dolomites	-0.51	0.05	-4.52	0.05							7
	M50	741.91	LHST-dolomites	**0.77**		**-4.47**		-22.74	2.31	23.51	96.31	3.69	0.09	9
	K50a	743.16	LHST-dolomites	-0.22	0.05	-4.50	0.07							10
	K50b	744.16	2nd-sequence-dolomites	1.75	0.04	-4.76	0.06							9
	K50c	745.16	2nd-sequence-dolomites	2.50	0.05	-5.88	0.05							6
	K50d	746.16	2nd-sequence-dolomites	2.56	0.04	-5.49	0.07							5
	M51	747.16	2nd-sequence-dolomites	**2.50**		**-5.7**		-21.48	5.40	23.98	99.18	0.82	0.04	6
	K51a	748.16	2nd-sequence-dolomites	2.27	0.05	-5.94	0.06							6
	K51b	749.16	2nd-sequence-dolomites	2.23	0.06	-5.02	0.06							6
	K51c	750.16	2nd-sequence-dolomites	2.32	0.05	-4.95	0.05							6

Section	Sample	m	Stage	$\delta^{13}C_{carb}$ (‰ - V-PDB)	error $\delta^{13}C_{carb}$ (‰)	$\delta^{18}O_{carb}$ (‰ - V-PDB)	error $\delta^{18}O_{carb}$ (‰)	$\delta^{13}C_{org}$ (‰ - V-PDB)	%C	$\Delta^{13}C$ (‰)	Carbonate (%)	IR (%)	TOC (%)	Sr/Ca (x 10^{-4})
	K51d	751.16	2nd-sequence-dolomites	1.62	0.07	-3.81	0.07							6
	M52	752.16	2nd-sequence-dolomites	**1.49**		**-4.42**								7
	K52a	753.16	2nd-sequence-dolomites	1.34	0.06	-4.75	0.06	-22.54	4.61	23.87	98.37	1.63	0.08	7
	K52b	754.16	2nd-sequence-dolomites	-0.55	0.05	-5.30	0.06							9
	K52c	755.16	2nd-sequence-dolomites	1.08	0.05	-5.13	0.05							5
	K52d	756.16	2nd-sequence-dolomites	1.61	0.04	-4.82	0.05							8
	M53	757.16	2nd-sequence-dolomites	**1.50**		**-4.65**		-22.17	2.01	23.68	97.77	2.23	0.04	7
	MD1	758.16	2nd-sequence-dolomites	1.42	0.04	-4.63	0.05							8
	MD2	759.16	2nd-sequence-dolomites	1.33	0.04	-5.37	0.07							9
	MD3	760.16	2nd-sequence-dolomites	-0.13	0.04	-4.43	0.05							10
	MD4	761.16	2nd-sequence-dolomites	5.27	0.04	-4.84	0.06							11
	M54	762.16	2nd-sequence-dolomites	5.41	0.04	-7.64	0.06	-22.37	0.61	27.78	91.65	8.35	0.05	6
	MD5	763.16	2nd-sequence-dolomites	5.57	0.04	-7.74	0.07							10
	MD6	764.16	2nd-sequence	6.61	0.04	-7.25	0.05							49

Section	Sample	m	Stage	$\delta^{13}C_{carb}$ (‰ - V-PDB)	error $\delta^{13}C_{carb}$ (‰)	$\delta^{18}O_{carb}$ (‰ - V-PDB)	error $\delta^{18}O_{carb}$ (‰)	$\delta^{13}C_{org}$ (‰ - V-PDB)	%C	$\Delta^{13}C$ (‰)	Carbonate (%)	IR (%)	TOC (%)	Sr/Ca (x 10^{-4})
	MD7	765.16	2nd-sequence	7.85	0.05	-7.33	0.07							26
	MD8	766.16	2nd-sequence	7.38	0.05	-6.22	0.07							26
	M55	767.16	2nd-sequence	**7.34**		**-7.63**		-22.22	0.84	29.56	84.50	15.50	0.13	19
Well 1	WS-01	1122.08	TST	-3.28	0.10	-7.20	0.10	-28.32	0.13	25.04	86.83	13.17	0.02	8
	WS-02	1118.54	TST	-3.13	0.08	-7.11	0.07	-27.58	0.17	24.45	73.29	26.71	0.04	4
	WS-02a	1116.88	TST	-2.91	0.09	-6.90	0.10	-27.06	0.15	24.15	78.56	21.44	0.03	5
	WS-02b	1112.34	TST	-3.77	0.07	-6.66	0.08	-26.64	0.41	22.87	95.07	4.93	0.02	5
	WS-03a	1110.49	TST	-3.65	0.08	-6.86	0.08	-27.75	0.17	24.10	81.49	18.51	0.03	5
	WS-03b	1108.66	TST	-4.06	0.07	-7.47	0.08	-27.41	0.62	23.35	92.81	7.19	0.04	5
	WS-04	1107.09	TST	-4.44	0.09	-10.30	0.06	-27.43	0.39	22.99	91.22	8.78	0.03	7
	WS-04a	1105.51	TST	-3.62	0.10	-8.28	0.10	-28.34	0.07	24.72	66.58	33.42	0.02	10
	WS-04b	1102.98	TST											13
	WS-05	1000	TST					-28.89	0.27		65.40	34.60	0.09	
	WS-06	1097.05	TST											52
	WS-07	1091.99	TST					-29.63	0.84		26.34	73.66	0.62	14
	WS-08	1087.8	TST											12
	WS-09	1082.94	TST					-28.63	0.39		48.67	51.33	0.20	
	WS-11	1072.28	TST					-30.30	1.99		9.75	90.25	1.79	
	WS-12	1069.85	TST					-28.36	0.47		56.21	43.79	0.21	
	WS-15	1053.56	TST					-29.07	3.00		12.00	88.00	2.64	
	WS-16	1049.37	TST											27
	WS-18	1043.1	EHST	-7.78	0.10	-11.96	0.09	-28.22	1.35	20.44	27.87	72.13	0.97	19
	WS-20	1034.57	EHST					-26.82	0.31		58.59	41.41	0.13	19
	WS-21	1029.86	EHST					-26.23	0.22		45.42	54.58	0.12	15
	WS-22	1025.1	EHST	-3.90	0.06	-12.48	0.07	-26.67	0.17	22.78	23.06	76.94	0.13	27

Section	Sample	m	Stage	$\delta^{13}C_{carb}$ (‰ - V-PDB)	error $\delta^{13}C_{carb}$ (‰)	$\delta^{18}O_{carb}$ (‰ - V-PDB)	error $\delta^{18}O_{carb}$ (‰)	$\delta^{13}C_{org}$ (‰ - V-PDB)	%C	$\Delta^{13}C$ (‰)	Carbonate (%)	IR (%)	TOC (%)	Sr/Ca (x 10^{-4})
	WS-23	1020.25	EHST	-5.34	0.08	-12.52	0.06	-25.90	0.47	20.56	91.27	8.73	0.04	12
	WS-24	1015.84	EHST	-3.33	0.08	-12.09	0.07	-26.91	0.08	23.58	77.36	22.64	0.02	35
	WS-25	1010.1	EHST					-25.23	0.13		53.89	46.11	0.06	37
	WS-26	1006.63	EHST	-2.93	0.09	-12.56	0.09	-25.45	0.22	22.52	69.48	30.52	0.07	15
	WS-27	1001.9	EHST	-2.23	0.07	-12.55	0.07	-26.87	0.11	24.64	56.54	43.46	0.05	15
	WS-28	996.77	EHST	-1.64	0.06	-12.43	0.05	-26.95	0.18	25.31	80.56	19.44	0.03	11
	WS-29	992	EHST	-1.97	0.09	-12.38	0.07	-26.18	0.13	24.21	70.23	29.77	0.04	14
	WS-30	987.03	EHST	-1.83	0.08	-12.28	0.07	-27.12	0.36	25.29	83.41	16.59	0.06	13
	WS-31	982.43	EHST	-1.71	0.05	-12.01	0.05	-27.87	0.31	26.16	86.41	13.59	0.04	12
	WS-32	977.82	EHST	-1.77	0.06	-12.00	0.06	-27.71	0.14	25.94	74.71	25.29	0.04	11
	WS-33	973.34	EHST	-1.79	0.05	-11.92	0.05	-27.71	0.09	25.92	53.42	46.58	0.04	16
	WS-34	968.74	EHST	-1.73	0.05	-11.95	0.07	-27.15	0.04	25.43	46.86	53.14	0.02	11
	WS-35	964.3	EHST	-1.53	0.08	-11.71	0.08	-27.28	0.05	25.75	36.95	63.05	0.03	11
	WS-36	959.52	EHST	-1.55	0.09	-11.76	0.10	-27.52	0.09	25.97	60.98	39.02	0.03	11
	WS-38	950.09	EHST					-26.78	0.04		48.49	51.51	0.02	
	WS-39	945.61	EHST	-1.58	0.08	-11.09	0.07	-25.46	0.07	23.88	73.41	26.59	0.02	
	WS-40	940.81	EHST	-1.57	0.08	-11.01	0.05	-25.78	0.08	24.21	62.76	37.24	0.03	11
	WS-41	936.28	EHST	-1.67	0.08	-10.76	0.08	-26.94	0.09	25.28	63.82	36.18	0.03	11
	WS-42	932.21	EHST	-1.69	0.09	-10.80	0.08	-26.42	0.12	24.73	51.91	48.09	0.06	13
	WS-43	927.55	EHST	-0.93	0.08	-10.55	0.07	-26.70	0.04	25.78	24.82	75.18	0.03	14
	WS-44	922.85	EHST	-0.81	0.04	-10.55	0.04	-26.50	0.09	25.70	54.40	45.60	0.04	10
	WS-45	918.49	EHST	-0.45	0.05	-10.44	0.04	-27.42	0.06	26.98	41.48	58.52	0.04	11
	WS-46	913.5	EHST	-0.02	0.09	-10.50	0.11	-28.10	0.12	28.08	59.57	40.43	0.05	17
	WS-47	909.23	EHST	0.18	0.07	-10.28	0.08	-28.14	0.05	28.32	52.09	47.91	0.02	14
	WS-48	904.28	EHST	0.44	0.05	-10.40	0.06	-28.60	0.07	29.05	27.30	72.70	0.05	12

Section	Sample	m	Stage	$\delta^{13}C_{carb}$ (‰ - V-PDB)	error $\delta^{13}C_{carb}$ (‰)	$\delta^{18}O_{carb}$ (‰ - V-PDB)	error $\delta^{18}O_{carb}$ (‰)	$\delta^{13}C_{org}$ (‰ - V-PDB)	%C	$\Delta^{13}C$ (‰)	Carbonate (%)	IR (%)	TOC (%)	Sr/Ca (x 10^{-4})
	WS-49	899.7	EHST	0.60	0.08	-10.38	0.05	-28.60	0.06	29.20	49.23	50.77	0.03	10
	WS-50	895.12	EHST	0.85	0.07	-10.36	0.09	-28.00	0.03	28.84	64.61	35.39	0.01	10
	WS-51	890.26	EHST	0.75	0.10	-10.37	0.09	-27.97	0.04	28.72	65.69	34.31	0.01	11
	WS-52	886.04	EHST	0.59	0.09	-10.40	0.07	-28.34	0.05	28.93	42.84	57.16	0.03	20
	WS-53	881.15	EHST	0.65	0.08	-10.48	0.07	-28.15	0.06	28.80	38.81	61.19	0.04	17
	WS-54	876.74	LHST	1.68	0.08	-9.93	0.07	-21.17	0.97	22.86	86.94	13.06	0.13	16
	WS-55	872.2	LHST	2.84	0.05	-9.01	0.05	-20.12	1.21	22.96	90.60	9.40	0.11	25
	WS-56	867.65	LHST	4.42	0.08	-3.78	0.10	-19.68	0.91	24.10	41.16	58.84	0.53	38
	WS-57	863.81	LHST	3.49	0.09	-7.11	0.06	-18.15	13.76	21.64	99.83	0.17	0.02	63
	WS-58	859.12	LHST	3.64	0.08	-6.76	0.08	-20.21	0.85	23.84	47.52	52.48	0.45	51
	WS-59	854.56	LHST	3.40	0.08	-7.52	0.09	-20.14	1.27	23.55	95.45	4.55	0.06	29
	WS-60	850.11	LHST	3.76	0.06	-6.63	0.07	-19.71	1.71	23.47	84.94	15.06	0.26	65
	WS-61	845.24	LHST	3.19	0.07	-6.93	0.07	-20.08	3.01	23.27	97.08	2.92	0.09	64
	WS-62	840.74	LHST	3.79	0.08	-6.41	0.06	-19.41	4.23	23.19	99.81	0.19	0.01	53
	WS-63	836.14	LHST	3.02	0.07	-7.20	0.10	-20.30	2.20	23.33	89.03	10.97	0.24	66
	WS-64	832.03	LHST	3.02	0.07	-7.60	0.10	-20.56	3.77	23.58	98.52	1.48	0.06	60
	WS-65	827.07	LHST	3.28	0.09	-6.63	0.05	-20.09	4.20	23.37	97.42	2.58	0.11	62
	WS-66	822.75	LHST	3.49	0.07	-5.84	0.06	-20.34	5.18	23.83	98.33	1.67	0.09	64
	WS-67	818.14	LHST	2.34	0.09	-8.46	0.06	-22.15	0.54	24.49	40.49	59.51	0.32	69
	WS-68	813.7	LHST	2.27	0.09	-8.11	0.06	-22.37	1.76	24.64	88.89	11.11	0.20	44
	WS-69	809.01	LHST	2.68	0.10	-8.28	0.06	-22.02	1.78	24.71	82.82	17.18	0.30	54
	WS-70	804.41	LHST	2.72	0.06	-8.32	0.08	-22.21	0.45	24.93	41.61	58.39	0.26	67
	WS-71	799.41	LHST	2.97	0.09	-7.85	0.06	-20.28	2.04	23.25	95.47	4.53	0.09	56
	WS-72	794.52	LHST	2.62	0.07	-8.38	0.06	-22.37	0.86	25.00	17.54	82.46	0.71	54
	WS-73	789.86	LHST	2.92	0.07	-8.41	0.06	-20.66	2.00	23.59	94.32	5.68	0.11	54

Section	Sample	m	Stage	$\delta^{13}C_{carb}$ (‰ - V-PDB)	error $\delta^{13}C_{carb}$ (‰)	$\delta^{18}O_{carb}$ (‰ - V-PDB)	error $\delta^{18}O_{carb}$ (‰)	$\delta^{13}C_{org}$ (‰ - V-PDB)	%C	$\Delta^{13}C$ (‰)	Carbonate (%)	IR (%)	TOC (%)	Sr/Ca (x 10^{-4})
	WS-74	784.93	LHST	3.20	0.07	-8.23	0.06	-20.86	2.78	24.06	97.64	2.36	0.07	57
	WS-75	780.16	LHST	3.06	0.07	-8.47	0.07	-21.36	1.01	24.42	94.96	5.04	0.05	38
	WS-76	775.42	LHST	3.46	0.10	-8.36	0.09	-21.40	1.19	24.86	94.89	5.11	0.06	51
	WS-77		LHST		0.07		0.07	-22.33	0.24		12.73	87.27	0.21	50
	WS-78	766.36	LHST	3.84	0.06	-4.95	0.06	-19.61	0.27	23.45	78.24	21.76	0.06	40
	WS-79	761.63	LHST	4.50	0.06	-7.07	0.05	-20.08	0.91	24.58	67.19	32.81	0.30	60
	WS-80	756.7	LHST	7.76	0.04	-6.78	0.04	-14.84	6.92	22.59	99.73	0.27	0.02	76
	WS-81	750.45	LHST	9.44	0.06	-7.39	0.08	-19.53	41.27	28.96	98.97	1.03	0.42	55
	WS-82	747.94	LHST	10.38	0.04	-7.40	0.05	-18.36	7.40	28.73	99.74	0.26	0.02	66
	WS-83	743.31	LHST	10.45	0.06	-7.92	0.06	-14.33	5.87	24.78	92.34	7.66	0.45	78
	WS-84	738.61	LHST	10.64	0.05	-13.08	0.05	-15.93	10.28	26.57	95.96	4.04	0.41	77
	WS-85	733.93	2nd-sequence					-17.98	1.97		64.45	35.55	0.70	75
	WS-86	729.14	2nd-sequence	10.38	0.08	-13.30	0.09	-17.31	2.07	27.69	55.88	44.12	0.91	
	WS-87	724.45	2nd-sequence	9.34	0.07	-12.73	0.07	-17.07	1.40	26.42	88.82	11.18	0.16	121
	WS-88	719.16	2nd-sequence	8.80	0.07	-12.95	0.08	-17.21	1.25	26.01	23.62	76.38	0.95	
	WS-89	715	2nd-sequence	8.82	0.08	-13.31	0.09	-17.79	1.14	26.61	29.57	70.43	0.81	
	WS-90	710.22	2nd-sequence	8.79	0.08	-13.80	0.08	-18.13	0.88	26.92	28.55	71.45	0.63	
	WS-91	705.37	2nd-sequence											
	WS-92	700.58	2nd-sequence											
	WS-93	695.68	2nd-sequence					-21.46	0.25		21.19	78.81	0.20	21

Carbon and oxygen isotope compositions in bold were provided by Kuchenbecker et al. (2016).

APPENDIX C – SUPPLEMENTARY MATERIALS: CHAPTER 5 – PAIRED CARBON ISOTOPE AND EARLY DIAGENESIS SIGNATURES SUGGEST COMPLEX OXYGENATION IN LATE EDIACARAN BENTHIC MARINE ENVIRONMENTS

Table S1: Geochemical data for the studied sections from the Tamengo Formation.

	m	$\delta^{13}C$ carb	$\delta^{18}O$ carb	$\delta^{13}Corg$	C (%)	$\Delta^{13}C$	Carb (%)	IR (%)	TOC (%)	XRF			ICP-MS (µg/g)									
										Ca (%)	Sr (ppm)	Sr/Ca	Mn	Fe	Ca	Mg	Sr	Mn/Sr	Fe/Sr	Mg/Sr	Sr/Ca	Sr/Ca $x10^{-4}$	Mg/Ca x 10^{-4}
Laginha section	5	-3.51	-7.79							35.53	243	7											
	6	-2.50	-7.81	-27.17	0.73	24.67	94.05	5.95	0.04	36.42	297	8											
	7	-2.68	-3.55							40.79	190	5											
	8	-2.15	-4.13							35.62	197	6											
	9	-2.12	-3.52							32.28	179	6											
	10	-1.85	-4.39	-25.18	1.00	23.34	97.82	2.18	0.02	33.72	209	6											
	11	-1.32	-4.63							36.68	274	7											
	12	-1.80	-4.53							33.97	198	6											
	13	-1.33	-7.68							35.95	251	7											
	14	-0.95	-7.26							36.12	297	8											
	15	-1.12	-7.58	-25.25	1.47	24.13	98.15	1.85	0.03	36.18	466	13	43.7	116.3	338287.6	4230.4	540.1	0.081	0.215	7.833	0.002	16	125
	17	-0.96	-7.50							35.59	440	12											
	18	-1.46	-2.48							36.75	252	7											
	19	-0.66	-7.16							35.63	426	12											
	20	-0.88	-5.55	-24.95	0.95	24.07	97.63	2.37	0.02	33.08	259	8											
	21	-1.21	-7.89							39.48	489	12											
	22	-1.02	-7.47							31.65	443	14											
	23	-0.98	-7.57							33.65	482	14											
	24	-0.89	-7.63	-25.88	2.08	24.99	98.07	1.93	0.04	35.59	495	14											
	25	-1.16	-8.16							31.99	259	8											
	26	-1.06	-6.78							35.61	640	18	45.0	265.4	338666.5	5900.1	752.7	0.060	0.353	7.838	0.002	22	174
	27	-1.75	-1.79							37.02	266	7											
	28	-2.19	-4.55							39.41	217	6											

m	$\delta^{13}C$ carb	$\delta^{18}O$ carb	$\delta^{13}C$org	C (%)	$\Delta^{13}C$	Carb (%)	IR (%)	TOC (%)	XRF			ICP-MS (µg/g)										
									Ca (%)	Sr (ppm)	Sr/Ca	Mn	Fe	Ca	Mg	Sr	Mn/Sr	Fe/Sr	Mg/Sr	Sr/Ca	Sr/Ca $x10^{-4}$	Mg/Ca x 10^{-4}
29	-1.70	-4.98	-24.56	1.05	22.86	98.76	1.24	0.01	34.78	234	7											
30	-1.83	-3.76							31.04	245	8											
31	-1.68	-4.23							38.98	232	6											
32	-1.72	-5.64							39.36	230	6											
33	-1.68	-4.68							35.44	206	6											
34	-1.51	-5.57	-25.74	1.55	24.23	97.94	2.06	0.03	35.61	202	6											
35	-1.59	-4.45							38.08	265	7											
36	-0.90	-5.56							40.10	367	9											
37	-0.04	-7.05							36.73	573	16											
39	-0.08	-7.41	-23.94	2.86	23.86	99.40	0.60	0.02	39.62	761	19											
40	-0.39	-7.71							37.12	683	18											
42	-0.03	-7.11							35.64	762	21											
43	-0.36	-7.43							34.97	718	21											
44	-0.13	-7.71	-25.28	7.41	25.16	98.55	1.45	0.11	34.23	715	21											
45	0.93	-4.82							19.74	200	10											
46	1.58	-6.51							36.66	1244	34	19.6	111.3	424773.5	3875.3	1256.2	0.016	0.089	3.085	0.003	30	91
47	1.30	-6.31							40.94	858	21											
48	0.96	-6.77							29.90	1132	38											
49	1.46	-6.37	-21.61	3.97	23.07	99.85	0.15	0.01	35.62	1073	30											
50	0.98	-6.71							37.21	653	18											
51	-0.85	-8.05							39.75	435	11											
55	4.74	-6.97							13.39	2025	151											
56	3.62	-6.31							35.93	3221	90											
57	2.44	-6.61	-23.88	9.25	26.32	94.77	5.23	0.48	40.83	957	23											
58	4.29	-6.35							36.98	3729	101											

m	$\delta^{13}C$ carb	$\delta^{18}O$ carb	$\delta^{13}Corg$	C (%)	$\Delta^{13}C$	Carb (%)	IR (%)	TOC (%)	XRF			ICP-MS (µg/g)									
									Ca (%)	Sr (ppm)	Sr/Ca	Mn	Fe	Ca	Mg	Sr	Mn/Sr	Fe/Sr	Mg/Sr	Sr/Ca	Sr/Ca $x10^{-4}$	Mg/Ca x 10^{-4}
59	4.13	-5.92							36.94	4024	109											
60	4.44	-5.91							36.40	5044	139	17.5	294.4	401500.2	2230.8	6269.3	0.003	0.047	0.356	0.016	156	56
61	5.36	-6.36							36.86	4204	114											
62	5.54	-6.37	-22.95	3.91	28.49	92.25	7.75	0.30	40.38	3947	98											
63	5.40	-6.52							35.57	3237	91											
65	5.51	-6.71							29.71	3824	129											
66	5.58	-6.53							29.08	2669	92											
67	5.91	-6.97	-24.37	3.01	30.29	66.49	33.51	1.01	36.15	3596	99											
68	5.72	-7.04							11.50	2059	179											
69	6.02	-5.71							28.75	3460	120											
70	5.85	-6.79							32.50	2936	90											
71	3.30	-6.47	-22.86	1.40	26.16	85.74	14.26	0.20	16.38	2308	141	53.3	237.5	363508.6	3752.4	3557.2	0.015	0.067	1.055	0.010	98	103
72	3.24	-6.77							36.96	1522	41											
73	3.14	-6.47							36.69	1228	33											
74	2.61	-6.81							36.34	1110	31											
75	2.56	-7.13							37.01	1045	28											
76	2.30	-6.72							39.35	1261	32											
77	2.61	-6.22							41.50	1355	33											
78	3.21	-6.05							36.85	1598	43											
79	2.86	-6.46							40.81	1590	39											
80	2.85	-5.87	-23.33	9.69	26.19	99.20	0.80	0.08	41.51	1706	41											
81	2.63	-6.32							40.89	1092	27											
82	2.59	-7.12							35.83	1201	34											
83	3.06	-5.89							37.35	1431	38											
84	2.79	-6.56							40.85	1300	32											

m	$\delta^{13}C$ carb	$\delta^{18}O$ carb	$\delta^{13}C$org	C (%)	$\Delta^{13}C$	Carb (%)	IR (%)	TOC (%)	XRF			ICP-MS (µg/g)									
									Ca (%)	Sr (ppm)	Sr/Ca	Mn	Fe	Ca	Mg	Sr	Mn/Sr	Fe/Sr	Mg/Sr	Sr/Ca	Sr/Ca x10^{-4}	Mg/Ca x 10^{-4}
85	2.56	-6.87							41.47	1000	24											
86	2.62	-6.93							24.41	607	25											
87	2.76	-7.17							40.74	1047	26											
88	2.77	-7.04							40.77	1206	30											
89	2.54	-6.66							36.85	1339	36											
90	2.54	-6.52	-23.68	4.59	26.22	99.15	0.85	0.04	40.76	1373	34	7.9	62.2	370256.2	1944.9	1427.2	0.006	0.044	1.363	0.004	39	53
91	2.61	-7.55							36.90	1148	31											
92	2.37	-6.92							41.19	1014	25											
93	2.45	-6.09							37.75	982	26											
94	2.75	-7.19							38.75	1232	32											
95	2.93	-6.17							36.23	1387	38											
96	3.15	-6.33							40.29	1829	45											
97	2.61	-6.34							36.49	1411	39											
98	3.01	-6.59							36.36	1375	38											
99	3.19	-6.38							41.41	1794	43											
100	2.92	-6.64							36.38	1376	38											
101	2.82	-6.33							40.82	1472	36											
102	2.68	-6.38	-24.17	5.28	26.85	99.43	0.57	0.03	41.05	1398	34	73.9	967.5	365851.4	2665.9	2030.6	0.036	0.476	1.313	0.006	56	73
103	3.20	-5.03							36.72	1848	50											
104	3.23	-5.19							32.04	1605	50											
105	2.98	-6.06							35.98	1738	48											
106	3.01	-5.68							41.18	1734	42											
107	2.86	-6.87							35.37	1338	38											
108	2.83	-7.16							37.10	1368	37											
109	3.26	-7.03							30.91	1447	47											

	m	$\delta^{13}C$ carb	$\delta^{18}O$ carb	$\delta^{13}Corg$	C (%)	$\Delta^{13}C$	Carb (%)	IR (%)	TOC (%)	XRF			ICP-MS (µg/g)									
										Ca (%)	Sr (ppm)	Sr/Ca	Mn	Fe	Ca	Mg	Sr	Mn/Sr	Fe/Sr	Mg/Sr	Sr/Ca	Sr/Ca x10^{-4}	Mg/Ca x 10^{-4}
	110	2.14	-7.38							41.18	1268	31											
	111	3.07	-6.12							40.92	2329	57	5.3	45.1	345265.7	1104.9	2900.4	0.002	0.016	0.381	0.008	84	32
	112	2.63	-7.44	-24.01	4.38	26.64	99.38	0.62	0.03	41.74	1334	32											
	113	2.41	-6.51							32.41	1543	48											
	114	2.67	-7.05							37.44	1691	45											
	115	2.65	-7.10							37.70	1404	37											
	116	2.40	-6.86							37.45	1757	47											
	117	2.85	-7.25							36.83	1486	40	6.0	44.6	340046.0	1982.0	2052.9	0.003	0.022	0.965	0.006	60	58
	118	2.08	-7.53							41.35	1197	29											
	119	2.61	-7.72							41.44	1656	40											
	125	2.85	-6.51							37.44	2074	55											
	126	2.19	-6.66							41.45	2003	48											
	127	2.22	-7.56							41.58	1831	44											
	128	2.55	-6.31							37.38	2590	69											
	129	2.51	-7.59	-26.71	1.03	29.21	21.06	78.94	0.81	41.58	1905	46											
	130	2.80	-7.33							41.37	2089	50											
	131	2.83	-7.82							41.35	1768	43											
	132	3.30	-8.67							37.10	2725	73											
	133	3.36	-8.13							41.61	3124	75	6.8	71.9	370754.2	1251.7	3495.9	0.002	0.021	0.358	0.009	94	34
	134	3.03	-10.91							42.08	2658	63											
	135	3.13	-6.88							36.31	2257	62											
	136	3.24	-7.53							35.29	2133	60											
Corcal	0.60	3.23	-9.28																				
	0.80	4.01	-9.33																				
	1.00	3.81	-7.53	-22.89	1.58	26.70	97.59	2.41	0.04	34.07	1971	58	164.7	597.1	418766.5	1910.1	1593.5	0.103	0.375	1.199	0.004	38	46

m	$\delta^{13}C$ carb	$\delta^{18}O$ carb	$\delta^{13}C$org	C (%)	$\Delta^{13}C$	Carb (%)	IR (%)	TOC (%)	XRF			ICP-MS (µg/g)									
									Ca (%)	Sr (ppm)	Sr/Ca	Mn	Fe	Ca	Mg	Sr	Mn/Sr	Fe/Sr	Mg/Sr	Sr/Ca	Sr/Ca x10^{-4}	Mg/Ca x 10^{-4}
1.60	3.60	-8.71																			
2.00	2.61	-8.18							35.24	1228	35										
2.50	3.94	-8.13							34.73	1230	35										
3.20	4.34	-7.06																			
3.60	3.67	-8.07																			
4.20	3.64	-7.93										103.2	403.7	430395.0	2558.7	1667.7	0.062	0.242	1.534	0.004	39	59
4.60	3.27	-7.92																			
5.00	3.49	-7.74	-27.47	1.52	30.96	94.03	5.97	0.09	36.51	1507	41										
5.40	1.37	-5.34	-24.95	0.69	26.32	91.67	8.3343	0.06													
5.80	3.80	-8.08																			
6.00	2.72	-7.67	-25.64	1.71	28.36	96.28	3.722	0.06	34.74	1739	50										
6.50	3.58	-7.93							36.40	1389	38										
7.00	4.04	-7.30	-24.89	7.06	28.93	98.85	1.15	0.08	31.88	1468	46										
7.60	3.83	-7.78							31.74	1059	33										
8.00	4.34	-7.61	-23.76	0.67	28.10	93.67	6.33	0.04	34.33	2760	80	507.3	1032.0	428173.7	3569.0	3322.6	0.153	0.311	1.074	0.008	78	83
8.50	2.03	-7.45	-24.59	1.27	26.62	96.95	3.05	0.04	32.60	1436	44										
9.00	4.35	-7.69	-23.98	3.59	28.33	98.53	1.47	0.05	34.61	2128	61										
9.60	4.87	-5.53	-25.37	2.23	30.24	96.43	3.57	0.08													
10.00	2.34	-6.59	-20.66	0.28	23.00	93.53	6.47	0.02	38.92	2368	61										
10.60	3.87	-7.64																			
11.00	4.32	-7.54	-23.98	2.52	28.29	98.84	1.16	0.03	34.79	1472	42										
11.50	5.01	-6.34							35.73	1539	43										
12.00	3.72	-6.95	-23.04	1.18	26.76	98.31	1.69	0.02	36.05	2453	68	22.8	431.2	429974.1	2729.8	2965.7	0.008	0.145	0.920	0.007	69	63
12.60	5.57	-4.85	-22.73	3.05	28.29	99.08	0.92	0.03													
13.00	2.29	-6.93							36.64	1312	36										

m	$\delta^{13}C$ carb	$\delta^{18}O$ carb	$\delta^{13}Corg$	C (%)	$\Delta^{13}C$	Carb (%)	IR (%)	TOC (%)	XRF			ICP-MS (µg/g)									
									Ca (%)	Sr (ppm)	Sr/Ca	Mn	Fe	Ca	Mg	Sr	Mn/Sr	Fe/Sr	Mg/Sr	Sr/Ca	Sr/Ca $x10^{-4}$	Mg/Ca x 10^{-4}
13.60	3.91	-7.93																			
14.00	4.36	-6.79							32.99	1446	44										
14.60	2.36	-7.09																			
15.00	3.61	-7.47							35.75	1743	49										
15.50	4.89	-7.20	-22.63	4.33	27.53	98.48	1.52	0.07	41.39	2577	62	46.5	472.9	434467.9	2034.6	2867.1	0.016	0.165	0.710	0.007	66	47
15.60	4.82	-7.18																			
16.00	4.23	-7.71							37.20	2227	60										
16.60	4.29	-6.40																			
17.00	3.23	-6.93																			
17.60	4.99	-6.50																			
18.00	5.06	-6.68							36.28	2672	74										
18.60	3.94	-7.27																			
19.00	5.75	-6.11							35.12	1564	45										
19.50	5.35	-6.90							36.01	2161	60										
20.00	2.53	-6.79	-22.10	1.73	24.63	96.30	3.70	0.06	37.36	2437	65										
20.60	4.77	-6.91																			
21.00	4.81	-6.79							36.02	2456	68										
21.60	5.65	-5.76																			
22.00	4.71	-8.09							38.52	976	25										
22.60	4.84	-9.56																			
23.10	3.79	-10.40							24.15	1995	83										
23.60	2.89	-9.99							30.50	3608	118	443.8	1456.6	422944.7	3451.8	4914.8	0.090	0.296	0.702	0.012	116	82
24.30	4.36	-10.56							34.53	2316	67										
25.80	3.21	-10.14																			
26.00	5.68	-10.35	-23.21	2.02	28.89	94.94	5.06	0.10	34.39	4335	126	97.4	1372.7	398761.9	2668.5	4917.2	0.020	0.279	0.543	0.012	123	67

m	$\delta^{13}C$ carb	$\delta^{18}O$ carb	$\delta^{13}Corg$	C (%)	$\Delta^{13}C$	Carb (%)	IR (%)	TOC (%)	XRF			ICP-MS (µg/g)									
									Ca (%)	Sr (ppm)	Sr/Ca	Mn	Fe	Ca	Mg	Sr	Mn/Sr	Fe/Sr	Mg/Sr	Sr/Ca	Sr/Ca $x10^{-4}$	Mg/Ca x 10^{-4}
28.00	4.16	-5.90							40.91	3151	77											
28.50	0.66	-9.63							40.46	5000	124	45.6	1338.9	402091.0	3695.8	4771.1	0.010	0.281	0.775	0.012	119	92
29.00	4.67	-8.34							36.12	1450	40											
29.40	2.19	-6.87																				
29.60	4.78	-7.35																				
30.00	4.95	-6.86	-21.20	4.01	26.14	98.48	1.52	0.06	39.41	2523	64											
30.60	5.19	-4.61																				
31.00	4.98	-7.28							36.82	2421	66											
31.60	4.44	-7.36																				
32.00	5.57	-5.66							35.60	2452	69											
32.60	4.29	-8.71																				
33.00	4.93	-8.97							35.73	1739	49											
33.60	4.42	-8.73																				
34.00	5.20	-4.47							35.65	2327	65											
34.60	5.25	-6.61																				
35.00	5.51	-6.33	-22.14	2.42	27.65	97.58	2.42	0.06	33.84	2513	74											
35.60	5.47	-4.66																				
36.00	5.55	-4.66							36.36	2638	73											
36.40	5.16	-6.66																				
37.00	5.63	-4.44							30.65	2186	71	29.4	210.6	405956.9	3165.4	3084.2	0.010	0.068	1.026	0.008	76	78
37.50	5.45	-3.66							36.91	2735	74											
38.20	5.04	-4.98																				
38.60	5.35	-4.97																				
39.00	5.09	-7.25							41.82	2314	55											
39.60	5.09	-5.89																				

m	$\delta^{13}C$ carb	$\delta^{18}O$ carb	$\delta^{13}Corg$	C (%)	$\Delta^{13}C$	Carb (%)	IR (%)	TOC (%)	XRF			ICP-MS (µg/g)										
									Ca (%)	Sr (ppm)	Sr/Ca	Mn	Fe	Ca	Mg	Sr	Mn/Sr	Fe/Sr	Mg/Sr	Sr/Ca	Sr/Ca $x10^{-4}$	Mg/Ca x 10^{-4}
40.00	4.56	-7.43	-22.71	3.79	27.27	98.94	1.06	0.04	35.23	2078	59											
40.20																						
40.40																						
40.50	5.15	-7.58							38.80	1890	49											
40.60																						
40.80																						
41.00	5.03	-7.60							34.60	1953	56											
41.20																						
41.40																						
41.50	5.08	-7.39							35.88	2194	61	18.7	256.9	405431.3	2733.7	1953.8	0.010	0.132	1.399	0.005	48	67
41.60																						
41.50																						
42.00	5.43	-6.91							33.23	2142	64											
42.20																						
42.40																						
42.50									40.42	2650	66											
42.60	5.65	-5.05																				
42.80																						
43.00	5.58	-5.90							33.06	2373	72											
43.20																						
43.40																						
43.50									34.72	2661	77	14.1	218.7	414854.0	4768.8	3154.2	0.004	0.069	1.512	0.008	76	115
43.60	5.38	-5.97																				
43.80																						
44.00	4.18	-7.72							38.54	1078	28											

	m	$\delta^{13}C$ carb	$\delta^{18}O$ carb	$\delta^{13}Corg$	C (%)	$\Delta^{13}C$	Carb (%)	IR (%)	TOC (%)	XRF			ICP-MS (µg/g)										
										Ca (%)	Sr (ppm)	Sr/Ca	Mn	Fe	Ca	Mg	Sr	Mn/Sr	Fe/Sr	Mg/Sr	Sr/Ca	Sr/Ca x10^{-4}	Mg/Ca x 10^{-4}
	44.60	5.20	-8.11																				
	45.00	5.21	-8.64	-22.03	1.52	27.23	97.66	2.34	0.04	39.34	1289	33											
	45.60	4.39	-9.90																				
	46.00	4.01	-9.24							33.61	1154	34											
	46.60	4.68	-9.36																				
	47.00	4.69	-9.42																				
	47.60	4.88	-10.40							33.40	1318	39											
	48.20	4.24	-10.50																				
	49.00	4.88	-9.62							36.63	1247	34											
	49.50	3.63	-10.27																				
	50.00	3.97	-10.19	-24.28	0.74	28.25	97.03	2.97	0.02	39.06	1564	40	34.4	579.7	416114.9	2098.5	1674.1	0.021	0.346	1.254	0.004	40	50
	50.60	3.15	-9.94																				
	51.00	4.80	-11.23							40.80	1438	35											
Sobramil section	0.00	4.40	-9.12	-25.35	1.33	29.75	79.51	20.49	0.27														
	1.00	4.45	-8.04																				
	2.00	4.31	-7.27		0.29		97.81	2.19	0.01														
	3.00	3.93	-7.29																				
	4.00	4.00	-7.53																				
	5.00	4.41	-7.66	-25.39	16.07	29.80	97.82	2.18	0.35														
	6.00	4.39	-7.37																				
	7.00	4.52	-7.65	-23.06	0.76	27.58	95.29	4.71	0.04														
	8.00	3.67	-6.05																				
	9.00	3.22	-9.65	-25.50	34.56	28.73	97.39	2.61	0.90														
	9.60	3.12	-9.68																				
	13.00	4.93	-8.25																				

m	$\delta^{13}C$ carb	$\delta^{18}O$ carb	$\delta^{13}C$org	C (%)	$\Delta^{13}C$	Carb (%)	IR (%)	TOC (%)	XRF			ICP-MS (µg/g)										
									Ca (%)	Sr (ppm)	Sr/Ca	Mn	Fe	Ca	Mg	Sr	Mn/Sr	Fe/Sr	Mg/Sr	Sr/Ca	Sr/Ca $x10^{-4}$	Mg/Ca x 10^{-4}
14.00	4.46	-7.10																				
15.00	5.44	-5.75	-22.91	4.50	28.35	98.08	1.92	0.09														
16.00	4.49	-6.71																				
17.00	4.67	-6.63	-23.23	3.29	27.91	97.86	2.14	0.07														
18.00	4.25	-7.27																				
19.00	4.65	-7.99	-24.65	9.18	29.30	98.35	1.65	0.15														
20.00	4.49	-7.51																				
21.00	4.46	-9.37	-22.88	3.20	27.35	84.01	15.99	0.51														
22.00	4.88	-9.88																				
23.00	4.60	-6.22	-23.62	5.36	28.22	99.87	0.13	0.01														

APPENDIX D– SUPPLEMENTARY MATERIALS: CHAPTER 6 – SULFUR BIOGEOCHEMICAL CYCLING IN MARGINAL AND EPICONTINENTAL MARINE SETTINGS DURING LATE EDIACARAN-CAMBRIAN: SUPERHEAVY $\delta^{34}S$ PYRITE TRENDS, SULFATE-DISTILLATION CYCLES AND IMPLICATIONS FOR EARLY ANIMAL COLONIZATION

Table S1: Multiple sulfur isotope data for the studied sections from Tamengo Formation and Bambuí Group.

		Pyrite (‰)							CAS (‰)										
Section	**m**	**$\delta^{33}S$**	**$\delta^{34}S$**	**$\delta^{36}S$**	**$\Delta^{33}S$**	**$\Delta^{36}S$**	**$\delta^{34}S$ vs S1**	**$\delta^{34}S$ vs CDT**	**$\delta^{33}S$**	**$\delta^{34}S$**	**$\delta^{36}S$**	**$\Delta^{33}S$**	**$\Delta^{36}S$**	**$\delta^{34}S$ vs S1**	**$\delta^{34}S$ vs CDT**	**$\Delta^{34}S_{CAS-py}$**	**Py (%)**	**CAS (ppm)**	**Fe (%)**
Januária	0.35	4.69	9.14	17.35	0.000	0.010	26.27	25.97	12.36	24.20	46.68	-0.028	0.45	41.59	41.28	15.31	0.015	9	
	0.75																NR		
	1.15																NR		0.66
	1.55																NR		
	2.15																NR		
	2.75	1.31	2.58	4.70	-0.018	-0.171	19.60	19.30									0.001		0.28
	3.45	8.50	16.57	31.27	0.006	-0.273	33.83	33.52									0.001		
	3.87																		0.35
	4.27																NR		
	4.67																		0.33
	5.27																NR		
	16.50								16.10	31.42	60.25	0.046	0.04	48.93	48.62		NR	30	
	21.50	-4.94	-9.71	-18.79	0.071	-0.510	7.11	6.80									0.001		0.30
	27.50																		0.04
	31.90	3.99	7.64	13.98	0.061	-0.510	24.75	24.45	19.01	37.35	72.39	-0.049	0.63	54.97	54.65	30.20	0.033	14	0.06
	43.10																		0.04
	48.80	12.02	23.44	44.80	0.019	0.034	40.82	40.51									0.006		
	54.50																		0.04
	59.50	11.35	22.19	42.44	-0.019	0.094	39.55	39.24									0.004	0	0.03
	69.50																		0.06
	80.30	10.28	20.09	38.70	-0.017	0.391	37.41	37.10									0.002	0	
	92.50	9.23	18.02	34.50	-0.007	0.172	35.31	35.00									0.002		
	150.00	-3.70	-7.20	-13.89	0.01	-0.32	9.66	9.36	2.13	4.26	8.25	-0.07	0.18	21.32	21.01	11.66	0.386	3	
	154.00	-1.76	-3.43	-6.94	0.01	-0.47	13.50	13.19									0.040		
	158.00	-4.88	-9.51	-17.92	0.03	-0.02	7.31	7.01									0.030		

		Pyrite (‰)							CAS (‰)										
Section	**m**	**$\delta^{33}S$**	**$\delta^{34}S$**	**$\delta^{36}S$**	**$\Delta^{33}S$**	**$\Delta^{36}S$**	**$\delta^{34}S$ vs S1**	**$\delta^{34}S$ vs CDT**	**$\delta^{33}S$**	**$\delta^{34}S$**	**$\delta^{36}S$**	**$\Delta^{33}S$**	**$\Delta^{36}S$**	**$\delta^{34}S$ vs S1**	**$\delta^{34}S$ vs CDT**	**$\Delta^{34}S_{CAS-py}$**	**Py (%)**	**CAS (ppm)**	**Fe (%)**
	162.00	-1.16	-2.28	-4.64	0.02	-0.35	14.67	14.36									0.013	0	
	166.00	-6.37	-12.31	-23.31	-0.01	-0.16	4.46	4.16									0.028		
	1116.88	6.43	12.61	24.24	-0.048	0.273	29.75	29.44									0.004		
	1112.34	-4.36	-8.64	-16.93	0.100	-0.653	8.19	7.89									0.031	1	0.28
	1110.49	-0.16	-0.09	-0.29	-0.116	-0.121	16.86	16.56									0.020		
	1108.66	-4.05	-7.01	-13.00	-0.433	0.206	9.85	9.55									0.020		0.23
	1107.09	3.06	5.99	11.37	-0.018	0.015	23.01	22.71									0.006		
	1105.51	-1.28	-2.35	-4.17	-0.067	0.263	14.60	14.29	5.10	10.00	18.99	-0.039	0.00	27.16	26.85	12.56	0.010	6	2.58
	1102.98	-9.64	-18.35	-34.06	-0.147	0.345	-1.74	-2.04									0.029		
	1091.99	-18.68	-35.97	-67.64	0.013	-0.742	-19.60	-19.89									0.121		
	1072.28	-11.34	-22.07	-41.86	0.090	-0.556	-5.46	-5.76									1.040		
	1043.10	-9.17	-17.97	-34.48	0.119	-0.801	-1.29	-1.59									0.571		3.16
	1034.57	-8.52	-16.67	-32.18	0.098	-0.910	0.03	-0.27									0.083		
	1025.10	-5.78	-11.33	-22.08	0.077	-0.769	5.46	5.16									0.034		6.25
Well 1	1015.84	4.33	8.41	15.81	0.007	-0.136	25.53	25.22									0.026		5.00
	1006.63	-4.00	-7.82	-15.10	0.034	-0.377	9.04	8.73									0.075		2.53
	1001.90	-6.75	-13.18	-25.45	0.065	-0.682	3.58	3.27									0.030	0	
	996.77																		1.41
	992.00	-3.24	-6.38	-12.70	0.051	-0.669	10.43	10.13											
	982.43	3.22	6.42	11.69	-0.081	-0.471	23.51	23.20									0.011		1.19
	973.34	2.09	3.96		0.055		20.95	20.64	13.24	25.87	49.64	-0.005	0.18	43.30	42.98	22.34	0.019	6	0.52
	964.30	-0.32	-0.66	-1.56	0.021	-0.309	16.31	16.01									0.035		0.79
	950.09																0.000		
	940.81	7.67	14.91	28.39	0.017	0.031	32.14	31.83									0.005		1.37
	932.21	-6.11	-11.60	-23.23	-0.119	-1.418	5.19	4.89									0.022		2.66
	927.55																0.012		
	922.85																0.006		0.86

		Pyrite (‰)							CAS (‰)										
Section	**m**	**$\delta^{33}S$**	**$\delta^{34}S$**	**$\delta^{36}S$**	**$\Delta^{33}S$**	**$\Delta^{36}S$**	**$\delta^{34}S$ vs S1**	**$\delta^{34}S$ vs CDT**	**$\delta^{33}S$**	**$\delta^{34}S$**	**$\delta^{36}S$**	**$\Delta^{33}S$**	**$\Delta^{36}S$**	**$\delta^{34}S$ vs S1**	**$\delta^{34}S$ vs CDT**	**$\Delta^{34}S_{CAS-py}$**	**Py (%)**	**CAS (ppm)**	**Fe (%)**
	918.49	-5.55	-10.77	-20.33	0.01	-0.08	6.03	5.73											
	909.23																0.002		
	904.28	-1.47	-2.84	-5.38	-0.01	-0.03	14.10	13.79									0.004		1.20
	899.70	-1.99	-3.79	33.47	-0.04		13.07	12.76									0.007		0.50
	895.12																0.000		
	890.26																0.000		
	886.04	7.23	14.26	27.82	-0.087	0.700	31.48	31.18									0.009		1.69
	881.15	6.77	13.26	25.55	-0.043	0.333	30.47	30.16									0.012		
	876.74	-4.42	-8.59	-16.42	0.009	-0.247	8.25	7.95	10.02	19.93	38.76	-0.193	0.76	37.25	36.94	28.99	0.172	3	1.56
	872.20	0.24	0.50	0.86	-0.014	-0.076	17.49	17.18									0.306		
	859.12	16.79	32.90	63.41	-0.021	0.317	50.38	50.07									0.458		4.44
	850.11	16.27	31.85	60.35	-0.009	-0.696	49.37	49.06									0.478		0.16
	840.74	17.33	34.00	64.84	-0.03	-0.39	51.56	51.24									0.089		
	832.03	16.18	31.72	59.99	-0.04	0.00	49.21	48.90									0.052	NR	0.15
	822.75	14.97	29.33	56.59	-0.03	0.42	46.81	46.50									0.133		0.11
	818.14	11.45	22.34	42.86	0.00	0.22	39.64	39.33											
	809.01	14.60	28.60	54.65	-0.03	-0.09	46.07	45.75									0.375		0.08
	799.41	14.67	28.80	55.15	-0.06	0.02	46.27	45.96									0.085	NR	
	789.86	17.09	33.51	64.76	-0.03	0.48	51.06	50.75									0.239		0.22
	780.16	11.31	22.10	42.24	-0.01	0.07	39.45	39.14									0.238		
	766.36	11.57	22.66	46.36	-0.035		39.97	39.65									0.071		0.10
	761.63	2.46	4.90	9.53	-0.064	0.247	21.91	21.60	9.37	18.52	35.85	-0.124	0.55	35.82	35.51	13.91	0.409	2	
	756.70	10.31	20.19	38.70	-0.035	0.188	37.52	37.21									0.153		
	750.45	13.14	25.79	49.85	-0.062	0.536	43.22	42.90									0.032		0.05
	747.94	11.48	22.54	43.04	-0.07	0.01	39.91	39.60									0.018		
	743.31	14.53	28.57	55.37	-0.08	0.69	46.04	45.72	-1.44	-2.47	-3.69	-0.17	0.97	14.47	14.17	-31.56	0.004	6	
	738.61	12.65	24.86	48.16	-0.08	0.65	42.27	41.95									0.134		0.18

		Pyrite (‰)							CAS (‰)										
Section	**m**	**$\delta^{33}S$**	**$\delta^{34}S$**	**$\delta^{36}S$**	**$\Delta^{33}S$**	**$\Delta^{36}S$**	**$\delta^{34}S$ vs S1**	**$\delta^{34}S$ vs CDT**	**$\delta^{33}S$**	**$\delta^{34}S$**	**$\delta^{36}S$**	**$\Delta^{33}S$**	**$\Delta^{36}S$**	**$\delta^{34}S$ vs S1**	**$\delta^{34}S$ vs CDT**	**$\Delta^{34}S_{CAS-py}$**	**Py (%)**	**CAS (ppm)**	**Fe (%)**
	729.14	-8.42	-16.22	-30.37	-0.031	0.066	0.49	0.18	1.47	3.00	6.01	-0.072	0.33	20.03	19.73	19.54	0.548	13	
	724.45	-4.55	-8.79	-16.67	-0.011	-0.125	8.05	7.74									0.403		
	719.16	-6.45	-12.46	-23.81	-0.012	-0.390	4.25	3.95											
	715	-6.69	-12.99	-24.36	0.017	0.037	3.78	3.48									0.833		
	710.22	-3.90	-7.52	-14.14	-0.022	0.036	9.33	9.03									1.521		
	695.68	1.88	3.85	7.85	-0.099	0.571	20.90	20.59									0.097		
Santa Maria da Vitória	2.00																NR		
	5.50																NR		
	13.30																NR		
	17.00																NR		
	34.00	8.97	17.56	33.65	-0.035	0.206	34.84	34.53									0.029		
	44.60	10.44	20.27	38.27	0.046	-0.390	37.60	37.29									0.002		
	55.60																NR		
	60.60	14.29	27.89	53.26	0.024	-0.109	45.35	45.03									0.002		
	70.60	7.67	14.96	28.75	-0.010	0.289	32.20	31.89									0.040		
	79.60	9.97	19.56	37.73	-0.056	0.446	36.87	36.56									0.008		
	95.30	11.86	23.20	44.61	-0.027	0.306	40.58	40.27									0.013		
	105.30	11.48	22.54	43.38	-0.061	0.362	39.90	39.59									0.001	NR	
	112.30	12.16	23.82	45.94	-0.039	0.437	41.21	40.90									0.001		
	118.80																NR		
	119.80																NR		
	124.80	8.08	15.94	30.84	-0.100	0.498	33.19	32.88									0.001		
	129.80	7.27	14.31	27.80	-0.07	0.59	31.53	31.22									0.002		
	148.30	5.09	10.02	19.33	-0.06	0.31	27.17	26.86									0.019	1	
Laginha	6	3.71	7.12	13.09	0.044	-0.419	24.23	23.92									0.224		
	10	3.44	6.60	12.67	0.046	-0.327	23.69	23.39									0.108		

		Pyrite (‰)							CAS (‰)										
Section	**m**	**$\delta^{33}S$**	**$\delta^{34}S$**	**$\delta^{36}S$**	**$\Delta^{33}S$**	**$\Delta^{36}S$**	**$\delta^{34}S$ vs S1**	**$\delta^{34}S$ vs CDT**	**$\delta^{33}S$**	**$\delta^{34}S$**	**$\delta^{36}S$**	**$\Delta^{33}S$**	**$\Delta^{36}S$**	**$\delta^{34}S$ vs S1**	**$\delta^{34}S$ vs CDT**	**$\Delta^{34}S_{CAS-py}$**	**Py (%)**	**CAS (ppm)**	**Fe (%)**
	15	-1.55	-3.02	-5.91	0.014	-0.199	13.91	13.60									0.086		
	20	7.73	14.99	28.18	0.041	-0.339	32.23	31.92									0.139		
	24	2.98	5.78	10.74	0.009	-0.206	22.86	22.55									0.011		
	29	4.18	8.06	15.01	0.036	-0.277	25.18	24.87									0.129		
	34	6.46	12.49	23.94	0.045	-0.374	29.68	29.37									0.100		
	39																0.001		
	44	-2.61	-5.07	-9.67	-0.002	-0.122	11.83	11.53									0.034		
	49	7.74	15.04	28.39	0.020	-0.221	32.28	31.97									0.066		
	57	10.17	19.73	37.11	0.057	-0.501	37.04	36.73									0.114		
	62	4.06	7.77	14.27	0.066	-0.467	24.89	24.58									0.253		
	67	7.99	15.45	28.91	0.061	-0.497	32.70	32.39									0.965		
	71	7.33	14.17	26.58	0.054	-0.369	31.39	31.08									0.839		
	80	8.30	16.10	30.16	0.041	-0.493	33.36	33.05									0.088		
	102	-1.06	-2.00	-3.76	-0.026	0.014	14.95	14.65									0.024		
	112	7.01	13.63	25.83	0.011	-0.088	30.85	30.54									0.003		
	129	9.19	17.81	33.48	0.055	-0.453	35.10	34.79									1.778		
Corcal	1.00	2.29	4.30	7.53	0.082	-0.604	21.35	21.05									0.004		
	5.00	0.12	0.09	-0.40	0.067	-0.571	17.08	16.77									0.028	NR	
	11.00	5.37	10.27	18.91	0.094	-0.595	27.43	27.12									0.010		

		Pyrite (‰)							CAS (‰)										
Section	**m**	**$\delta^{33}S$**	**$\delta^{34}S$**	**$\delta^{36}S$**	**$\Delta^{33}S$**	**$\Delta^{36}S$**	**$\delta^{34}S$ vs S1**	**$\delta^{34}S$ vs CDT**	**$\delta^{33}S$**	**$\delta^{34}S$**	**$\delta^{36}S$**	**$\Delta^{33}S$**	**$\Delta^{36}S$**	**$\delta^{34}S$ vs S1**	**$\delta^{34}S$ vs CDT**	**$\Delta^{34}S_{CAS-py}$**	**Py (%)**	**CAS (ppm)**	**Fe (%)**
	15.50	8.83	17.07	32.16	0.077	-0.341	34.34	34.03									0.007		
	20.00	10.00	19.35	36.43	0.077	-0.461	36.67	36.35									0.023		
	26.00	10.74	20.78	39.08	0.090	-0.549	38.11	37.80	13.19	25.76	49.26	0.004	0.01	43.179	42.866	5.066	0.074	3	
	30.00	5.97	11.44	21.20	0.095	-0.530	28.62	28.31									0.022		
	35.00	5.77	10.99	20.08	0.120	-0.797	28.16	27.85									0.055		
	40.00	5.46	10.46	19.34	0.082	-0.524	27.62	27.32									0.008		
	45.00	7.81	15.05	28.12	0.086	-0.516	32.29	31.98									0.005		
	50.00	8.36	16.25	30.54	0.029	-0.390	33.51	33.20									0.006		
Sobramil	0.00	9.30	18.04	34.07	0.052	-0.298	35.33	35.02									0.100		
	2.00	6.14	11.81	22.19	0.076	-0.242	28.99	28.68									0.049		
	5.00	4.34	8.28	15.30	0.083	-0.40	25.40	25.09									0.010		
	7.00	5.45	10.49	19.49	0.065	-0.424	27.65	27.34									0.023		
	9.00	2.46	4.73	8.84	0.032	-0.116	21.79	21.48									0.007		
	15.00	4.39	8.43	15.50	0.059	-0.486	25.55	25.25									0.038		
	17.00	9.75	18.81	35.25	0.100	-0.609	36.12	35.81									0.022		
	19.00	8.31	16.04	29.94	0.078	-0.589	33.29	32.98									0.023		
	21.00	8.65	16.76	31.48	0.048	-0.443	34.03	33.72									0.073		
	23.00	6.57	12.65	23.39	0.076	-0.658	29.85	29.54									0.030		

NR = Not recovered.

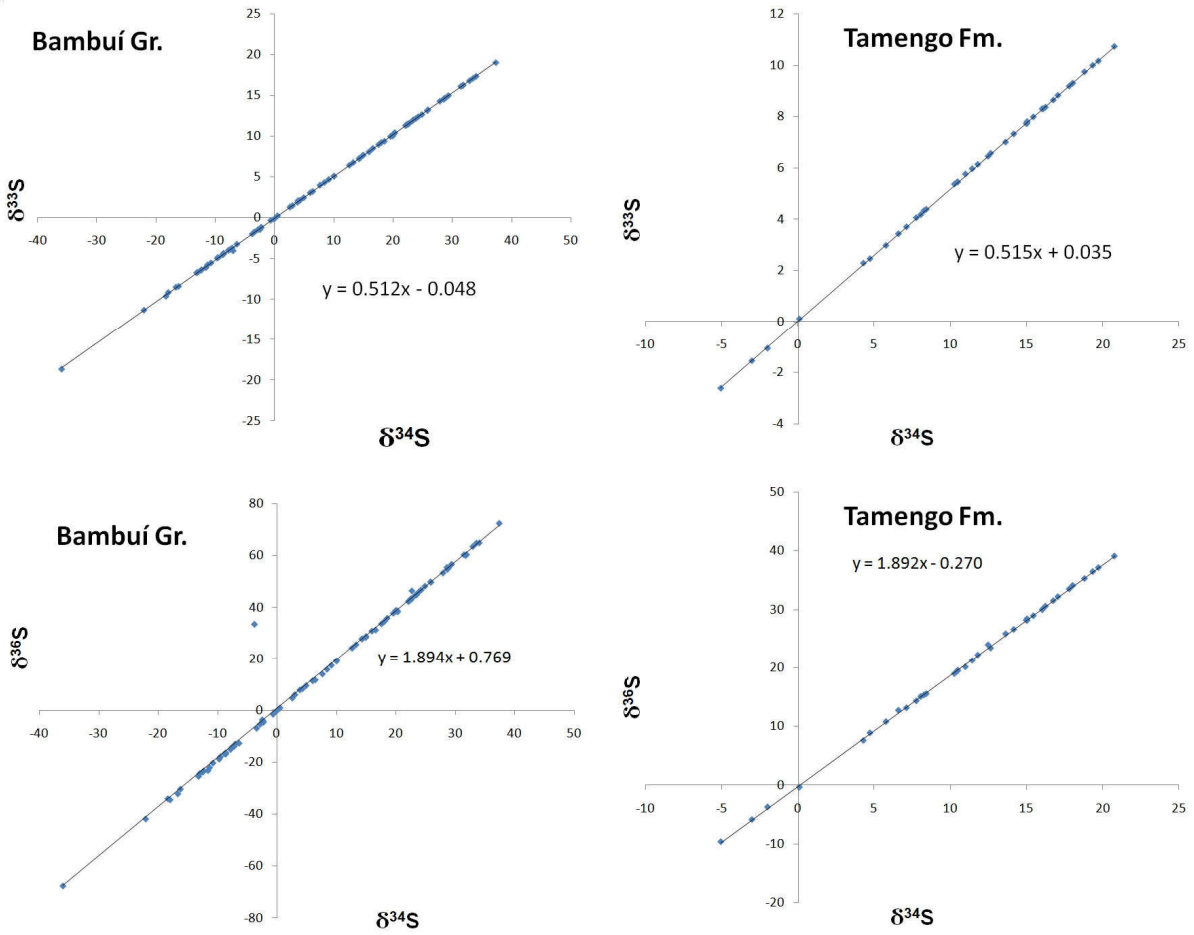

Figure S1: $\delta^{34}S$ *vs* $\delta^{33}S$ and $\delta^{34}S$ *vs* $\delta^{36}S$ relationships for Bambuí Group and Tamengo Formation.

272

Table S2: Parameters set for Rayleigh distillation trends for multiple sulfur isotope data from the Bambuí Group.

$^{34}S/^{32}S$						$^{33}S/^{32}S$						$\delta^{34}Srr$	$\delta^{34}Sip$	$\delta^{34}Spp$	$\delta^{33}Srr$	$\delta^{33}Sip$	$\delta^{33}Spp$	$\Delta^{33}Srr$	$\Delta^{33}Sip$	$\Delta^{33}Spp$
Rrr	**Ro**	**F**	**α(p-r)**	**Rip**	**Rpp**	**Rrr**	**Ro**	**F**	**α(p-r)**	**Rip**	**Rpp**									
1.035	1.035	1	0.945	0.978075		1.01777	1.01777	1	0.971451	0.988714		35	-21.925		17.76956	-11.2863		-0.10504	0.065754	
1.035572	1.035	0.99	0.945	0.978616	0.978345	1.018062	1.01777	0.99	0.971451	0.988997	0.988855	35.57227	-21.3842	-21.6551	18.06163	-11.0026	-11.1447	-0.10279	0.067995	0.066869
1.036151	1.035	0.98	0.945	0.979162	0.97861 7	1.018357	1.01777	0.98	0.971451	0.989284	0.988998	36.15068	-20.8376	-21.3832	18.35674	-10.7159	-11.0021	-0.1005	0.07026	0.067986
1.036735	1.035	0.97	0.945	0.979715	0.978891	1.018655	1.01777	0.97	0.971451	0.989574	0.989142	36.73534	-20.2851	-21.1094	18.65497	-10.4262	-10.8585	-0.0982	0.07255	0.069105
1.037326	1.035	0.96	0.945	0.980273	0.979166	1.018956	1.01777	0.96	0.971451	0.989867	0.989286	37.3264	-19.7265	-20.8337	18.95637	-10.1334	-10.7139	-0.09587	0.074865	0.070225
1.037924	1.035	0.95	0.945	0.980838	0.979444	1.019261	1.01777	0.95	0.971451	0.990163	0.989432	37.92399	-19.1618	-20.5559	19.26103	-9.83743	-10.5682	-0.09351	0.077205	0.071346
1.038528	1.035	0.94	0.945	0.981409	0.979724	1.019569	1.01777	0.94	0.971451	0.990462	0.989578	38.52826	-18.5908	-20.276	19.569	-9.53825	-10.4216	-0.09112	0.079572	0.072468
1.039139	1.035	0.93	0.945	0.981987	0.980006	1.01988	1.01777	0.93	0.971451	0.990764	0.989726	39.13934	-18.0133	-19.9941	19.88035	-9.23578	-10.2738	-0.08871	0.081965	0.073592
1.039757	1.035	0.92	0.945	0.982571	0.98029	1.020195	1.01777	0.92	0.971451	0.99107	0.989875	39.7574	-17.4293	-19.7101	20.19518	-8.92995	-10.125	-0.08627	0.084386	0.074716
1.040383	1.035	0.91	0.945	0.983162	0.980576	1.020514	1.01777	0.91	0.971451	0.991379	0.990025	40.38258	-16.8385	-19.4239	20.51354	-8.62068	-9.97504	-0.08381	0.086834	0.075842
1.041015	1.035	0.9	0.945	0.983759	0.980864	1.020836	1.01777	0.9	0.971451	0.991692	0.990176	41.01506	-16.2408	-19.1355	20.83551	-8.30789	-9.824	-0.08131	0.089311	0.076968
1.041655	1.035	0.89	0.945	0.984364	0.981155	1.021161	1.01777	0.89	0.971451	0.992008	0.990328	41.65499	-15.636	-18.8449	21.16119	-7.99151	-9.67182	-0.07878	0.091818	0.078095
1.042303	1.035	0.88	0.945	0.984976	0.981448	1.021491	1.01777	0.88	0.971451	0.992329	0.990482	42.30256	-15.0241	-18.5521	21.49066	-7.67145	-9.51848	-0.07623	0.094354	0.079223
1.042958	1.035	0.87	0.945	0.985595	0.981743	1.021824	1.01777	0.87	0.971451	0.992652	0.990636	42.95793	-14.4048	-18.2569	21.824	-7.34763	-9.36397	-0.07364	0.096921	0.080351
1.043621	1.035	0.86	0.945	0.986222	0.982041	1.022161	1.01777	0.86	0.971451	0.992978	0.990792	43.6213	-13.7779	-17.9594	22.1613	-7.01995	-9.20827	-0.07103	0.09952	0.08148
1.044293	1.035	0.85	0.945	0.986857	0.98234	1.022503	1.01777	0.85	0.971451	0.993312	0.990949	44.29286	-13.1432	-17.6595	22.50267	-6.68834	-9.05135	-0.06837	0.10215	0.082609
1.044973	1.035	0.84	0.945	0.987499	0.982643	1.022848	1.01777	0.84	0.971451	0.993647	0.991107	44.97281	-12.5007	-17.3572	22.84818	-6.35268	-8.89319	-0.06569	0.104814	0.083737
1.045661	1.035	0.83	0.945	0.988115	0.982948	1.023198	1.01777	0.83	0.971451	0.993987	0.991266	45.66135	-11.85	-17.0525	23.19796	-6.01289	-8.73378	-0.06297	0.107511	0.084866
1.046359	1.035	0.82	0.945	0.988809	0.983255	1.023552	1.01777	0.82	0.971451	0.994331	0.991427	46.3587	-11.191	-16.7452	23.55209	-5.66887	-8.57308	-0.06022	0.110242	0.085995
1.047065	1.035	0.81	0.945	0.989476	0.983565	1.023911	1.01777	0.81	0.971451	0.99468	0.991589	47.06507	-10.5235	-16.4353	23.9107	-5.3205	-8.41108	-0.05743	0.113013	0.087123
1.047781	1.035	0.8	0.945	0.990153	0.983877	1.024274	1.01777	0.8	0.971451	0.995032	0.991752	47.78071	-9.84722	-16.1229	24.27389	-4.96768	-8.24775	-0.05461	0.115813	0.088253
1.048506	1.035	0.79	0.945	0.990838	0.984192	1.024642	1.01777	0.79	0.971451	0.995392	0.991917	48.50585	-9.16197	-15.8077	24.64178	-4.61029	-8.08306	-0.05175	0.118654	0.089376
1.049241	1.035	0.78	0.945	0.991533	0.98451	1.025014	1.01777	0.78	0.971451	0.995752	0.992083	49.24074	-8.4675	-15.4899	25.01449	-4.24822	-7.917	-0.04885	0.121533	0.090502

$^{34}S/^{32}S$						$^{33}S/^{32}S$						$\delta^{34}Srr$	$\delta^{34}Sip$	$\delta^{34}Spp$	$\delta^{33}Srr$	$\delta^{33}Sip$	$\delta^{33}Spp$	$\Delta^{33}Srr$	$\Delta^{33}Sip$	$\Delta^{33}Spp$
Rrr	**Ro**	**F**	**α(p-r)**	**Rip**	**Rpp**	**Rrr**	**Ro**	**F**	**α(p-r)**	**Rip**	**Rpp**									
1.049986	1.035	0.77	0.945	0.992236	0.984831	1.025392	1.01777	0.77	0.971451	0.996119	0.99225	49.98564	-7.76357	-15.1693	25.39215	-3.88134	-7.74953	-0.04591	0.124451	0.091626
1.050741	1.035	0.76	0.945	0.99295	0.985154	1.025775	1.01777	0.76	0.971451	0.99649	0.992419	50.74081	-7.04993	-14.8459	25.77489	-3.50953	-7.58063	-0.04292	0.127409	0.092749
1.051507	1.035	0.75	0.945	0.993674	0.98548	1.026163	1.01777	0.75	0.971451	0.996867	0.99259	51.50655	-6.32631	-14.5196	26.16284	-3.13266	-7.41026	-0.0399	0.130409	0.09387
1.052283	1.035	0.74	0.945	0.994408	0.98581	1.026556	1.01777	0.74	0.971451	0.997249	0.992762	52.28312	-5.59245	-14.1904	26.55615	-2.75058	-7.23841	-0.03684	0.133452	0.09499
1.053071	1.035	0.73	0.945	0.995152	0.986142	1.026955	1.01777	0.73	0.971451	0.997637	0.992935	53.07085	-4.84804	-13.8582	26.95496	-2.36315	-7.06503	-0.03373	0.136538	0.096107
1.05387	1.035	0.72	0.945	0.995907	0.986477	1.027359	1.01777	0.72	0.971451	0.99803	0.99311	53.87005	-4.0928	-13.523	27.35944	-1.97022	-6.89011	-0.03057	0.139669	0.097221
1.054681	1.035	0.71	0.945	0.996674	0.986815	1.02777	1.01777	0.71	0.971451	0.998428	0.993286	54.68104	-3.32641	-13.1846	27.76973	-1.57164	-6.7136	-0.02737	0.142847	0.098333
1.055504	1.035	0.7	0.945	0.997451	0.987157	1.028186	1.01777	0.7	0.971451	0.998833	0.993465	55.50418	-2.54855	-12.8431	28.18601	-1.16724	-6.53548	-0.02412	0.146072	0.099441
1.05634	1.035	0.69	0.945	0.998241	0.987502	1.028608	1.01777	0.69	0.971451	0.999243	0.993644	56.33982	-1.75887	-12.4983	28.60845	-0.75686	-6.35571	-0.02082	0.149346	0.100547
1.057188	1.035	0.68	0.945	0.999043	0.98785	1.029037	1.01777	0.68	0.971451	0.99966	0.993826	57.18833	-0.95703	-12.1502	29.03724	-0.34031	-6.17425	-0.01747	0.152671	0.101648
1.05805	1.035	0.67	0.945	0.999857	0.988201	1.029473	1.01777	0.67	0.971451	1.000083	0.994009	58.05011	-0.14265	-11.7987	29.47256	0.082581	-5.99107	-0.01407	0.156048	0.102745
1.058926	1.035	0.66	0.945	1.000685	0.988556	1.029915	1.01777	0.66	0.971451	1.000512	0.994194	58.92556	0.684659	-11.4437	29.91462	0.512019	-5.80614	-0.01061	0.159478	0.103838
1.059815	1.035	0.65	0.945	1.001525	0.988915	1.030364	1.01777	0.65	0.971451	1.000948	0.994381	59.81513	1.525298	-11.0852	30.36362	0.948202	-5.61941	-0.0071	0.162964	0.104925
1.060719	1.035	0.64	0.945	1.00238	0.989277	1.03082	1.01777	0.64	0.971451	1.001391	0.994569	60.71925	2.379693	-10.7231	30.81979	1.391342	-5.43083	-0.00353	0.166507	0.106007
1.061638	1.035	0.63	0.945	1.003248	0.989643	1.031283	1.01777	0.63	0.971451	1.001842	0.99476	61.6384	3.24829	-10.3573	31.28334	1.841662	-5.24038	0.000102	0.170108	0.107084
1.062573	1.035	0.62	0.945	1.004132	0.990012	1.031755	1.01777	0.62	0.971451	1.002299	0.994952	62.57307	4.131556	-9.98765	31.75452	2.299395	-5.04801	0.003793	0.173771	0.108154
1.063524	1.035	0.61	0.945	1.005033	0.990386	1.032234	1.01777	0.61	0.971451	1.002765	0.995146	63.52379	5.029981	-9.61413	32.23359	2.764785	-4.85366	0.007548	0.177497	0.109216
1.064491	1.035	0.6	0.945	1.005944	0.990763	1.032721	1.01777	0.6	0.971451	1.003238	0.995343	64.49109	5.944081	-9.23664	32.72081	3.23809	-4.6573	0.011368	0.181288	0.110272
1.065476	1.035	0.59	0.945	1.006874	0.991145	1.033216	1.01777	0.59	0.971451	1.00372	0.995541	65.47555	6.874397	-8.85506	33.21644	3.719578	-4.45887	0.015256	0.185146	0.111319
1.066478	1.035	0.58	0.945	1.007821	0.991531	1.033721	1.01777	0.58	0.971451	1.00421	0.995742	66.47778	7.821499	-8.46931	33.7208	4.209535	-4.25833	0.019214	0.189074	0.112357
1.067498	1.035	0.57	0.945	1.008786	0.991921	1.034234	1.01777	0.57	0.971451	1.004708	0.995944	67.4984	8.785988	-8.07927	34.23418	4.708258	-4.05562	0.023245	0.193073	0.113386
1.068538	1.035	0.56	0.945	1.009768	0.992315	1.034757	1.01777	0.56	0.971451	1.005216	0.996149	68.53809	9.768496	-7.68484	34.75691	5.216064	-3.85069	0.027352	0.197148	0.114405
1.069598	1.035	0.55	0.945	1.010777	0.992714	1.035289	1.01777	0.55	0.971451	1.005733	0.996357	69.59756	10.76969	-7.2859	35.28933	5.733283	-3.64348	0.031537	0.201301	0.115413
1.070678	1.035	0.54	0.945	1.011779	0.993118	1.035832	1.01777	0.54	0.971451	1.00626	0.996566	70.67754	11.79028	-6.88233	35.8318	6.260266	-3.43393	0.035803	0.205534	0.116409

$^{34}S/^{32}S$						$^{33}S/^{32}S$						$\delta^{34}Srr$	$\delta^{34}Sip$	$\delta^{34}Spp$	$\delta^{33}Srr$	$\delta^{33}Sip$	$\delta^{33}Spp$	$\Delta^{33}Srr$	$\Delta^{33}Sip$	$\Delta^{33}Spp$
Rrr	**Ro**	**F**	**α(p-r)**	**Rip**	**Rpp**	**Rrr**	**Ro**	**F**	**α(p-r)**	**Rip**	**Rpp**									
1.071779	1.035	0.53	0.945	1.012831	0.993526	1.036385	1.01777	0.53	0.971451	1.006797	0.996778	71.77884	12.831	-6.47401	36.3847	6.797384	-3.22197	0.040153	0.20985	0.117393
1.072902	1.035	0.52	0.945	1.013893	0.993939	1.036948	1.01777	0.52	0.971451	1.007345	0.996992	72.90227	13.89265	-6.0608	36.94844	7.345028	-3.00755	0.044591	0.21425 3	0.118362
1.074049	1.035	0.51	0.945	1.014976	0.994357	1.037523	1.01777	0.51	0.971451	1.007904	0.997209	74.04874	14.97606	-5.64257	37.52344	7.903614	-2.79059	0.04912	0.21874 7	0.119318
1.075219	1.035	0.5	0.945	1.016082	0.994781	1.03811	1.01777	0.5	0.971451	1.008474	0.997429	75.21917	16.08212	-5.21917	38.11015	8.47358	-2.57103	0.053743	0.22333 5	0.120257
1.076415	1.035	0.49	0.945	1.017212	0.99521	1.038709	1.01777	0.49	0.971451	1.009055	0.997651	76.41456	17.21176	-4.79046	38.70907	9.055393	-2.34878	0.058466	0.22802 1	0.12118
1.077636	1.035	0.48	0.945	1.018366	0.995644	1.039321	1.01777	0.48	0.971451	1.00965	0.997876	77.63598	18.366	-4.35629	39.32068	9.64955	-2.12378	0.063292	0.23280 8	0.122084
1.078885	1.035	0.47	0.945	1.019546	0.996084	1.039946	1.01777	0.47	0.971451	1.010257	0.998104	78.88453	19.54588	-3.91647	39.94555	10.25658	-1.89593	0.068225	0.23770 3	0.12297
1.080161	1.035	0.46	0.945	1.020753	0.996529	1.040584	1.01777	0.46	0.971451	1.010877	0.998335	80.16144	20.75256	-3.47086	40.58424	10.87704	-1.66516	0.07327	0.24270 8	0.123834
1.081468	1.035	0.45	0.945	1.021987	0.996981	1.041237	1.01777	0.45	0.971451	1.011512	0.998569	81.46797	21.98723	-3.01925	41.23738	11.51153	-1.43138	0.078432	0.24783	0.124676
1.082805	1.035	0.44	0.945	1.023251	0.997439	1.041906	1.01777	0.44	0.971451	1.012161	0.998806	82.8055	23.2512	-2.56146	41.90562	12.16069	-1.19448	0.083717	0.25307 4	0.125494
1.084175	1.035	0.43	0.945	1.024546	0.997903	1.04259	1.01777	0.43	0.971451	1.012825	0.999046	84.17549	24.54584	-2.0973	42.58966	12.82521	-0.95437	0.089131	0.25844 4	0.126286
1.08558	1.035	0.42	0.945	1.025873	0.998373	1.04329	1.01777	0.42	0.971451	1.013506	0.999289	85.57951	25.87264	-1.62654	43.29027	13.50581	-0.71095	0.094679	0.26394 9	0.127051
1.087019	1.035	0.41	0.945	1.027233	0.998851	1.044008	1.01777	0.41	0.971451	1.014203	0.999536	87.01926	27.2332	-1.14897	44.00825	14.2033	-0.4641	0.100368	0.26959 3	0.127786
1.088497	1.035	0.4	0.945	1.028629	0.999336	1.044744	1.01777	0.4	0.971451	1.014918	0.999786	88.49653	28.62922	-0.66436	44.74447	14.9185	-0.21371	0.106206	0.27538 5	0.128488
1.090013	1.035	0.39	0.945	1.030063	0.999828	1.0455	1.01777	0.39	0.971451	1.015652	1.00004	90.0133	30.06257	-0.17244	45.49987	15.65233	0.040348	0.112201	0.28133 2	0.129156
1.091572	1.035	0.38	0.945	1.031535	1.000327	1.046275	1.01777	0.38	0.971451	1.016406	1.00029 8	91.57166	31.53522	0.32704 7	46.27547	16.40578	0.298203	0.11836	0.28744 2	0.129788
1.093174	1.035	0.37	0.945	1.033049	1.000834	1.047072	1.01777	0.37	0.971451	1.01718	1.00056	93.1739	33.04934	0.83437 5	47.07234	17.17991	0.559995	0.124693	0.29372 4	0.130379
1.094822	1.035	0.36	0.945	1.034607	1.00135	1.047892	1.01777	0.36	0.971451	1.017976	1.00082 6	94.8225	34.60726	1.34984 6	47.89168	17.97586	0.82587	0.131209	0.30018 8	0.130927
1.09652	1.035	0.35	0.945	1.036212	1.001874	1.048735	1.01777	0.35	0.971451	1.018795	1.00109 6	96.52013	36.21152	1.87377 8	48.73478	18.79489	1.095986	0.137919	0.30684 5	0.131428
1.09827	1.035	0.34	0.945	1.037865	1.002407	1.049603	1.01777	0.34	0.971451	1.019638	1.00137 1	98.26972	37.86488	2.40650 9	49.60302	19.63834	1.370509	0.144835	0.31370 5	0.13188
1.100074	1.035	0.33	0.945	1.039577	1.002948	1.050498	1.01777	0.33	0.971451	1.020508	1.00165	100.0745	39.57037	2.94839 9	50.49794	20.50771	1.649618	0.151969	0.32078 2	0.132277
1.101938	1.035	0.32	0.945	1.041331	1.0035	1.051421	1.01777	0.32	0.971451	1.021405	1.00193 4	101.9379	41.33127	3.49983 5	51.42119	21.40461	1.933503	0.159335	0.32808 9	0.132615
1.103864	1.035	0.31	0.945	1.043151	1.004061	1.052375	1.01777	0.31	0.971451	1.022331	1.00222 2	103.8637	43.15121	4.06123 1	52.37461	22.33081	2.222368	0.166949	0.33564 1	0.13289
1.105856	1.035	0.3	0.945	1.045034	1.004633	1.053366	1.01777	0.3	0.971451	1.023288	1.00251 6	105.8563	45.03417	4.63303 1	53.3602	23.28826	2.516432	0.174826	0.34345 5	0.133095

$^{34}S/^{32}S$						$^{33}S/^{32}S$						$\delta^{34}Srr$	$\delta^{34}Sip$	$\delta^{34}Spp$	$\delta^{33}Srr$	$\delta^{33}Sip$	$\delta^{33}Spp$	$\Delta^{33}Srr$	$\Delta^{33}Sip$	$\Delta^{33}Spp$
Rrr	**Ro**	**F**	**α(p-r)**	**Rip**	**Rpp**	**Rrr**	**Ro**	**F**	**α(p-r)**	**Rip**	**Rpp**									
1.10792	1.035	0.29	0.945	1.046985	1.005216	1.05438	1.01777	0.29	0.971451	1.024279	1.002816	107.9201	46.98454	5.215715	54.38018	24.27912	2.81593	0.182986	0.351549	0.133226
1.110061	1.035	0.28	0.945	1.049007	1.00581	1.055437	1.01777	0.28	0.971451	1.025306	1.003121	110.0605	49.00719	5.809797	55.437	25.30577	3.121117	0.191449	0.359943	0.133275
1.112283	1.035	0.27	0.945	1.051108	1.006416	1.056533	1.01777	0.27	0.971451	1.026371	1.003432	112.2831	51.10754	6.415836	56.53337	26.37084	3.432266	0.200237	0.368659	0.133235
1.114594	1.035	0.26	0.945	1.053292	1.007034	1.057672	1.01777	0.26	0.971451	1.027477	1.00375	114.5943	53.29161	7.034437	57.67233	27.47728	3.749674	0.209376	0.377724	0.133097
1.117001	1.035	0.25	0.945	1.055566	1.007666	1.058857	1.01777	0.25	0.971451	1.028628	1.004074	117.0012	55.56616	7.666258	58.85726	28.62839	4.073664	0.218894	0.387164	0.132853
1.119512	1.035	0.24	0.945	1.057939	1.008312	1.060092	1.01777	0.24	0.971451	1.029828	1.004405	119.5119	57.93879	8.312018	60.09198	29.82786	4.404589	0.228823	0.397011	0.132493
1.122136	1.035	0.23	0.945	1.060418	1.008972	1.061381	1.01777	0.23	0.971451	1.03108	1.004743	122.1355	60.41809	8.9725	61.3808	31.07988	4.742832	0.239198	0.407301	0.132004
1.124882	1.035	0.22	0.945	1.063014	1.009649	1.062729	1.01777	0.22	0.971451	1.032389	1.005089	124.8823	63.01382	9.648568	62.72858	32.38918	5.088815	0.250062	0.418075	0.131374
1.127764	1.035	0.21	0.945	1.065737	1.010341	1.064141	1.01777	0.21	0.971451	1.033761	1.005443	127.7642	65.73713	10.34117	64.14091	33.76119	5.443004	0.26146	0.429378	0.130588
1.130795	1.035	0.2	0.945	1.068601	1.011051	1.065624	1.01777	0.2	0.971451	1.035202	1.005806	130.7945	68.60083	11.05137	65.62417	35.20211	5.805912	0.273446	0.441265	0.129628
1.133989	1.035	0.19	0.945	1.07162	1.01178	1.067186	1.01777	0.19	0.971451	1.036719	1.006178	133.9892	71.61975	11.78032	67.18576	36.71912	6.17811	0.286082	0.453796	0.128475
1.137366	1.035	0.18	0.945	1.074811	1.012529	1.068834	1.01777	0.18	0.971451	1.038321	1.00656	137.3663	74.81117	12.52935	68.83428	38.32058	6.560236	0.299441	0.467043	0.127107
1.140947	1.035	0.17	0.945	1.078195	1.0133	1.07058	1.01777	0.17	0.971451	1.040016	1.006953	140.9475	78.19538	13.29991	70.57982	40.01628	6.953005	0.313608	0.48109	0.125498
1.144758	1.035	0.16	0.945	1.081796	1.014094	1.072434	1.01777	0.16	0.971451	1.041818	1.007357	144.7582	81.79647	14.09368	72.43433	41.81784	7.357228	0.328683	0.496039	0.123616
1.148829	1.035	0.15	0.945	1.085643	1.014913	1.074412	1.01777	0.15	0.971451	1.043739	1.007774	148.8288	85.64326	14.91256	74.41209	43.73915	7.773824	0.344788	0.512007	0.121427
1.153196	1.035	0.14	0.945	1.089771	1.015759	1.07653	1.01777	0.14	0.971451	1.045797	1.008204	153.1965	89.77067	15.75871	76.53039	45.79697	8.203848	0.362069	0.529141	0.118885
1.157906	1.035	0.13	0.945	1.094222	1.016635	1.07881	1.01777	0.13	0.971451	1.048012	1.008649	157.9064	94.22158	16.63467	78.81039	48.01188	8.64852	0.380704	0.547617	0.115941
1.163015	1.035	0.12	0.945	1.099049	1.017543	1.081278	1.01777	0.12	0.971451	1.050409	1.009109	163.0152	99.04934	17.54339	81.27841	50.40944	9.109267	0.400919	0.567658	0.11253
1.168594	1.035	0.11	0.945	1.104322	1.018488	1.083968	1.01777	0.11	0.971451	1.053022	1.009588	168.5943	104.3216	18.48835	83.9677	53.02195	9.587772	0.422996	0.589545	0.108575
1.174736	1.035	0.1	0.945	1.110126	1.019474	1.086921	1.01777	0.1	0.971451	1.055891	1.010086	174.7362	110.1257	19.47376	86.92116	55.8911	10.08605	0.447301	0.613639	0.103978
1.181563	1.035	0.09	0.945	1.116577	1.020505	1.090195	1.01777	0.09	0.971451	1.059072	1.010607	181.5634	116.5774	20.50472	90.19542	59.07189	10.60657	0.474319	0.640421	0.098616
1.189242	1.035	0.08	0.945	1.123834	1.021588	1.093867	1.01777	0.08	0.971451	1.062639	1.011152	189.2424	123.8341	21.58761	93.86742	62.63905	11.15236	0.50471	0.670545	0.092325
1.198009	1.035	0.07	0.945	1.132118	1.022731	1.098045	1.01777	0.07	0.971451	1.066698	1.011727	198.0087	132.1182	22.73053	98.04534	66.6977	11.7273	0.539405	0.704932	0.084888
1.208209	1.035	0.06	0.945	1.141757	1.023944	1.102888	1.01777	0.06	0.971451	1.071402	1.012336	208.2089	141.7574	23.94411	102.8883	71.40235	12.33646	0.579776	0.744942	0.076002

$^{34}S/^{32}S$						$^{33}S/^{32}S$						$\delta^{34}Srr$	$\delta^{34}Sip$	$\delta^{34}Spp$	$\delta^{33}Srr$	$\delta^{33}Sip$	$\delta^{33}Spp$	$\Delta^{33}Srr$	$\Delta^{33}Sip$	$\Delta^{33}Spp$
Rrr	**Ro**	**F**	**α(p-r)**	**Rip**	**Rpp**	**Rrr**	**Ro**	**F**	**α(p-r)**	**Rip**	**Rpp**									
1.220385	1.035	0.05	0.945	1.153264	1.025243	1.108644	1.01777	0.05	0.971451	1.076994	1.012987	220.3854	153.2642	25.24287	108.6438	76.99356	12.98671	0.62797	0.792701	0.06523
1.235455	1.035	0.04	0.945	1.167505	1.026648	1.115729	1.01777	0.04	0.971451	1.083876	1.013688	235.4553	167.5053	26.64769	115.7289	83.87638	13.68793	0.68761	0.851802	0.05189
1.255159	1.035	0.03	0.945	1.186125	1.028191	1.12493	1.01777	0.03	0.971451	1.092815	1.014455	255.1588	186.1251	28.19096	124.93	92.81482	14.45532	0.76559	0.929066	0.03486
1.283464	1.035	0.02	0.945	1.212874	1.029929	1.138027	1.01777	0.02	0.971451	1.105538	1.015315	283.464	212.8735	29.92931	138.0272	105.5381	15.31533	0.87760	1.04001	0.01197
1.333338	1.035	0.01	0.945	1.260005	1.031986	1.160771	1.01777	0.01	0.971451	1.127633	1.016325	333.3383	260.0047	31.98648	160.7712	127.6328	16.3251	1.074881	1.235373	-0.02214

Table S3: Parameters set for Rayleigh distillation trends for multiple sulfur isotope data from the Tamengo Formation.

$^{34}S/^{32}S$						$^{33}S/^{32}S$						$\delta^{34}Srr$	$\delta^{34}Sip$	$\delta^{34}Spp$	$\delta^{33}Srr$	$\delta^{33}Sip$	$\delta^{33}Spp$	$\Delta^{33}Srr$	$\Delta^{33}Sip$	$\Delta^{33}Spp$
Rrr	**Ro**	**F**	**α(p-r)**	**Rip**	**Rpp**	**Rrr**	**Ro**	**F**	**α(p-r)**	**Rip**	**Rpp**									
1.03	1.03	1	0.955	0.98365	-	1.015339	1.015339	1	0.976566	0.991546	-	30	-16.35		15.33924	-8.45391		0	0	0
1.030466	1.03	0.99	0.955	0.984095	0.983872	1.015578	1.015339	0.99	0.976566	0.99178	0.991663	30.46594	-15.905	-16.1279	15.5784	-8.22036	-8.33733	0.00264	0.002579	0.001285
1.030937	1.03	0.98	0.955	0.984545	0.984096	1.01582	1.015339	0.98	0.976566	0.992016	0.99178	30.93682	-15.4553	-15.9042	15.82004	-7.98438	-8.21995	0.005309	0.005185	0.002575
1.031413	1.03	0.97	0.955	0.984999	0.984321	1.016064	1.015339	0.97	0.976566	0.992254	0.991898	31.41275	-15.0008	-15.679	16.06422	-7.74592	-8.10175	0.008006	0.007819	0.003869
1.031894	1.03	0.96	0.955	0.985459	0.984548	1.016311	1.015339	0.96	0.976566	0.992495	0.992017	31.89384	-14.5414	-15.4521	16.31099	-7.50493	-7.98272	0.010733	0.010481	0.005168
1.03238	1.03	0.95	0.955	0.985923	0.984776	1.01656	1.015339	0.95	0.976566	0.992739	0.992137	32.38019	-14.0769	-15.2236	16.5604	-7.26136	-7.86285	0.013489	0.013173	0.006472
1.032872	1.03	0.94	0.955	0.986393	0.985007	1.016813	1.015339	0.94	0.976566	0.992985	0.992258	32.87192	-13.6073	-14.9934	16.81252	-7.01515	-7.74212	0.016276	0.015894	0.007781
1.033369	1.03	0.93	0.955	0.986868	0.985238	1.017067	1.015339	0.93	0.976566	0.993234	0.992379	33.36915	-13.1325	-14.7616	17.06739	-6.76625	-7.62052	0.019094	0.018646	0.009095
1.033872	1.03	0.92	0.955	0.987348	0.985472	1.017325	1.015339	0.92	0.976566	0.993485	0.992502	33.872	-12.6522	-14.528	17.32509	-6.51459	-7.49804	0.021944	0.021429	0.010414
1.034381	1.03	0.91	0.955	0.987833	0.985707	1.017586	1.015339	0.91	0.976566	0.99374	0.992625	34.38059	-12.1665	-14.2926	17.58567	-6.26012	-7.37466	0.024826	0.024244	0.011737
1.034895	1.03	0.9	0.955	0.988325	0.985945	1.017849	1.015339	0.9	0.976566	0.993997	0.99275	34.89506	-11.6752	-14.0555	17.8492	-6.00277	-7.25036	0.027742	0.027092	0.013065
1.035416	1.03	0.89	0.955	0.988822	0.986183	1.018116	1.015339	0.89	0.976566	0.994258	0.992875	35.41553	-11.1782	-13.8166	18.11574	-5.74248	-7.12513	0.030692	0.029973	0.014398
1.035942	1.03	0.88	0.955	0.989325	0.986424	1.018385	1.015339	0.88	0.976566	0.994521	0.993001	35.94215	-10.6752	-13.5758	18.38536	-5.47917	-6.99896	0.033677	0.032888	0.015736
1.036475	1.03	0.87	0.955	0.989834	0.986667	1.018658	1.015339	0.87	0.976566	0.994787	0.993128	36.47506	-10.1663	-13.3331	18.65814	-5.21279	-6.87183	0.036698	0.035838	0.017078
1.037014	1.03	0.86	0.955	0.990349	0.986911	1.018934	1.015339	0.86	0.976566	0.995057	0.993256	37.01442	-9.65123	-13.0886	18.93414	-4.94325	-6.74372	0.039755	0.038823	0.018425
1.03756	1.03	0.85	0.955	0.99087	0.987158	1.019213	1.015339	0.85	0.976566	0.99533	0.993385	37.56036	-9.12985	-12.8421	19.21345	-4.67049	-6.61461	0.042849	0.041845	0.019778
1.038113	1.03	0.84	0.955	0.991398	0.987406	1.019496	1.015339	0.84	0.976566	0.995606	0.993516	38.11307	-8.60202	-12.5936	19.49614	-4.39442	-6.4845	0.045982	0.044905	0.021134
1.038673	1.03	0.83	0.955	0.991932	0.987657	1.019782	1.015339	0.83	0.976566	0.995885	0.993647	38.67268	-8.06759	-12.3431	19.7823	-4.11497	-6.35335	0.049155	0.048003	0.022496
1.039239	1.03	0.82	0.955	0.992474	0.987909	1.020072	1.015339	0.82	0.976566	0.996168	0.993779	39.23939	-7.52638	-12.0906	20.07201	-3.83205	-6.22115	0.052367	0.05114	0.023862
1.039813	1.03	0.81	0.955	0.993022	0.988164	1.020365	1.015339	0.81	0.976566	0.996454	0.993912	39.81337	-6.97823	-11.836	20.36536	-3.54557	-6.08789	0.055621	0.054317	0.025233
1.040395	1.03	0.8	0.955	0.993577	0.988421	1.020662	1.015339	0.8	0.976566	0.996745	0.994046	40.39481	-6.42296	-11.5792	20.66243	-3.25546	-5.95353	0.058917	0.057536	0.026609
1.040984	1.03	0.79	0.955	0.99414	0.98868	1.020963	1.015339	0.79	0.976566	0.997038	0.994182	40.98388	-5.86039	-11.3203	20.96334	-2.96161	-5.81807	0.062256	0.060797	0.027989
1.041581	1.03	0.78	0.955	0.99471	0.988941	1.021268	1.015339	0.78	0.976566	0.997336	0.994319	41.5808	-5.29033	-11.0592	21.26816	-2.66392	-5.68148	0.06564	0.064102	0.029374

$^{34}S/^{32}S$						$^{33}S/^{32}S$						$\delta^{34}Srr$	$\delta^{34}Sip$	$\delta^{34}Spp$	$\delta^{33}Srr$	$\delta^{33}Sip$	$\delta^{33}Spp$	$\Delta^{33}Srr$	$\Delta^{33}Sip$	$\Delta^{33}Spp$
Rrr	**Ro**	**F**	**α(p-r)**	**Rip**	**Rpp**	**Rrr**	**Ro**	**F**	**α(p-r)**	**Rip**	**Rpp**									
1.042186	1.03	0.77	0.955	0.995287	0.989204	1.021577	1.015339	0.77	0.976566	0.997638	0.994456	42.18578	-4.71258	-10.7959	21.57701	-2.36231	-5.54374	0.06907	0.067451	0.030763
1.042799	1.03	0.76	0.955	0.995873	0.98947	1.02189	1.015339	0.76	0.976566	0.997943	0.994595	42.79902	-4.12694	-10.5302	21.89	-2.05666	-5.40483	0.072546	0.070846	0.032157
1.043421	1.03	0.75	0.955	0.996467	0.989738	1.022207	1.015339	0.75	0.976566	0.998253	0.994735	43.42075	-3.53319	-10.2622	22.20723	-1.74686	-5.26472	0.076071	0.074289	0.033555
1.044051	1.03	0.74	0.955	0.997069	0.990008	1.022529	1.015339	0.74	0.976566	0.998567	0.994877	44.0512	-2.9311	-9.99188	22.52881	-1.43281	-5.12339	0.079646	0.077779	0.034958
1.044691	1.03	0.73	0.955	0.99768	0.990281	1.022855	1.015339	0.73	0.976566	0.998886	0.995019	44.69062	-2.32046	-9.71909	22.85488	-1.11439	-4.98082	0.083271	0.081319	0.036364
1.045339	1.03	0.72	0.955	0.998299	0.990556	1.023186	1.015339	0.72	0.976566	0.999209	0.995163	45.33926	-1.701	-9.44382	23.18555	-0.79147	-4.83698	0.086948	0.084911	0.037776
1.045997	1.03	0.71	0.955	0.998928	0.990834	1.023521	1.015339	0.71	0.976566	0.999536	0.995308	45.99739	-1.0725	-9.16601	23.52095	-0.46392	-4.69185	0.09068	0.088555	0.039191
1.046665	1.03	0.7	0.955	0.999565	0.991114	1.023861	1.015339	0.7	0.976566	0.999868	0.995455	46.66527	-0.43467	-8.88562	23.86122	-0.13163	-4.54539	0.094467	0.092253	0.04061
1.047343	1.03	0.69	0.955	1.000213	0.991397	1.024207	1.015339	0.69	0.976566	1.000206	0.995602	47.3432	0.212752	-8.6026	24.20651	0.205568	-4.39759	0.098311	0.096007	0.042034
1.048031	1.03	0.68	0.955	1.00087	0.991683	1.024557	1.015339	0.68	0.976566	1.000548	0.995752	48.03147	0.870054	-8.31687	24.55695	0.547801	-4.2484	0.102213	0.099818	0.043461
1.04873	1.03	0.67	0.955	1.001538	0.991972	1.024913	1.015339	0.67	0.976566	1.000895	0.995902	48.7304	1.537535	-8.02839	24.91271	0.895224	-4.09781	0.106176	0.103688	0.044892
1.04944	1.03	0.66	0.955	1.002216	0.992263	1.025274	1.015339	0.66	0.976566	1.001248	0.996054	49.44032	2.215509	-7.7371	25.27395	1.247994	-3.94578	0.110202	0.107619	0.046327
1.050162	1.03	0.65	0.955	1.002904	0.992557	1.025641	1.015339	0.65	0.976566	1.001606	0.996208	50.16158	2.904304	-7.44293	25.64083	1.606278	-3.79229	0.114292	0.111613	0.047765
1.050895	1.03	0.64	0.955	1.003604	0.992854	1.026014	1.015339	0.64	0.976566	1.00197	0.996363	50.89452	3.604263	-7.14581	26.01353	1.970248	-3.63728	0.118448	0.115672	0.049207
1.05164	1.03	0.63	0.955	1.004316	0.993154	1.026392	1.015339	0.63	0.976566	1.00234	0.996519	51.63952	4.315746	-6.84568	26.39225	2.340086	-3.48074	0.122673	0.119798	0.050651
1.052397	1.03	0.62	0.955	1.005039	0.993458	1.026777	1.015339	0.62	0.976566	1.002716	0.996677	52.39699	5.039129	-6.54246	26.77716	2.715981	-3.32263	0.126968	0.123993	0.052099
1.053167	1.03	0.61	0.955	1.005775	0.993764	1.027168	1.015339	0.61	0.976566	1.003098	0.996837	53.16734	5.774809	-6.23609	27.16848	3.098132	-3.16291	0.131337	0.128259	0.05355
1.053951	1.03	0.6	0.955	1.006523	0.994074	1.027566	1.015339	0.6	0.976566	1.003487	0.996998	53.951	6.523201	-5.92649	27.56643	3.48675	-3.00154	0.135781	0.132599	0.055003
1.054748	1.03	0.59	0.955	1.007285	0.994386	1.027971	1.015339	0.59	0.976566	1.003882	0.997162	54.74842	7.284743	-5.61358	27.97122	3.882054	-2.83848	0.140303	0.137015	0.056459
1.05556	1.03	0.58	0.955	1.00806	0.994703	1.028383	1.015339	0.58	0.976566	1.004284	0.997326	55.5601	8.059894	-5.29728	28.38309	4.284276	-2.6737	0.144907	0.141511	0.057917
1.056387	1.03	0.57	0.955	1.008849	0.995023	1.028802	1.015339	0.57	0.976566	1.004694	0.997493	56.38653	8.849139	-4.9775	28.8023	4.693658	-2.50714	0.149594	0.146088	0.059377
1.057228	1.03	0.56	0.955	1.009653	0.995346	1.029229	1.015339	0.56	0.976566	1.00511	0.997661	57.22826	9.652988	-4.65415	29.2291	5.110458	-2.33876	0.154368	0.15075	0.060839
1.058086	1.03	0.55	0.955	1.010472	0.995673	1.029664	1.015339	0.55	0.976566	1.005535	0.997831	58.08584	10.47198	-4.32714	29.66377	5.534945	-2.16852	0.159232	0.1555	0.062302
1.05896	1.03	0.54	0.955	1.011307	0.996004	1.030107	1.015339	0.54	0.976566	1.005967	0.998004	58.95988	11.30668	-3.99638	30.10661	5.967406	-1.99637	0.164189	0.160342	0.063767

$^{34}S/^{32}S$						$^{33}S/^{32}S$						$\delta^{34}Srr$	$\delta^{34}Sip$	$\delta^{34}Spp$	$\delta^{33}Srr$	$\delta^{33}Sip$	$\delta^{33}Spp$	$\Delta^{33}Srr$	$\Delta^{33}Sip$	$\Delta^{33}Spp$
Rrr	**Ro**	**F**	**α(p-r)**	**Rip**	**Rpp**	**Rrr**	**Ro**	**F**	**α(p-r)**	**Rip**	**Rpp**									
1.059851	1.03	0.53	0.955	1.012158	0.996338	1.030558	1.015339	0.53	0.976566	1.006408	0.998178	59.85099	12.1577	-3.66176	30.55792	6.408142	-1.82225	0.169244	0.165278	0.065232
1.06076	1.03	0.52	0.955	1.013026	0.996677	1.031018	1.015339	0.52	0.976566	1.006857	0.998354	60.75985	13.02566	-3.32317	31.01803	6.857472	-1.64612	0.174399	0.170312	0.066697
1.061687	1.03	0.51	0.955	1.013911	0.997019	1.031487	1.015339	0.51	0.976566	1.007316	0.998532	61.68716	13.91124	-2.98052	31.48729	7.315735	-1.46792	0.179659	0.175449	0.068162
1.062634	1.03	0.5	0.955	1.014815	0.997366	1.031966	1.015339	0.5	0.976566	1.007783	0.998712	62.63367	14.81516	-2.63367	31.96606	7.783287	-1.28758	0.185028	0.180692	0.069627
1.0636	1.03	0.49	0.955	1.015738	0.997717	1.032455	1.015339	0.49	0.976566	1.008261	0.998895	63.60018	15.73817	-2.28252	32.45474	8.260508	-1.10506	0.19051	0.186046	0.071091
1.064588	1.03	0.48	0.955	1.016681	0.998073	1.032954	1.015339	0.48	0.976566	1.008748	0.99908	64.58752	16.68108	-1.92694	32.95372	8.747804	-0.92028	0.196111	0.191516	0.072553
1.065597	1.03	0.47	0.955	1.017645	0.998433	1.033463	1.015339	0.47	0.976566	1.009246	0.999267	65.59659	17.64474	-1.56679	33.46347	9.245601	-0.73319	0.201835	0.197106	0.074013
1.066628	1.03	0.46	0.955	1.01863	0.998798	1.033984	1.015339	0.46	0.976566	1.009754	0.999456	66.62835	18.63007	-1.20193	33.98443	9.754359	-0.5437	0.207689	0.202822	0.075471
1.067684	1.03	0.45	0.955	1.019638	0.999168	1.034517	1.015339	0.45	0.976566	1.010275	0.999648	67.68382	19.63805	-0.83222	34.51712	10.27456	-0.35175	0.213676	0.208669	0.076925
1.068764	1.03	0.44	0.955	1.02067	0.999542	1.035062	1.015339	0.44	0.976566	1.010807	0.999843	68.76409	20.66971	-0.4575	35.06206	10.80674	-0.15726	0.219805	0.214654	0.078375
1.06987	1.03	0.43	0.955	1.021726	0.999922	1.03562	1.015339	0.43	0.976566	1.011351	1.00004	69.87033	21.72617	-0.07762	35.61983	11.35143	0.039846	0.226081	0.220783	0.07982
1.071004	1.03	0.42	0.955	1.022809	1.000308	1.036191	1.015339	0.42	0.976566	1.011909	1.00024	71.00379	22.80862	0.307602	36.19104	11.90925	0.239663	0.232512	0.227064	0.08126
1.072166	1.03	0.41	0.955	1.023918	1.000698	1.036776	1.015339	0.41	0.976566	1.012481	1.00044	72.1658	23.91834	0.69834	36.77633	12.48084	0.442277	0.239105	0.233502	0.082692
1.073358	1.03	0.4	0.955	1.025057	1.001095	1.037376	1.015339	0.4	0.976566	1.013067	1.00064	73.35782	25.05672	1.094786	37.37643	13.06687	0.647782	0.245869	0.240107	0.084117
1.074581	1.03	0.39	0.955	1.026225	1.001497	1.037992	1.015339	0.39	0.976566	1.013668	1.00085	74.5814	26.22523	1.49714	37.99207	13.66809	0.856281	0.252811	0.246887	0.085533
1.075838	1.03	0.38	0.955	1.027425	1.001906	1.038624	1.015339	0.38	0.976566	1.014285	1.00106	75.83821	27.42549	1.905616	38.62409	14.2853	1.067878	0.259943	0.253851	0.086939
1.07713	1.03	0.37	0.955	1.028659	1.00232	1.039273	1.015339	0.37	0.976566	1.014919	1.00128	77.13006	28.65921	2.32044	39.27337	14.91936	1.282688	0.267273	0.26101	0.088333
1.078459	1.03	0.36	0.955	1.029928	1.002742	1.039941	1.015339	0.36	0.976566	1.015571	1.00150	78.45893	29.92828	2.74185	39.94086	15.5712	1.500829	0.274814	0.268374	0.089714
1.079827	1.03	0.35	0.955	1.031235	1.00317	1.040628	1.015339	0.35	0.976566	1.016242	1.00172	79.82695	31.23474	3.170103	40.6276	16.24185	1.722431	0.282577	0.275955	0.091081
1.081236	1.03	0.34	0.955	1.032581	1.003605	1.041335	1.015339	0.34	0.976566	1.016932	1.00194	81.23644	32.5808	3.605471	41.33472	16.9324	1.947627	0.290576	0.283766	0.092431
1.08269	1.03	0.33	0.955	1.033969	1.004048	1.042063	1.015339	0.33	0.976566	1.017644	1.00217	82.68993	33.96888	4.048243	42.06346	17.64406	2.176565	0.298824	0.291822	0.093762
1.08419	1.03	0.32	0.955	1.035402	1.004499	1.042815	1.015339	0.32	0.976566	1.018378	1.00240	84.1902	35.40164	4.498731	42.81516	18.37815	2.409397	0.307339	0.300137	0.095073
1.08574	1.03	0.31	0.955	1.036882	1.004957	1.043591	1.015339	0.31	0.976566	1.019136	1.00264	85.74028	36.88196	4.957267	43.59129	19.13609	2.646291	0.316136	0.308728	0.09636
1.087344	1.03	0.3	0.955	1.038413	1.005424	1.044393	1.015339	0.3	0.976566	1.019919	1.00288	87.34351	38.41306	5.424208	44.39348	19.91948	2.887424	0.325236	0.317614	0.097621

$^{34}S/^{32}S$						$^{33}S/^{32}S$						$\delta^{34}Srr$	$\delta^{34}Sip$	$\delta^{34}Spp$	$\delta^{33}Srr$	$\delta^{33}Sip$	$\delta^{33}Spp$	$\Delta^{33}Srr$	$\Delta^{33}Sip$	$\Delta^{33}Spp$
Rrr	**Ro**	**F**	**α(p-r)**	**Rip**	**Rpp**	**Rrr**	**Ro**	**F**	**α(p-r)**	**Rip**	**Rpp**									
1.089004	1.03	0.29	0.955	1.039998	1.0059	1.045224	1.015339	0.29	0.976566	1.02073	1.003133	89.0036	39.99844	5.899939	45.22351	20.73007	3.132987	0.334658	0.326816	0.098854
1.090725	1.03	0.28	0.955	1.041642	1.006385	1.046083	1.015339	0.28	0.976566	1.02157	1.003383	90.72461	41.64201	6.384873	46.08337	21.56978	3.383188	0.344426	0.336355	0.100053
1.092511	1.03	0.27	0.955	1.043348	1.006879	1.046975	1.015339	0.27	0.976566	1.022441	1.003638	92.51109	43.34809	6.879459	46.97526	22.44076	3.638248	0.354567	0.346258	0.101217
1.094368	1.03	0.26	0.955	1.045122	1.007384	1.047902	1.015339	0.26	0.976566	1.023345	1.003898	94.3681	45.12153	7.384182	47.90161	23.3454	3.898409	0.365108	0.356552	0.10234
1.096301	1.03	0.25	0.955	1.046968	1.0079	1.048865	1.015339	0.25	0.976566	1.024286	1.004164	96.30129	46.96773	7.899571	48.86516	24.28638	4.163933	0.376082	0.367269	0.103417
1.098317	1.03	0.24	0.955	1.048893	1.008426	1.049869	1.015339	0.24	0.976566	1.025267	1.004435	98.31703	48.89277	8.4262	49.869	25.26669	4.435107	0.387524	0.378443	0.104444
1.100423	1.03	0.23	0.955	1.050904	1.008965	1.050917	1.015339	0.23	0.976566	1.02629	1.004712	100.4225	50.90351	8.9647	50.91658	26.28973	4.712242	0.399477	0.390116	0.105414
1.102626	1.03	0.22	0.955	1.053008	1.009516	1.052012	1.015339	0.22	0.976566	1.027359	1.004996	102.6259	53.00777	9.515761	52.01186	27.35934	4.995684	0.411986	0.402332	0.106319
1.104937	1.03	0.21	0.955	1.055214	1.01008	1.053159	1.015339	0.21	0.976566	1.02848	1.005286	104.9366	55.21445	10.08015	53.15932	28.47991	5.285801	0.425105	0.415143	0.107152
1.107365	1.03	0.2	0.955	1.057534	1.010659	1.054364	1.015339	0.2	0.976566	1.029656	1.005583	107.3652	57.53377	10.6587	54.36412	29.65648	5.583019	0.438894	0.428609	0.107904
1.109924	1.03	0.19	0.955	1.059978	1.011252	1.055632	1.015339	0.19	0.976566	1.030895	1.005888	109.9242	59.97759	11.25235	55.63222	30.89486	5.8878	0.453423	0.442798	0.108564
1.112628	1.03	0.18	0.955	1.06256	1.011862	1.056971	1.015339	0.18	0.976566	1.032202	1.006201	112.6279	62.55968	11.86216	56.97055	32.20183	6.20066	0.468775	0.45779	0.109119
1.115493	1.03	0.17	0.955	1.065296	1.012489	1.058387	1.015339	0.17	0.976566	1.033585	1.006522	115.4934	65.29624	12.48929	58.38724	33.58532	6.52218	0.485046	0.47368	0.109554
1.118541	1.03	0.16	0.955	1.068206	1.013135	1.059892	1.015339	0.16	0.976566	1.035055	1.006853	118.5408	68.20645	13.13509	59.89191	35.05473	6.853016	0.50235	0.490578	0.109854
1.121794	1.03	0.15	0.955	1.071313	1.013801	1.061496	1.015339	0.15	0.976566	1.036621	1.007194	121.794	71.31328	13.80106	61.49608	36.62131	7.193915	0.520825	0.50862	0.109997
1.125282	1.03	0.14	0.955	1.074645	1.014489	1.063214	1.015339	0.14	0.976566	1.038299	1.007546	125.2822	74.64454	14.48894	63.21365	38.29863	7.545731	0.540634	0.527965	0.109959
1.129041	1.03	0.13	0.955	1.078234	1.015201	1.065062	1.015339	0.13	0.976566	1.040103	1.007909	129.0412	78.23431	15.20075	65.06166	40.10333	7.909453	0.561982	0.548812	0.109711
1.133115	1.03	0.12	0.955	1.082125	1.015939	1.067061	1.015339	0.12	0.976566	1.042056	1.008286	133.1152	82.12502	15.93884	67.06126	42.05608	8.286237	0.58512	0.571408	0.109216
1.137561	1.03	0.11	0.955	1.08637	1.016706	1.069239	1.015339	0.11	0.976566	1.044183	1.008677	137.5606	86.3704	16.70599	69.23922	44.183	8.677445	0.610369	0.596065	0.10843
1.14245	1.03	0.1	0.955	1.09104	1.017506	1.07163	1.015339	0.1	0.976566	1.046518	1.009085	142.4501	91.03981	17.50555	71.63	46.51775	9.084711	0.63814	0.623186	0.107296
1.14788	1.03	0.09	0.955	1.096225	1.018342	1.074279	1.015339	0.09	0.976566	1.049105	1.00951	147.8795	96.22495	18.34158	74.27911	49.10478	9.510022	0.66898	0.653304	0.105742
1.15398	1.03	0.08	0.955	1.102051	1.019219	1.077248	1.015339	0.08	0.976566	1.052004	1.009956	153.9797	102.0506	19.21916	77.24831	52.00441	9.955842	0.703632	0.687143	0.103674
1.160935	1.03	0.07	0.955	1.108693	1.020145	1.080624	1.015339	0.07	0.976566	1.055301	1.010425	160.9348	108.6927	20.1447	80.62445	55.30143	10.4253	0.743141	0.725726	0.100962
1.169016	1.03	0.06	0.955	1.11641	1.021127	1.084535	1.015339	0.06	0.976566	1.05912	1.010922	169.0159	116.4102	21.12664	84.53507	59.12041	10.92248	0.789048	0.770558	0.097429

$^{34}S/^{32}S$						$^{33}S/^{32}S$						$\delta^{34}Srr$	$\delta^{34}Sip$	$\delta^{34}Spp$	$\delta^{33}Srr$	$\delta^{33}Sip$	$\delta^{33}Spp$	$\Delta^{33}Srr$	$\Delta^{33}Sip$	$\Delta^{33}Spp$
Rrr	**Ro**	**F**	**α(p-r)**	**Rip**	**Rpp**	**Rrr**	**Ro**	**F**	**α(p-r)**	**Rip**	**Rpp**									
1.178647	1.03	0.05	0.955	1.125607	1.022176	1.089179	1.015339	0.05	0.976566	1.063655	1.011453	178.6465	125.6074	22.1765	89.17862	63.65514	11.45296	0.843759	0.823987	0.092814
1.190541	1.03	0.04	0.955	1.136967	1.023311	1.094889	1.015339	0.04	0.976566	1.069232	1.012025	190.5415	136.9671	23.31077	94.88894	69.23165	12.02467	0.911335	0.88998	0.086712
1.206054	1.03	0.03	0.955	1.151782	1.024555	1.102295	1.015339	0.03	0.976566	1.076464	1.01265	206.054	151.7816	24.55503	102.295	76.46417	12.64989	0.999463	0.976042	0.078445
1.228262	1.03	0.02	0.955	1.17299	1.025954	1.112818	1.015339	0.02	0.976566	1.086741	1.01335	228.2616	172.9898	25.95384	112.8184	86.74099	13.34987	1.125617	1.09924	0.066699
1.267177	1.03	0.01	0.955	1.210154	1.027604	1.131042	1.015339	0.01	0.976566	1.104537	1.014171	267.1768	210.1539	27.60427	131.0415	104.5371	14.17053	1.346636	1.31508	0.048214